

ACTA TECHNICA

Volume 61 (2016), Number 4A

ISSN 0001-7043



Institute of Thermomechanics AS CR, v.v.i.

Publisher

Institute of Thermomechanics CAS, v.v.i.
Czech Academy of Sciences

Jiří Plešek Head of the Publisher

Editor

Ivo Doležel Editor-in-Chief, Production Editor and Managing Editor

Editorial Board

Bernard Baron • Silesian University of Gliwice, Poland
Pavel Chráska • Institute of Plasma Physics CAS, Czech Republic
Miloš Drdácý • Institute of Theoretical and Applied Mechanics CAS, Czech Republic
Petr Filip • Institute of Hydrodynamics CAS, Czech Republic
Arun K. Gupta • M. S. College, Saharanpur, India
Zbyněk Jaňour • Institute of Thermomechanics CAS, Czech Republic
Pavel Karban • University of West Bohemia, Czech Republic
Dobroslav Kováč • Technical University of Košice, Slovakia
Miklós Kuczmann • Széchenyi István University of Győr, Hungary
Marian Pasko • Silesian University of Gliwice, Poland
Jiří Plešek • Institute of Thermomechanics CAS, Czech Republic
Jaromír Příhoda • Institute of Thermomechanics CAS, Czech Republic
Josef Tlustý • Czech Technical University in Prague, Czech Republic
Pavel Záskalický • Technical University of Košice, Slovakia

Editorial Office

Address: Acta Technica
Institute of Thermomechanics CAS, v.v.i.
Dolejšková 5
182 00 Praha 8, Czech Republic

E-mail: journal@it.cas.cz *Phone:* +420 26605 2058 *Fax:* +420 28689 0433

Home Page: <http://journal.it.cas.cz/>

Subscription Information

Address: Ivo Doležel
Kolínská 19/1666
130 00 Praha 3

E-mail: dolezel@it.cas.cz *Phone:* +420 72324 8626

CONTENTS

ANG WANG, JING HUANG: Research and implementation of open source cloud computing platform based on Open Stack	001–010
JUAN XIONG: Research on static image feature extraction based on hierarchical structure and sparse representation	011–024
XU ZHANG, BINGZHI CHEN, JITAO LI: A study on reliability of high-speed passenger transport network based on complex network analysis	025–038
BINWU JI, RUI HUANG: Network anomaly traffic monitoring based on improved immune genetic algorithm	039–048
KANGMING LIU: Wireless sensor network target coverage algorithm based on energy saving	049–062
LIJUN MAO: Research on the data processing and rotation mode transfer of cloud computing based on the virtual machine (VM)	063–074
BI RONGRONG: An efficient face recognition algorithm based on multi-kernel regularization learning	075–084
HONGLAI YAN: Research on bridgeless PFC circuit control algorithm of electric vehicle charging pile	085–094
CANBIN YIN, MIN WANG: Stability control and consolidation sedimentation analysis on soft soil foundation subjected to surcharge preloading treatment	095–108
PING HUANG: Fault diagnosis system of wind turbine gearbox based on GRNN and fault tree analysis	109–122
YINGLIU CUI: Robust radar waveform algorithm based on beam steering vector estimation	123–132
JIAOZHEN ZHAO: Gauge point positioning method based on computer vision	133–140
JUN HE: Research on hand movement recognition based on static image decomposition	141–150
YUN MIAO: A study on control system of electronic treadmill based on neural network theory	151–160
BAOYING LI, JIANGUANG QI: Key technology simulation of equipment anomaly detection based on image processing	161–168

JISONG BAI, LONGJIE PANG, QIANG ZHANG: Underwater robots detection based on image segmentation	169–180
HONGLIAN WANG, HU CHEN, WEI HE: Home control system design based on internet of things	181–188
JIANRONG BU, JUNYAN XU: Research on time optimal trajectory planning of 7-DOF manipulator based on genetic algorithm	189–200
REN DUAN, DINYI FANG, KAIGUO QIAN: A local location-based self-adjusting deployment algorithm for MSN	201–214
HANG YANG, XIAOQING LI, BING WU: A hybrid model for scale forecast of regional highway network	215–228
JINGYAN WU, QINGDONG YAN, CHENG LIU, WEI WEI: Cascade design and optimization for hydraulic torque-retarder assembly	229–246
ZEYU YU, HUAYUN YU, YUNCAI ZHOU: Research on virtual technology of data caching and data real-time allocation in cloud computing	247–256
WENBING JIN, SUO ZHANG, YINNI JIN: Research on the winding control system in winding vacuum coater	257–268
ZHAOZHUN ZHONG, MIAO GUAN, XINPEI LIU: Hybrid discrete-time modelling and explicit model predictive control for brushed DC motor speed control	269–280
JUAN ZOU: Batch delivery scheduling with simple linear deterioration on a single machine	281–290

Research and implementation of open source cloud computing platform based on Open Stack

ANG WANG¹, JING HUANG¹

Abstract. Implementation of open source cloud computing platform based on Open Stack is developed. Open Stack is a cloud computing operating system which aims to provide an open source cloud computing platform for both public and private clouds. In terms of infrastructure as a service (IaaS) platform, the Open Stack cloud platform faces a resource allocation limitation problem. This paper involves a customization of Open Stack Dashboard (horizon) to generate virtual network requests and then processing these requests. It also uses Open-Stack Computer to provide bandwidth limitations for the virtual network requests, as well as a modification of the data structure used between the Open Stack Horizon and Nova Modules. It implements a proposed virtual network embedded problem algorithm (VNE-Greedy) on top of the Open Stack Cloud platform. This paper also includes extended research of the Open Stack cloud computing system and its associated virtual network embedding strategies.

Key words. Evaluation model, implementation, open source, cloud computing platform, Open Stack..

1. Introduction

Cloud computing involves a large number of computers connected through a communication platform such as the Internet. It is similar to utility computing. Cloud computing is also defined as a large-scale distributed computing model. Here, the cloud providers and users can have their own private infrastructure, and several types of services can be provided to clients using virtual machines hosted by the providers. It includes utilization techniques for improving the efficiency of the system. These include: Network utility, Disk I/O utility, CPU utilization of a system as well as available memory for performing operations. Cloud Computing is a term that renames some common technologies and techniques that we know in IT. It can be understood to mean data center hosting [1–2]. The principal concept of computing goes back to the 1950s.

¹Henan University of Chinese Medicine, Henan, 450046, China

This includes things like processing power resources at each node and bandwidth resources on the links that the embedding must fulfill [3]. For example, to run an experiment, a researcher may need 1 GHz of CPU for each virtual node and 10 Mbps for each virtual link [4]. Added to these requirements are the constraints on location and any link propagation delay problems [5]. In another example, a gaming service needs virtual nodes in many cities, as well as virtual links with very small propagation delays. These combinations of node and link constraints would make the embedding problem computationally difficult to approach and solve, see [6–7]. Figure 1 shows a simple virtual network request and how it was mapped on a substrate network.

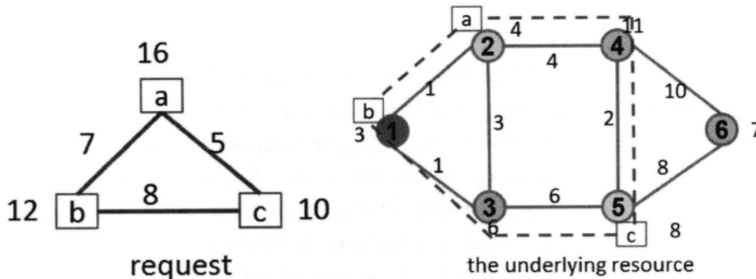


Fig. 1. Virtual network embedding

2. Open Stack overview

In 2012, the Open Stack community was deeply involved in core technology development, as well as deploying and managing Open Stack projects [8]. Currently, Open Stack consists of seven core components: Compute, Object Storage, Block Storage, Network, Dashboard, Image Service and Identity. Few studies or research have conducted to test the usage and the benefits of implementing virtual network embedding strategies within the Open Stack cloud operating system architecture. Currently, there is much need for this type of research since Open-Stack is a new and emerging Internet technology, and as such, is facing a resources allocation problem. Open Stack is the leading cloud computing technology and it has now received attention from members of the scientific community. In this chapter, we provide a brief introduction to Open Stack, including its components, development, and research status. We also provide a brief introduction into the current research and study implications for connecting Open Stack and virtual networking. In this paper, we will discuss the virtual network embedding problem and the existing strategies for solving this problem. Open Stack is a cloud operating platform which controls resources of computing, networking and storage throughout a datacenter, in which all are managed through a dashboard that gives administrators control and authorizes their users to use resources through a web interface (dashboard). The goals of the Open Stack originality are to support cloud services and allow businesses to

build cloud services in their own data centers. Open Stack is available under the Apache 2.0 license freely, referred as "the Linux of the Cloud" and also comparing to Eucalyptus and the Apache Cloud Stack projects. Open Stack has a modular architecture that currently has three main components: compute, storage and image service [9–10].

3. Open Stack model and algorithm

Open Stack consists of a modular architecture along with various codes for the components. It also has several shared services which extend the three main components (computing, storage and networking). This makes it much easier to implement and operate on your own cloud. These services integrate the Open Stack components with each other along with external systems to deliver an integrated experience for users.

1. Open Stack Computer Nova is a cloud computing controller (considered as the IaaS system's main component). It uses Python language as well as many external libraries like Event let, Kombu (for AMQP communication), and SQL Alchemy (for database access). Nova's architecture is designed to be scaled horizontally on substrate hardware with no additional hardware or software requirements. This simultaneously provides the ability to integrate it with current legacy systems and third party technologies. Nova is designed to manage pools of computer resources and it can work with almost all available virtualization technologies. It can also work with high-performance computing (HPC).
2. Open Stack Object Storage (Swift) is a scalable storage system in which objects and files are written to multiple disks in the data center servers. Open Stack ensures data replication and integrity across the cluster. Storage clusters scale simply by adding new servers. If a server or a hard driver fails, Open Stack replicates its content to new locations in the cluster. Due to the fact that Open Stack uses software logic to ensure data replication and distribution across different devices, inexpensive servers and hard drivers can be used.
3. Open Stack Block Storage (Cinder) provides the software to create and manage a service that provides storage in the format of block devices known as Cinder volumes. Cinder provides persistent storage to guest virtual machines (instances) which are managed via Open Stack Compute. It can also be used independently with other Open Stack services.
4. Open Stack Network (Neutron) provides virtual networking service for the compute module. The networking module can manage IP addresses, which allows for dedicated DHCP or IPs. Network module suits the requirements of applications or user groups.
5. Open Stack Dashboard (Horizon) gives users and administrators an interface to access, automate and provide cloud resources. The design makes it easy

to plug in as well use third party products and services. This includes such things as monitoring, billing, and management tools. The dashboard can be customized for service providers and vendors who desire to use it. Dashboard is also a way to interact with Open Stack software resources.

6. Open Stack Image Service (Glance) provides location and delivery for services for disks and server images. It has the ability to snapshot and copy a server image and store it away. This is a something very useful about the Open Stack cloud operating system. The stored snapshots and images can be used to get servers mining faster and more consistently. It also can be used to catalogue and store many backups.
7. Open Stack Identity (Keystone) controls the central directory of users mapped to the Open Stack services and can access it. It works as an authentication system across every part of the cloud operating system and can be integrated with already existing backed directory services such as LDAP. The Keystone module supports many types of authentication, including username and password credentials, as well as AWS-style and token based systems.

Open Stack Compute (Nova) is a controller for cloud computing and managing large networks of virtual machines (VMs). Open Stack Object Storage is a storage system that provides support for both block storage and object storage. Image Service is a Service which provides discovery as well as registration for visual disk images. Among many Open Stack services and projects (the list is growing with every release), only Compute is considered within this paper. Compute or "Nova" is the service responsible for providing a compute provisioning function to clouds. It can be considered as a management layer which operates on top of a free option of supported hypervisors, exposing a REST API for the purpose of management and provisioning. It consists of a set of service binaries that work together to accomplish one common goal. They all interact directly through messaging and through a shared state which is stored in a central database. This is shown in Fig. 2. To interact with other services, we can directly target the REST API or use the Python language provided by in the Python-Nova client library. This also includes a command-line client. Other interfaces, such as the web-based Dashboard, use this as client libraries for interacting with the different Open Stack services as well. Provisioning requests, which enter the API and then pass the initial authorization and verification, will step before being sent out to the Nova-scheduler to decide which one of the available compute nodes should be handling the request. Our main focus of this chapter is the customization of the Nova Open Stack main component. The actual code for the Nova services are in. /nova and the corresponding unit tests are in the related directory under nova tests. The following represents a short explanation of the Nova source directory structure.

The basic equation of key algorithm is

$$(N, sk) \leftarrow Key(1^k), \quad (1)$$

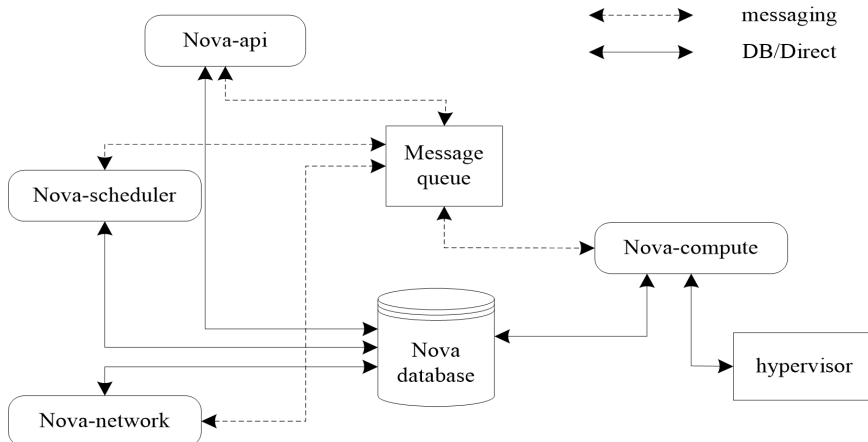


Fig. 2. Open Stack compute architecture overview

where N is the node number, sk is the scheduler and k is the database dimension. This formula is used to generate file checksum parameter which is denoted as

$$\begin{aligned} r &\leftarrow \{0, 1\}^k; sk \leftarrow \{e, d, r\}; \\ \text{Output}\{N, sk\}; \end{aligned} \quad (2)$$

where r is the hypervisor. The Euler function is

$$\phi(N) = (p - 1)(q - 1), \quad (3)$$

where p, q are the parameters of the file storage block. The function $\phi(N)$ satisfies the following constraints

$$\gcd(e, \phi(N)) = 1, \quad 1 < e < \phi(N), \quad (4)$$

where e is the natural constant and $\gcd()$ returns the maximum common divisor.

4. Experiment and discussion

The Hardware Layer and the Virtualization Layer are operated by the cloud services provider, while the Client Layer is provided by the end users. Basically, clouds can be defined in three ways.

1. Private Clouds: where data and processes are managed in the organization without security exposures and legal required menu.
2. Public Clouds: where a set of computers and computer network resources, in which a service provider provide resources (like storage and applications) is available to the general public over the Internet.

3. Hybrid cloud: a combination of two or more clouds (private, public and community) that remain different entities but bound together. These provide the benefits of multiple cloud models. Therefore, hybrid cloud means the ability to connect, manage and dedicate services with cloud resources. A hybrid cloud service crosses isolation boundaries so it cannot simply be categorized as a private, public or community cloud. Virtual network embedding (VNE) has been a major challenge for future Internet (FI). The problem of embedding virtual networks within a substrate network is the main resource allocation in network virtualization.

The target of the VNE problem is the allocation of virtual resources in nodes and links. Therefore, it is divided in two sub problems: first, Virtual Node Mapping (VNoM), where virtual nodes are mapped in physical nodes; and second, Virtual Link Mapping (VLiM), where the virtual links linking virtual nodes have to be mapped on paths connecting these nodes in the substrate network. Future Internet architectures have been evolving to become based on the Infrastructure as a Service (IaaS). This is a model that divides the role of current Internet Service Providers (ISPs) into two new main roles: first, the Infrastructure Provider on P which deploys and keeps the network equipment operating; and second, Service Provider (SP). Service provider (SP) is responsible for deploying various network protocols and providing end to end services. For example, Voice over IP (known as VoIP) can run on a virtual network which provides anticipated performance.

This is done by provisioning dedicated resources and employing routing protocols which can ensure fast recovery from any equipment failures that might occur. On the other hand, online banking runs on a virtual network that provides security guarantees. This is done through addresses and secure routing protocols. Making efficient usage of the substrate resources demands effective techniques for virtual network embedding (a new virtual network mapping). The VNE problem is extremely difficult for two main reasons, the first of which being node and link constraints. Each VN request has resource limitations.

Open Stack Compute scheduler is also known as the Nova-scheduler service. It is responsible for mapping instance requests onto the physical hosts named compute nodes. Compute nodes execute the Nova-compute service on top of a hypervisor. When the scheduler service is launched, it will load a scheduler driver which holds the actual scheduling logic and policies. A scheduler driver is derived from a base driver class and implements interface. A number of simple scheduler drivers are included in Open Stack Nova. Advanced filters can be written as long as they able to implement the required interface of the base driver. In addition to defining the interface requirements, it also holds some of the basic requirements which are needed by every scheduler; this includes easy access to the global system state and some utility methods used by most schedulers. Figure 3 shows us the existing network and connected virtual bridges. When entering the command to view virtual bridge and virtual network port status we bet the Fig. 4.

The core Open Stack services are: API, Compute, Scheduler and Network. We also need the Glance Image Service as a guest of OS images (which is backed using the Swift Storage Module Service). We will now dive into each of these services,

```
root@IPL213: /home/openstack# ovs-vsctl list-br
br-eth1
br-int
root@IPL213: /home/openstack# ovs-vsctl list-ports br-eth1
eth1
phy-br-eth1
root@IPL213: /home/openstack# ovs-vsctl list-ports br-int
int-br-eth1
tap215779b8-aa
tap24ebecf2-1a
tap556ebc58-c8
tap9f9a565a-e1
tapba36604e-e9
```

Fig. 3. Obtain VN information

and I will explain each one's job and task within the module. API is the HTTP interface used in Nova. Compute communicates with the hypervisor serving each host (usually one Compute service for each host). Network manages IP address real-time communicating with the routers, switches, firewalls and other devices. Scheduler chooses the most appropriate computing node from the available pool (though it may also be used in selecting the Volumes). The database is not considered to be a Nova service, but a database can be retrieved directly from any of Nova services (however it should not be accessed via the Compute service). We can also run a stand-alone Authentication service or Volume service for disk management, but this is not required. Open Stack Nova uses AMQP (also known as Rabbit MQ) as the communication pass between the services. AMQP messages are written to special queues and one of the related services picked for processing. This is actually how Nova scales. If you find a single Compute node that can't handle the requests number, you can throw in another Compute node service. The same goes for the other services. Figure 5 shows the Iperf bandwidth test and Fig. 6 shows the Iperf client side bandwidth test.

Figure 7 below is snapshot of the use of the tool iperf to test the bandwidth between IPL2 1 2 and IPL2 1 3 before implementing the proposed method. As we call notice, the bandwidth is not limited and it has allocated large resources of bandwidth for the given request. The initial allocation for the bandwidth is 83 0 Mbit/sec. Furthermore, if AMQP is considered to be the only way to communicate with the Services, how do the users issue commands? The answer is definitely the API service. This service is an HTTP service (a WSGI application known in Python). The API service listens for the coming REST commands via the HTTP service and interprets them into AMQP messages for those services. Similarly, responses from the services come in via AMQP and the API service turns them into valid HTTP responses in the format the user has requested. Open Stack currently uses EC2 (API) and Open Stack. However, it is not only API that communicates with the services. Services can also communicate with each other.

```

root@IPL213: /home/openstack# ovs-vsctl show br-int
OFPT_FEATURES_REPLY (xid=0x1): ver: 0x1, dpid: 00007e2e3d4a0940
n_tables: 255, n_buffers: 256
features: capabilities: 0xc7, action: 0xfff
 1(tap556ebc58-c8): addr: fe: 16: 3e: af: ff: 54
   config: 0
   state: 0
   current: 10MB-FD COPPER
 2(tap215779b8-aa): addr: fe: 16: 3e: 6e: 4a: 81
   config: 0
   state: 0
   current: 10MB-FD COPPER
 4(tap24ebecf2-1a): addr: fe: 16: 3e: 39: 86: fd
   config: 0
   state: 0
   current: 10MB-FD COPPER
 5(tap9f9a565a-e1): addr: fe: 16: 3e: ba: d2: bc
   config: 0
   state: 0
   current: 10MB-FD COPPER
 6(tapba36604e-e9): addr: fe: 16: 3e: 97: 52: f5
   config: 0
   state: 0
   current: 10MB-FD COPPER
 7(int-br-eth1): addr: 8a: bc: e5: 63: 0b: cb
   config: 0
   state: 0
   current: 10MB-FD COPPER
LOCAL(br-int): addr: 7e: 2e: 3d: 4a: 09: 40
   config: PORT_DOWN
   state: LINK_DOWN
OFPT_GET_CONFIG_REPLY (xid=0x3): frags=normal miss_send_len=0

```

Fig. 4. Virtual bridge status

```

root@openstack-virtual-machine: /home/openstack# iperf -s -D
root@openstack-virtual-machine: /home/openstack# Running Iperf Server
as a daemon
The Iperf daemon process ID: 3846

```

Fig. 5. Iperf bandwidth test

```

root@openstack-virtual-machine: /home/openstack# iperf -c 10.0.1.7
-----
Client connecting to 10.0.1.7, TCP port 5001
TCP window size: 22.9 Kbyte (default)
-----
[ 3] local 10.0.1.5 port 51594 connected with 10.0.1.7 port 5001
[ ID] Interval      Transfer    Bandwidth
[ 3] 0.0-10.1 sec   93.4 Mbytes 77.7 Mbits/sec

```

Fig. 6. Iperf client side bandwidth test

Figure 8 shows the bandwidth allocation after implementing the method proposed in this thesis between the nodes IPL2 1 2 and IPL2 1 3. Compute may need to communicate with Network and Volume to get the necessary resources. If we are not careful with how we organize the source code, all of this communication will experience problems. Therefore, for our initial article, let us dive into the Service and RPC mechanism will be using the Python unites notation for the modules, methods and functions. Specifically, `nova.compute.api`: APL run the instance connects to the run instance method of the API class in the `./novalcompute/api.py` file. With the exception of the API service, each Nova service must have a related Python module to handle RPC command marshaling. For example: The network service has `.lnovalnetworklapi.py`. The compute service has `.lnovalcomputelapi.py`. The scheduler service has `./nova/scheduler/api.py`. These modules are usually just large collections of functions that make the service do something. However, sometimes they contain classes that have methods to do something. It all depends on if we need to intercept the service calls. We will touch on these use cases a little later.

5. Conclusion

Through this paper, our objective was to implement, evaluate and demonstrate of VNE strategy in Open Stack. And that was done by first conducting research on related cloud computing and virtualization moreover by gaining an understanding of the Open-Stack Operating system more specifically Dashboard (Horizon) and Compute (Nova) architecture and its scheduler component. Later, a working test bed built using Open-Stack was set up and used to implement a scheduler for initial VMs nodes. Finally, the test bed was used to validate and conduct experimental evaluation to showcase its performance.

Customization and modification of the Open Stack Horizon, by customizing the GUI interface for the users to input the nodes and links intend to be embedded in Open Stack, intensive reading and comprehends for Open Stack source code, this all was required along with a good commend of Python and Django to accomplish this task (Customizing Open Stack Dashboard). We also used debugging tools such PDB to capture the data flow and parameters handling in the fabric of the Open Stack.

```
[ 3] local 10.0.2.5 port 37327 connected with 10.0.2.4 port 5001
[ ID] Interval      Transfer    Bandwidth
[ 3] 0.0-10.0 sec   990 Mbytes  830 Mbits/sec
```

Fig. 7. Bandwidth between VMs in IPL212 and 213

```
root@openstack-virtual-machine: ~# iperf -c 10.0.2.4
-----
Client connecting to 10.0.2.4, TCP port 5001
TCP window size: 22.9 Kbyte (default)
-----
[ 3] local 10.0.2.5 port 36155 connected with 10.0.2.4 port 5001
[ ID] Interval      Transfer    Bandwidth
[ 3] 0.0-11.0 sec   3.75 Mbytes  2.87 Mbits/sec
```

Fig. 8. Bandwidth between IPL 212 and IPL 213 after implementing VNE

References

- [1] B. J. LIU: *Consideration on improving the efficiency in open-stack borrowing*. Journal of Baoding University (2005), No. 4, 107–108.
- [2] T. NAKAI: *Architectural planning and design for the library as a place*. J Information Science & Technology Association 63 (2013), No. 6, 228–234.
- [3] M. J. BENNETT, D. T. BUXTON, E. CAPRIOTTI: *Shelf-reading in a large, open-stack library*. J Academic Librarianship 5 (1979), No. 1, 4–8.
- [4] L. DE GIOVANNI, G. MASSI, F. PEZZELLA: *An adaptive genetic algorithm for large-size open stack problems*. IJ Production Research 51 (2013), No. 3, 682–697.
- [5] H. LI, Y. WAN, G. MA: *A CPU-GPU hybrid computing framework for real-time clothing animation*. Proc. IEEE IC on Cloud Computing and Intelligence Systems, 15–17 Sept. 2011, Beijing, China, 391–396.
- [6] S. XI, C. LI, C. LU, C. D. GILL, M. XU, L. T. X. PHAN, I. LEE, O. SOKOLSKY: *RT-Open Stack: CPU resource management for real-time cloud computing*. Proc. IEEE 8th IC on Cloud Computing, 27 June–2 July 2015, New York, USA, 179–186.
- [7] K. RUI: *Research on cloud computing system based on open stack platform*. J Chongqing University of Science and Technology (Natural Sciences Edition) 17 (2015) No. 1, 122–124.
- [8] R. KUMAR, K. JAIN, H. MAHARWAL, A. DADHICH: *Open source infrastructure as a service cloud computing platform*. IJ Advancement in Engineering Technology, Management and Applied Science 1 2014, No. 2, 681–684.
- [9] A. BABAR, B. RAMSEY: *Tutorial: Building secure and scalable private cloud infrastructure with open stack*. Proc. IEEE 19th International Enterprise Distributed Object Computing Workshop IEEE, 21–25 Sept. 2015, Adelaide, Australia, 166–166.
- [10] A. BARKAT, A. D. DOS SANTOS, T. T. N. HO: *Open stack and cloud stack: open source solutions for building public and private clouds*. Proc. 16th IS Symbolic and Numeric Algorithms for Scientific Computing, 22–25 Sept. 2014, Timisoara, Romania, 429–436.

Research on static image feature extraction based on hierarchical structure and sparse representation¹

JUAN XIONG²

Abstract. A new technique to improve feature extraction task is proposed. The main benefit of using scaling process is to avoid attributes in greater numeric ranges dominating those in smaller numeric ranges. Moreover, the adoption of this developed technique achieves best accuracy with low computational complexity for object recognition. Note that, through experiment, the method has been proven to be accurate at 63.75%. We concluded that the recognition of image is hard and complicated not only because of the handwriting ambiguity but also due to the similarity between characters and their positions in a word. This paper has presented a simple scheme for binary template selection in a context of feature extraction based on entropy. It is experimentally shown that the proposed algorithm can be employed to select an effective template. In addition, this method uses low computational processes, which provide hierarchical sparse method (HSM) to increase recognition rate within fewer computations and short time.

Key words. Static image, feature extraction, hierarchical structure, sparse representation.

1. Introduction

The first stage in image recognition is how to make a computer know the content of image, regarding that computer can only process mathematical computations. Scientists proposed to compute the likelihood between digital images, but the remaining problem is the likelihood of what [1–2]. Composed of hundreds of pixels, an image set incurs a huge amount of calculations that computers can hardly afford. Depending on the scientific fact mentioned previously, in computing with images, it is more suitable to work with both the notions of digital image and analog image. The image function is a mathematical model that is frequently used in analysis where it is profitable to consider the object (i.e. image) as a function of two variables. Consequently, for analyzing images, all of functional analysis is then available. The

¹The author acknowledges the National Natural Science Foundation of China (Grant 51578109 and Grant 51121005).

²Huanghuai University, Henan, 463000, China

digital image is just a 2D rectangular matrix of discrete values. In order to allowing the image to be stored in a 2D computer memory structure, both image space and intensity range are quantified into a discrete set of values [3–5]. Figure 1 shows the instance of mathematical vision of image.

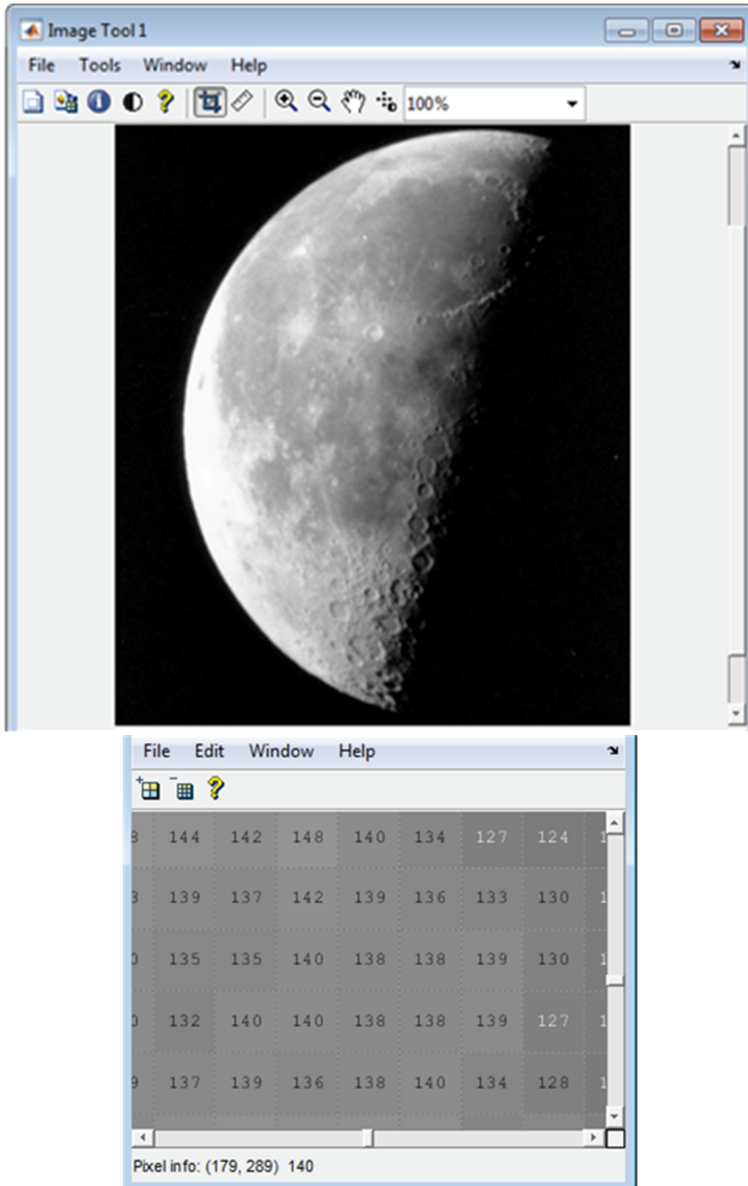


Fig. 1. Instance of mathematical vision of image

2. Feature extraction

The significance of feature extraction is mainly due to three reasons [6]:

Data Reduction: Feature extraction can be viewed as a powerful data reduction tool via reducing the space of measurement and storage requirements. For instance, when a machine learning program is given too many variables to operate, a large number of features do not always lead to better decision and the running time space storage also increases. Therefore, it is necessary to select a much smaller number of features as they are more important and more relevant.

Automatic Investigation and Data Mining: In many classical applications, discriminatory and informative features are often selected as a priori experts in the field of feature extraction, i.e., investigators pick out which are the most important variables to build a model. More and more often in modern data-mining applications, however, there is a growing demand for fully automated "black-box" type of prediction models that are capable of identifying the important features on their own. The need for such automated systems arises for two reasons. On one hand, there are economic needs to process large amounts of data in a short period of time with a little manual supervision. On the other hand, sometimes the problem and the data are so novel moreover, there are simply no field experts who can understand the data well enough and be able to pick out the important variables prior to the analysis. Under such circumstances, automatic exploratory data analysis becomes the key. Instead of relying on pre-conceived ideas, there is a need (as well as interest) to let the data speak for it.

Data Visualization: The last but not the least application of feature extraction that shares the flavor of exploratory data analysis is data visualization. Here, this concept can be best understood by considering examples of its applications. The human eye has an amazing capability in recognizing systematic patterns in the data. At the same time, human eyes are usually unable to make good sense for data if it is more than three dimensions. To maximize the use of the highly developed human faculty in visual identification, we often wish to identify two or three of the most informative features in the data so that we can plot the data in a reduced space.

3. Hierarchical sparse method and algorithm

The basic assumption underlying hierarchical learning algorithms is that each input can be decomposed to a hierarchy of parts of increasing size with increasing semantic complexity. In fact, the hierarchy is useful for reducing the sample complexity of the problem. Given the representation of the smallest parts, the hierarchical architecture recursively builds at each layer a representation of the next larger parts by using a combination of sparse coding and pooling operations. Intuitively, the sparse coding step induces discrimination while the pooling step induces invariance in the architecture. Thus, the alternating applications of the sparse coding and pooling operations yield a complex representation of the input data with non-trivial discrimination and invariance properties. As natural images, can be sparsely represented by a set of localized, oriented filters, therefore, by imposing the norm

regularization on representation coefficients, sparse coding can be solved efficiently.

Recent progress in computer vision has demonstrated that sparse coding is an effective tool for representing visual data at different levels, e.g. image classification and image delousing. In simple word, a code is sparse if most of its components are zero. The idea is based on a simple concept that high dimensional signals can be represented as a linear combination of very small number of basis function taken from dictionary. Commonly, intensity record is an 8-bit (1-byte) number which permits values of 0 to 255. It is worth mentioning that 256 different levels is generally enough to satisfy the consumer and also mostly represents the precision available from the sensor, as well as bytes suitable for computers. The following definitions are intended to clarify important concepts and also to establish notation used through this research. An image is generally 3D, but mostly represented in 2D on the computer. Analog images are 2D images $F(x, y)$ which have infinite precision in spatial parameters x and y and infinite precision in intensity at each spatial point (x, y) . Digital images are 2D images [row; col] represented by a discrete 2D matrix of intensity samples, each of which being represented by using a limited precision. It can be stored in physical memory (like hard drives) and is easier to process. Raster images are represented as a 2D array of pixels. A pixel is the smallest visual element of a picture. The resolution is defined as the total number of pixels in a picture. Aspect Ratio refers to the ratio of width to height of a picture. Binary images are the digital images that comprised of two possible colors for each pixel (i.e. white (1) and black (0)). Gray scale images are comprised of only shades of gray (i.e. no color) in between white (255) and black (0). Color images are the digital images that are formed by a combination of different colors for each pixel. The depth of an image denotes the number of shades of color in between 1 and 0 in a picture. A coordinate system must be used to address individual pixels of an image (as shown in Fig.1); to operate on it in a computer program, refer to it in a mathematical formula, or to address its device-relative coordinates. The mathematical model of an image as a function of two real spatial parameters is enormously useful in both describing images and defining operations on them. A picture function is a mathematical representation $f(x, y)$ of a picture as a function of two spatial variables x and y , where symbols x and y are real values defining points of the picture and $f(x, y)$ is usually a real value describing the intensity of the picture at point x, y .

Formally, if x is a column signal and D is the dictionary (whose columns are the atom signals), the sparse representation of x is obtained by carrying out the following optimization

$$\min \|s\|_0 \text{ s.t. } x = Ds, \quad (1)$$

where s is the sparse representation of x and $\|\cdot\|_0$ is the pseudo norm which counts the non-zero entries. The nonlinear mapping approach has been defined as the following nonlinear mapping function

$$N^v = f(x^v, T_u) \quad (2)$$

where T_u is the image patch of size u . The single matrix T_u is defined as

$$T_u = [t_1, t_2, \dots, t_m] = \begin{bmatrix} t_{11} & t_{21} & \dots & t_{m1} \\ t_{12} & t_{22} & \dots & t_{m2} \\ \dots & \dots & \dots & \dots \\ t_{1n} & t_{2n} & \dots & t_{mn} \end{bmatrix},$$

where t_i is the i th candidate. Figure 2 illustrates the sparse coding operation. Through this research, in particular, the goal of sparse coding is to represent a training image signal x approximately as a weighted linear combination of small numbers of dictionary (e.g. basis vectors). Generally, in the class of hierarchical architectures that we have considered in suggested technique, the inputs to the sparse coding operation will in general have different lengths from layer to layer. To cope with this problem, we have defined the sparse coding S on a sufficiently large space which contains all the possible inputs which works with the restrictions of S on the appropriate domains of the inputs.

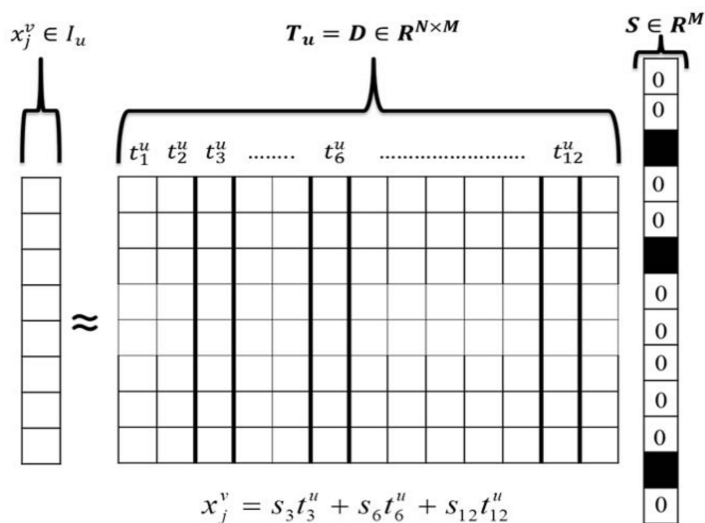


Fig. 2. Scheme of sparse coding operation

A spatial pooling stage is a very important step in many of the computer vision architecture. Since it combines the responses of feature detectors obtained at adjacent locations into some statistic that summarizes the joint distribution of the features over some region of interest. It is worth mentioning that, the pooling operation is typically an average, a max, a sum, or more rarely some other commutative (i.e., independent of the order of the contributing features) combination rules. Meanwhile, the pooling operation can be described as a function that summarizes the content of a sequence of values with a single value, similar to aggregation functions used in voting schemes and database systems. Following sparse coding, the inputs to the

pooling operation generally have different lengths at different layers but the actions of pooling operation on input values is not related to the layers of sparse coding. We now turn to describe the mathematical framework formalizes the hierarchical structure of the architecture, that each input is composed of parts of increasing size. Figure 3 shows the domains of nested patch.

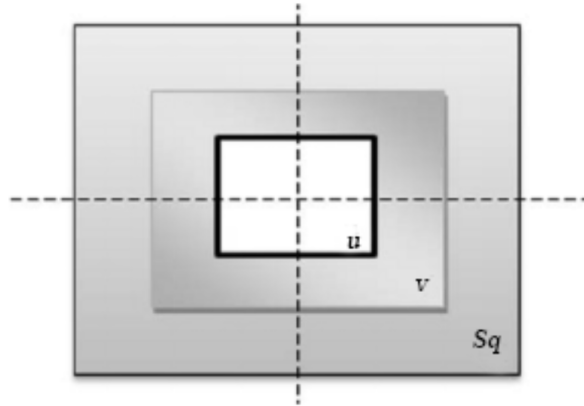


Fig. 3. Domains of Nested patch

4. Experiment result and data analysis

Feature extraction is a long-standing research topic in computer vision. It has become the main focus and objective of most researches in the areas of both computer vision and machine learning because the good feature extraction is a central to achieve high performance in any computer vision task. Nevertheless, there is still a need to develop efficient feature extraction algorithm that can represent an informative properties of an object. This paper is concerned with problems of developed hierarchical feature extraction method to perform a successful recognition target. The latter refers to approach of computer Science interested in giving the computer human learning capability. In other words, how to build an efficient predictive model using a computer? In this part, overview feature extraction is considered. Definition of Feature Extraction: Indeed, feature can be defined as a scale on which human can easily recognize a collection of objects. On the other hand, feature extraction can be defined as the problem of finding the most relevant and informative set of features to improve the data representation for classification and regression task. Actually, we are able to extract informative features in our everyday lives. For example, we can easily identify person's sex from a distance, without examining full characteristics of the person. This is because a certain signature for the two genders was known, e.g., body shape, hair style, or perhaps a combination of the two. In other words, we can say that, it is not necessary for us to process all the charac-

teristics of items to be capable to recognize them. In this sense, the goal of feature extraction method is finding feature which is informative and relevant in order to give the computer its ability to understand and simulate the operation of the human vision system. To produce such plots, feature extraction is the crucial analytical step. Feature Extraction and Feature Selection Feature extraction is one of the key steps in both computer vision and machine learning. It becomes the focus of much research, because a good feature extraction is a central to achieve high performance in any computer vision task. Actually, feature extraction includes simplifying the amount of resources required to distinguish a large set of data accurately. Practically, feature extraction concept can be decomposed into two consecutive phases: feature construction and feature selection. On one hand, in feature construction the step obtaining all features that appears reasonable but it causes increase in the dimensionality of the data and thereby immerses the relevant information into a sea of possibly irrelevant, noisy or redundant features. Here, we can point out some of generic feature construction approaches including: basic linear transforms of the input variables (PCA/SVD, LDA); clustering; singular value decomposition (SVD); applying simple functions to subsets variable like products to create monomials; more sophisticated linear transforms like spectral transforms, wavelet convolutions or transforms of kernels.

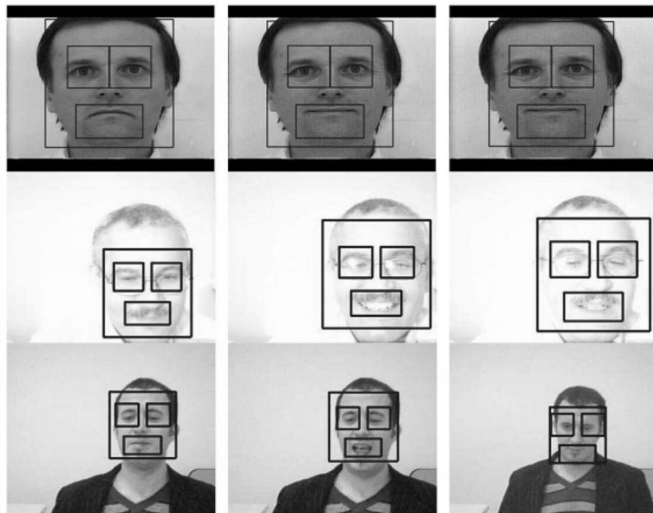


Fig. 4. Example of feature extraction for face recognition problem

Nested Feature Subset Selection Methods A number of learning machines extract features as part of the learning process. Practically, there are two types of nested methods: (1) backward elimination styles and (2) forward selection styles. These contain neural networks whose internal nodes are feature extractors. Figure 4 shows the example of feature extraction for face recognition problem. **Definition of Feature Hierarchies:** is a technique used features composed of image patches during a

learning step. Indeed, such tactic was often based on natural modeling, motivated by the structure of the primate visual cortex. Mainly due two reasons this algorithm is successful: First, they detect common object components that characterize the different objects within the class and secondly, the components are combined in a way that allows differences can be learned from training data. To make this notion clearer this example can be taken: the part itself (such as an eye in face detection) is decomposed into own optimal components (e.g. eye corner, eye pupil, eyelid, etc.), and the allowed variations in the configuration of the sub-parts are learned from the training data (an example is given in Figure 5).

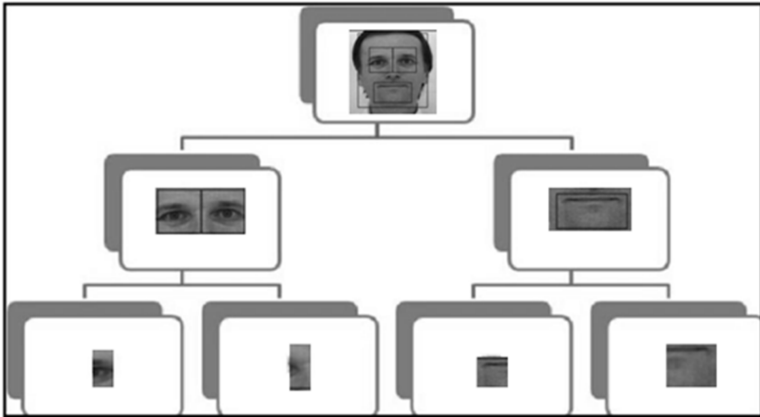


Fig. 5. Examples of the hierarchies used in the proposed algorithm

The hierarchical architecture has a key semantic component; a dictionary of templates that is usually learned from data. The templates will play the role of the sparsely through the proposed model, where this template is used as set of the dictionary in the sparse coding operation. The advantage to this idea of representation is the template set which is adapted to the data. The template also links the architecture to the underlying distribution of the input data. One way to create template is to sample from the probability distribution on the function space. Finally, the paper determines template sets as $T_u \subset \text{Im}(u)$ and $T_v \subset \text{Im}(v)$, that are considered to be finite, discrete, and endowed with the uniform probability measure (see Fig.6). Actually, the success for the sparse representation features depends heavily on a good choice of dictionary.

Experimental result show that for some classes of signals, learned dictionaries can be benefited from template sets, which ultimately lead to a similar/better recognition performance in comparison with other classical methods. For more detail, please refer to [7–10]. In this paper, we applied proposed method on the two domains images and speech.

For the domain of images, we evaluated hierarchical sparse on the well-known MNIST digit recognition benchmark, and COIL-30 dataset. In the other hand for the speech, isolated words speech recognition is selected. We tested our recognition algorithm using training data and testing data from two distinct vocabularies. After

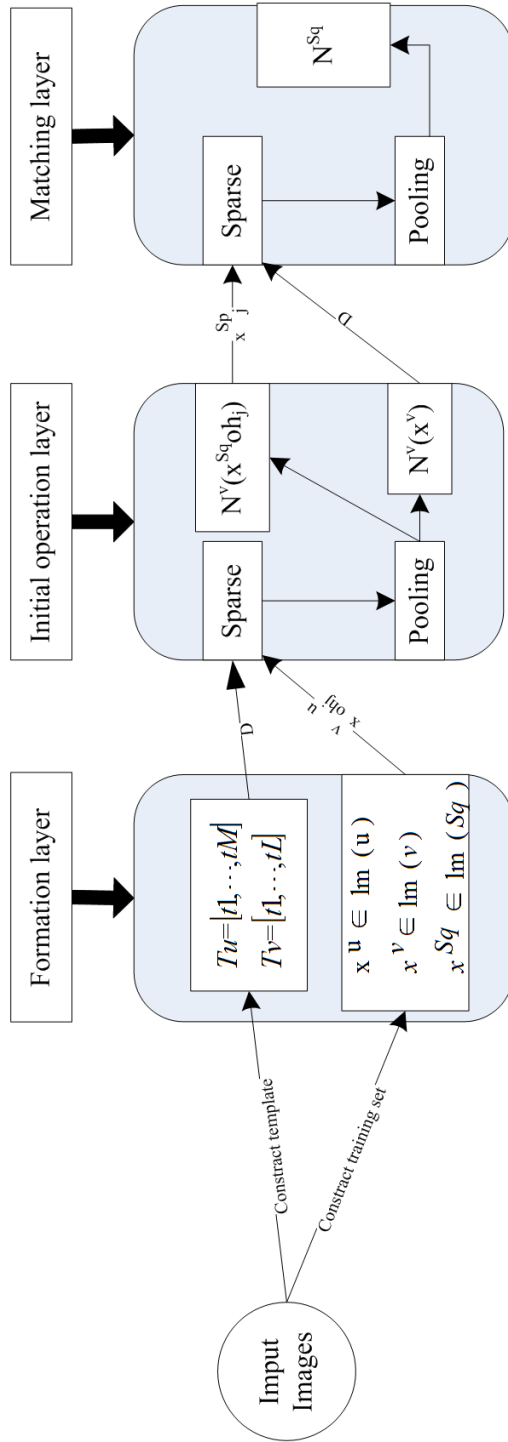


Fig. 6. Layered proposed hierarchical structure of sparse representation method

that we used the representation as a feature extraction step for a classification algorithm such as Support Vector Machines (SVM) and 1-Nearest Neighbors (1NN). We first verified developed method with object recognition experiments using the M-NIST hand-written digit recognition benchmark, where there are 70.000 data examples, and each is of 28×28 gray scale images. In the experiments, we used some images randomly selected from the MNIST data set. We considered eight classes of images: 2s through 9s (see Fig. 7).

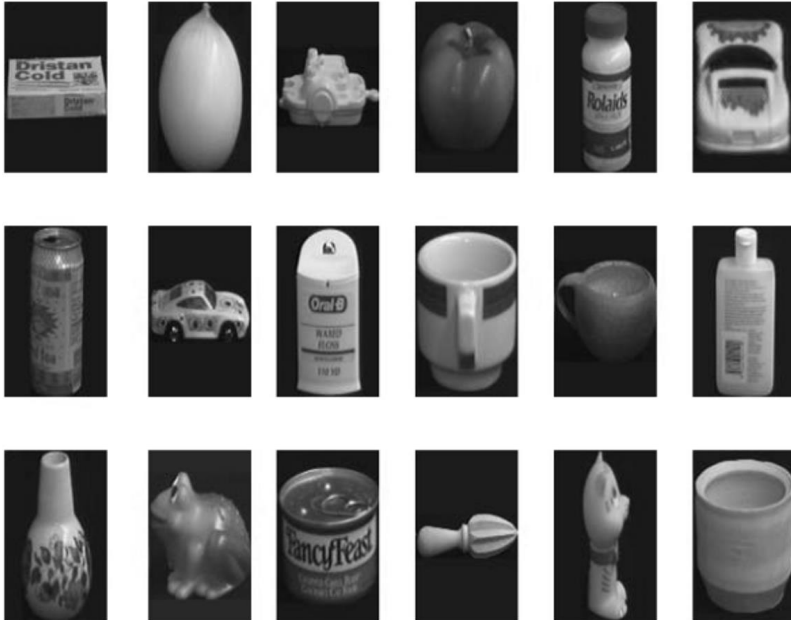


Fig. 7. Eighteen instances from the set of training examples for Coil-30

The digits in this dataset include a small amount of natural translation, found in a corpus containing the handwriting of human subjects. The labeled image sets that we have used contain 5 examples per class, while the out-of-sample test sets contain 30 examples per class. The Tu and Tv are template sets constructed by randomly extracting 500 image patches (of size u and/or v) from images, which are not used in the train or test sets (in experiments we set $D = Tu$). For the digit dataset, templates of size 10×10 pixels are large enough to include semi-circles and distinct stroke intersections, while larger templates, closer to 20×20 , are seen to include nearly full digits where more discriminatory structure is present. For the experiments we set the first layer template $u = 11 \times 11$ pixels and the second layer template $v = 19 \times 19$ pixels. After the features are learned we can obtain classification accuracy by applying a k -NN with $k = 1$ and SVM note that classifier are averaged over 50 random test sets, holding the training and template sets fixed. Experiment is performed under the same Smale's environment, comparison of results shows that the

developed model consistently outperforms the Smale's methods. Here we adapted our model to the case of one-dimensional of length n . We built a template in this setting by considering patches that are segmentation of original signal(i.e. the word is segmented into sub-word units as shown in Fig. 8, and the transformations are taken to be all possible translations. In the experiment, the used dataset consists of seven different names of fruit consists of "apple", "banana", "kiwi", "lime", "orange", "peach", and "pineapple". The algorithm is tested for the percentage of accuracy. We tested the ten utterances of each seven words, while the training was done five utterances of each seven words (i.e. the first 5 utterances in the corpus are kept as training set. The left utterances are used for testing.) We tested proposed method for the speech signals as an input instead of the images; features extracted from the speech signal are passed to each word as shown in Fig. 9.

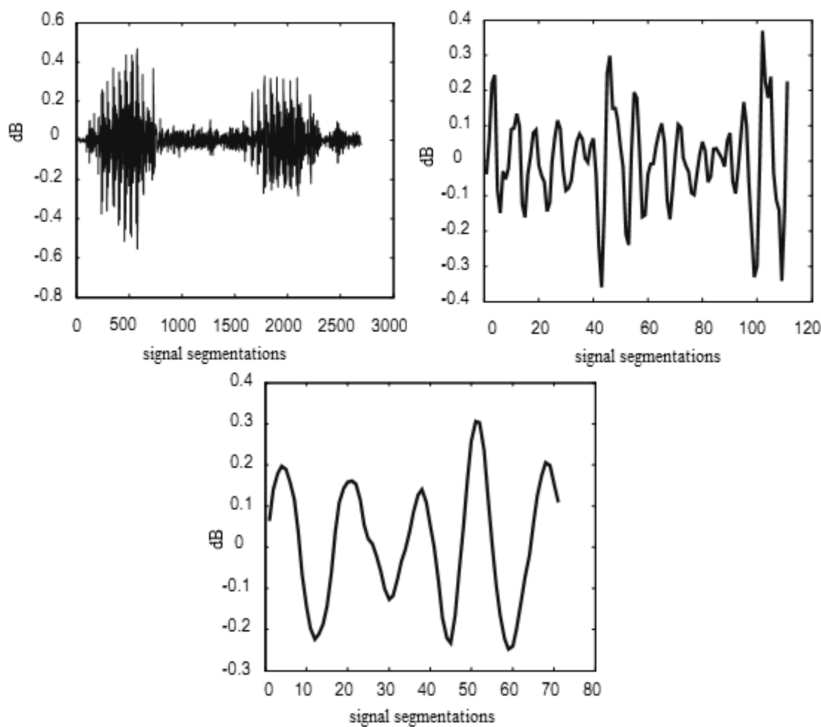


Fig. 8. One example from the set of template (Isolated Word Speech): up left–full word (Apple) of size 2694, up right–subword (Apple) of size 110, bottom–subword (Apple) of size 70

5. Conclusion

Feature extraction algorithms considered as a pillar key task to make vision modeling systems fully operative. It has been effectively utilized to minimize the

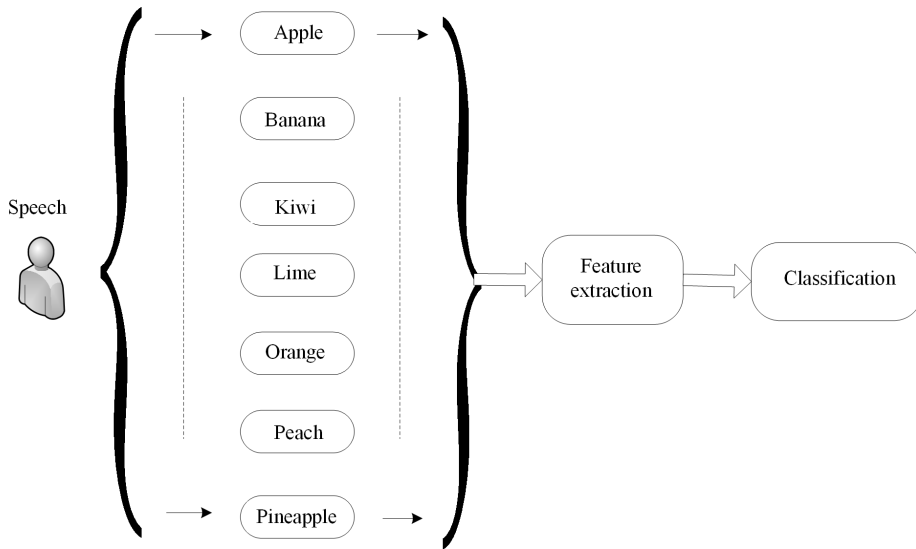


Fig. 9. Isolated Word Speech recognition process

computation difficulty and to perform ideal classification through extraction of the significant pattern information. An essential component of a successful classification system is the selection of an effective object features. Throughout this paper, we seek to tease out basic principles that underlie the recent in hierarchical feature extraction method. The paper introduces a new algorithm for template selection based on the entropy concept. Algorithm suggests picking of the template of more information and discards the templates of less information. The proposed method provides HSM with better discriminatory ability. Experimental results show that the introduced method achieves good performance in template selection with fewer computation processes and shorter time.

References

- [1] F. J. PULIDO, L. MANDOW, J. L. PEREZ-DE-LA-CRUZ: *Dimensionality reduction in multiobjective shortest path search*. *Computers & Operations Research* 64 (2015), 60 to 70.
- [2] A. A. AGAFONOV, V. V. MYASNIKOV: *Method for the reliable shortest path search in time-dependent stochastic networks and its application to GIS-based traffic control*. *Computer Optics* 40 (2016), No. 2, 275–283 (in Russian).
- [3] F. J. PULIDO, L. MANDOW, J. L. PEREZ-DE-LA-CRUZ: *Multiobjective shortest path problems with lexicographic goal-based preferences*. *European Journal of Operational Research* 239 (2014), No. 1, 89–101.
- [4] M. MAIRE, X. Y. STELLA, P. PERONA: *Reconstructive sparse code transfer for contour detection and semantic labeling*. *Lecture Notes in Computer Science*, 90069 (2014), 273–287.

- [5] S. ZHANG, X. XU, L. LU, Y. CHEN: *Sparse code multiple access: An energy efficient uplink approach for 5G wireless systems*. Proc. IEEE Globecom 2014—Wireless Networking Symposium, 8–12 Dec. 2014, Austin, TX, USA, 4782–4787.
- [6] D. NI, H. MA: *Hyperspectral image classification via sparse code histogram*. IEEE Geoscience and Remote Sensing Letters 12 (2015), No. 9, 1–5.
- [7] K. BADNI: *Windows and mirrors – interaction design, digital art, and the myth of transparency*. The Design Journal (An International Journal for All Aspects of Design) 7 (2004), No. 1, 57–58.
- [8] X. W. LIU: *Environmental art design based on digital technology*. Applied Mechanics & Materials 543–547 (2014), 4145–4148.
- [9] S. DHAKAL, A. BAYESTEH, S. HRANILOVIC, A. MOBASHER, T. SEXTON: *Sparse codes for MIMO channel and detector alternatives for sparse code*. Patent PCT/US2011/055361, <http://www.google.st/patents/US20130182791>.

Received November 16, 2016

A study on reliability of high-speed passenger transport network based on complex network analysis¹

XU ZHANG², BINGZHI CHEN², JITAO LI²

Abstract. On the basis of relative theories of complex network, a high-speed passenger transportation network using Pajek software is proposed and its topological characteristics as well as network structure are analyzed. Analyzed is also its reliability under two kinds of attacks, and suggestions on its construction recommended. The research in this paper helps to complete the overall network structure of high-speed passenger transportation, strengthens the node stability and enhances the connection, reliability and effectiveness of high-speed passenger transportation network.

Key words. Integrated transportation, reliability, global efficiency, high speed passenger transportation network, complex network.

1. Introduction

After years of efforts, China has gradually built the civil aviation network, which is centered by Beijing, Shanghai, Guangzhou and other hub airports with the airports in provincial capital and key cities as the backbone and under close relation among various main and feeder airports. In recent years, density of civil air routes has been increased and the connection among various civil airports has become increasingly close. The continuous improvement and advancement of civil aviation network enables the passengers to travel more conveniently and faster. Along with the rapid development of civil aviation industry, China's high-speed rail has entered a period of leapfrog development. Four Horizontal and Four Lengthwise high-speed rail networks are built, by which, the distance in time and space among different regions has been dramatically shortened and the tiring long journey of rushing about for Chinese passengers has been changed.

¹This research was supported by the National Social Science Foundation major research project (No. 13&ZD170), and LiaoNing Doctoral Scientific Research Foundation (No. 201501182).

²School of Traffic and transportation Engineering, Dalian Jiaotong University, Dalian, 116026, China

Foreign scholars have first started their study of complex network in the end of the 20th century. A. L. Barabási and R. Albert revealed scale-free characteristic of a complex network through their study [1]. On this basis, research fellow from different scientific research fields have paid their attention to complex networks and conducted researches on topological characteristics, reliability, complexity and other parameters [2]. Other scholars in traffic and transportation field have also applied the analytical methods for complex network in analysis of transportation network and made some researches on complexity of civil aviation and railway and other transportation networks [3]. Chinese scholars have also applied theories concerning complex network into researches in transportation field [4]. To be more specific, they analyzed topological property of civil aviation network, railway network and urban rail network, and they utilized two methods of random attack and attempted attack to study the reliability of transportation network [5], [6]. Because of a relatively shorter history of high-speed rail in China, scholars have only completed few researches on characteristics of complex network related to high-speed rail. Thus, there are only few complex analyses of the high-speed passenger transport network composed of high-speed rail and civil aviation. Based on the above mentioned works, this paper gives an analysis of the characteristics of the complex network of high-speed passenger transport, discusses its stability and provides corresponding suggestions on construction of the network.

2. Basic model structures of complex network

At present, complex network is mainly divided into two types, namely small-world network and scale-free network, of which, the construction algorithm is as follows.

2.1. *Small-world network model*

The construction algorithms for small-world network model starts from the rule network: it is assumed to be a nearest-neighbor coupled network containing N nodes forming a loop, among which, each node is connected with all adjacent $K/2$ nodes to the left and right (K being an even number). It must also satisfy randomization reconnection: to reconnect each edge in the network with the probability P randomly, that is to say, to remain one of the endpoint of the edge to be reconnected unchanged and the other endpoint is randomly selected in the network. Wherein, there can only be one edge between any two different nodes and no edge of any node can be connected to itself.

In order to guarantee the network sparsity, the requirement $N \ll K$ shall be met so that the network model to be built can be of a higher clustering coefficient. And the randomization reconnection process greatly declines the average path length of the network, thus the network model possesses the small-world characteristics. When P is relatively small, the randomization reconnection process exerts little influence on network clustering coefficient. When $P = 0$, the model degrades into a rule network. When $P = 1$, the model degrades into random network. That is to say,

transition from a completely rule network into a completely random network of the model can be realized by adjusting the value of P .

2.2. Scale-free network model

A large number of empirical studies show that degree distribution function of many large-scale real networks (such as the Internet, metabolic networks, etc.) presents in the form of a power-law distribution $P(k) \sim k^{-\gamma}$. In such networks, degree of most nodes is relatively smaller, however, a small amount of nodes are of quite big degree with no characteristic scaling. Such kind of network is called scale-free network for there is no distinctive characteristic scaling of the connectivity degree of its nodes.

The construction algorithms for small-world network model includes is based on the following assumptions: at the initial moments, it is assumed that the network already contains m_0 nodes, and in each time step afterwards, a node with the connectivity degree of m ($m \leq m_0$) is added, and the newly added node is connected to the m existing nodes in the network without repeated connection. Then, during selection of connection point for new nodes, the probability Π_i of the connection between a new node and an existing node i is in direct proportion to the degree k_i of node i , which can be written in the form

$$\Pi_i = \frac{k_i}{\sum_j k_j}. \quad (1)$$

3. Construction of high-speed passenger transport network

High-speed passenger transport network refers to the high-speed passenger transport complex formed in the socialized transportation coverage and during united transportation process in accordance with the technical and economic characteristics of high-speed rail and civil aviation. Such complex is under coordination and distribution of responsibilities, organic combination, orderly organization and close connection. For the ease of study, the paper gives the following assumptions for Construction of the complex of high-speed rail and civil aviation network:

1. High-speed passenger transport network is a complex network built in p space. It is defined, according to flight or number of high-speed rail, that an air route or a train with the same number passing through every two cities, it is regarded that there is an edge between the two cities.
2. High-speed passenger transport network is a undirected weighted network. As long as every two cities are connected via airplanes or trains, no matter where they are going, an edge without vector pointing between the two cities shall be erected, that is to say, if one can get to city B from city A and vice versa, it is regarded that city A and city B are connected. No matter how far it is or how many airlines or trains connections are between the two connected cities, the weight is considered 1, namely, the departure frequency and number of the

high-speed trains and airlines in the high-speed passenger transport compound network is not taken into account.

3. In case there is high-speed rail station and airport in one city, or there are two and more airports or high-speed rail stations in one city, it is regarded that the city is a node.

4. Analysis of characteristics of high-speed passenger transport network

4.1. Construction of civil aviation sub-network

The data concerning civil aviation sub-network is obtained from the flight schedule in the summer of 2015 and covers 10,093 flights (except for flights from Hong Kong, Macao and Taiwan) from more than 20 airlines in China, and 196 airway destinations. With the use of Pajek, the topological graph of civil aviation network is obtained (as shown in Fig. 1).

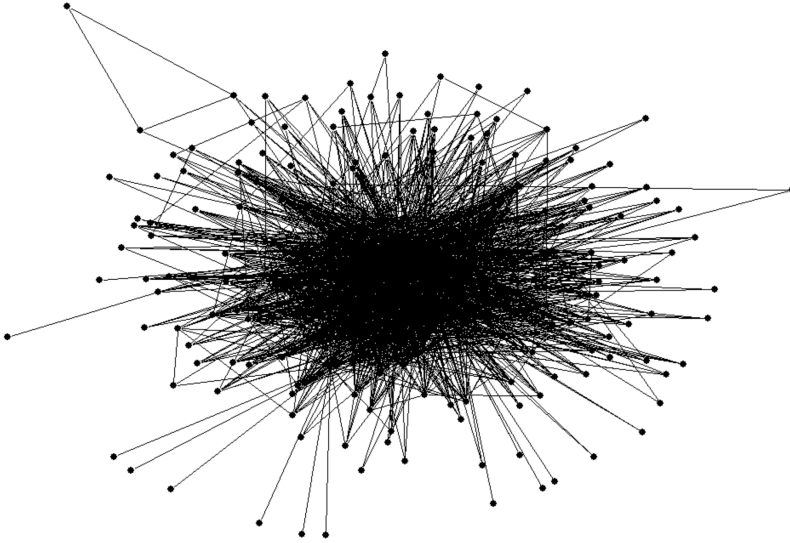


Fig. 1. Topological graph of civil aviation network

4.2. Construction of high-speed passenger transport network

The data of high-speed rail sub-network is obtained from statistics of the operation scheme of the high-speed rail, motor car and interurban rail. This network involves in about 4,000 high-speed trains and 425 high-speed rail stations. Refer to Fig. 2 for the network topological graph.

4.3. Construction of high-speed rail sub-network

The high-speed passenger transport network composed of 579 nodes and 14,312 edges is established according to the assumed conditions and in combination with relevant data of the civil aviation network and high-speed rail sub-network. The topological graph of high-speed passenger transport network is shown in Fig. 3.

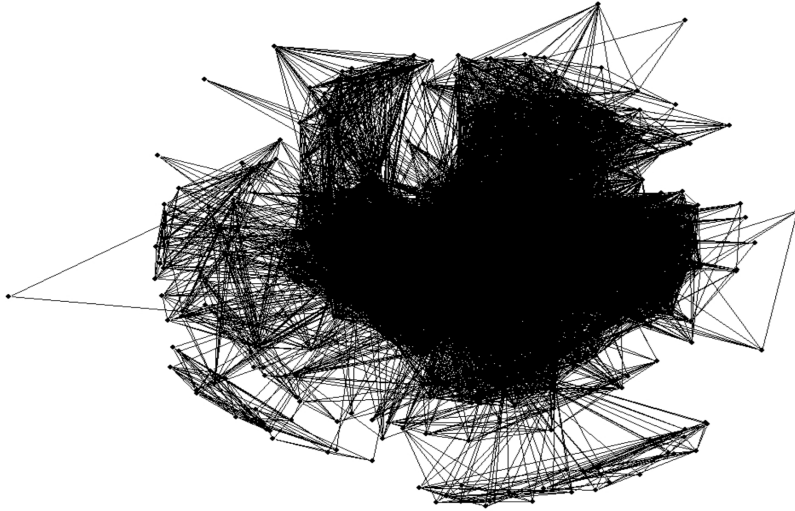


Fig. 2. Topological graph of high-speed rail sub-network

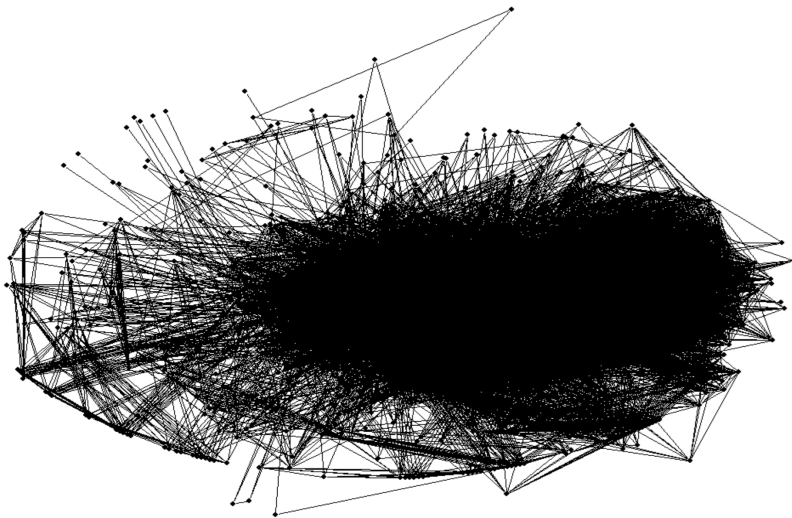


Fig. 3. Topological graph of high-speed passenger transport network

5. Numerical solution and discussion

The topological characteristic parameters of the high-speed passenger transport network and its sub-networks are obtained by statistical analysis, whose results are shown in Table 1.

Table 1. Comparison of network characteristics

Network	Number of nodes	Average degree	Average path length	Clustering coefficient
Civil aviation sub-network	196	19.67	2.058	0.8013
High-speed rail sub-network	425	56.18	2.195	0.7401
High-speed passenger transport network	579	47.43	2.248	0.7728

It is found (using Table 1) that the high-speed passenger transport network and its sub-network is of bigger clustering coefficient and shorter average path length and shows characteristics of small-world network.

Meanwhile, the degree distribution diagram and cumulative degree distribution diagram of high-speed passenger transport network and its sub-network is obtained by statistical analysis (as shown in Figs. 4–9).

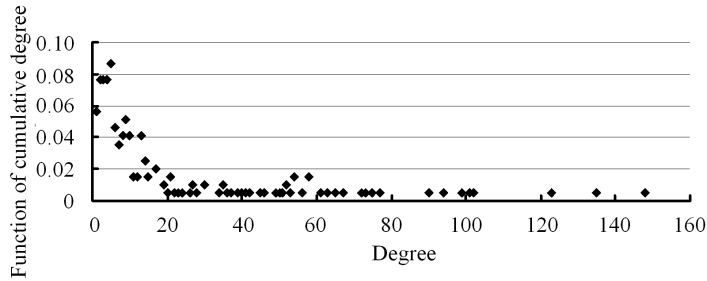


Fig. 4. Degree distribution diagram of civil aviation sub-network

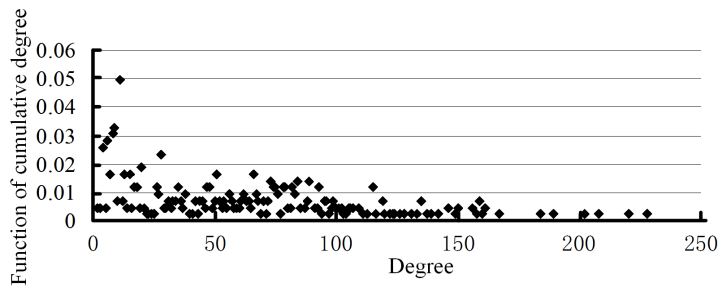


Fig. 5. Degree distribution diagram of high-speed rail sub-network

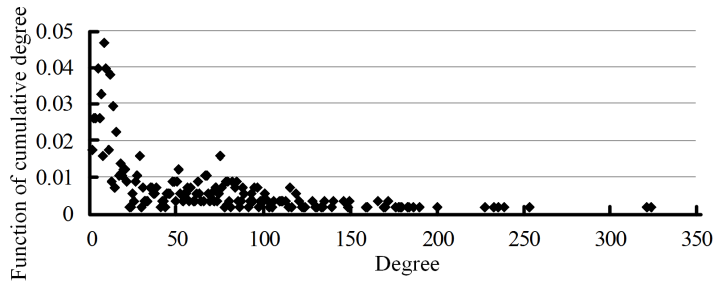


Fig. 6. Degree distribution diagram of high-speed passenger transport network

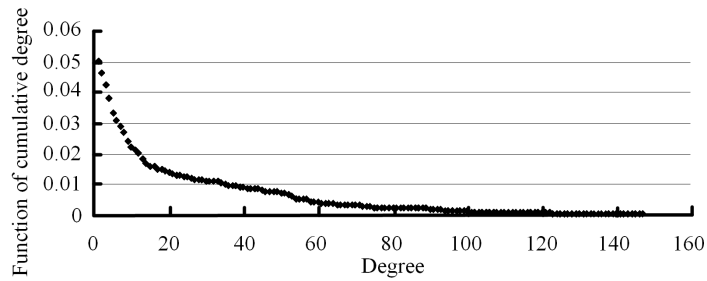


Fig. 7. Cumulative degree distribution of civil aviation sub-network

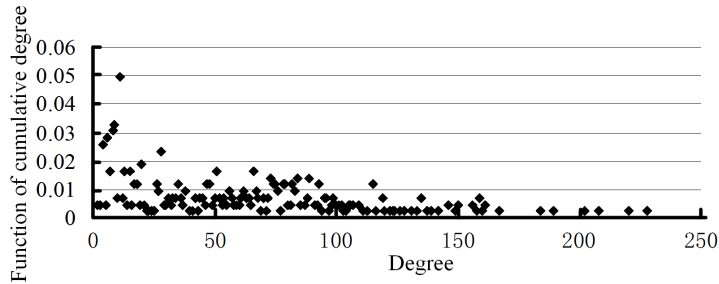


Fig. 8. Cumulative degree distribution of high-speed rail sub-network

From Figs. 4–9 we can see that the degree distribution of high-speed passenger transport network, high-speed rail network and civil aviation network conform to power-law distribution and cumulative degree distributions also follow exponential distribution with scale-free characteristics. Hence, the high-speed passenger transport network, high-speed rail network and civil aviation network are all scale-free small-world complex network.

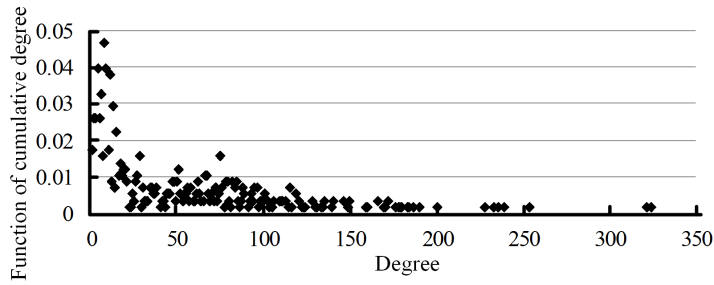


Fig. 9. Cumulative degree distribution of high-speed passenger transport network

6. Reliability analysis of high-speed passenger transport network

6.1. Measurement index for reliability of high-speed passenger transport network

The reliability of complex networks refers to the performance of the network to resist the impact brought by fault in case of attack or change in structure. Network attack comprises two modes, namely attempted attack and random attack. The former is also called targeted attack, refers to destruction of network nodes by certain strategies, among which, the strategy of deleting nodes generally starts from the biggest node of the network and the highest node is removed each time.

Reliability of high-speed passenger transport network can be measured by the global efficiency of the network under attack, which is calculated through the shortest distance E^{global} between the nodes via the following formula

$$E^{\text{global}} = \frac{\sum_{i=1}^n \sum_{j=1}^n \frac{1}{d_{ij}}}{N(N-1)} \quad (2)$$

Here, N represents the total amount of nodes in the network, V denotes the set of points of the network nodes, d_{ij} is the distance between the nodes i and j ($i, j \in V, i \neq j$). The global efficiency is the average efficiency of the local sub-graph, plays a similar role as that of the clustering coefficient C , and represents the efficiency of the compound network with some nodes deleted. Thus, $E^{\text{local}} \approx C$.

6.2. Reliability analysis of high-speed passenger transport network

With the use of Pajek and R-software, the variation diagram of the global efficiency of civil aviation sub-network under two attack modes was calculated and shown in Fig. 10.

It is found using Fig. 10 that the resistance of civil aviation sub-network to attempted attack is dramatically stronger than that to random attack as its global efficiency declines to 0 under attempted attack to about 60 nodes and about 180

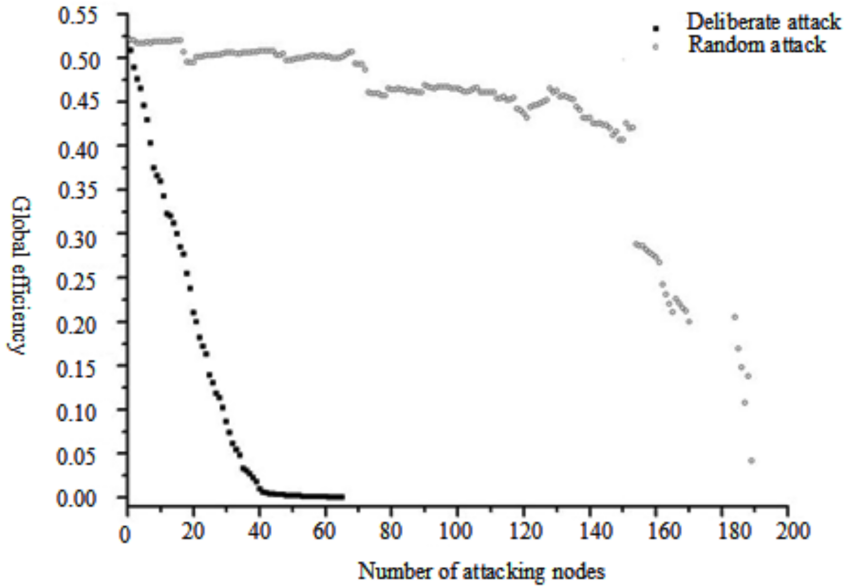


Fig. 10. Variation diagram of global efficiency of civil aviation sub-network under two attack modes

nodes under random attack. Using the same method, we can analyze the variation diagram of global efficiency of high-speed rail sub-network and high-speed passenger transport network under two modes of attack (as shown in Figs. 11 and 12).

The high-speed rail sub-network presents similar characteristics to those of the civil aviation sub-network under two modes of attack. Its global efficiency declines to 0 under attempted attack to about 360 nodes and about 420 nodes under random attack. Thus, it can be seen that, the high-speed rail sub-network is more reliable than civil aviation sub-network.

Global efficiency of high-speed passenger transport network declines to 0 under attempted attack to 410 nodes, and 550 nodes under random attack. Thus, it can be seen that, the high-speed passenger transport network is more reliable under random attack.

From comparison of Figs. 10, 11, 12, the initial values of efficiency of the three kinds of networks are about 0.5. The number of nodes under random attack civil aviation sub-network high-speed rail sub-network is 420 and 180 respectively, at which point, the efficiency declines to 0, whereas, the efficiency of high-speed passenger transport declines to 0 under such attack to 550 nodes; in the face of attempted attack, the global efficiency of civil aviation sub-network high-speed rail sub-network declines to 0 under attack to 60 and 360 nodes respectively, but that of high-speed passenger transport declines to 0 under attack to 410 nodes. It is shown that, under two modes of attack, the high-speed passenger transport network is more reliable than civil aviation and high-speed rail network.

Under attempted attack, the global efficiency decreases by more than 0.01 after

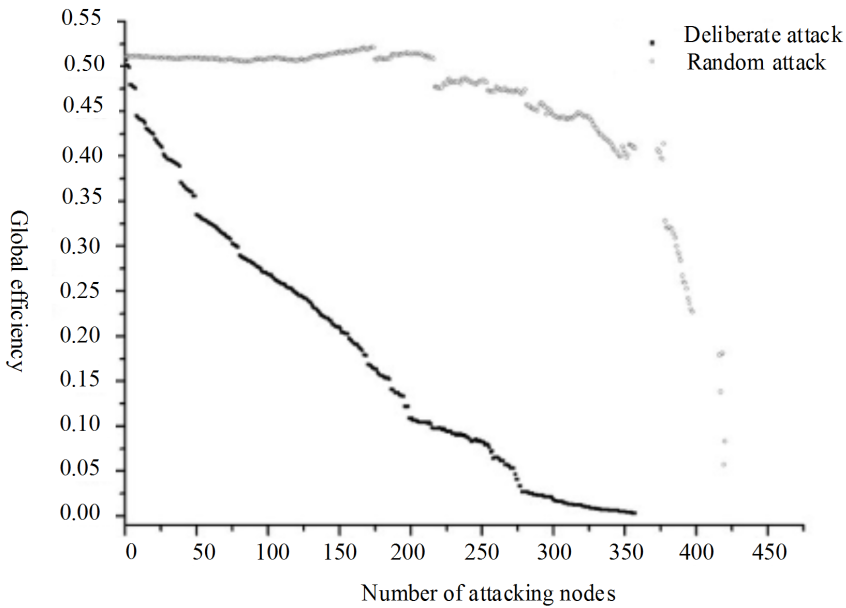


Fig. 11. Variation diagram of global efficiency of high-speed rail network under two attack modes

removal of the 10 of the deleted 410 nodes, which are Chengdu, Xi'an, Xianning, Dalian, Kunming, Urumqi, Haikou, Sanya, Luoyang. Those are key nodes in high-speed passenger transport network and in case of abnormal operation of those nodes, certain influence will be exerted on the network.

Take the above mentioned nodes as the dividing points, the nodes with similar global efficiency in the high-speed passenger transport network can be classified into a group. Thus, all the nodes can be divided into 11 groups, among which, the first group includes Beijing, Shanghai, Guangzhou, Hangzhou, Nanjing, Shenzhen, Wuhan and Changsha. Those nodes are all of big degree and connect main cities throughout the country and play as central hubs in the whole network. The second group includes Chengdu, Nanchang, Kunshan, Xiamen, Hefei, Jinan, Zhengzhou, Chongqing, Fuzhou, Wuxi, Xuzhou, Changzhou, Ningbo and Suzhou, which are backbone node cities of the high-speed passenger transport network and combine well the high-speed rail network and civil aviation network. Therefore, they play the role of diversion and stabilization for the central hubs.

7. Corresponding suggestions on construction of high-speed passenger transport network

By comparison of the calculation results in this paper and those concluded by relevant scholars according to data in 2012, it is found that the number of nodes

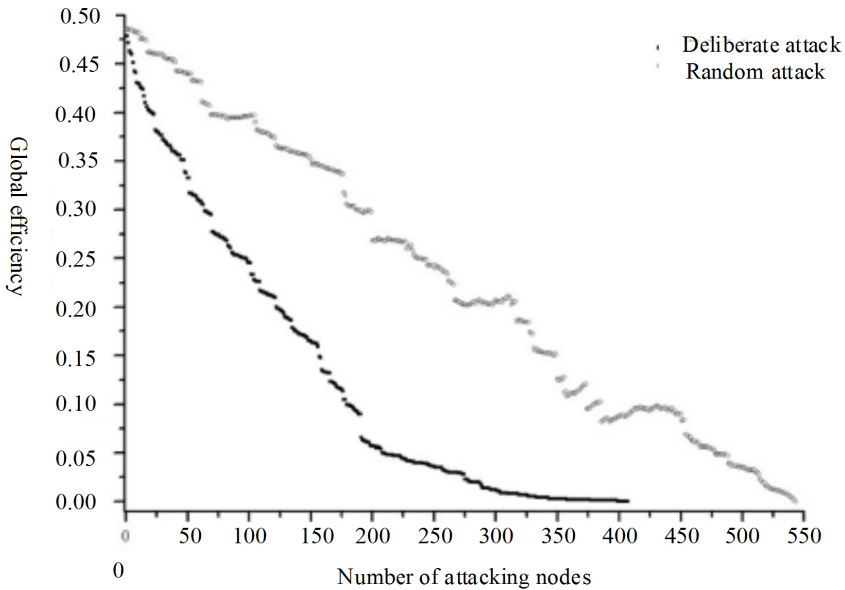


Fig. 12. Variation diagram of global efficiency of high-speed passenger network under two attack modes

of some existing high-speed passenger transport network has increased to two times that of the former high-speed passenger transport network and the number of edges has increased to three times, in addition, the average degree and other indexes have increased substantively. The former high-speed passenger transport network is disrupted under attempted attack to 40 nodes and 215 nodes under random attack, however, the existing high-speed passenger transport network is disrupted under the two modes of attack to 410 and about 550 nodes, respectively. Comparatively speaking, the resistance to destruction of the existing network is greatly enhanced. Yet, the existing high-speed passenger transport network only yields a global efficiency of 0.4861, which is slightly higher than that of the former network 0.4753, which means the reliability of the network is slightly increased. The existing network is still dependent on several key hub cities in transfer of passenger flow with poor coverage in remote areas and the increase in network nodes and edges fails to bring dramatic enhancement in network efficiency. Based on the above mentioned, this paper gives following suggestions on construction of China high-speed passenger transport network:

1. To add more hub nodes: the hub nodes in high-speed passenger transport network play an important role of transfer and can lighten the burden of central hub nodes, enhance resistance to destruction of the network and improve network stability. In reality, if the central hub nodes fail to operate smoothly under certain trouble including bad weather, it is quite helpful to add more hub nodes playing the role of transfer to slow down increase in the average

path length of the network.

2. To improve the network structure: at present, central and western regions in China, the high-speed passenger transport network still relies on civil aviation nodes in transfer and the high-speed rail network is yet to be closely connected with the intensive network lines in the eastern region. Such network structure is liable to hamper the operation efficiency of the entire region in the case of attack of certain node in the central and western regions in China. For this reason, it is necessary to accelerate extension into the sub-line regions of the civil aviation to cover more cities, and at the same time, to quicken construction and improvement of the high-speed rail sub-network so as to realize coverage of the central and western regions with some remote areas to enable the hub urban nodes in central and western regions to play a more important role.
3. To add more cross-regional trains: it is helpful to realize more close connection among nodes in the network, reduce transfer, enhance reliability and present more options for the passengers by adding more cross-regional and overline trains. Currently, the high-speed rails lines in normal operation cannot fully meet the need of passengers, thus, more cross-regional high-speed rail lines shall be opened to meet the travel demand of passengers.
4. To diversify arrangement of flights in airports at the end-point of civil aviation network: some small airports in China (for example: Jiuhuang Airport) basically connect the provincial cities where they are located with few flights to airports in the neighboring areas. In case of attack of the provincial attack, connectivity among those small airports drops to zero, thus passengers are forced to travel by high-speed rail that is rarely seen in those cities often-times. Therefore, it is of certain necessity to diversify arrangement of flights in airports at the end-point of civil aviation network so as to enhance network stability.

8. Conclusion

Through calculation of relevant indexes of high-speed passenger transport network, this paper proves the high-speed passenger transport network is a typical complex network, and on this basis, it combines the two kinds of networks in construction of the high-speed passenger transport network. At first, the paper proves high-speed passenger transport network is a typical scale-free small-world network with its characteristics of better connectivity, fewer times of transfer and higher clustering coefficient. And then, through reliability analysis of the network under attempted and random attack respectively, it is found by simulation, that it is more reliable under random attack and less reliable under attempted attack and it is more reliable than high-speed rail and civil aviation network. Finally, the paper gives corresponding suggestions on construction of the high-speed passenger transport network from four perspectives of hub node, network construction, overline

trains and flights according to the current condition and deficiencies revealed by simulated attack to the network.

References

- [1] A. L. BARABÁSI, R. ALBERT: *Emergence of scaling in random networks*. Science, PubMed, US National Library of Medicine 286 (1999), No. 5439, 509–512.
- [2] D. J. WATTS, S. H. STROGATZ: *Collective dynamics of ‘small-world’ networks*. Nature, International Weekly Journal of Science 393 (1998), 440–442.
- [3] R. ALBERT, H. JEONG, A. L. BARABÁSI: *Error and attack tolerance of complex networks*. Nature, International Weekly Journal of Science 406 (2000), 378–382.
- [4] F. XU, J. F. ZHU, W. D. YANG: *Construction of high-speed railway and airline compound network and the analysis of its network topology characteristics*. Complex Systems and Complexity Science (2013), No. 3, 1–11.
- [5] W. ZHAO, K. Q. YANG, H. S. HE, Z. C. LIN: *The study of properties of Chinese railway passenger transport network*. Acta Physica Sinica 55 (2006), No. 8, 3906–3911.
- [6] H. K. LIU, T. ZHOU: *Empirical study of Chinese city airline network*. Acta Physica Sinica 56 (2007) No. 1, 106–112.

Received November 16, 2016

Network anomaly traffic monitoring based on improved immune genetic algorithm

BINWU JI¹, RUI HUANG¹

Abstract. A novel network anomaly traffic monitoring method is proposed. The network anomaly traffic monitoring system consists of three steps, that is, 1) Data preprocessing, 2) SVM training, and 3) Anomaly detection. In step 1, a feature set is constructed from training dataset. In step 2, parameters of SVM are optimized by an improved Immune genetic algorithm. In step 3, network anomaly traffic is detected by classifying testing samples to “Normal” and “Attacks”. Particularly, the main innovation of this paper is to integrate the immune concept to genetic algorithm together to optimize parameters of SVM classifier. The improved immune genetic algorithm is able to restrain the degenerative phenomena arising in the process of evolution, and then makes the fitness of population increase slowly. Finally, experiments are conducted based on 1998 DARPA dataset and KDD-CUP’99 dataset. Experimental results prove that the proposed method can detect network anomaly traffic more accurately after optimizing SVM parameters by the improved immune genetic algorithm.

Key words. Network anomaly traffic monitoring, Immune genetic algorithm, crossover operation, mutation operation, memory set.

1. Introduction

In recent years, with the rapid development of Internet technology, the traditional network cannot meet the growing requirements of Internet users [1]. How to effectively manage Internet has been attracted more and more attention, and network traffic monitoring has been a crucial issue in computer network [2], [3]. The data of network traffic provides significant information for computer network, and is also very crucial to distribute network resources and analyze of service quality and computer network security [4].

Due the diversification of IP business and the complexity of the network environment, it is difficult to detect abnormal in a small amount from massive network data flow [5]. The abnormality in network traffic denotes the irregular and transpar-

¹Guilin University of Aerospace Technology, Guilin, 541004, China

ent changes in it. There are two major types of network abnormality, such as local incident and overall incident [6], [7]. Local incident includes temporary congestion, attack of refusing serving, on the other hand, overall incident contains network route abnormality [8].

Network traffic is able to represent the activities of the network and user behaviors, therefore, network traffic analysis can help us to understand and manage the network [9], [10]. Particularly, the anomaly detection and the application type identification of the network traffic are two types of the basic and important issues. In this paper, we aim to propose an efficient algorithm to detect and discover traffic anomalies. The major innovations of this paper are to introduce immune genetic algorithm in network anomaly traffic monitoring. Immune genetic algorithm has been widely used in many fields, such as weapon system portfolio optimization [11], articulated industrial robotic manipulator [12], touch panel cover glass design [13], fault diagnosis of rolling-element bearings [14], dynamic clustering approach [15], the bi-level linear programming problem [16], Emulating human society education and experiential inheritance mechanism [17].

The rest of the paper is organized as follows. We express the framework of the network anomaly traffic monitoring system in section. In Section 3, we illustrate how to optimize SVM parameters by an improved immune genetic algorithm. Section 4 designs and implements a series of experiments to show the effectiveness of the proposed algorithm. Section 5 concludes the whole paper.

2. Overview of the network anomaly traffic monitoring system

The framework of network anomaly traffic monitoring system is shown in Fig. 1, which is made up of three steps: 1) Data preprocessing, 2) SVM training, and 3) Anomaly detection. In the first step, feature set is constructed from training dataset, which is history data of Network anomaly traffics. In the second step, SVM classifier is trained after the data normalization process, afterwards, parameters of SVM are optimized by an improved Immune genetic algorithm. In the third step, anomaly detection is done by classifying testing samples to two classes (Normal and Attacks). Particularly, in this work, the attacks are considered as anomalies.

It can be observed from Fig. 1 that the key component of the proposed system is SVM classifier, and then the network anomaly traffic monitoring problem is converted to a classification problem.

Suppose that the training samples are represented as $x_i, y_i, i = 1, 2, \dots, l$, conditions $x_i \in R^n, y_i \in \langle 1, -1 \rangle$ are satisfied, $y_i(x) = wx + b$ is the discriminant function, and n is the dimension of training sample space. In particular, SVM aims to solve the following optimization problem:

$$\min \|w\|^2 / 2, \quad (1)$$

$$\text{s.t. } y_i[wx_i + b] - 1 \geq 0, \quad i \in \langle 1, 2, 3, \dots, l \rangle. \quad (2)$$

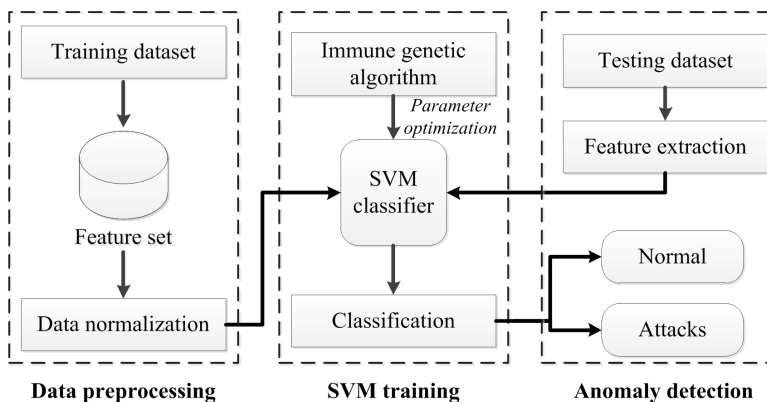


Fig. 1. Framework of network anomaly traffic monitoring system

Expressions (1) and (2) are convex functions, so that the required optimization problem can be transformed into solving a quadratic convex optimization problem. Among them, $\|w\|/2$ is the classified interval, and b is the constant of discriminant function.

Here vector x_i is mapped to a high-dimensional space by the function $\varphi()$, and C denotes the penalty parameter.

Thus, the classification issue is tackled by the following equation.

$$\text{sgn}\{(w \bullet x) + b\} = \text{sgn}\left\{\sum_{i=1}^l \alpha^* y_i (x \bullet x_i + b^*)\right\} \quad (3)$$

where $(x_i \bullet x)$ is the vector product of two vectors, while α^*, b^* are parameters of the classification hyperplane.

To promote the SVM's performance, Gaussian kernel is utilized in our work, that is defined as follows.

$$K(x_i, x) = e^{-\frac{|x-x_i|^2}{\sigma^2}}, \quad (4)$$

where x_i is the kernel function center and σ is the width parameter of the function, which controls the radial range of the function.

3. SVM parameters estimation by immune genetic algorithm

To optimize parameters of SVM, we introduce the immune concept to genetic algorithm, by using local characteristic information to obtain optimal solutions. That is to say, the immune genetic algorithm (denoted as IGA) refrains the degenerative phenomena arising in the process of evolution, and then lets the fitness of population increase slowly. Next, we proposed an improved immune genetic algorithm, which is used to optimize parameters of SVM. The flowchart of the immune genetic algorithm is illustrated in Fig. 2.

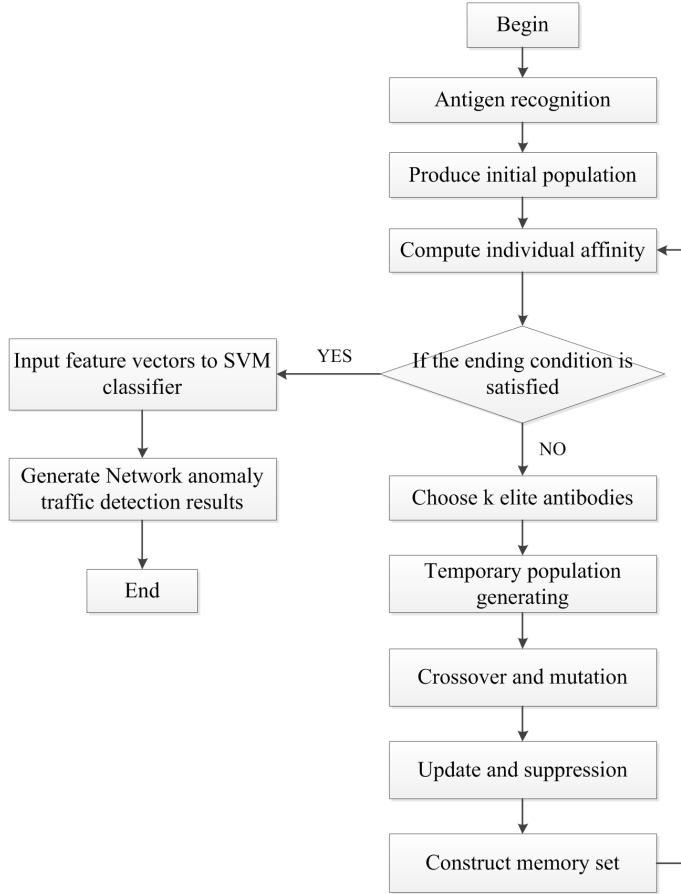


Fig. 2. Flowchart of immune genetic algorithm

As shown in Fig. 2, the immune genetic algorithm is made up of the following steps:

1. Randomly produce an initial population of antibodies.
2. Estimate the value of affinity for each antibody by the following equation.

$$c(x, y) = \frac{1}{1 + d(x, y)}, \quad (5)$$

where

$$d(x, y) = \frac{1}{n} \sum_{i=1}^n |x(i) - y(i)|, \quad (6)$$

$d(x, y)$ denoting the proximity degree between the antibody x and y .

3. Choose k antibodies which have the largest affinity value.
4. Clone the antibodies of step 3.
5. Execute crossover and mutation operations for the cloning sets.
6. Construct memory set and then update the antibodies in it.
7. If the ending condition is satisfied, input feature vectors to SVM classifier and then generate network anomaly traffic detection results.
8. Otherwise, go to step 2.

In order to promote the performance of immune genetic algorithm, some modifications are made in this work.

The probability of choosing antibody K is calculated as follows

$$P(k) = \frac{f_k e^{-\chi C_k}}{\sum_{i=1}^N f_i e^{-\chi C_i}}, \quad (7)$$

where parameter χ denotes the regulation, which refers to the weight of affinity f_k and concentration c_k , and N refers to the number of antibody in a given population. We randomly choose antibody $x(k)$ and $x(l)$ in a population, and crossover the process of $x(k)$ and $x(l)$ in the q th bit is defined as follows

$$\begin{aligned} x_{kq} &= (1 - \eta)x_{kq} + \eta x_{lq}, \\ x_{lq} &= (1 - \eta)x_{lq} + \eta x_{kq}, \end{aligned} \quad (8)$$

where η is a random number which is valued in the range $[0,1]$.

Afterwards, the mutation operation is executed to avoid premature convergence of the immune genetic algorithm. For a given antibody $x(k)$, the mutation of q th base is defined by the following equation.

$$\begin{aligned} x_{kq} &= (b_q - x_{kq}) \cdot f(t) \quad \text{for } \eta > 0.5, \\ x_{kq} &= (x_{kq} - a_q) \cdot f(t) \quad \text{for } \eta \leq 0.5. \end{aligned} \quad (9)$$

Here, parameters a_q and b_q denote the low and upper bounds, $f(t)$ means the probability of mutation, and t means the number of iterations.

4. Experiment

In order to test the capability of the proposed method, we collect five weeks of the 1998 DARPA dataset [18], which has been successfully exploited in network intrusion detection evaluation. The DARPA dataset is made up of nearly 1.5 million traffic instances with half of them is tagged attacks. Particularly, to illustrate the input data, six types of network traffic instance are chosen in this dataset, including: 1) connection time, 2) protocol type, 3) source port, 4) destination port, 5) source IP

address and 6) destination IP address. Afterwards, a 14-dimensional feature vector is input to SVM, which is illustrated in Table 1.

Table 1. Features utilized in network anomaly traffic monitoring

Feature description	Number of features
Connection time	3
Packet type	1
Source port number	1
Destination port number	1
Address of source IP	4
Address of destination IP	4

Table 1 shows that fourteen features are used to describe feature vector of network anomaly traffic monitoring. Moreover, to enhance the accuracy of network anomaly traffic detection, we normalize all features to the range $[0,1]$. The performance criteria used in this work are 1) Attack Detection rate (denoted as DR) and 2) False Alarm rate (denoted as FA). DR is defined as the ratio between the number of truly detected attacks and the whole attacks; on the other hand, FA is defined as the ratio between the number of normal connections which are falsely classified as attacks and the whole normal connections.

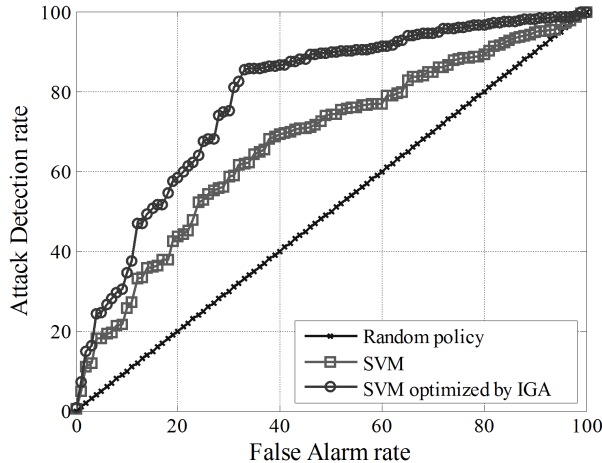


Fig. 3. ROC Curve under 20% attack distribution

Integrating experimental results from Fig. 3 to Fig. 6, we can see that the proposed SVM classifier optimized by IGA performs better than SVM, that is to say the improved genetic algorithm is able to estimate parameters of SVM with high accuracy. Moreover, with the degree of attack distribution increasing, the areas of ROV curve significantly decrease.

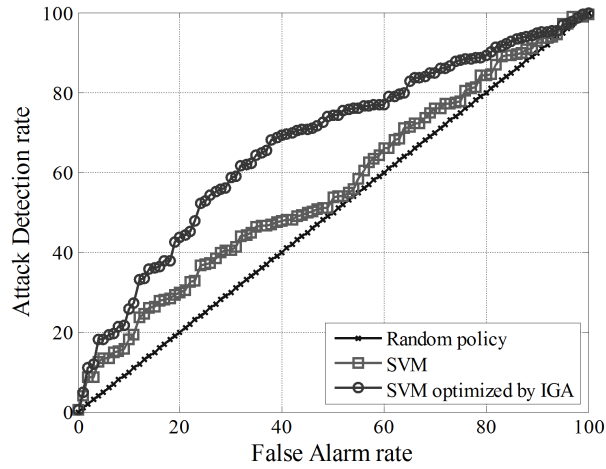


Fig. 4. ROC Curve under 40% attack distribution

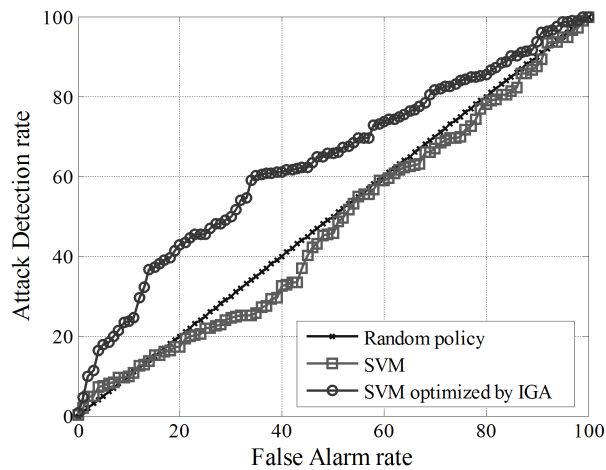


Fig. 5. ROC Curve under 60% attack distribution

Apart from the above experiments, we also utilize KDD-CUP'99 anomaly detection dataset to further test the effectiveness of our method. In KDD-CUP'99 dataset, the simulated attacks are classified into four classes, which are 1) DoS: Denial of Service, 2) R2L: unauthorized access from a remote computer, 3) U2R: unauthorized access to super users, and 4) Probing: surveillance and probing for vulnerabilities. The accuracy of network anomaly detection for all the above four types of attacks is given in Fig. 7.

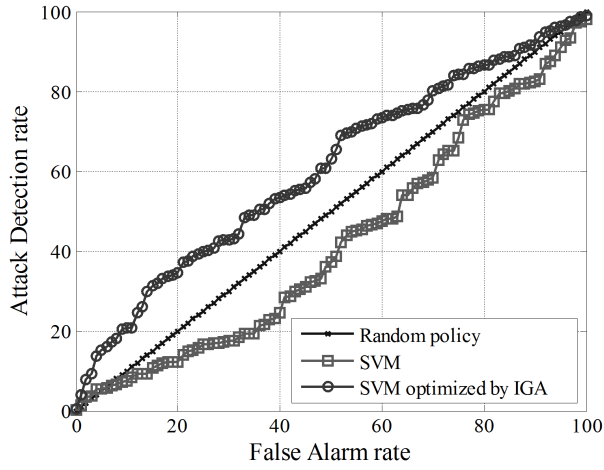


Fig. 6. ROC Curve under 80% attack distribution

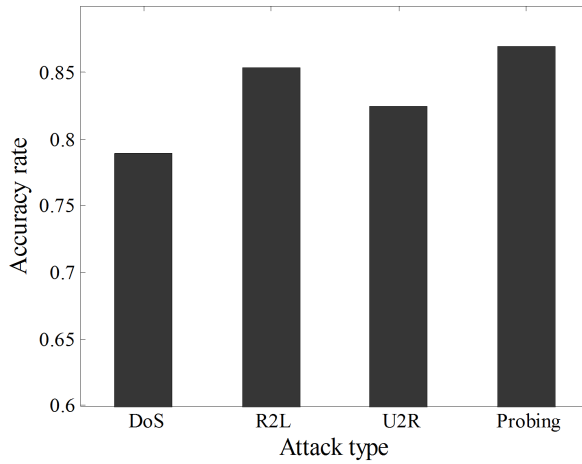


Fig. 7. Network anomaly detection accuracy for different attack types

Figure 7 demonstrates that the proposed algorithm can effectively detect four different types of attack in the KDD-CUP'99 dataset.

5. Conclusion

This paper presents a new network anomaly traffic monitoring method based on an improved immune genetic algorithm. The network anomaly traffic monitoring system is made up of three steps, including a) Data preprocessing, b) SVM train-

ing, and c) Anomaly detection. The main idea of this paper lies in that we convert the network anomaly traffic detection to a classification problem. Experiments are conducted using both 1998 DARPA dataset and KDD-CUP'99 dataset, and experimental results reveal that the proposed method can detect network anomaly traffic with high accuracy.

References

- [1] Y. LOU, P. LI, X. HONG: *A distributed framework for network-wide traffic monitoring and platoon information aggregation using V2V communications*. Transportation Research Part C: Emerging Technologies 69 (2016), 356–374.
- [2] Y. LIU, J. LING, Q. WU, B. QIN: *Scalable privacy-enhanced traffic monitoring in vehicular ad hoc networks*. Soft Computing 20 (2016), No. 8, 3335–3346.
- [3] T. D. TRUONG, G. CHENG, A. JAKALAN, X. J. GUO, A. P. ZHOU: *Detecting DGA-based botnet with DNS traffic analysis in monitored network*. J Internet Technology 17 (2016), No. 2, 217–230.
- [4] J. J. FERNÁNDEZ-LOZANO, M. M. GUZMÁN, J. M. ÁVILA, A. G. CEREZO: *A wireless sensor network for urban traffic characterization and trend monitoring*. Sensors 15 (2015), No. 10, 26143–26169.
- [5] A. JANECEK, D. VALERIO, K. A. HUMMEL, F. RICCIATO, H. HLAVACS: *The cellular network as a sensor: From mobile phone data to real-time road traffic monitoring*. IEEE Trans. Intelligent Transportation Systems 16 (2015), No. 5, 2551–2572.
- [6] A. BAIOCCHI, F. CUOMO, M. DE FELICE, G. FUSCO: *Vehicular ad-hoc networks sampling protocols for traffic monitoring and incident detection in intelligent transportation systems*. Transportation Research Part C: Emerging Technologies 56 (2015), 177–194.
- [7] W. XUE, L. WANG, D. WANG: *A prototype integrated monitoring system for pavement and traffic based on an embedded sensing network*. IEEE Trans. Intelligent Transportation Systems 16 (2015), No. 3, 1380–1390.
- [8] J. ZHANG, L. JIA, S. NIU, F. ZHANG, L. TONG, X. ZHOU: *A space-time network-based modeling framework for dynamic unmanned aerial vehicle routing in traffic incident monitoring applications*. Sensors 15 (2015), No. 6, 13874–13898.
- [9] C. W. CHANG, G. HUANG, B. LIN, C. N. CHUAH: *LEISURE: load-balanced network-wide traffic measurement and monitor placement*. IEEE Trans. Parallel & Distributed Systems 26 (2015), No. 4, 1059–1070.
- [10] M. A. HANNAN, C. T. GEE, M. S. JAVADI: *Automatic vehicle classification using fast neural network and classical neural network for traffic monitoring*. Turkish Journal of Electrical Engineering and Computer Sciences 23, (2015), No. Sup. 1, 2031–2042.
- [11] S. YANG, M. YANG, S. WANG, K. HUANG: *Adaptive immune genetic algorithm for weapon system portfolio optimization in military big data environment*. Cluster Computing 19 (2016), No. 3, 1359–1372.
- [12] H. C. HUANG, S. S. D. XU, C. H. WU: *A hybrid swarm intelligence of artificial immune system tuned with Taguchi-genetic algorithm and its field-programmable gate array realization to optimal inverse kinematics for an articulated industrial robotic manipulator*. Advances in Mechanical Engineering 8 (2016), No. 1, paper 1687814015626380.
- [13] T. S. WANG: *Integrating grey sequencing with the genetic algorithm-immune algorithm to optimize touch panel cover glass polishing process parameter design*. IJ Production Research 54 (2016), No. 16, 4882–4893.
- [14] W. A. YANG, M. XIAO, W. ZHOU, Y. GUO, W. LIAO, G. SHEN: *Trace ratio criterion-based kernel discriminant analysis for fault diagnosis of rolling element bearings using binary immune genetic algorithm*. Shock and Vibration (2016), No. 15, paper 8631639.

- [15] R. J. KUO, S. H. LIN, Z. Y. CHEN: *Integration of particle swarm optimization and immune genetic algorithm-based dynamic clustering for customer clustering*. IJ Artificial Intelligence Tools 24 (2015), No. 5, paper 1550019.
- [16] R. J. KUO, Y. H. LEE, F. E. ZULVIA, F. C. TIEN: *Solving bi-level linear programming problem through hybrid of immune genetic algorithm and particle swarm optimization algorithm*. Appl. Math. Compu. 266 (2015), 1013–1026.
- [17] D. SONG, X. P. FAN, Z. L. LIU: *An immune memory optimization algorithm based on the non-genetic information*. Acta Physica Sinica 64 (2015), No. 14, paper 140203.
- [18] M. M. MOHAMMADI, A. AKBARI, B. RAAHEMI, B. NASSERSHARIF, H. ASGHARIAN: *A fast anomaly detection system using probabilistic artificial immune algorithm capable of learning new attacks*. Evolutionary Intelligence 6 (2014), No. 3, 136–156.

Received November 16, 2016

Wireless sensor network target coverage algorithm based on energy saving

KANGMING LIU¹

Abstract. Energy efficiency optimization of wireless sensor network is studied based on improved multi-objective particle swarm optimization. The network coverage rate, energy consumption and the number of working node are taken into account comprehensively. The improved multi-objective particle swarm optimization algorithm is based on the dominance method. By means of the dominance relationship, it determines non-dominated solution set, and then it is stored in the external archive set. The particles beyond the scale is deleted by means of arrange crowded distance in descending order, and the disturbance factor is joined to maintain the diversity of swarm. On parameter settings of the iteration formula of particle swarm optimization algorithm, the method of dynamically adjusting inertia weight and learning factors are put forward. The simulation results show that the proposed energy saving algorithm based on improved multi-objective particle swarm optimization enhances the network coverage, saves the energy consumption and prolongs the network life cycle to a certain extent.

Key words. Wireless sensor network, multi-objective particle swarm optimization, coverage rate, energy consumption.

1. Introduction

Coverage control is a basic problem in Wireless Sensor Network (WSN). The main content of coverage control is to ensure the network does have certain quality of service. Then, it can be optimized by some technology or protocol, so that it can meet the maximization of coverage area [1]. People may get reliable monitoring data and target tracking service. Effective strategies of the coverage control and algorithms can be used to optimize the allocation of resources of WSN, increase the efficiency of the energy usage of network nodes, and improve the perceived quality of service and the overall survival time [2]. How to combine different environmental demands and design a practical strategy for coverage is a significant research field.

Researchers have put forward the strategies for reducing energy consumption and

¹Information Engineering Institute, Huanghuai University, Henan, 463000, China

prolong the network life cycle from all aspects of the wireless sensor network [3–6]. These strategies can be divided into four basic categories, sleep scheduling scheme, adjusting the sensing radius of the nodes, choosing the best route, and highly effective data fusion system. A scheduling algorithm for connected target coverage under probabilistic coverage model was proposed by Kim [7]. Energy-efficient probabilistic area coverage in wireless sensor networks was put forward by Qianqian [8]. Sensor scheduling for p-percent coverage in wireless sensor networks was proposed by Li [1]. Sleep scheduling for partial coverage in heterogeneous wireless sensor networks was proposed by Mostafei [9]. Energy-efficient protocol for deterministic and probabilistic coverage in sensor networks was presented by Hefeeda [10]. A coverage monitoring algorithm based on learning automata for wireless sensor networks was put forward by Mostafaei [11]. Centralized and clustered k-coverage protocols for wireless sensor networks was proposed by Ammari [12]. Genetic algorithm for sensor scheduling with adjustable sensing range was put forward by Arivudainambi [13]. Arivudainambi put forward a method to improve energy efficient target coverage in wireless sensor networks [8]. A kind of energy efficient sensor scheduling for target coverage in wireless sensor network was proposed by Arivudainambi [14]. These methods are based on single objective optimization. Optimization problems, especially multi-objective optimization problem using intelligent algorithm is one of the focus areas of evolutionary computation. Particle swarm optimization algorithm as a relatively new optimization technique, the concept is simple, less control parameters, the optimization result has nothing to do with the initial value, with a certain parallelism, and it has gained more attention and has good prospects for development. However, the traditional particle swarm algorithm still has some deficiencies in global search and convergence, the algorithm has attracted the interest of many researchers and scholars and almost all of them are devoted to the study of the performance improvement algorithm. It is confirmed that the particle swarm algorithm has a very good application for single objective optimization problems, but the multi-objective particle swarm optimization algorithm and its application remains to be further studied. Based on the standard particle swarm algorithm and multi-objective optimization theory, the multi-objective particle swarm optimization algorithm is studied intensively in this paper, the concrete content and innovative points can be summarized as follows. In the next section, a kind of improved multi-objective particle swarm optimization algorithm is put forward. In section 3, a novel energy saving model based on improved multi-objective particle swarm optimization algorithm is proposed. In section 4, in order to test the performance of proposed energy saving model, experiments are done. In the end, some conclusions are given.

2. Improved multi-objective particle swarm optimization algorithm

For solving multi-objective optimization problem, it is not as direct and simple as to solve the single objective optimization problem. It only needs to compare the size of the fitness value, and the key is to find a series of multi-objective better trade-off solution set that is called the non-dominated solution set, namely the Pareto optimal

set (Pareto optimal set). The key of using particle swarm optimization algorithm to solve multi-objective optimization problem is to determine the individual optimal value and global optimal value, so as to guide the population search to Pareto optimal set of the optimization problem. Due to the velocity updating formula of particle swarm algorithm mainly relies on a certain individual optimal location and the global optimal position, but the multi-objective optimization problem does not have the only optimal solution, so particle swarm optimization needs to be modified in combination with other methods, so as to choose the individual optimal solution and the global optimal solution of each particle. In solving multi-objective optimization problems, compared with other optimization algorithm, particle swarm optimization algorithm is simple, search efficiency is high, and the general performance is good. Combining with other algorithm is easy. So, research and improvement of multi-objective particle swarm optimization algorithm has important significance for solving multi-objective optimization problem.

Basic particle swarm optimization algorithm can only return a solution, but the main goal of multi-objective optimization algorithm is to find a set of solutions, and the optimal solution set makes best trade-off of different target for multi-objective problems, so the basic particle swarm algorithm cannot be directly used for solving multi-objective optimization problem. To make it widely used in the multi-objective optimization problem, the key task of multi-objective particle swarm optimization algorithm is to generate multiple solutions, thus to determine a set of solutions, namely the Pareto optimal set.

Multi-objective algorithm not only should complete the task, but also should cover the true Pareto optimal boundary approximately. At the same time it should achieve three goals. The distance between the solution and Pareto boundary should be minimized. The diversity of the non-dominant solution should be maximized to represent Pareto boundary as fully as possible. The found non-dominated solution should be maintained. In order to achieve the first goal, we should determine an appropriate fitness function to measure the quality of a solution on the multi-objective level. Fitness function has three kinds. The first kind is based on aggregation and fitness function is a weighted sum of the objective function. The second is based on the criterion and fitness function varies between different targets under different condition in the process of optimization. The third is based on the Pareto dominance, fitness function is directly proportional to control sequence of solution scheme. Most of the control sequence scheme uses a series of non-dominant methods.

In order to achieve the second goal, we will introduce a variety of methods to keep the diversity of non-dominated solutions. These methods increase the probability of decision vector tending to Pareto boundary. Finally, in order to realize the third goal, the use of previously found solution archives can be used to implement which is a kind of elite strategy, and in this strategy, the best solution is stored in a repository. To sum up, several basic particle swarm optimization algorithm based on modified methods mainly include the method based on aggregation, the method based on rules and the method based on dominant. These methods are able to fix the basic particle swarm algorithm to generate multiple solutions.

Archive of the multi-objective optimization algorithm is used to track all non-

dominated solution so far. The use of the archive is similar to elite strategy in the evolutionary algorithm. In addition, in order to maintain the found solution, archive is used to select the global optimal position and individual optimal position. In archive method, global optimal and individual optimal non-dominant solution is called global wizard and individual wizard, respectively. The wizard's goal is to attract particles to fly to Pareto front. A lot of methods are used to select the guide, these methods usually cause each particle produce different global guide. Generally speaking, it is because of these different guides selection, the Pareto optimal set diversity can be maintained. For archive design, the most important is to prevent the explosive expansion of archive size. Allowing uncertainty increasing of archive has the following advantages.

The number of the non-dominant solutions is not restricted. Multi-objective optimization algorithm without using archive can position number of non-dominated solution at maximum. For one archive, more than solutions can be found. The obvious advantage is that archive algorithm can use small group than the non-archive method.

Using unlimited archive is helpful to maintain better diversity of population. Unlimited archive, however, also has its own disadvantages. When the archive size and target quantity increase, the computational complexity will increase significantly. Computational complexity increasing is mainly due to the non-dominated sorting and the choice of the guide. In order to solve the problem of archive algorithm computational complexity, a series of methods have been developed. We can use different data structure to express non-dominant solution. Non-dominant solution is clustered, and clustering center is used to replace each focus class. The archive is truncated, for example, the size of the archive is restricted to a predetermined value. We investigate a kind of multi-objective optimization algorithm based on truncated archive. An upper limit is set on the size of the archive. Once the archive reaches its limit capacity, the non-dominated solution beyond the size are deleted. So at this time, we should pay attention to keep the diversity of population. If we do not pay attention, the deletion of non-dominant can make the Pareto optimal set diversity loss.

The proposed multi-objective particle swarm optimization algorithm is mainly based on the control method. The non-dominated solutions are determined according to the Pareto dominance relation, which is the optimal solution of optimization problem. A competitive mechanism is used to quickly compare the dominance relationship between swarm individual. External archive set is used to store the non-dominant solutions, and the truncation archive method is used to limit the size of the archive. If the non-dominated solution set is beyond archive size, the descending order is carried out according to the crowded distance between each particle, thus eliminating the particles beyond the archive size. At the same time, in the process of searching dominant solutions, disturbance factor is joined to maintain the diversity of population following a certain probability. We also put forward the improvement strategy for speed update formula of particle swarm algorithm, and the main research object is inertia weight and learning factors. We propose a kind of competition mechanism, which can quickly search the non-dominant solution and

build the external archive set. In swarm S , a particle x is chosen randomly and $S = S - \{x\}$. The other particles are compared with particle x in turn according to Pareto dominant relation of target function value. If $x \prec y$, the particle y is deleted from the particle swarm. If $y \prec x$, $x = y$. $N = N \cup \{x\}$, it stops until $S = \emptyset$ and N is the non-dominant solution set. For non-dominated solution set being inserted into the external file set, we also adopt the same method. When more particles are eliminated, the algorithm runs faster, and also it reduces the complexity of the algorithm.

Particle swarm algorithm needs to generate a set of Pareto solutions in each iteration for solving multi-objective optimization problem. Therefore, the external archive is used to store each generation of non-dominated solution, and these solutions construct Pareto frontier. Along with the iteration, each generation of Pareto solution is used to update the external archive. However, with the increasing of the number of iterations, the external archive size also gradually increases, then algorithm computational complexity will be increased extremely. If we don't control the external archive size, it will greatly increase the computational complexity. Therefore, we use the crowding distance descending order to limit the size of the external archive set. In the whole iterative process of particle swarm optimization, it will continue to produce the non-dominated solution to be stored in one external archive set, global optimal location of each particle is randomly selected from the archive, the selection strategy can make non-dominant solutions in dense area get more opportunities, thus it loses the diversity of population and is easy to cause the algorithm into premature convergence and local optimum.

So, in order to keep the diversity of particles, improve population's ability to jump out of local optimal solution, based on a certain probability p , the Pareto solutions in external archive are disturbed to produce new solutions and guide population flight. The perturbation expression is

$$x_i^d = x_i^d \cdot (0.5 + \sigma), \quad (1)$$

where σ represents disturbance factor between $0 < \sigma < 1$ with mean value 0 and variance 1, x_i^d represents the d th dimension of variable of particle i . The large inertia weight is advantageous to the particle's ability to explore new areas, namely the swarm global search for population. And small inertia weight is beneficial to the particle's local search ability, which is conducive to local search of the population. At first, the population tends to global search, and later it will gradually tends to local search. According to this characteristic, dynamic adjustment calculation formula is

$$w(r) = [w_{\max} - w_{\min}] \frac{r_{\max} - r}{r_{\max}} + w_{\min}, \quad (2)$$

where r represents iteration times, r_{\max} represents the maximum iteration times, $w_{\min} = 0.4$ and $w_{\max} = 0.9$. The dynamic adjustments of learning factor are

$$c_1 = 1 + \frac{r_{\max} - r}{r_{\max}} \quad (3)$$

$$c_2 = 1 + \frac{r}{r_{\max}} \quad (4)$$

The process of improved multi-objective particle swarm optimization is shown in Fig. 1 and explanation of particular steps follows.

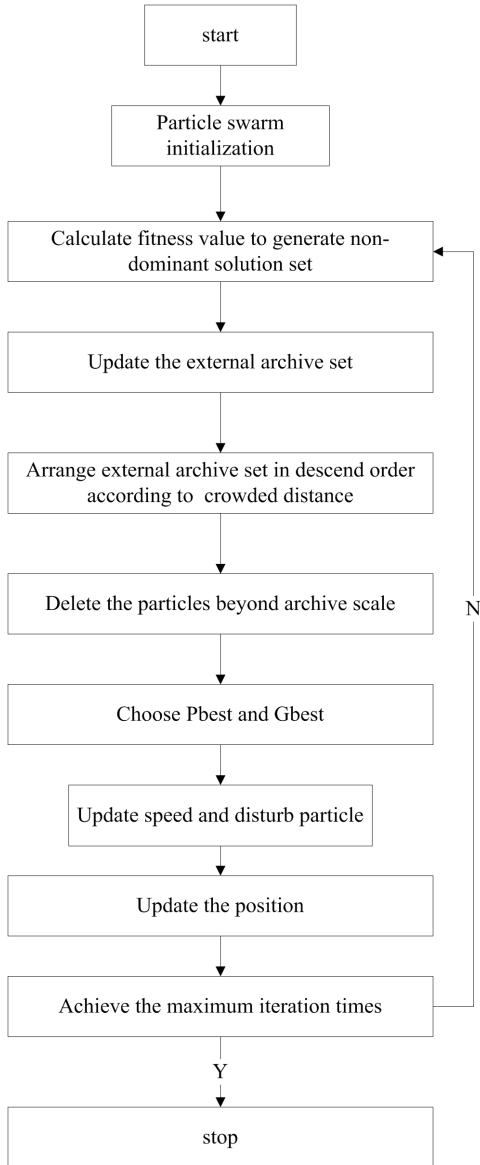


Fig. 1. Process of improved multi-objective particle swarm optimization

1. Initialize speed and position of all the particles and the swarm size is n .
2. Calculate the fitness function value of each particle. Based on dominance relation, it forms non dominated solution set.
3. Update external archive set.
4. The crowded distance between each particle of the external archive set is sorted in descending order. Check whether it is beyond the distance according to the set scale. If it is beyond the distance, the non-dominant solutions beyond the scale are deleted.
5. Update individual optimal P_{best} . If it is the first generation, the initial position of each particle is directly set to be P_{best} . If it is not the first generation, it chooses whether to replace update based on the Pareto dominance relation.
6. The global optimal position G_{best} is selected from the external archive set in the top 10% of the non-dominant solution.
7. Update speed of the particle. If the speed $v_i > v_{\text{max}}$, then $v_i = v_{\text{max}}$. If the speed $v_i < v_{\text{min}}$, then $v_i = v_{\text{min}}$.
8. Update the position of the new generation of particle and the particle is disturbed according to probability $p = 1 - r/r_{\text{max}}$ to prevent the algorithm from being trapped into local optimum.
9. Determine whether it achieves the maximum iteration times. If it meets the termination condition, the algorithm stops. Otherwise, it turns to step 2 to go on.

3. Energy saving model based on improved multi-objective PSO

Wireless sensor network usually has a dense area of sensor nodes within the target area in monitoring. If these sensors nodes work at the same time, causing collision conflict of a large number of sensor nodes in the network, at the same time, a lot of data redundancy also causes the network energy waste. Therefore, on the premise of guarantee the quality of network service, scheduling activities of sensor nodes make part of the sensor nodes into the active state, and the redundant nodes into idle state, to save the network energy consumption and prolong network lifetime, which is an important content in the research of wireless sensor network.

Suppose N number of sensor nodes randomly deployed in the target monitoring area, which is responsible for collecting all target information in the monitoring area. All sensor nodes perception radius and information computing ability are the same. Sensor perception model is the disc perception model. When perception radius of the sensor is R , it can cover all the target points taking itself as the circle center with radius R . A large number of sensor nodes is randomly deployed in the target area, the sensor node is divided into several subsets, and each covered subset can

completely cover the target area. The proposed scheme can periodically schedule these covers subset, maximize the sum of the working time of each subset, and extend the life cycle of the whole network.

Let k be the number of covered set (N_1, N_2, \dots, N_k) . Each subset is endowed with random number between 0 and 1. When the random number is greater than idle probability, the particle set is set to be 1 and the corresponding particle goes into work state. Otherwise, the particle set is set to be 0 and the particle goes into idle state. The idle probability is calculated as

$$p = a \left(1 - \frac{E_{ci}}{E_{mi}} \right) + b \frac{I_n - 1}{I_n}, \quad (5)$$

where a and b are constants such that $a + b = 1$. Symbol E_{ci} represents the left energy of node i and symbol E_{mi} represents initial energy of node i . Symbol I_n represents the number of neighbor nodes within perception range of node i , N is the number of sensors that are deployed in the whole target area randomly $(N = \{n_1, n_2, \dots, n_N\})$. Each sensor has initial energy E , the sensor radius is R , the corresponding energy is $\{e_1, e_2, \dots, e_n\}$. Subset $N' \in N$ is defined which satisfies the following objective: the first object is to make network coverage rate maximum.

$$\text{Max } f_1(x) = \frac{A_{\text{area}}(N')}{A_s}, \quad (6)$$

$$\text{s. t. } U = \frac{1}{N} \sum_{i=1}^N U_i = \sqrt{\frac{1}{k_i} (d(n_i, n_j) - D_j)^2}, \quad (7)$$

where U represents the uniformity, k_i represents the number of neighbors of node n_i , $d(n_i, n_j)$ represents the distance between two nodes, D_i denotes the mean distance value of all nodes intersected with perception radius of node n_i . The second objective is that the number of sensors should be minimized.

$$\text{Max } f_2(x) = 1 - \frac{|N'|}{N}. \quad (8)$$

The third objective is to make unit energy consumption minimum.

$$\text{Max } f_3(x) = -u \sum_{i=1}^n r_i^2 / A_{\text{area}}, \quad (9)$$

where A_{area} represents the monitoring area of N' and n represents the total number of work nodes.

The process of energy saving model based on improved multi-objective PSO is as follows.

Step 1: Initialize the N number of particles, namely produce position and speed of each individual randomly in the problem domain.

Step 2: Initialize the external sets and individual extreme, calculate the fitness of

each particle value.

Step 3: The swarm is divided into several sub-swarm, and give each child population a random number between 0 and 1.

Step 4: Calculate idle probability of each particle.

Step 5: Update the particle's position and speed.

Step 6: Calculate the new fitness value. The fitness value of each particle is compared with its own best location P_{best} , if it is better, P_{best} is reset.

Step 7: Coverage of each particle is compared with coverage of group best position G_{best} , if it is better, G_{best} is reset.

Step 8: Update the external set. If the stop condition is met, the algorithm stops. Otherwise, it returns to step 4.

4. Verification

In order to test the performance of proposed energy saving model, improved multi-objective optimization algorithm are compared with traditional multi-objective optimization algorithm. Coverage rate is shown in Fig. 2 and energy consumption curve is shown in Fig. 3. In $20\text{ m} \times 20\text{ m}$ monitoring area, 30 sensor nodes are deployed. The perception radius of the node is 5 and swarm scale is 30. It can be seen that the network coverage rate and energy consumption of improved multi-objective particle swarm optimization is better than traditional multi-objective particle swarm optimization. Another experiment is also done to test the influence of perception radius to coverage performance. The number of node is 40 and iteration time is 300.

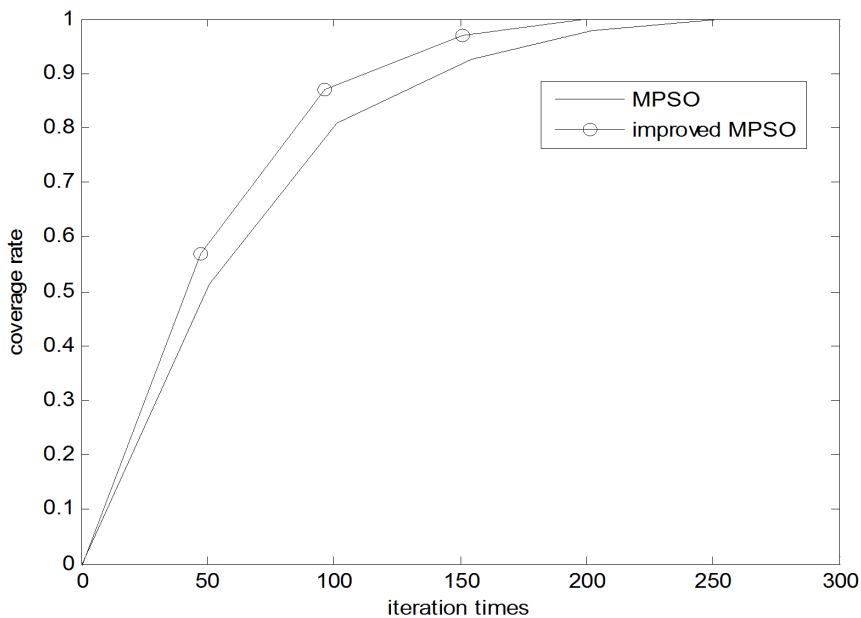


Fig. 2. Coverage rate comparison

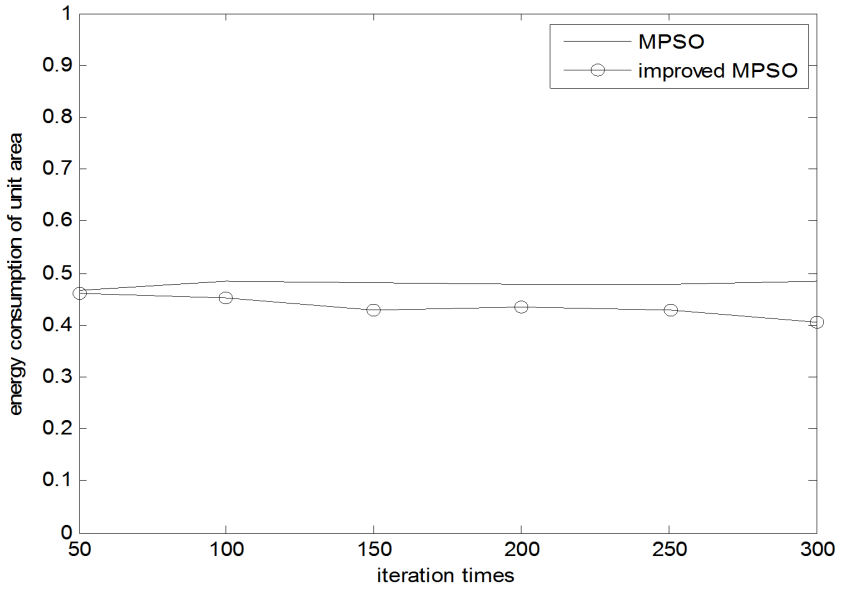


Fig. 3. Energy consumption comparison

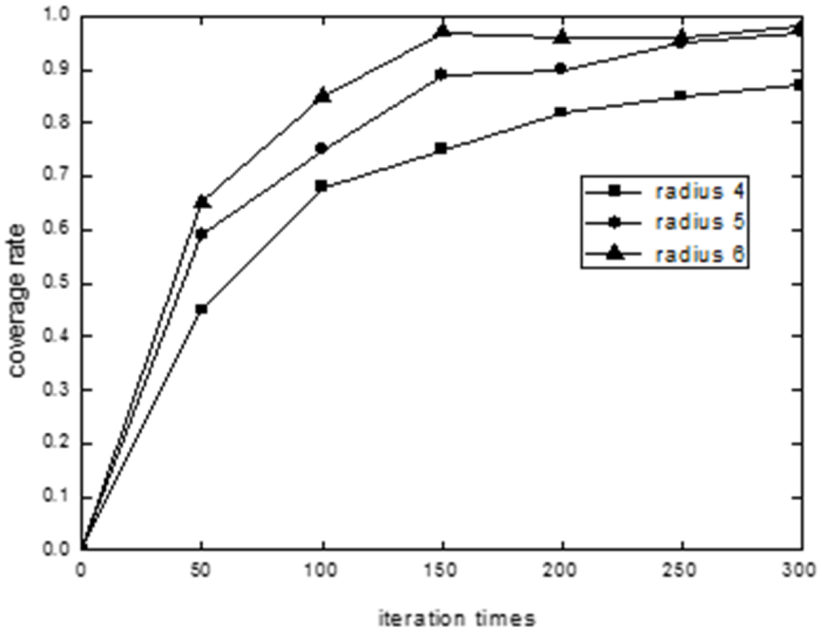


Fig. 4. Coverage rate with different radius

From Fig. 4, we can see that coverage rate has obvious ascension with the increasing of perception radius. At about 200 generation, network coverage rate of perception radius of 5 and 6 is almost the same. When the perception radius is 4, coverage rate is slightly lower. It can be seen that energy consumption of unit area is associated with perception radius (see Fig. 5). The greater the perception radius, the greater the energy consumption of unit area. Considering coverage rate and energy consumption, the network coverage performance is better when the perception radius is 5.

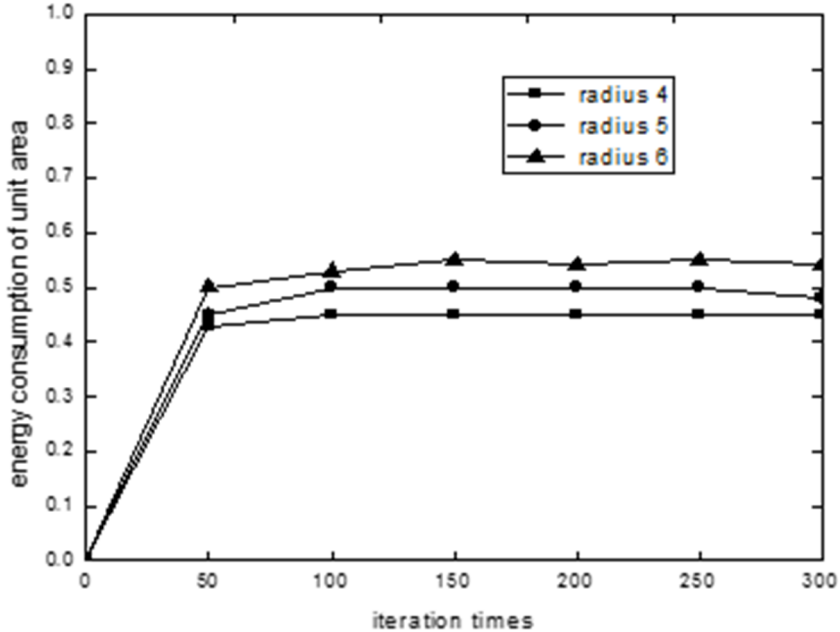


Fig. 5. Energy consumption with different radius

Figure 6 shows energy consumption with different sensor nodes. We can conclude that with the increasing of sensor nodes, energy consumption of unit area of the improved energy saving model does not exhibit much change. On the whole, the proposed model has higher energy efficiency.

5. Conclusion

Wireless sensor network has a wide range of applications in military, environment science, health care and other areas. Because it involves many disciplines and fields, there are some problems need to be solved. Coverage is one of the fundamental issues in research of wireless sensor network. Because random high density of node distribution may result in coverage area overlapped and large energy consumption, we propose a kind of energy consumption covering strategy based on multi-objective

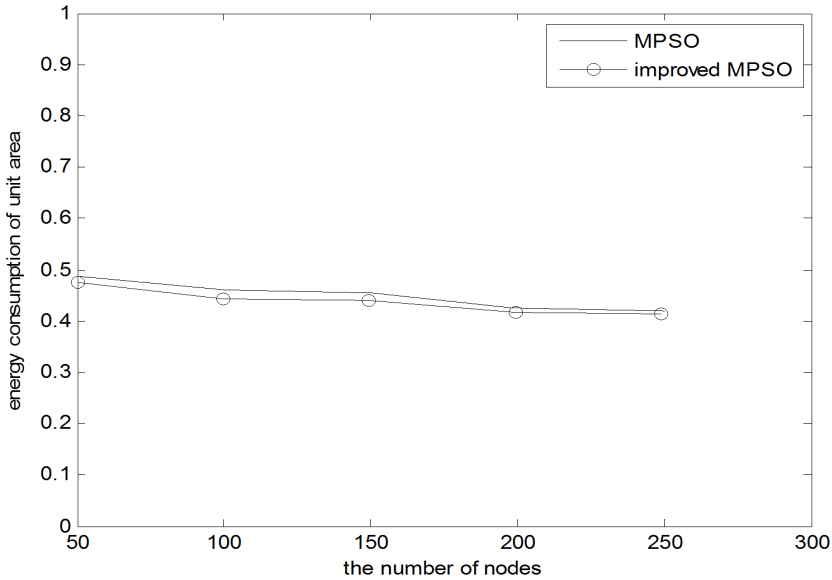


Fig. 6. Energy consumption with different nod

particle swarm. When selecting the optimal coverage node set, we consider the network energy consumption and the coverage rate at the same time. In each cycle, node calculates its sleep probability according to its own energy consumption and their neighbor's information. Network coverage, the number of working nodes and the energy consumption are taken as the optimized goal, and then improved multi-objective particle swarm optimization algorithm is used to get the optimal coverage solution. Simulation results show that the coverage control strategy can achieve high coverage rate and effectively reduce the energy consumption at the same time. So it ensures the network energy balance, keep stable network operation and prolong survival time of the network.

References

- [1] Y. LI, C. AI, Z. CAI, R. BEYAH: *Sensor scheduling for p-percent coverage in wireless sensor networks*. Cluster Computing 14 (2011), No. 1, 27–40.
- [2] J. JIA, J. CHEN, G. CHANG, Y. WEN, J. SONG: *Multi-objective optimization for coverage control in wireless sensor network with adjustable sensing radius*. Computers & Mathematics with Applications 7 (2009), Nos. 11–12, 1767–1775.
- [3] J. H. MOSTAFAEI, M. R. MEYBODI, M. ESNAASHARI: *A learning automata based area coverage algorithm for wireless sensor networks*. J Electronic Science and Technology 8 (2010), No. 3, 200–205.
- [4] T. YARDIBI, E. KARASAN: *A distributed activity scheduling algorithm for wireless sensor networks with partial coverage*. Wireless Networks 16 (2010), No. 1, 213–225.

- [5] Z. QUN, M. GURUSAMY: *Lifetime maximization for connected target coverage in wireless sensor networks*. IEEE/ACM Trans. Networking 16 (2008), No. 6, 1378–1391.
- [6] S. A. NIKOLIDAKIS, D. KANDRIS, D. D. VERGADOS, C. DOULIGERIS: *Energy efficient routing in wireless sensor networks through balanced clustering*. Algorithms 6 2013, No. 1, 29–42.
- [7] J. LIANG, M. LIU, X. KUI: *A survey of coverage problems in wireless sensor networks*. Sensors & Transducers 163 (2014), No. 1, 240–246.
- [8] Q. YANG, S. HE, J. LI, J. CHEN, Y. SUN: *Energy-efficient probabilistic area coverage in wireless sensor networks*. IEEE Trans. Vehicular Technology 64 (2015), No. 1, 367 to 377.
- [9] H. MOSTAFAEI, A. MONTIERI, V. PERSICO, A. PESCAPÉ: *An efficient partial coverage algorithm for wireless sensor networks*. Proc. IEEE Symposium on Computers and Communication, 27–30 June 2016, Messina, Italy, 501–506.
- [10] M. HEFEEDA, H. AHMADI: *Energy-efficient protocol for deterministic and probabilistic coverage in sensor networks*. IEEE Trans. Parallel and Distributed Systems 21 (2010), No. 5, 579–593.
- [11] H. MOSTAFAEI, M. ESNAASHARI, M. R. MEYBODI: *A coverage monitoring algorithm based on learning automata for wireless sensor networks*. Appl. Math. & Info. Sci. 9 (2015), No. 3, 1317–1325.
- [12] H. M. AMMARI, S. K. DAS: *Centralized and clustered k-coverage protocols for wireless sensor networks*. IEEE Trans. Computers 61 (2012), No. 1, 118–133.
- [13] D. ARIVUDAINAMBI, G. SREEKANTH, S. BALAJI: *Genetic algorithm for sensor scheduling with adjustable sensing range*. IJ Eng. & Technol. 6 (2014), No. 5, 2282 to 2289.
- [14] D. ARIVUDAINAMBI, G. SREEKANTH, S. BALAJI: *Energy efficient sensors scheduling for target coverage in wireless sensor network*. Wireless Communications Networking and Applications, Lecture Notes in Electrical Engineering 348 (2016).

Received November 16, 2016

Research on the data processing and rotation mode transfer of cloud computing based on the virtual machine (VM)

LIJUN MAO¹

Abstract. In order to improve the efficiency and security in the data processing and rotation mode transfer of cloud computing, the visual machine method is proposed in this paper. The paper achieves this through workload consolidation onto a set of servers and powering off servers that become idle after consolidation. The main idea is to reduce power wastage by idle servers that do not have any workload. This paper presents an efficient method of server consolidation through virtual machine migration among server farms. The paper makes major contributions by providing a comprehensive consolidation strategy using secure VM live migration. It discusses efficient ways of deploying virtual machines to servers and migrating virtual machines among server's clusters based on sever workload utilization using dynamic round-robin algorithm. The ultimate result of the method is the reduction of the number of physical machines used since the number of physical machines used greatly affects the overall power consumption. The paper further discusses known security threats to VM'S during live migration and presents mitigation strategies to the threats.

Key words. Data processing, rotation mode, cloud computing, virtual machine.

1. Introduction

Cloud computing can be defined as “a type of parallel and distributed system consisting of a collection of inter-connected and virtualized computers that are dynamically provisioned” and presented as one or more unified computing resources based on service-level agreements established through negotiation between the service provider and consumers. Some of the examples for emerging Cloud computing infrastructures/platforms are Microsoft Azure, Amazon EC2, Google App Engine, and Aneka 121. From the energy efficiency perspective, a cloud computing data center Can be defined as a pool of computing and communication resources organized in the way to transform the received power into computing or data transfer work to satisfy user demands [1–2]. The operation of large geographically distributed data

¹General Education Center, Xi'an Peihua University, Shaanxi, 710125, China

centers requires considerable amount of energy that accounts for a large slice of the total operational costs for cloud data centers. One implication of Cloud platforms is the ability to dynamically adapt (scale up or scale-down) the amount of resources provisioned to an application in order to attend variations in demand that are either predictable, and occur due to access patterns observed during the day and during the night; or unexpected, and occurring due to a subtle increase in the popularity of the application service [3].

This capability of clouds is especially useful for elastic (automatically scaling of) applications, such as web hosting, content delivery, and social networks that are susceptible to such behavior. These applications often exhibit transient behavior (usage pattern) and have different Quality of Service (QoS) requirements depending on time criticality and users' interaction patterns (online/offline). Virtualization in computing is the creation of a virtual (rather than actual) version of something, such as a hardware platform, operating system, a storage device or network resources [4]. Virtualization can be viewed as part of an overall trend enterprise IT that includes autonomic computing, a scenario in which the IT environment will be able to manage itself based on perceived activity and utility computing, in which computer processing power is seen as a utility that clients can pay for only as needed. The usual goal of virtualization is to centralize administrative tasks while improving scalability and overall hardware-resource utilization.

A virtual machine (VM) is a software implementation of a machine (i.e. a computer) that executes programs like a physical machine [5]. VM's are separated into two major categories, based on their use and degree of correspondence to any real machine. A system virtual machine provides a complete system platform which supports the execution of a complete operating system (OS). Technologies, such as Dynamic Voltage and Frequency Scaling (DVFS), and Dynamic Power Management (DPM) were extensively studied and widely deployed. Because the aforementioned techniques rely on power-down and power-off methodologies, the efficiency of these techniques is at best limited. In fact, an idle server may consume about 2/3 of the peak load [6–8]. However most of the methods presented have security vulnerabilities and low energy saving. The way to address high energy problem is power required to feed a completely utilized system. This workload consolidation onto a set of servers by minimizing the peak can be achieved through idle after consolidation. The main idea is to and powering off servers that become do not have reduce power wastage by idle servers that any workload. This paper presents an efficient method of server consolidation through virtual machine migration among server farms.

2. Overview

Current Cloud computing providers have several data centers at different geographical locations over the Internet in order to optimally serve customer needs around the world. Figure 1 depicts such a Cloud computing architecture that consists of service consumers' (Software as a Service-SaaS providers') brokering and providers' coordinator services that support utility-driven internet working of clouds:

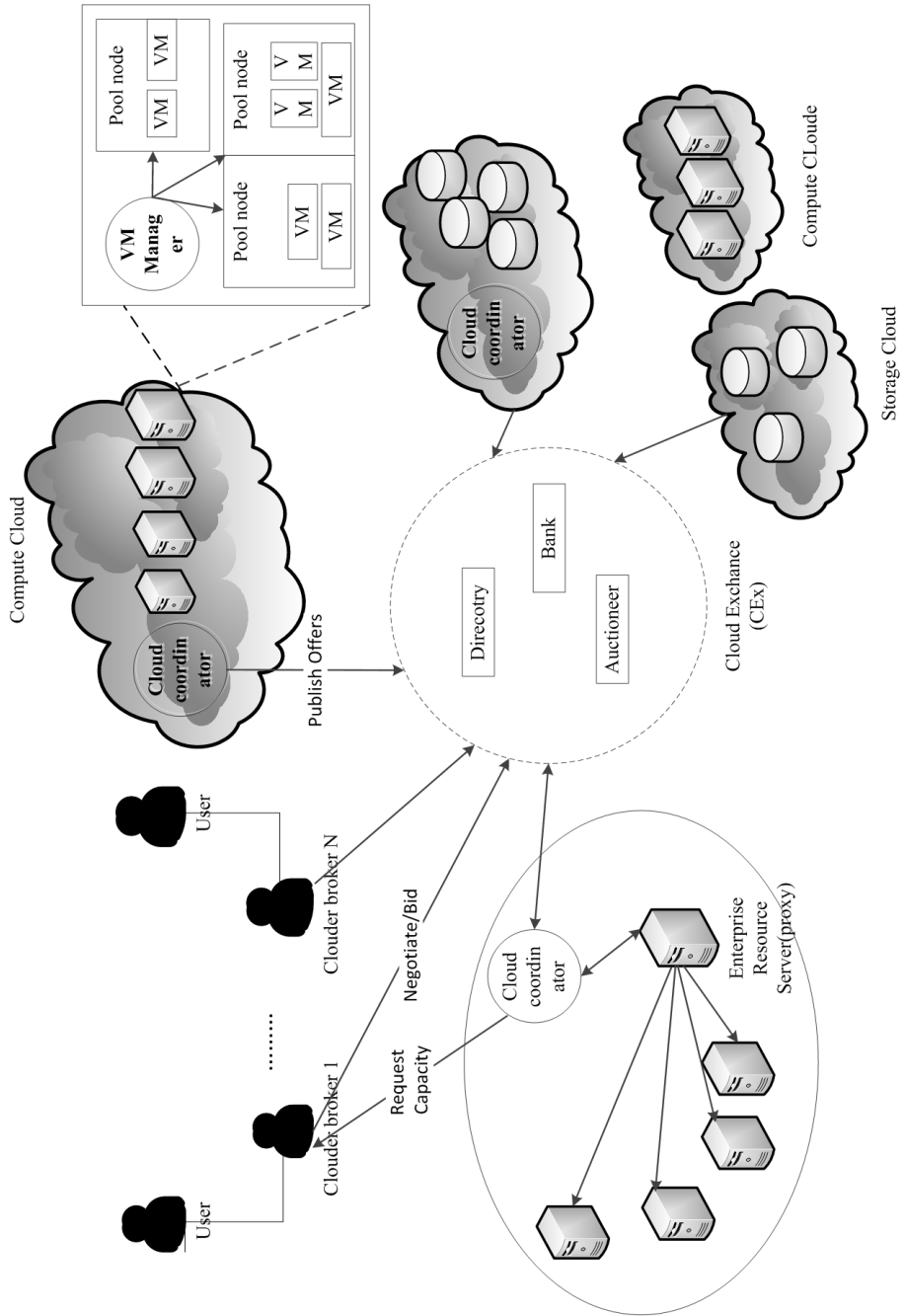


Fig. 1. Clouds and their federated network

application provisioning and workload migration. Federated inter-networking of administratively distributed clouds offers significant performance and financial benefits such as:

(i) Improving the ability of Software as a Service (SaaS) providers in meeting QoS levels for clients and offer improved service by optimizing the service placement and scale.

(ii) Enhancing the peak-load handling and dynamic system expansion capacity of every member cloud by allowing them to dynamically acquire additional resources from federation. This frees the Cloud providers from the need of setting up a new data center in every location.

(iii) Adapting to failures such as natural disasters and regular system maintenance is more graceful as providers can transparently migrate their services to others domains in the federation, thus avoiding Software License Agreement (SLA) violations and resulting penalties. Hence, federation of clouds not only ensures business continuity but also augments the reliability of the participating Cloud providers. One of the key components of the architecture presented in Fig. 1 is the Cloud Coordinator.

3. Layered model design and algorithm

Physical Cloud resources along with core middleware capabilities form the basis for delivering Infrastructure as a Service (IaaS) and Platform as a service (PaaS). The user-level middleware aims at providing SaaS capabilities. The top layer focuses on application services (SaaS) by making use of services provided by the lower layer services. PaaS/SaaS services are often developed and provided by 3rd party service providers, who are different from the IaaS providers.

3.1. *Cloud applications*

This layer includes applications that are directly available to define end-users as the active entity applications over the Internet. These applications may be that utilizes the SaaS supplied by the Cloud provider (SaaS providers) and accessed by end-users either via a subscription model or a pay-per-use basis. Alternatively, in this layer, users deploy their own applications. In the former case, there are applications such as Salesforce.com that supply business process models on clouds (namely, customer relationship management software) and social networks. In the latter, there are e-Science and e-Research applications, and Content-Delivery Networks. User-Level Middleware: This layer includes the software frameworks such as Web 2.0 Interfaces (Ajax, IBM Workplace) that help developers in creating rich, cost-effective user-interfaces for browser-based applications. The layer also provides those programming environments and composition tools that ease the creation, deployment, and execution of applications in clouds. Finally, in this layer several frameworks that support multi-layer applications development, such as spring and Hibernate, can be deployed to support applications running in the upper level.

3.2. Core middleware

This layer implements the platform level services that provide runtime environment for hosting and managing User-Level application services. Core services at this layer include Dynamic SLA Management, Accounting, Billing, Execution monitoring and management, and Pricing. The well-known examples of services operating at this layer are Amazon EC2, Google App Engine, and Aneka. The functionalities exposed by this layer are accessed by both SaaS (the services represented at the top-most layer in Figure 1) and IaaS (services shown at the bottom-most layer in Figure 1) services. Critical functionalities that need to be realized at this layer include messaging, service discovery, and load balancing. These functionalities are usually implemented by Cloud providers and offered to application developers at an additional premium. For instance, Amazon offers a load balancer and a monitoring service (Cloud watch) for the Amazon EC2 developers consumers. Similarly, developers building applications on Microsoft Azure clouds can use the .NET Service Bus for implementing message passing mechanism. System Level: The computing power in Cloud environments is supplied by a collection of data centers that are typically installed with hundreds to thousands of hosts. At the System Level layer, there exist massive physical resources (storage servers and application servers) that power the data centers. These servers are transparently managed by the higher-level virtualization services and toolkits that allow sharing of their capacity among virtual instances of servers. These VMs are isolated from each other, thereby making fault tolerant behavior and isolated security context possible.

The estimated finish time of a task managed by a VM is given as

$$eft(p) = est(p) + \frac{rlis}{capacity}, \quad (1)$$

where $est(p)$ is the estimated start time of task p and $rlis$ is the total number of instructions that the cloud network will need to execute. Thus the total capacity of a VM has multiple p tasks given as

$$capacity = \frac{\sum_{i=1}^{np} cap(i)}{np}, \quad (2)$$

where i is the processing strength of an individual element. Therefore, the total capacity of a VM in the cloud computing network is

$$capacity = \frac{\sum_{i=1}^{nap} cap(i)}{\max(\sum_{j=1}^{network} cores(j), np)}, \quad (3)$$

where $cap(i)$ is the processing strength of an individual element.

4. Experimental result and discussion

This paper considered two sets of experiments to evaluate the proposed approach. The first set of experimental tests was done to test the approach in a two-tier (2T), three-tier (3T), and three-tier high-speed (3Ths) architectures. The second experiments that were done validate the effectiveness of energy-conscious VM provisioning technique proposed. Proposed algorithms were evaluated through simulations using the C1oudSim toolkit which offers the following novel features

(i) Support for modeling and simulation of large scale Cloud computing environments, including data centers, on a single physical computing node.

(ii) A self-contained platform for modeling Clouds, service brokers, provisioning, and allocations policies.

(iii) Support for simulation of network connections among the simulated system elements.

(iv) Facility for simulation of federated Cloud environment that inter-networks resources from both private and public domains, a feature critical for research studies related to Cloud-Bursts and automatic application scaling. Some of the unique, compelling features that make C1oudSim our chosen simulation framework are:

(i) Availability of a virtualization engine that aids in creation and management of multiple, independent, and co-hosted virtualized services on a data center node.

(ii) Flexibility to switch between space-shared and time-shared allocation of processing cores to virtualized services. In contrast with other architectures 2T data center does not include aggregation switches. The core switches are connected to the access network directly using 1 GE links (referred as C2-C3) and interconnected between them using i0 GE links (referred as C1-C2). The 3Ths architecture mainly improves the 3T architecture with providing more bandwidth in the core and aggregation parts of the network. The bandwidth of the C1-CZ and C2-C3 links in 3Ths architecture is ten times of that in 3T and corresponds to 100 GE and LOGE respectively. The availability of 100 GE links allows keeping the number of core switches as well as the number of paths in the ECMP routing limited to 2 serving the same amount switches in the access. The propagation delay of all the links is set to 10 ns. The workload generation events and the size of the workloads are exponentially distributed. The average size of the workload and its computing requirement depends on the type of task. For CIW workloads the relation between computing and data transfer parts is chosen to be 1/10, meaning that with a maximum load of the data center, its servers will be occupied for 100 % while the communication network will be loaded for 10 % of its maximum capacity. For DIW workloads the relation is reverse. Under the maximum load the communication network is loaded for 100 % while computing servers far only 10 %. Balanced workloads load computing servers and data center network proportionally. The workloads arriving at the data center are scheduled for execution using secure energy-aware C1oudSim scheduler. This scheduler tends to group the workloads on a minimum possible amount of computing servers. In order to account for DIW workloads the scheduler continuously tracks buffer occupancy of network switches on the path. In case of a congestion the scheduler avoids using congested routes even if they lead to the servers able to

satisfy computational requirement of the workloads. The servers left idle are put into sleep mode (DNS scheme) while on the under-loaded servers the supply voltage is reduced (DVFS scheme). The time required to change the power state in either mode is set to 100 ms.

Figure 2 presents a workload distribution among servers. The whole load of the data center (around 30% of its total capacity) is mapped onto approximately one third of the servers maintaining load at a peak rate (left part of the chart). This way, the remaining two thirds of the servers can be shut down using DNS technique. A tiny portion of the approximately 50 out of 1536 servers which load represents a falling slope of the chart are under-utilized on average, and DVFS technique can be applied on them. Figure 3 presents data center energy consumption comparison for different types of user workloads: balanced. Balanced workloads consume the most as the consumptions of both servers and switches become proportional to the offered load of the system. CIWs stress the computing servers and leave data center network almost unutilized. On the contrary, execution of DIWs creates a heavy traffic load at the switches and links leaving the servers mostly idle. The process of scheduling for DIWs requires performing load balancing for redistributing the traffic from congested links. As a result, these workloads cannot be fully grouped at the minimum amount of the servers due to the limitations of the data center topology. This way, in real data centers with the mixed nature of workloads the scheduler may attempt a grouped allocation of CIWs and DIWs as optimal allocation policy.

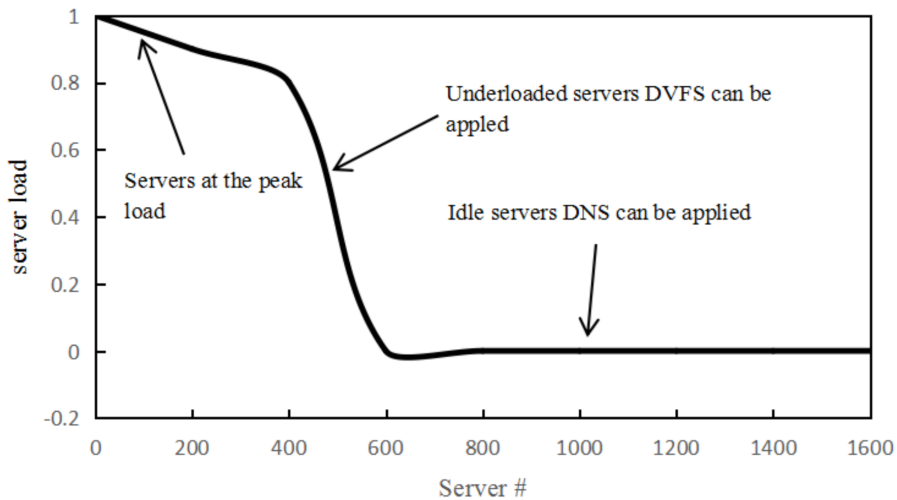


Fig. 2. Server workload distribution with a CloudSim scheduler

This component is instantiated by each cloud in the system whose responsibility is to undertake the following important activities:

- (i) Exporting Cloud services, both infrastructure and platform-level, to the federation
- (ii) Keeping track of load on the Cloud resources (VMs, computing services) and

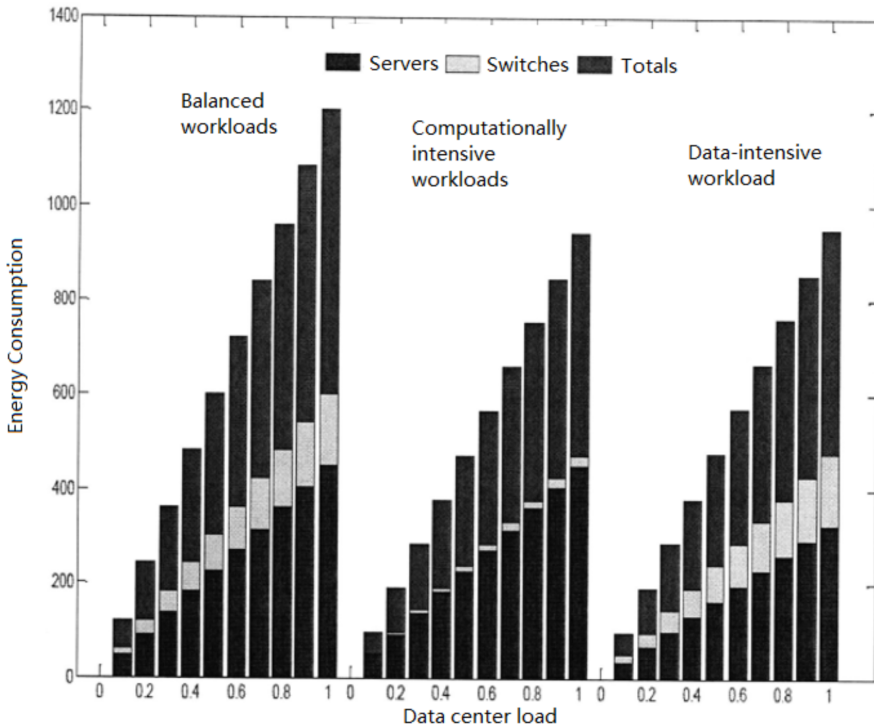


Fig. 3. Data center energy consumption for different types of workloads

undertaking negotiation with other Cloud providers in the federation for handling the sudden peak in resource demand at local cloud.

(iii) Monitoring the application execution over its lifecycle and overseeing that agreed SLAs are delivered. The Cloud brokers acting on behalf of SaaS providers identify suitable Cloud service providers through the Cloud Exchange. Further, Cloud brokers can also negotiate with respective Cloud Coordinators for allocation of resources that meets the QoS needs have hosted or to be hosted SaaS applications. The Cloud Exchange (CEX) acts as a market maker by bringing together Cloud service (IaaS) and SaaS providers. It aggregates the infrastructure demands from the Cloud brokers and evaluates them against the available supply currently published by the Cloud Coordinators. The applications that may benefit from the aforementioned federated Cloud computing infrastructure include social networks such as Facebook and MySpace, and Content Delivery Networks (CDNs). Social networking sites serve dynamic contents to millions of users, whose access and interaction patterns are difficult to predict. In general, social networking web-sites are built using multi-tiered web applications such as Web Sphere and persistency layers like the MySQL relational database. Usually, each component will run in a different virtual machine, which can be hosted in data centers owned by different

Cloud computing providers. Additionally, each plug-in developer has the freedom to choose which Cloud computing provider offers the services that are more suitable to run his/hers plug-in. As a consequence, a typical social networking web application is formed by hundreds of different services, which may be hosted by dozens of Cloud-oriented data centers around the world. Whenever there is a variation in temporal and spatial locality of workload (usage pattern), each application component must dynamically scale to offer good quality of experience to users [9–10]. Figure 4 shows the data center energy consumption comparison and Fig. 5 shows the total energy consumption by the system in the proposed model.

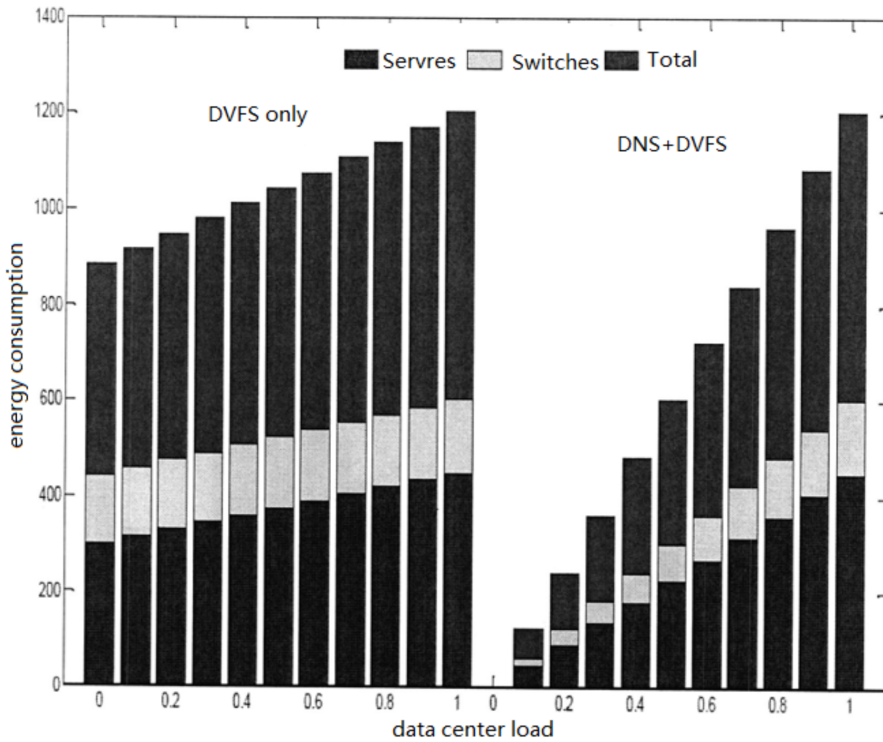


Fig. 4. Data center energy consumption comparison

Domain experts and scientists can also take advantage of such mechanisms by using the cloud to leverage resources for their high-throughput e-Science applications, such as Monte-Carlo simulation and Medical Image Registration. In this scenario, the clouds can be augmented to the existing cluster and grid based resource pool to meet research deadlines and milestones. Cloud computing servers applications as localized attacker or malware to use the same operating systems, enterprise and web virtual machines and physical servers. The ability for a remotely exploit vulnerabilities in these systems and threat to virtualized cloud computing environments. Figure 6 shows the Number of VM migrations and Fig. 7 shows the number of SLA

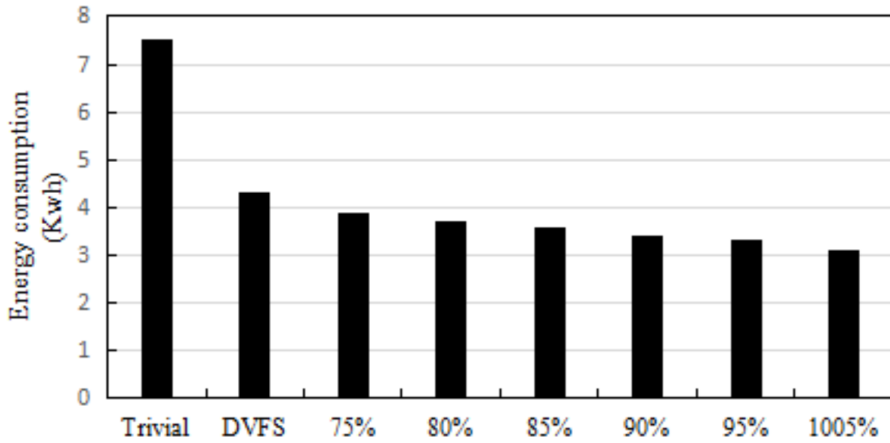


Fig. 5. Total energy consumption by the system in the proposed model

violations. In virtual machines increases the attack surface and risk of VM-to-VM compromise. Furthermore, several security vulnerabilities exist in migration, especially live migration of such systems that may degrade the protection strength or even break the protection. In VM live migration, the challenges lie in the following three aspects:

- (i) Preserving the privacy and integrity of protected contents.
- (ii) Packing the maintenance metadata in the Virtual Machine Monitor (VMM), conflict, and re-establishing the protection base on the solving the namespace target platform.
- (iii) Eliminating the security vulnerabilities imposed by live migration. Time-of-Check to time-of-use (TOCTTOU) attack and replay attack have identified as possible attacks that a VM faces during live migration. This provides mitigation strategies against these vulnerabilities that a VM is exposed Live Migration.

5. Conclusion

This paper has done extensive investigation on various power-aware VM provisioning schemes like DVFS and DNS. The paper does two sets of experiments to test the presented approach in various architectures like two-tier (2T), three-tier (3T), and three-tier high-speed (3Ths) architectures. Previously, other researcher had performed simulation on two tier architecture only. They overlooked the fact that data centers behave differently when implemented using 2T, 3t and 3Ths. For this purpose, the paper is able to present an optimal power aware provisioning scheme based on comparative evaluation the existing schemes on various architectures. The effectiveness of these contributions has been appraised through a comprehensive simulation-driven analysis of the proposed approach based on realistic and well-known data center conditions in order to capture the transient behaviors that prevail in existing

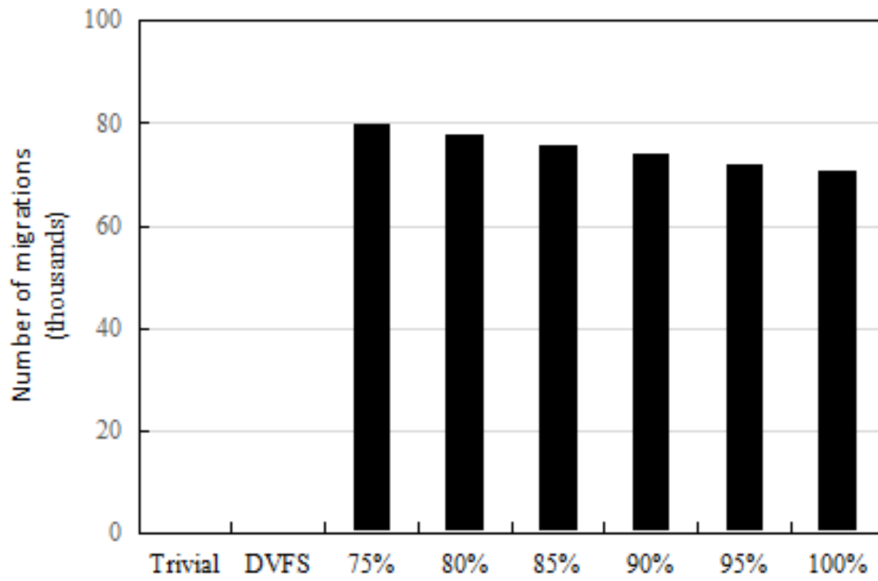


Fig. 6. Number of VM migrations

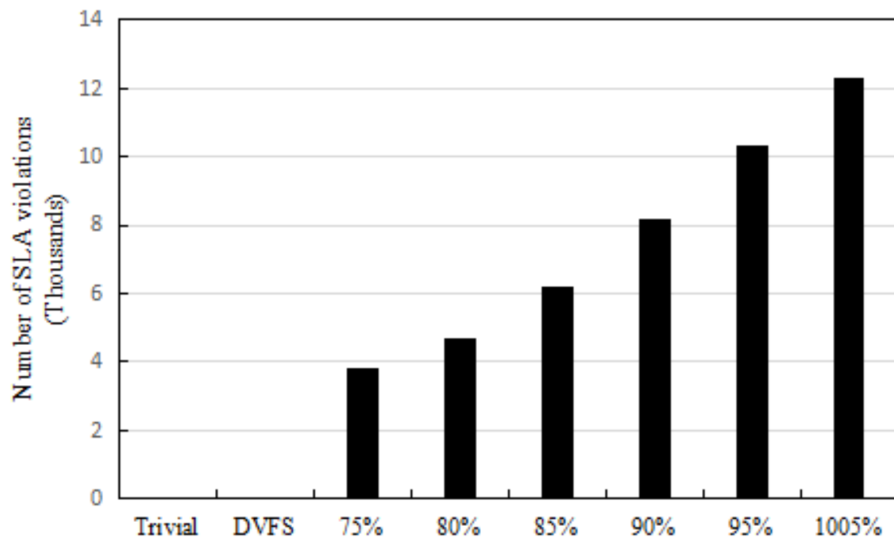


Fig. 7. Number of SLA violations

data center environments.

References

- [1] M. JALALI, A.,BOUZER, B. ARASTEH, M. MOLOUDI: *The effect of cloud computing technology in personalization and education improvements and its challenges*. Procedia - Social and Behavioral Sciences 83 (2013), 655–658.
- [2] P. BARHAM, B. DRAGOVIC, K. FRASER, S. HAND, T. HARRIS, A. HO, R. NEUGEBAUER, I. PRATT, A. WARFIELD: *Virtual machine monitors: xen and the art of virtualization*. ACM Symposium on Operating System Principles (SOSP'03), 19–22 Oct. 2003, Bolton, Landing, New York, USA, 36, No. 8, 164–177.
- [3] T. GARFINKEL, B. PFAFF, J. CHOW, M. ROSENBLUM, D. BONEH: *Terra: a virtual machine-based platform for trusted computing*. ACM Symposium on Operating System Principles SOSP'03), 19–22 Oct. 2003, Bolton, Landing, New York, USA, 37, No. 5, 193–206.
- [4] A.KIVITY, Y. KAMAY, Y. LAOR, U. LUBLIN, A. LIGUORI: *Kvm: the linux virtual machine monitor*. Proceedings of the Linux Symposium, 27–30 June 2007, Ottawa, Ontario, Canada, 1, 225–230.
- [5] T. GARFINKEL, M. ROSENBLUM: *A virtual machine introspection based architecture for intrusion detection*. Internet Society's 2003 Symposium on Network and Distributed System Security (NDSS'03), 6–7 Feb. 2003, San Diego, California, USA, 191 to 206.
- [6] P. LEVIS, D. CULLER: *Matd: A tiny virtual machine for sensor networks*. ACM SIGOPS Operating Systems Review 36 (2002) No. 5, 85–95.
- [7] A. GEIST, A. BEGUELIN, J. DONGARRA, J. JIANG, W. MANCHEK, V. SUNDERAM, M. NOVOTNY, S. MCKAY: *PVM-parallel virtual machine: A users' guide and tutorial for networked parallel computing*. Computers in Physics 9 (1995), No. 6, 607–607.
- [8] R. P. GOLDBERG: *Survey of virtual machine research*. J Computer 7 (1974), No. 9, 34–45.
- [9] G. W. DUNLAP, S. T. KING, S. CINAR, M. A. BASRAI, P. M. CHEN: *Revirt: enabling intrusion analysis through virtual-machine logging and replay*. ACM SIGOPS Operating Systems Review 36 (2002), No. SI, 211–224.
- [10] T. LINDHOLM, F. YELLIN: *The java TM virtual machine specification*. Institute of Information & Computing Sciences 15, (1997), No. 6, 27–59.

Received November 16, 2016

An efficient face recognition algorithm based on multi-kernel regularization learning

BI RONGRONG¹

Abstract. A novel face recognition algorithm based on multi-kernel regularization learning is proposed. Firstly, we present three types of visual features to describe human faces, including: 1) Local Gabor Gradient Pattern (LGGP), 2) Histogram of Gabor Ordinal Ratio Measures (HGORM) and 3) Densely Sampled Local Binary Pattern (DSLBP). Secondly, we integrate the multiple kernel based method and the manifold regularization together to solve the face recognition issue. Particularly, the face recognition problem is solved by minimizing an optimization problem based on manifold regularization calculation using the graph Laplacian. Finally, three typical human face databases are used to test the performance of our proposed algorithm. Experimental results show that the proposed algorithm can achieve high recognition accuracy even when occlusion happens.

Key words. Face recognition, multi-kernel regularization learning, manifold regularization, loss function.

1. Introduction

With the development of information science, biometric technology has become a key mode for personal identification or authentication technology [1]. ID authentication refers to a crucial issue in human's daily life. We need to prove our own ID in many occasions, such as electronic business, bank online, public security. However, existing ID authenticating methods can no longer satisfy our requirements [2], [3]. In particular, face recognition refers to an important branch of biometrics, which is more easily accepted for the most intuitive means of identification. Face features of humans will not be changed with age varying [4]. Different from other biometric identification methods (such as fingerprint, retina, iris, and so on), face recognition is a more humanitarian approach, which is more direct and friendly [5].

However, due to the issues of face recognition (e.g. illumination, angle, and occlusion) which have not been tackled well, the accuracy of face recognition still cannot be satisfied. Face recognition is made up of two steps: 1) face detection

¹Harbin University of Science and Technology; Heilongjiang Harbin 150080, China

and 2) face identification [6], [7]. Face detection aims to obtain the location and size of faces in the host image. On the other hand, face identification analyzes and extracts visual feature vector from the target image [8]. In general, face recognition has significant theoretical research values and wide application values [9].

The main idea of this paper is to introduce regularization learning to solve the human face recognition problem. To tackle an ill-posed issue and avoid overfitting, regularization learning has been proposed, and it is hot topic in machine learning and computer science. In the following, we introduce related works about applications of regularization learning, such as Real-time visual tracking [10], high dimensional classification [11], MRI reconstruction [12], image classification [13], Multiple task learning [14], object tracking [15], human face-based age estimation [16], Text categorization [17], Learning Gene Expression Programs [18], image noise reduction [19], Image Understanding [20].

2. Feature description for human face recognition

For the face recognition task, effective feature description is a crucial problem. Therefore, in this section, we explain what visual features are chosen to describe human faces. Particularly, in this paper, we assume that a human face image is represented as $I \in R^{128 \cdot 128}$.

2.1. Feature type 1: Local Gabor Gradient Pattern (denoted as LGGP)

In order to code Gabor magnitude responses, we exploit a gradient descriptor which is defined as follows.

$$\xi(x_c) = \arctan\left(\beta \cdot \frac{N_v}{N_h + \lambda}\right), \quad (1)$$

where N_v and N_h denote the gradients, which should be calculated in both vertical direction v and horizontal directions h . The parameters β and λ are used to stabilize the gradient descriptor. Function $\arctan()$ and parameters β , λ are exploited to avoid the output from increasing or decreasing too fast. Then, the gradients are calculated as follows.

$$N_v = \gamma_{\text{mod}(i+4,R)} - \gamma_i, \quad (2)$$

$$N_h = \gamma_{\text{mod}(i+6,R)} - \gamma_{\text{mod}(i+2,R)}, \quad (3)$$

where the function $\text{mod}()$ means the modulo operator, and symbol i denotes the index of the neighbor pixel. Then, in order to obtain Local Gabor Gradient Pattern features, each gradient-encoded Gabor image is separated to several non-overlapping patches, and then histogram of these patches is constructed.

2.2. Feature type 2: Histogram of Gabor Ordinal Ratio Measures (denoted as HGORM)

In order to effectively describe Gabor phase responses, we utilize the Ordinal Measure to compare two various regions to make a decision which region has a higher value. We establish a horizontal ordinal filter, and we use this ordinal filtering to generate the output of Gabor phase responses. Afterwards, a ratio measure is exploited to calculate the features as follows.

$$OF = \arctan \left(\beta \cdot \frac{O_v}{O_h + \lambda} \right), \quad (4)$$

where symbols O_h and O_v refer to the convolution of horizontal and vertical ordinal filter with the Gabor phase response respectively. Furthermore, parameters β and λ refer to two constants which are exploited to ensure the function to be stable.

Then, HGORM feature is regarded as an updated version of the LGGP feature. The ratio measure utilized in HGORM is weighted through Gaussian kernel, and image is separated to several non-overlapping patches as well. The number of patches of an image is set to 64 with the patch size is $16 \cdot 16$, and the number of histogram bins is set to 16.

2.3. Feature type 3: Densely Sampled Local Binary Pattern (denoted as DS-LBP)

We use uniform LBP patterns which are obtained from the image, and then a 59-bin histogram feature vector is constructed. Furthermore, Uniform LBP patterns represent all binary patterns which have at most two bitwise transitions in the range $[0, 1]$. Next, to construct the DS-LBP feature vector, each image coded by LBP is separated to several overlapping patches, and then a histogram is extracted from image patch. Particularly, in this work we set the number of patches for in each image to 256 with the patch size is $16 \cdot 16$. Afterwards, feature vector of DS-LBP is represented as follows.

$$V_{DS-LBP}(I) = (s_1, s_2, \dots, s_N), \quad (5)$$

where N refers to the total number of patches in an image, and s refers to the histogram features.

Integrating all the above three feature types, overview of the feature descriptors used in this work is given in Table 1.

3. The proposed face recognition algorithm based on multi-kernel regularization learning

In this section, we discuss how to solve the face recognition problem by image classification, and the manifold regularized multiple kernel learning (denoted as

MKL) is used to design classifier. Multiple kernel learning is defined as follows.

$$\arg \min_{f \in H} C \sum_{i=1}^K L(x_i, y_i, f) + \gamma \|f\|_H^2, \quad (6)$$

where total K pairs of training data (x_i, y_i) , $i \in \{1, 2, \dots, K\}$, $L(x_i, y_i, f)$ refer to a loss function, $\|f\|_H^2$ denotes a norm restriction with the space H .

Table 1. Overview of the feature descriptors used in this work

Feature category	LGGP	HGORM	DS-LBP
Size of patch	16×16	16×16	16×16
Patch number	2560	2560	256
Number of bins for each patch	16	16	59
Patch organization mode	Non overlapping	Non overlapping	Overlapping

In terms of the Representer theory, to minimize the optimization problem in (8), the following equation should be solved in advance.

Considering that it is of great importance to integrate multiple kernel based policy and the manifold regularization. Therefore, the formation of the manifold regularized multiple kernel learning is given as follows

$$\arg \min_{f \in H} C \sum_{i=1}^K L(x_i, y_i, f) + \gamma_h \|f\|_H^2 + \gamma_p \|f\|_P^2, \quad (7)$$

where $\|f\|_P^2$ is used to represent the internal structure of data and parameter γ_h is able to control the penalty of manifold.

In order to calculate the manifold regularization, graph Laplacian (denoted as L) is used as follows.

$$\gamma_p \|f\|_P^2 = \frac{\gamma_p}{\ell^2} f^T L f, \quad (8)$$

where $L = D - W$, among which W is the data adjacency graph weight and D refers to a diagonal matrix. Furthermore, the following condition is satisfied.

$$D_{ij} = \sum_{j=1}^n W_{ij}. \quad (9)$$

Afterwards, the loss function is used as the hinge loss function and it is suitable to be utilized in classifier, such as support vector machine.

$$C \cdot \sum_{i=1}^K L(x_i, y_i, f) = C \cdot \sum_{i=1}^K \max(0, 1 - y_i f(x_i)). \quad (10)$$

Next, to estimate the error of hinge loss function, feature function is modified as follows.

$$f^*(x) = \arg \min_{f \in H} C \sum_{i=1}^K \max(0, 1 - y_i f(x_i)) + \gamma_h \|f\|_H^2 + \frac{\gamma_p}{\ell^2} f^T L f. \quad (11)$$

Therefore, the face recognition problem can be tackled by minimizing the optimization problem in (11).

4. Experiment

In this section, we choose three typical human face databases (named as D1: Extended Yale B dataset, D2: FERET dataset, and D3: CMU PIE) to test the performance of our proposed algorithm. D1 is made up of 2414 frontal human face images of 38 persons, and nearly 64 images are taken from one person. The original images in D1 are organized as 192×168 pixels. In order to test the adaptive capacity of our test algorithm, D1 dataset is designed based on different illumination conditions. D2 includes 1199 subjects more than 14000 images. Particularly, face images in D2 are taken under various lighting conditions, facial expressions, and pose angles. For simplicity, only face images which are taken from the front view are chosen. D3 dataset contains 68 subjects with 41386 human face images, and images in this dataset are taken under different illuminations and expressions.

To make performance comparison, Multiple Kernel Learning based face recognition (denoted as MKL) [21] and SVM based face recognition [22] are used to compared with ours method. The overall performance of MKL, SVM and our proposed method is shown in Table 2.

Table 2. Face recognition accuracy for different methods

Dataset	MKL (%)	SVM (%)	Our proposed method (%)
D1	85.69	88.95	91.64
D2	82.47	84.12	87.93
D3	84.61	86.08	89.37

Table 2 shows that our proposed method is able to achieve higher face recognition accuracy than other two methods for all three datasets. Afterwards, we illustrate ROC curves for all above datasets under different methods (shown in Figs. 1–3).

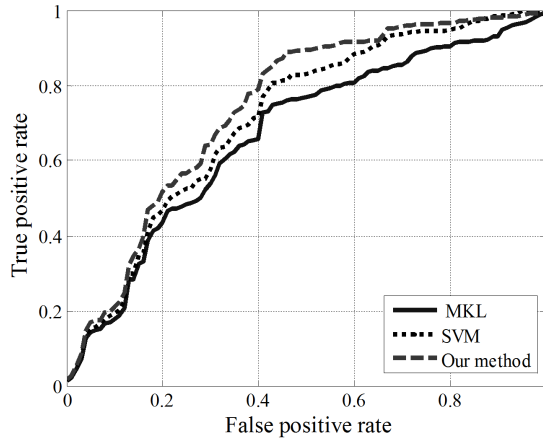


Fig. 1. ROC curve for dataset D1

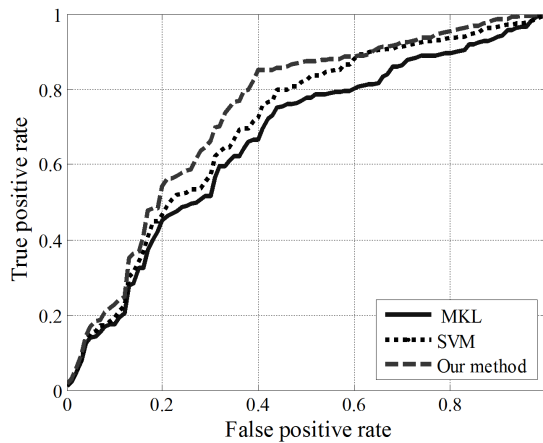


Fig. 2. ROC curve for dataset D2

To further test the performance of our proposed method when part of human face image is occluded, and experimental results are given in Figs. 4–6.

It can be observed that compared with MKL and SVM based face recognition methods, our proposed method can achieve higher recognition accuracy than other methods. When occlusion rate increasing, recognition accuracy of all methods decreases. However, we find that even when occlusion happens, our method still performs better than other methods.

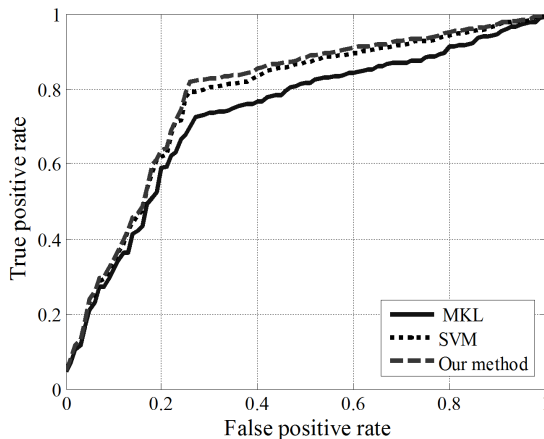


Fig. 3. ROC curve for dataset D3

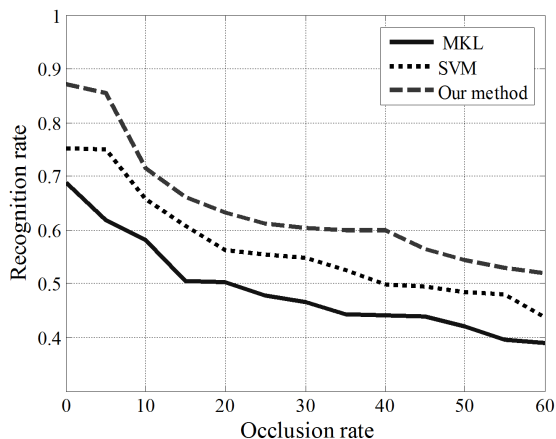


Fig. 4. Face recognition rate for different occlusion rate using dataset D1

5. Conclusion

This paper aims to present an efficient face recognition algorithm based on multi-kernel regularization learning. Three types of visual features are exploited to describe human faces, which are 1) Local Gabor Gradient Pattern, 2) Histogram of Gabor Ordinal Ratio Measures and 3) Densely Sampled Local Binary Pattern. Then, the multiple kernel and the manifold regularization are used to solve the human face recognition problem. Afterwards, the face recognition problem is solved by minimizing an optimization problem with manifold regularization calculation. In the end, experimental results demonstrate that that the proposed algorithm can achieve high

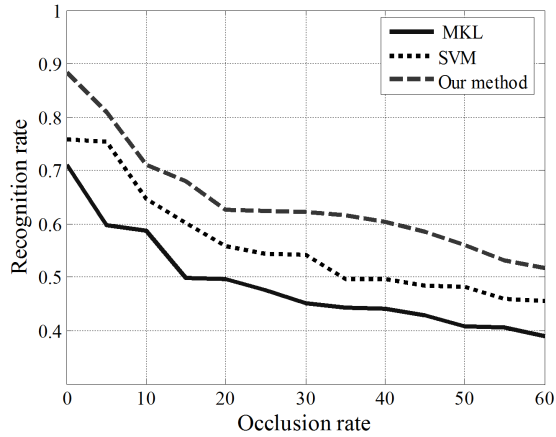


Fig. 5. Face recognition rate for different occlusion rate using dataset D2

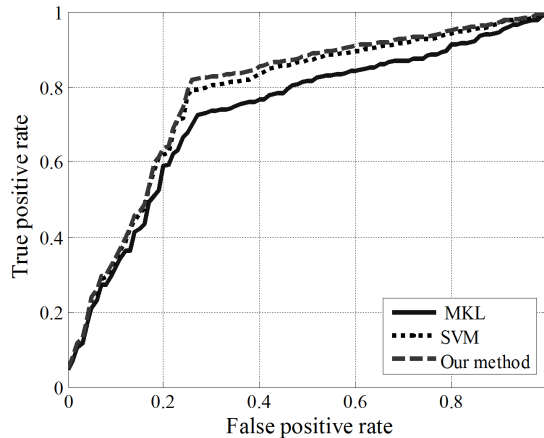


Fig. 6. Face recognition rate for different occlusion rate using dataset D3

recognition accuracy for various human face databases.

References

- [1] H. LI, C. Y. SUEN: *Robust face recognition based on dynamic rank representation*. Pattern Recognition 60 (2016), 13–24.
- [2] G. ZHANG, H. SUN, Z. JI, Y. H. YUAN, Q. SUN: *Cost-sensitive dictionary learning for face recognition*. Pattern Recognition 60 (2016), 613–629.
- [3] C. CHEN, A. DANTCHEVA, A. ROSS: *An ensemble of patch-based subspaces for makeup-robust face recognition*. Information Fusion, Part B 32 (2016), 80–92.

- [4] S. HUANG, L. ZHUANG: *Exponential discriminant locality preserving projection for face recognition*. *Neurocomputing* 208 (2016), 373–377.
- [5] Z. M. LI, Z. H. HUANG, K. SHANG: *A customized sparse representation model with mixed norm for undersampled face recognition*. *IEEE Trans. Information Forensics and Security* 11 (2016), No. 10, 2203–2214.
- [6] F. SHEN, W. YANG, H. LI, H. ZHANG, H. T. SHEN: *Robust regression based face recognition with fast outlier removal*. *Multimedia Tools and Applications* 75 (2016) No. 20, 12535–12546.
- [7] G. F. LU, Y. WANG, J. ZOU: *Graph maximum margin criterion for face recognition*. *Neural Processing Letters* 44 (2016), No. 2, 387–405.
- [8] Z. LEI, D. YI, S. Z. LI: *Learning stacked image descriptor for face recognition*. *IEEE Trans. Circuits and Systems for Video Technology* 26 (2016), No. 9, 1685–1696.
- [9] L. ZHAO, Y. ZHANG, B. YIN, Y. SUN, Y. HU, X. PIAO, Q. WU: *Fisher discrimination-based-norm sparse representation for face recognition*. *The Visual Computer* 32 (2016), No. 9, 1165–1178.
- [10] P. ZHANG, T. ZHUO, Y. N. ZHANG, L. XIE, D. P. TAO: *Real-time tracking-by-learning with high-order regularization fusion for big video abstraction*. *Signal Processing* 124, (2016), 246–258.
- [11] Y. J. WU, B. Y. LIU: *Spatial and anatomical regularization based on multiple kernel learning for neuroimaging classification*. *IEICE Trans. Information and Systems* 99 (2016), No. 4, 1272–1274.
- [12] A. K. TANC, E. M. EKSIÖGLU: *MRI reconstruction with joint global regularization and transform learning*. *Computerized Medical Imaging and Graphics* 53 (2016), 1–8.
- [13] F. M. SUN, Y. XU, J. ZHOU: *Active learning SVM with regularization path for image classification*. *Multimedia Tools and Applications* 75 (2016), No. 3, 1427–1442.
- [14] J. PU, J. WANG, Y. G. JIANG, X. XUE: *Multiple task learning with flexible structure regularization*. *Neurocomputing* 177 (2016), 242–256.
- [15] S. ZHANG, Y. SUI, S. ZHAO, X. YU, L. ZHANG: *Multi-local-task learning with global regularization for object tracking*. *Pattern Recognition* 48 (2015), No. 12, 3881–3894.
- [16] Q. TIAN, S. CHEN: *Cumulative attribute relation regularization learning for human age estimation*. *Neurocomputing* 165 (2015), 456–467.
- [17] W. ZHENG, Y. QIAN, H. LU: *Text categorization based on regularization extreme learning machine*. *Neural Computing and Applications* 22 (2013), No. 3, 447–456.
- [18] G. YE, M. TANG, J. F. CAI, Q. NIE, X. XIE: *Low-rank regularization for learning gene expression programs*. *Plos One* 8 (2013), No. 12, paper 82146.
- [19] S. YANG, L. ZHAO, M. WANG, Y. ZHANG, L. JIAO: *Dictionary learning and similarity regularization based image noise reduction*. *J Visual Communication and Image Representation* 24 (2013), No. 2, 181–186.
- [20] L. LI, S. Q. JIANG, Q. M. HUANG: *Learning hierarchical semantic description via mixed-norm regularization for image understanding*. *IEEE Trans. Multimedia* 14 (2012), No. 5, 1401–1413.
- [21] X. Z. LIU, G. C. FENG: *Multiple kernel learning in Fisher discriminant analysis for face recognition*. *SAGE journals, I. J. Advanced Robotic System* 10 (2013), No. 2, paper 142.
- [22] W. H. LI, L. J. LIU, W., G. GONG: *Multi-objective uniform design as a SVM model selection tool for face recognition*. *Expert Systems with Applications* 38 (2011), No. 6, 6689–6695.

Received November 16, 2016

Research on bridgeless PFC circuit control algorithm of electric vehicle charging pile

HONGLAI YAN¹

Abstract. In order to solve the problem of input voltage instability and output load fluctuation when the electric vehicle charging pile is charging the charging pile, the bridgeless power factor correcting (PFC) control algorithm of charging pile as the research object is taken, and made a detailed analysis and research. Firstly, the mathematical model of bridgeless PFC circuit is established, and the commonly used single cycle control algorithm is deduced. According to the theory, the simulation model of bridgeless PFC is established. According to the test data of simulation circuits in input voltage disturbance, output voltage fluctuation, power factor and other aspects, the algorithm is used as a control algorithm for the circuit, and the simulation verification is carried out on it.

Key words. Electric vehicle, bridgeless PFC, single cycle control algorithm.

1. Introduction

With the progress of science and technology and development of economy, the vehicle has become an indispensable means of transport in people's lives. At the same time, the energy and environmental problems caused by traditional vehicles are becoming more and more serious. In order to solve the energy and environmental problems, pure electric vehicles began to be widely promoted [1, 2]. With the increase in pure electric vehicles, the charging behavior of a large number of pure electric vehicles has a great impact on the power grid [3].

From the load point of view, charging pile is a harmonic source load. When the pure electric vehicle is charging through the charging pile, the charging pile injects the harmonic current into the grid, thus affecting the quality of the current and voltage in the grid. With a large number of pure electric vehicles entering the market, when a region has a large number of charging piles that charge purely electric vehicles, it leads to regional load fluctuations of the grid, which will also influence the power supply voltage of the grid. The floating of the grid voltage

¹Xi'an International University, Shaanxi, 710000, China

adversely affects the battery life of a pure electric vehicle which is charged through the charging pile. At the same time, the power conversion circuit of the charging pile inevitably produces electromagnetic interference in the course of work. The presence of electromagnetic interference not only has a great impact on the sensitive electronic equipment (meters, etc.) of the charging pile, but undesirable components of current also penetrate into the power grid and cause harmonic pollution. The battery model of the pure electric vehicle is different, and when the same battery is charged in different power conditions, the load will exhibit some differences. The existence of these problems makes the power conversion circuit of the charging pile need to have a good anti-interference barrier to the input voltage and output load fluctuations, and need to meet the electromagnetic compatibility in the normal operation process.

2. Methods

2.1. Analysis of the circuit model of bridgeless Boost PFC

The boost power factor correcting (Boost PFC) circuit has many kinds of structures [4, 5] at present, because the two switch tubes and the diode in the Boost PFC circuit are the same model. Especially, when the bridgeless Boost PFC uses two independent inductances, it needs to keep the inductance of the two inductors the same. Therefore, the bridgeless Boost PFC equivalent circuit can be expressed in a uniform form, that is, it can be equivalent to the combination of two Boost PFC which take turns to work when the frequency input voltage is in the positive and negative two-half cycles. In order to combine the circuit to analyze, the bridgeless Boost PFC in this paper is taken as an example to analyze the circuit. The analysis process and results of the bridgeless Boost PFC circuit can be applied to other topologies.

2.1.1. Large-signal model of bridgeless Boost PFC. Before the analysis of the bridgeless Boost PFC circuit the following assumptions need to be made:

1. All the semiconductor devices in the circuit are regarded as ideal device.
2. The bridgeless Boost PFC circuit works in continuous conduction mode (CCM mode).
3. Switching frequency is far higher than the frequency of AC input voltage

According to the analysis of two modes of Boost PFC circuit, the equivalent of Boost PFC is obtained. The circuit is shown in Fig. 1.

The equivalent circuit shown in Fig. 1 can be divided into two different operating states according to the turn-off of the switch S. According to the switch tube conduction and shutdown, the flow direction analysis of the voltaic is shown in Fig. 2, which is the equivalent circuit of the bridgeless Boost PFC in a cycle.

When the switch tube S is in the conduction, the state equation of the inductor current and capacitance voltage in the circuits under the condition of the breakover can be obtained according to the Kirchhoff's theorems:

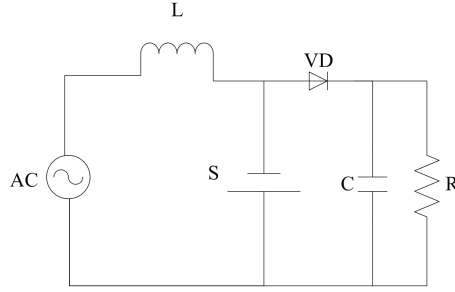


Fig. 1. Equivalent circuit of bridgeless Boost PFC

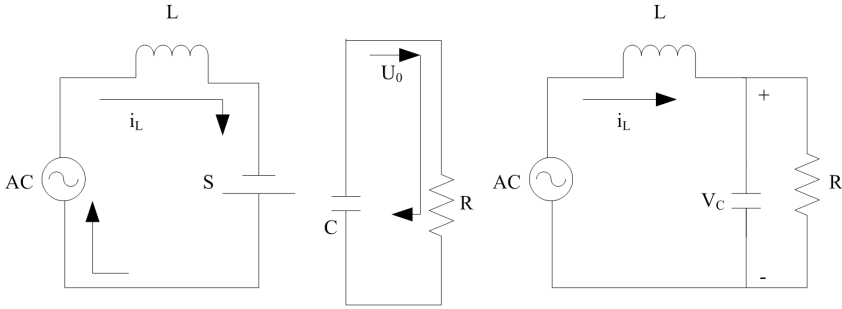


Fig. 2. Equivalent circuit of bridgeless Boost PFC in one cycle

$$\frac{di_L}{dt} = -\frac{1}{L}V_c, \quad (1)$$

$$\frac{dV_c}{dt} = -\frac{1}{RC}V_c, \quad (2)$$

where i_L is the input inductor current and V_c is the output capacitor voltage. When the switch tube is off, the state equations of the input inductor and capacitor voltage can be obtained in the form

$$\frac{di_L}{dt} = -\frac{1}{L}V_c + \frac{1}{L}v_{ac}, \quad (3)$$

$$\frac{dV_c}{dt} = \frac{1}{C}i_L - \frac{1}{RC}V_c. \quad (4)$$

Since it is assumed that the switching frequency is much greater than the frequency of the AC power, the input voltage U_{in} in the switching cycle is a fixed value. When the bridgeless Boost PFC is in the CCM mode, it is assumed that the duty cycle of the switch tube is d , the break duty cycle is d' , the input inductor current

i_L and the output capacitor voltage V_C are the state quantities for each switching cycle. The state equation for a switching period is given as

$$\begin{aligned} \begin{pmatrix} i_L^g \\ v_C^g \end{pmatrix} &= d \left(\begin{pmatrix} 0 & 0 \\ 0 & \frac{1}{RC} \end{pmatrix} \cdot \begin{bmatrix} i_L \\ v_C \end{bmatrix} + \begin{bmatrix} \frac{1}{L} \\ 0 \end{bmatrix} \cdot U_{in} \right) + \\ &+ d' \left(\begin{pmatrix} 0 & -\frac{1}{L} \\ \frac{1}{C} & -\frac{1}{RC} \end{pmatrix} \cdot \begin{bmatrix} i_L \\ v_C \end{bmatrix} + \begin{bmatrix} \frac{1}{L} \\ 0 \end{bmatrix} \cdot U_{in} \right). \end{aligned} \quad (5)$$

Assuming that $v_s(t)$ represents the voltage of the both ends of the switch tube, $i_D(t)$ is the current flowing through the diode D in the figure. In order to facilitate the analysis, the output voltage is expressed with $U_{in} = 1$. Since the uncontrollable rectifier bridge is eliminated in bridgeless PFC circuit, the input inductance is directly connected to the output side. The inductor current $i_L(t)$ and output current $i_0(t)$ is equal. Therefore, we can get the large signal expression between the mean current $i_D(t)$ across the diode and the voltage $v_s(t)$ of the both ends of the switch tube in a complete cycle:

$$v_s(t) = d'(t)U_0(t), \quad (6)$$

$$i_D(t) = d'(t)i_0(t). \quad (7)$$

2.1.2. Small-signal analysis of Boost PFC without bridge. In the process of bridgeless Boost PFC working, each system variable contains steady-state variables and perturbation components. Assuming that the voltage of the both ends of the switch tube S is $v_s(t)$ and output voltage is $v_0(t)$, the current of diode D is $i_D(t)$, the input current is $i_g(t)$, the steady-state components of the power switch tube S in off duty cycle $d'(t)$ are U_0, V_s, I_D, I_g, D' and the disturbance components can be expressed as $\hat{v}_s, \hat{v}_0, \hat{i}_D, \hat{i}_g, \hat{d}'$, the formulae (6)–(7) can be written as

$$v_s + \hat{v}_s = D'(U_0 + \hat{v}_0) + \hat{d}'(U_0 + \hat{v}_0), \quad (8)$$

$$i_D + \hat{i}_D = D'(I_g + \hat{i}_g) + \hat{d}'(I_g + \hat{i}_g). \quad (9)$$

Because the disturbance quantity of the circuit is set to be small, so $\hat{d}'\hat{v}_0$ and $\hat{d}'\hat{i}_g$ can be neglected. The small signal expressions (10) and (11) of the voltage $v_s(t)$ and the current $i_D(t)$ can be obtained.

$$\hat{v}_s = D'\hat{v}_0 + \hat{d}'V_0, \quad (10)$$

$$\hat{i}_D = D'\hat{i}_g + \hat{d}'I_g. \quad (11)$$

From the small signal model of the voltage $v_s(t)$ and current $i_D(t)$, the frequency

domain expression in the circuit can be obtained in the form

$$\hat{v}_g(s) = U_0 \hat{d}'(s) + D' \hat{v}(s) + SL \hat{i}_g(s), \quad (12)$$

$$D' \hat{i}_g(s) + I_g \hat{d}'(s) = SC \hat{v}_0(s) + \frac{\hat{v}_0(s)}{R}. \quad (13)$$

The expression for the $\hat{v}_0(s)$ can be obtained from (13). Then, putting it in (12), we can obtain the expression of the input current as follows

$$\hat{i}_g(s) = G_{ig}(s) \hat{v}_g(s) + G_{id}(s) \hat{d}(s). \quad (14)$$

Thus, the transfer function $G_{id}(s)$ that can be derived for the input current and duty cycle can be expressed as

$$G_{id}(s) = \frac{K_{id} \left(\frac{s}{w_2} + 1 \right)}{\frac{s^2}{w_0^2} + \frac{s}{Qw_0} + 1}, \quad (15)$$

where

$$K_{id} = \frac{2U_0}{R(1-D)^2} \quad w_2 = \frac{2}{RC},$$

$$w_0 = \frac{1-D}{\sqrt{LC}}, \quad Q = R(1-D)\sqrt{C/L}. \quad (16)$$

Here $G_{id}(s)$ represents the transfer function of the input current and duty cycle in the power stage of the bridgeless Cuk PFC circuit, and can be used as the control object during the analysis and design of the control circuit. The capacitance, resistance, and inductance in the transfer function expression are constant, so the duty cycle D and output voltage, V_0 change during the normal operation.

2.2. Single-cycle current control algorithm

The single-cycle control model [7] was introduced by Prof. Semdey from the California University, USA in the early 1990s. Single-cycle control method does not require multipliers, as a non-linear control technology, it has a dual function of control and regulation. The main idea of single-cycle control is: the average switch value in any switching cycle must be equal or proportional to its control reference by controlling the duty cycle of the switching tube. Thus, the advantage of the single-cycle control is that no matter whether the circuit is in a transient or a steady state during operation, it is possible to keep the average of the controlled quantity proportional to its given value. The disturbance on the power supply side is suppressed. In this control algorithm, the circuit will not produce the transient error and steady-state error during the entire process.

In the circuit design process, the use of single cycle control has the following advantages: constant switching frequency, faster dynamic response, strong anti-

jamming capability, and easy implementation. Therefore, many scholars will shift the focus of PFC research to single cycle control. Many scholars at home and abroad have done a lot of practical innovation in the field of single cycle control. The basic schematic diagram of the single cycle control algorithm is shown in Fig. 3.

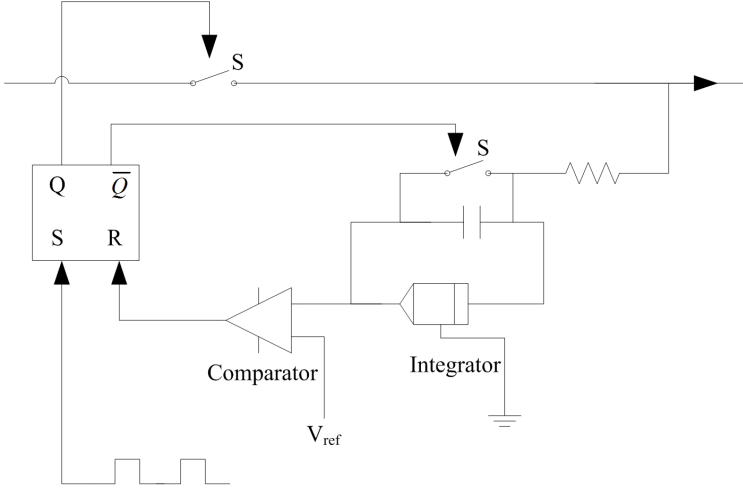


Fig. 3. Basic schematic diagram of single cycle control

The input signal of switch S is denoted by $x(t)$, and the output signal is denoted by $y(t)$. Assuming that the turn-on time in any switching cycle is T_{on} , the turn-off time is T_{off} and T_s is a complete switching period, then the duty cycle is $d = T_{on}/T_s$. The circuit operates at a constant switching frequency $f_s = 1/T_s$. Through the previous analysis we can know that the purpose of single cycle control is to adjust the breakover time T_{on} of the switch S . Through the adjustment of the breakover time, the average value of output $y(t)$ is equal to the reference value V_{ref} , so that the elimination of transient and steady-state errors is achieved. The operation of the integrator is achieved by controlling the on-off of the switch S by a CLOCK having a fixed frequency, and the integral value of the integrator is as follows

$$V_{int} = \frac{1}{T_s} \int_0^{T_s} x(t) dt, \quad (17)$$

where $T_s = C_{int}R_{int}$ is the integral time constant (switching cycle).

In any one switching cycle, when the integrator value V_{int} and reference voltage V_{ref} are equal, the comparator output flips, RS flip-flop resets, and then the switch signal will be low so that the switch S turns off. The integrator resets and waits for the next switching cycle. If the output of the switch $y(t)$ in each cycle can be made equal to the integral value of the given reference value V_{ref} by modulating the duty

cycle of the switch, it can be expressed as follows

$$\int_0^{T_{\text{on}}} x(t) dt = \int_0^{T_s} V_{\text{ref}}(t) dt. \quad (18)$$

Simultaneously dividing T_s at both ends of the above equation yields an average of the output signal in each cycle which equals to the average of the given reference values

$$\frac{1}{T_s} \int_0^{T_s} x(t) dt = \frac{1}{T_s} \int_0^{T_s} V_{\text{ref}}(t) dt. \quad (19)$$

Then the average value of the output signal in the current switching cycle is

$$\bar{y}(t) = \frac{1}{T_s} \int_0^{T_{\text{on}}} x(t) dt = \frac{1}{T_s} \int_0^{T_s} V_{\text{ref}}(t) dt = V_{\text{ref}}, \quad (20)$$

so that

$$\bar{y}(t) = V_{\text{ref}}(t). \quad (21)$$

In the case of stable output, the output voltage is represented by U_0 . The input current changes in same phases and same frequency following the input voltage, which is the target of the PFC. The circuit is purely resistive to the grid and can be expressed as R_e , so that

$$i_L = \frac{U_{\text{in}}}{R_e}. \quad (22)$$

For Boost PFC, the input voltage U_{in} and output voltage U_0 exhibit the following relationship

$$\frac{U_0}{U_{\text{in}}} = \frac{1}{1-D}. \quad (23)$$

Here D is the duty cycle, and the conditions that the governing equations need to satisfy can be derived by using the input equation for the unity power factor in the ideal state. From (21) and (22) we can find

$$R_e i_L = U_0(1-D). \quad (24)$$

If R_s is the sampling resistance in the bridgeless PFC, (23) provides

$$R_s i_L = \frac{R_s}{R_e} U_0(1-D). \quad (25)$$

From the above formula we can see that the average output value U_0 and input U_{in} are not related to each other. The average value $\bar{y}(t)$ of the output signal can be made equal to the reference value V_{ref} in the current switching cycle once the single-cycle control is used, and irrespective of the input signal U_{in} is constant or fluctuating. In other words, a non-linear branch in the single-cycle control can be turned into a linear branch.

The single-cycle control technology has the following advantages:

1. The realization of the circuit is simple.
2. The total harmonic distortion of the grid current is small.
3. The control loop is not sensitive to noise interference
4. Direct output voltage is smooth, the adjustment range is very large.
5. The control loop is stable and has good dynamic response

Therefore, the technology of single cycle control is also called the instantaneous value control technique of switching voltage. It can suppress the disturbance of the input side signal $x(t)$ and disturbance of the load side and output signal $y(t)$ is very well, so as to ensure that the output voltage is constant.

3. Simulation verification and analysis

3.1. Single cycle control simulation

Set the model parameters: AC input voltage is $220 \sin(50t)$, the rated load is the ideal load 100Ω .

According to the principle of single cycle control, the system simulation model is obtained. The inductor size is $L = 1.5 \text{ mH}$, the input filter capacitance is $C = 1 \mu\text{F}$, the filter inductor is $L1 = 1 \mu\text{H}$, and the output filter capacitor is $C1 = 660 \mu\text{F}$. $R1$ and $R2$ are the sampling resistors of the direct current side, and $R1$ is much higher than $R2$. The PID parameters of the voltage loop are: $p = 5$, $i = 0.5$, the parameters of the current loop PID are $p = 30$, $i = 0.1$, and the output voltage is 400 V .

Single-cycle control simulation: the waveform of the input current and output voltage under the ideal state are shown in Fig. 4.

3.2. Charging pile overall circuit simulation

From simulation waveform under the single cycle control algorithm, it can be obtained a more smooth output voltage waveform, and the overshoot is less than 1%. In the single cycle control algorithm, the output load increases by 30% fluctuations, and changes from the original 100Ω into 130Ω . The resulting waveform is shown in Fig. 5.

4. Conclusion

We firstly analyzed the circuit model of bridgeless Boost PFC in order to obtain the transfer function of duty cycle and input current in the circuit. Then, the single cycle control algorithm in bridgeless PFC control algorithm was introduced, used for carrying out the simulation experiment. The simulation results of single cycle control algorithm are analyzed under the condition of input voltage fluctuation and

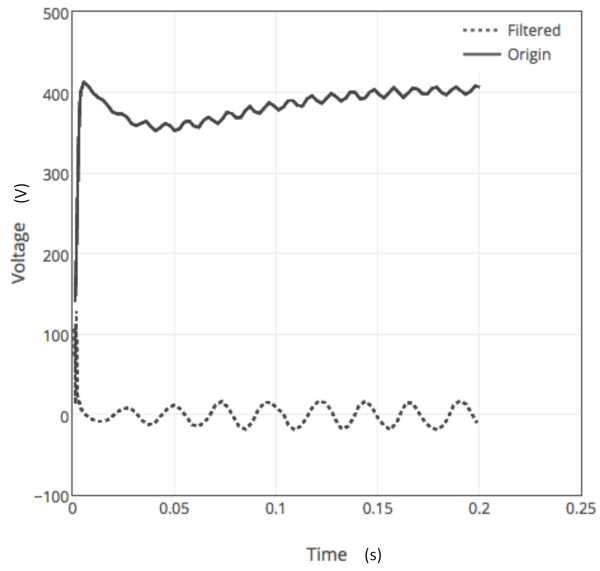


Fig. 4. Waveform obtained under single cycle control

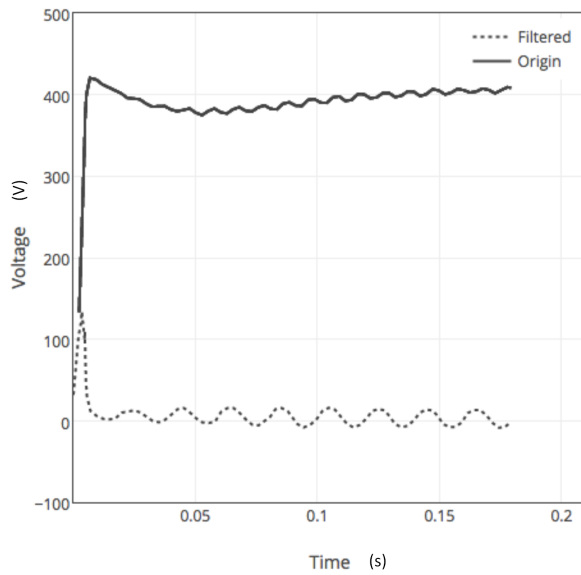


Fig. 5. Waveform of load fluctuation under single cycle control algorithm

load fluctuation. The single cycle control algorithm is applied to the whole circuit of the charging pile, and its feasibility is proved by simulation.

References

- [1] G. M. WALLER, E. D. WILLIAMS, S. W. MATTESON, T. A. TRABOLD: *Current and theoretical maximum well-to-wheels exergy efficiency of options to power vehicles with natural gas*. Applied Energy 127 (2014), 55–63.
- [2] E. FIGENBAUM, M. KOLBENSTVEDT, B. ELVEBAKK: *Electric vehicles – environmental, economic and practical aspects: As seen by current and potential users*. TOI Institute of Transport Economics Norwegian Centre for Transport Research, Report 1329, 2014.
- [3] Z. DARABI: *Impact of plug-in hybrid electric vehicles on the power grid in a smart environment*. Curtis Laws Wilson Library, Missouri University of Science and Technology, Doctoral Dissertation, 2012.
- [4] A. A. M. BENTO, A. R. C. D. SILVA: *Hybrid one-cycle controller for boost PFC rectifier*. IEEE Trans. Industry Applications 45 (2009), No. 1, 268–277.
- [5] G. CHEN, K. M. SMEDLEY: *Steady-state and dynamic study of one-cycle-controlled three-phase power-factor correction*. IEEE Trans. Industrial Electronics 52 (2005), No. 2, 355–362.
- [6] M. M. JOVANOVIĆ, Y. JANG: *State-of-the-art, single-phase, active power-factor-correction techniques for high-power applications - an overview*. IEEE Trans. Industrial Electronics 52 (2005) No. 3, 701–708.
- [7] A. J. SABZALI, E. H. ISMAIL, M. A. AL-SAFFAR, A. A. FARDOUN: *New bridgeless DCM SEPIC and CUK PFC rectifiers with low conduction and switching losses*. IEEE Trans. Industry Applications 47 (2011), No. 2, 873–881.

Received November 16, 2016

Stability control and consolidation sedimentation analysis on soft soil foundation subjected to surcharge preloading treatment

CANBIN YIN¹, MIN WANG²

Abstract. A method for controlling the treatment construction stability of several types of soft soil foundations is proposed, according to field measured data in combination with a Wuhan-Yingshan highway soft soil foundation treatment project case. The method is capable of more effectively controlling the stability of foundations during the construction process in combination with a sedimentation rate control method stipulated by standards. ABAQUS applies an expanded D-P model based on the creep rule and the consolidation theory to perform simulation numerical calculation on the project case, and a sedimentation calculation result of numerical simulation is compared with on-site measured sedimentation. By virtue of the contrast analysis on three consolidation degree calculation methods, namely inverse calculation on pore water pressure, sedimentation calculation and the consolidation theoretical calculation, and in combination with numerical analysis results, sedimentation inverse calculation comparison is performed, so that the method has certain guiding significance in researching consolidation degrees and sedimentation rules of roadbeds.

Key words. Soft soil foundation, stability, consolidation degree, ABAQUS, sedimentation analysis.

1. Introduction

As for a state that the foundations have relatively thick soft soil layers, surcharge preloading is performed on a soft soil roadbed by use of drainage systems such as a sand well or a plastic drainage plate and the like. Research on the stability control and roadbed sedimentation rules during a roadbed construction process has always been the hotspot in an existing soft soil foundation treatment technology, a stability control method stipulated by standards only considers the influence of the sedimentation rate on the roadbed stability, a more comprehensive and practical stability

¹Hunan City University, Hunan, 413000, China

²Construction Project Quality Safety Supervisory Station, Hunan, 413400, China

control method still needs further research and demonstration, and research on soft soil consolidation sedimentation rules is undergoing development. In recent years, a method for solving problems such as foundation deformation of roadbeds and constructions through applying analysis software and a finite element method on the predecessors' consolidation theory of predecessors by scholars at home and abroad has been extensively applied, so that development of the consolidation theory is greatly promoted. However, problems such as mutual relations among soft soil secondary consolidation-creep property analysis, soil solidification-creep coupling theory, soil sedimentation-consolidation degree and pore water pressure change remain to be further researched and improved.

In overall consideration of the above several problems, the paper provides several methods for controlling the roadbed stability during a construction process by virtue of construction on-site supervision on soft soil foundation treatment, in which one year and two months were spent, of the typical roadbed section K59+710 and comprehensive analysis on monitoring data under a project background of the soft soil roadbed test section of the Wuhan-Yingshan highway. Numerical simulation is performed by use of ABAQUS, key technical indexes such as roadbed sedimentation and consolidation degree are analyzed, so that the methods have relatively practical significance in guiding project construction and researching soft soil sedimentation rules.

2. Project profile

Main sections of the whole Wuhan-Yingshan highway have staggered bridges and soft soil foundations, and a considerable number of the main sections are bridgehead regions with relatively thick soft soils and relatively high bridgehead embankment filling height, so that problems of roadbed instability and uneven sedimentation at connection parts of the bridgeheads and embankments would be certainly caused. Furthermore, the influence of huge high-filled lateral pressure on the structure is unignorable especially for bridge abutment pile foundations which obliquely cross with the highway, if this problem is mishandled, the structure safety would be surely and seriously influenced. On this account, in combination with accumulated experience [1–2] in soft soil foundation treatment in recent years, a preloading method is adopted to treat soft soil foundations, roadbed filling construction is performed according to a thin turning method, a soft soil foundation monitoring system is established, and Table 1 is a partial data table including various indexes of project on-site construction monitoring.

3. Research on roadbed filling stability control method

According to requirements in the Highway Soft Soil Foundation Embankment Design and Construction Technique Standards [3], when the embankment reaches a limit equilibrium state, the embankment stability control standards are as follows: the sedimentation rate V of a single day is less than or equal to 15 mm/d, and the

lateral displacement rate V_c is less than or equal to 5.0 mm/d. Although such a stability control method is universally applied to construction processes, judgment only based on the sedimentation rate for different construction situations is biased. In many project cases [4], a roadbed instability problem also occurs under a situation that the sedimentation rates meet standard requirements. In order to guide construction more scientifically and specifically, the paper hereafter analyzes and discusses the roadbed stability according to the construction monitoring data of the Wuhan–Yingshan highway and provides several new stability control methods.

Table 1. In-situ test data table

Actual filling height (m)	2.33	2.55	2.73	3.06	3.84	4.43	5.38	6.35
Actual accumulated load (kPa)	44.27	48.45	51.87	58.14	72.96	84.17	102.22	120.65
Maximal lateral displacement rate V_c (mm/d)	0	0.14	0.41	0.3	0.8	0.63	0.09	0.08
Accumulated lateral displacement rate $\sum V_c$ (mm/d)	0	0.14	0.55	0.85	2.75	3.38	4.12	4.2
Accumulated lateral extrusion amount V_h (mm ³)	0	325	600	562	3500	6150	16912.5	17900
Maximal sedimentation rate V (mm/d)	2.60	0.80	3.33	1.50	2.24	4.43	0.89	1.69
Accumulated sedimentation rate $\sum V$ (mm/d)	2.60	3.40	7.73	9.23	16.41	20.84	23.30	24.99
Accumulated displacement $\delta_{3.5}$ (mm)	0	0.55	1.1	1.7	7.8	11.3	32.3	34.1
Accumulated sedimentation s (mm)	16.00	23.00	38.00	44.00	119.00	174.90	269.15	368.40
$\Delta u_{3.5}$	0.00	0.55	0.55	0.92	0.09	0.11	0.82	0.52
$\sum \Delta u_{3.5}$	0.00	0.55	1.10	2.02	2.22	2.33	3.15	3.67

3.1. Analysis of pore water pressure increase

By real-time monitoring on the pore water pressure during a roadbed filling process, it is easy to discover that changes of the pore water pressure undergo an “increase-dissipation-stabilization” process during each filled soil loading process. The dependence of $\sum u$ on $\sum \Delta P$ obtained from measurement results of pore water pressures in different depths is shown in Fig. 1. As shown in the figure, the curve

of each section is linear during the initial stage of filling, and the slope of each curve decreases in the later stage of filling, which indicates that the foundation consolidation degree at the later stage increases, the foundation strength increases, and the foundation tends to be stable. During the whole filling process, the curve in each section has flex points at the earlier stage of filling. The paper analyzes the physical significance corresponding to the first flex point of each section. In Fig. 1, the first flex point position occurs at the fourth-stage filled load (the corresponding filling height is 3.84 m), i.e., when the filling height is up to 3.84 m, the curve is still relatively straight; when the next-stage load is filled, the curve turns upwards with increased slope. According to elastoplasticity theoretical analysis of soils, when the filling height is up to 3.84 m, the soil reaches the plastic deformation stage. Therefore, the corresponding filling height which ensures that the soils are converted into the plastic stage from an elastic stage is about 3.84 m, which is approximately the limit filling height obtained by theoretical calculation. The above analysis shows that within the limit filling height, the curve is linear, and the foundation soils are in the elastic stage, so that loading can be accelerated at the moment. After the filling height exceeds the limit filling height, the curve has an upward flex point, and the foundation soils are in the plastic deformation stage, so that the loading rate can be slowed down, and loading is further performed after the foundation soils achieve the required consolidation degree. During the loading process, when the curve has an upward flex point, i.e., the slope of curve increases, the foundation might become unstable, and a loading stop measure or an unloading measure should be taken. Therefore, whether the foundation is stable or not can be judged according to the slope change of the curve, so as to guide the filling rate.

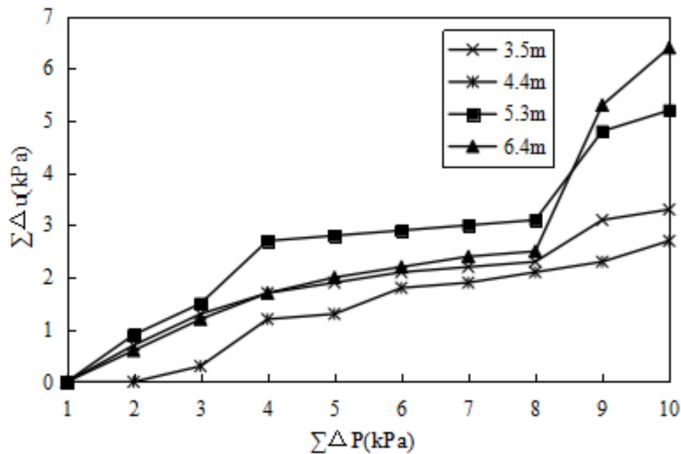


Fig. 1. Dependence of $\sum u$ on $\sum \Delta P$ in different depths

3.2. Flex point analysis method

In practical engineering application, after data processing is performed on instantaneous sedimentation quantity caused by loading of each stage, the displacement rate and pore pressure increase caused by loading of each stage implied by soil non-drainage deformation can be disclosed. The deformation stage and stability of soils can be judged by virtue of a comprehensive analysis.

Japanese Tominaga and Hashimoto pointed out that: when the ratio of the lateral displacement of the loading slope to the sedimentation quantity S of the loaded middle part increases sharply, it means that the foundation is nearly damaged (see the left graph of Fig. 2). When the preloading load is relatively small, the curve should have an included angle θ with S , and the measuring point moves along the line E. Finally, when the preloading load approaches the failure load, the increase is more obvious than increase of S as shown in I and II in the left graph of Fig. 2.

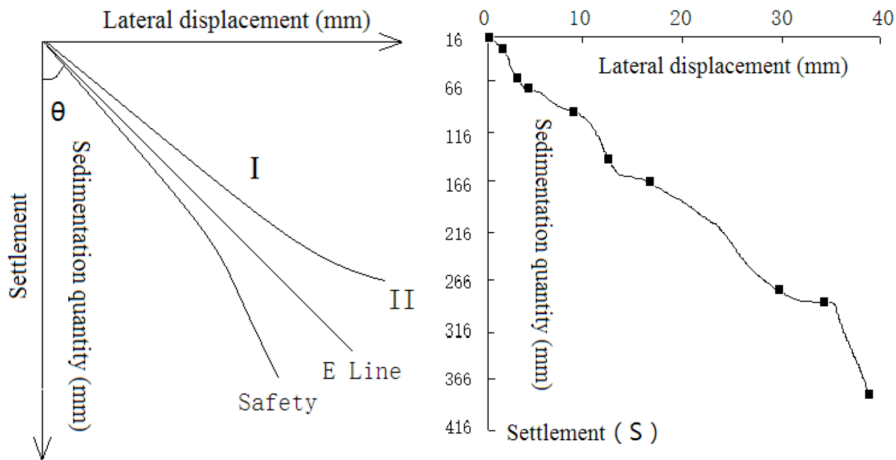


Fig. 2. Relation of lateral displacement and sedimentation quantity

4. Finite element simulation on consolidation sedimentation of soft soil roadbed

4.1. Selection of constitutive model of soil

Aiming at soil used as a special project material [5, 6], ABAQUS provides common elastic-plastic constitutive models [7] such as a modified Cambridge model, an expanded Drucker–Prager model and a Mohr–Coulomb model. As a further expansion of a modified Drucker–Prager model, the expanded Drucker–Prager model in the ABAQUS takes influence of a deviatoric stress invariant J_3 into consideration. It is configured with the corresponding creep rule and consolidation theory and can

well reflect the nonlinear characteristic of the soil material, so that the expanded Drucker–Prager model is extensively adopted in actual project calculation and can be used for calculating the deformation problem of soft soils, especially the rheological problem. The paper adopts the expanded Drucker–Prager model to perform relevant numerical calculation.

4.2. Determination of model parameters

The soil layer of the foundation in the test section of the Wuhan–Yingshan highway is divided into the first layer consisting of loam, second layer consisting of muddy clay, third layer again consisting of loam, fourth layer consisting of sludge and fifth layer consisting of fine sand. The fifth layer serves as a bottommost layer in the calculations. According to routine soil test results, specific physical and mechanical property indexes of each layer are shown in Table 2.

Table 2. Physical and mechanical properties of particular soil layers

Soil layer	1	2	3	4	5
Thickness (m)	0.9	3.0	2.2	0.6	13.2
Water content (%)	37.24	31.38	28.98	32.24	25.30
Density (N/cm ³)	14.3	15.5	13.7	14.7	14.9
Void ratio	0.903	0.762	0.863	0.838	0.817
Plastic limit	23.1	25.2	22.4	24.31	18.6
Liquid limit	38.6	45.5	36.7	40.15	34.0
Compressibility coefficient	0.545	0.496	0.384	0.356	0.328
Consolidation coefficient	1.54	1.21	1.10	1.66	0.525
Osmotic coefficient	4.48E-8	2.89E-8	1.78E-7	5.25E-8	2.40E-8
Fast shear - c	12	22	0	38	23
Fast shear - φ	27.0	23.1	31.0	15.5	11.5

A creep model [6], [8–11] corresponding to creep in the ABAQUS is capable of enlarging the use range of the Drucker–Prager model and solving complicated creep problems, especially a soft soil creep problem. Furthermore, the common Mohr–Coulomb model parameters can be obtained from a rheological test report and they can be converted into Drucker–Prager model parameters using the following equations.

When in associated flow $\psi = \beta$ (ψ representing the expansion angle on the p – w surface), then

$$\tan \beta = \frac{\sqrt{3} \sin \phi}{\sqrt{1 + \frac{1}{3} \sin^2 \phi}}, \quad (1)$$

$$\frac{d}{c} = \frac{\sqrt{3} \cos \phi}{\sqrt{1 + \frac{1}{3} \sin^2 \phi}}. \quad (2)$$

When no volume expansion exists ($\psi = 0$), then

$$\tan \beta = \sqrt{3} \sin \phi, \quad (3)$$

$$\frac{d}{c} = \sqrt{3} \cos \phi, \quad (4)$$

and

$$\sigma_c^0 = \frac{1}{1 - \frac{1}{3} \tan \beta}, \quad (5)$$

where σ_c^0 represents the initial yield stress.

According to rheological test results of the test section and conversion relation between the Drucker–Prager model parameters and Mohr–Coulomb model parameters, specific model parameters are shown in Table 3.

Table 3. Calculation parameters for finite element analysis

Soil layer	β	σ_c (kPa)	K	A	n	m
1	33.595	45.464	0.8187	4E-7	6	0
2	43	9.4	0.8715	1E-7	0.7	0
3	21.595	86.398	0.8834	4E-7	6	0
4	38.174	44.276	0.7927	8E-7	5.5	0
5	30.401	99.95	0.8364	4E-7	6	0

Here, A , n and m are three parameters for the time hardening criterion of the expanded Drucker–Prager model. In the initial stage of creep, the influence of creep parameter changes on soil deformation is not quite remarkable; however, excess pore water pressure gradually dissipates over time, so that the influence of excess pore water pressure on deformation is also gradually weakened, and the influence of the creep parameter plays a leading role. If the influence of the creep parameter m on creep development is relatively less and since the creep parameter m is not less than -1 and not greater than 0 , the influence of the creep parameter m can be ignored in calculation, i.e., m is equal to 0 .

4.3. Calculation conditions

The calculation grid is shown in Fig. 3. Two side surfaces are characterized by axial symmetry constraint in direction x , the bottom surface exhibits restraints in both directions x and y , and the ground serves as a boundary with excess pore water pressure equal to 0 . Coupled plane strain elements CPE8RP are adopted as soil units. According to exploration data, the bottom of the foundation is set as a non-drainage fixed boundary. In consideration of symmetry, the symmetry plane of the roadbed is set as a non-drainage boundary with horizontal restraint; the right boundary of the calculation section can be set as a non-drainage fixed boundary since it is far enough from the center of the roadbed.

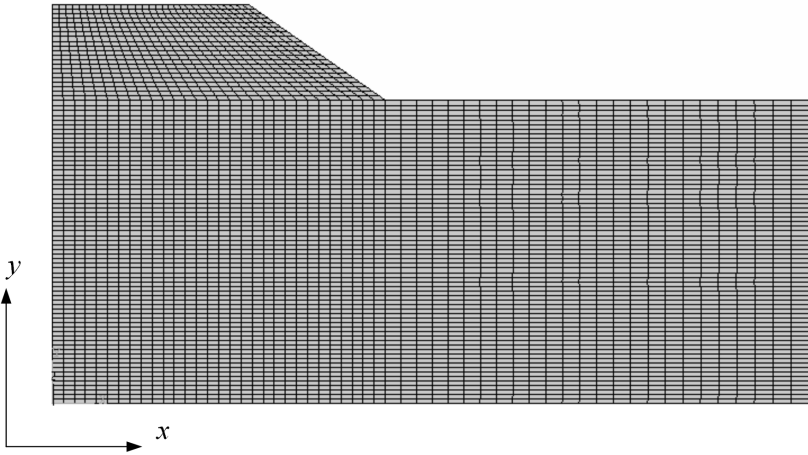


Fig. 3. Finite element grid of the roadbed

5. Analysis of calculation results

5.1. Sedimentation analysis

Results calculated by the expanded Drucker–Prager model considering the creep rules conform to measured values. According to Fig. 4, it can clearly be observed that certain rheological deformation exists in the preloading period, and this conforms to actual project situations; furthermore, numerical calculation results show that a finite element model and selected parameters are basically reasonable. According to the curve, since filling construction is simplified by the finite element model simulation, each simplified single layer is relatively thick in filling thickness. This is caused by relatively high sedimentation rate and relatively high instantaneous sedimentation of the roadbed during the filling period, which indicates that instantaneous sedimentation is relevant to the filling rate. Along with decrease of the later construction rate, the sedimentation rate of the foundation also decreases. After filling construction is finished, the sedimentation quantity and sedimentation rate of the roadbed decreases obviously; and the sedimentation quantity is basically stable about six months after construction.

5.2. Analysis on pore water pressure

The time dependence of pore water pressure in soft soils at different depths in a preloading reinforcement region for plastic drainage plates calculated by applying ABAQUS is shown in Fig. 5.

Figure 5 contains the time dependencies of pore water pressures in foundation soils at different positions below the middle line of the roadbed. Since the figure output by ABAQUS has no unit display, this paper introduces the units in Fig. 5 as

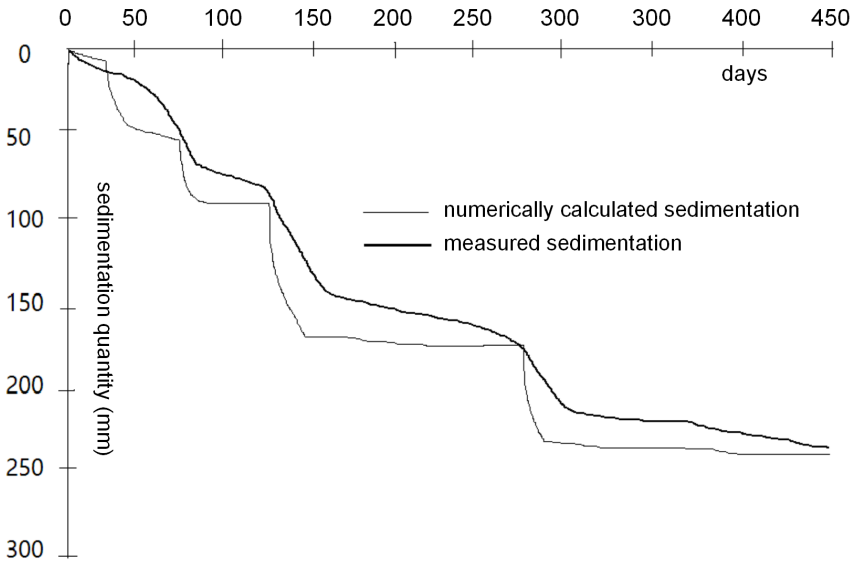


Fig. 4. Comparison of numerical calculation and measured sedimentation

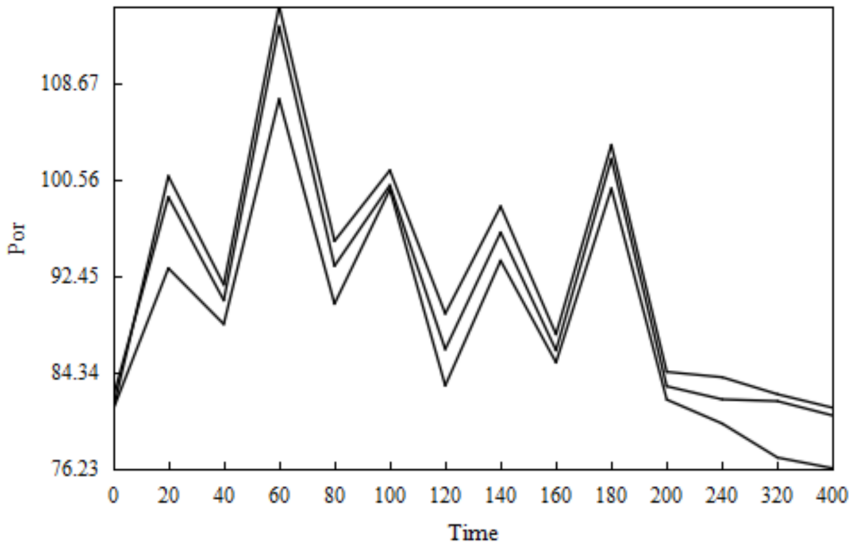


Fig. 5. Time dependencies of pore water pressures at different depths (5 m, 5.5 m and 6 m) of the roadbed

follows: axis Time is a time axis with the unit of one day, while axis P_{or} is the pore water pressure with the unit of kPa. According to the figure, it can be observed that the pore water pressures from once loading to next loading undergo an “increase-

dissipation-decrease-dissipation” process, which shows that additional total stress is constantly converted into the effective stress of soil. The soil consolidation process is obvious, the pore pressure dissipation rate is relatively high at the beginning of dissipation, but decreases over time and the pore pressure at the later stage tends to be stable. It can be observed that the consolidation degree further increases, and the foundation gradually reaches a stable state. The consolidation degree of the soft soil roadbed can be obtained from the dissipation situations of pore water pressures at different depths calculated by ABAQUS; by virtue of calculation, the consolidation degree of the soft soil roadbed is 93.87% for 180 days after the preloading is realized, and it conforms to the theoretical calculation result and the measured result, thus proving that the selected parameters are relatively accurate and a basis is provided for analyzing the consolidation degree and sedimentation below.

5.3. Consolidation degree comparison and sedimentation back calculation

According to the Terzaghi’s three-dimensional consolidation theory [12], the average total consolidation degree of the soil layers in a sand well foundation is caused by combined action of radial average consolidation degree and vertical average consolidation degree. The expression for the average total consolidation degree U_{rz} is [12–14]

$$U_{rz} = 1 - (1 - U_r)(1 - U_z). \quad (6)$$

Considering the Barron solution from 1948 [15] (without taking into account the consolidation coefficient changes in the soil consolidation process) we obtain

$$U_{rz} = 1 - \frac{8}{\pi^2} e^{\beta t}, \quad (7)$$

where

$$\beta = \frac{\pi^2}{4} \cdot \frac{C_v}{H^2} + \frac{8}{F(n)} \cdot \frac{C_r}{d_e^2}.$$

Theoretical calculation can be performed on the consolidation degree of soft soils in this project according to the above theoretical equations and in combination with soft soil parameters in the following table. If an H value of 7 m is taken, β is equal to 0.0036, the consolidation degree of soil layers in the soft soil foundation on the four hundredth day is calculated. Then U_r is equal to 91.5%, U_z is equal to 21.3% and U_{rz} is equal to 93.3%.

Figure 6 is a consolidation degree comparison analysis figure. According to the figure, the consolidation degree calculated by use of the consolidation theory is basically approximate to that measured according to sedimentation or pore pressure, so that it indicates that the consolidation degree theoretical calculation is reasonable in parameter selection, and the pore pressure and sedimentation observation results are accurate and are in mutual corroboration. In contrast, the consolidation degree obtained by sedimentation measurement is more approximate to that obtained by theoretical calculation, this is mainly due to the fact that the measurement of excess pore water pressure mainly depends on the underground static level, whereas, the

underground static level changes along with time and climate, so that measurement of the underground static level is quite difficult. When the consolidation degree of the test section is calculated according to the pore pressure, hydrostatic pressure changes are not taken into consideration, i.e., the hydrostatic pressure is assumed to be invariant.

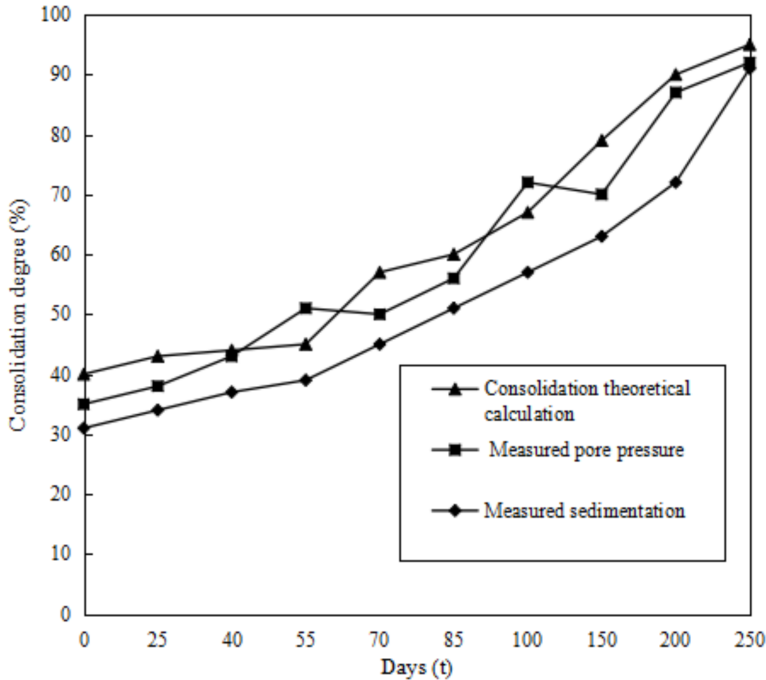


Fig. 6. Comparison of various calculated consolidation degree results

Through comparing the consolidation degree obtained by theoretical calculation with the measured consolidation degree, we can discover that although the consolidation degree obtained by theoretical calculation is less than the measured consolidation degree in the loading period or the earlier stage of preloading, and it is greater than the measured consolidation degree at the later stage of preloading (three months after preloading), thereby indicating that the consolidation coefficient constantly decreases along with increase of time and consolidation degree after soil is preloaded. Through comparing geotechnical tests before and after foundation treatment, the measurement results also prove this inference. This is because during the earlier stage of loading, the soil has relatively large pores, the pore pressure dissipates rapidly and the effective stress of soil increases rapidly, so that the consolidation of soil is relatively rapid, i.e., the consolidation coefficient is relatively large. Along with gradual compression of soil, the void ratio of soil becomes smaller and smaller, the pore pressure dissipation rate becomes lower and lower, and the effective stress increases slowly, so that the consolidation is slower and slower, i.e., the consolidation

coefficient becomes smaller.

According to definition of the consolidation degree, one point (t_1, s_1) taken from the measured sedimentation curve is utilized to calculate

$$U(t) = \frac{s_t - s_1}{s_\infty - s_1}, \quad (8)$$

where s_1 is the sedimentation quantity of the roadbed at the time t , and s_∞ is the final sedimentation quantity of the roadbed.

Any point taken from the sedimentation curve is utilized to perform reverse-reasoning calculation, and the final sedimentation quantity is 0.456 m. The consolidation degrees of the soft soil roadbed, which are calculated by different methods, are respectively utilized to calculate the final sedimentation quantity of the roadbed, and the results are shown in Table 4.

Table 1. Comparison of final sedimentation quantity calculated by different methods

Consolidation degree calculation method	Soft soil consolidation degree (%)	Final sedimentation quantity of roadbed (m)	Measured sedimentation quantity (m)
Three-dimensional consolidation theory	93.3	0.456	0.454
Measured pore water pressure	92.1	0.465	
ABAQUS numerical calculation	93.8	0.440	

The results shown in Table 4 indicate that the consolidation degree calculated according to the measured pore water pressure is slightly less than the result calculated by ABAQUS. This is because the pore water pressure changes caused by weather and underground water are not considered during the simulation performed by ABAQUS. In actual project, the pore water pressure is influenced by the above factors, so that the consolidation degree calculated according to the measured pore water pressure is smaller. The result of numerical simulation result conforms to the theoretical calculation, which further indicates that the model parameter selection is reasonable, and final sedimentation quantity calculation conforms to the measured sedimentation quantity. This lays foundations for research of the relation between preloading height of the filled soil and preloading time and post-construction sedimentation of the roadbed.

6. Conclusion and outlooks

1. By use of methods such as measured pore water pressure increase monitoring and flex point analysis in a construction process and in combination with judgment based on standard requirements, the method provided by the paper

- better conforms to actual project situations, and construction can be better guided.
2. The expanded Drucker-Prager model considering the creep rules is adopted by ABAQUS and takes the influence of rheology on sedimentation into consideration, the calculation results are approximate to the measured results, construction situations are simulated more truly, and a foundation is laid for more follow-up research.
 3. The final sedimentation quantity of the foundation, which inversely calculated by use of the consolidation degree, conforms to the calculation result of ABAQUS and the measured sedimentation quantity, thus indicating that a method for calculating roadbed sedimentation by use of theories and numerical values is practical.
 4. In analysis calculation of sedimentation and stability of the soft soil foundation, selected soil parameters conforming to actual situations have great influence on analysis results. In future research, how to select a more suitable soil constitutive model and perform inversion to obtain accurate soil property parameters on the basis of measured data has great research significance and practical value.

References

- [1] H. SABETAMAL, M. NAZEM, S. W. SLOAN, J. P. CARTER: *Frictionless contact formulation for dynamic analysis of nonlinear saturated porous media based on the mortar method*. IJ Numerical and Analytical Methods in Geomechanics 40 (2016), No. 1, 25 to 61.
- [2] J. P. CARTER, H. SABETAMAL, M. NAZEM, S. W. SLOAN: *One-dimensional test problems for dynamic consolidation*. Acta Geotechnica 10 (2015), No. 1, 173–178.
- [3] X. ZHANG, D. SHENG, S. W. SLOAN, K. KRABBENHOFT: *Second-order cone programming formulation for consolidation analysis of saturated porous media*. Computational Mechanics 58 (2016), No. 1, 29–43.
- [4] V. V. OREKHOV: *Analysis of interaction between structures and saturated soil beds subject to static and seismic effects*. Soil Mechanics & Foundation Engineering 52 (2015), No. 2, 68–73.
- [5] B. K. LOW: *Practical probabilistic slope stability analysis*. Subsurface Drainage for Slope Stabilization 2 (2003), No. 4, 2777–2784.
- [6] M. LU, S. WANG, S. W. SLOAN, B. INDRARATNA, K. XIE: *Nonlinear radial consolidation of vertical drains under a general time-variable loading*. IJ Numerical and Analytical Methods in Geomechanics 39, (2015), No. 1, 51–62.
- [7] G. CHEN, Z. ZHOU, H. PAN, T. SUN, X. LI: *The influence of undrained cyclic loading patterns and consolidation states on the deformation features of saturated fine sand over a wide strain range*. Engineering Geology 204 (2016), 77–93.
- [8] B. INDRARATNA, C. RUJIKIATKAMJORN, A. S. BALASUBRAMANIAM: *Ground improvement at the Port of Brisbane, Australia using vertical drains and vacuum assisted preloading*. Sound Geotechnical Research to Practice: Honoring Robert D. Holtz II (2013), 539–549.

- [9] N. J. JIANG, Y. J. DU, S. Y. LIU, M. L. WEI, P. S. HORPIBULSUK: *Multi-scale laboratory evaluation of the physical, mechanical, and microstructural properties of soft highway subgrade soil stabilized with calcium carbide residue*. Canadian Geotechnical Journal 53 (2015), No. 3, 373–383.
- [10] Z. ZHANG, M. HUANG: *Geotechnical influence on existing subway tunnels induced by multilane tunneling in Shanghai soft soil*. Computers and Geotechnics 56 (2014), No. 3, 121–132.
- [11] Z. CHEN, H. ZHU, Z. YAN, L. ZHAO, Y. SHEN, A. MISRA: *Experimental study on physical properties of soft soil after high temperature exposure*. Engineering Geology 204 (2016), 14–22.
- [12] H. LIU, C. ZHENG, X. DING, H. QIN: *Vertical dynamic response of a pipe pile in saturated soil layer*. Computers and Geotechnics 61 (2014), 57–66.
- [13] C. ZHENG, H. LIU, X. DING, Y. LV: *Torsional dynamic response of a large-diameter pipe pile in viscoelastic saturated soil*. IJ Numerical and Analytical Methods in Geomechanics 38 (2014), No. 16, 1724–1743.
- [14] L. LI, L. WU, X. WANG, Z. CUI: *Seismic response of underground structures in saturated soil based on the fluid-solid coupling dynamic formulation*. J Coastal Research 73 (2015), Suppl. 1, 432–435.
- [15] R. A. BARRON: *Consolidation of fine grained soil by drain well*. Geotechnical Special Publication 74 (1948), No. 118, 324–360.

Received November 16, 2016

Fault diagnosis system of wind turbine gearbox based on GRNN and fault tree analysis¹

PING HUANG²

Abstract. The gearbox fault diagnosis system based on General Regression Neural Network (GRNN) and fault tree analysis method are studied. We collected the fault information accumulated during the maintenance procedure of gearbox, drew the fault tree, and put forward the gearbox diagnosis method that integrates the fault diagnosis expert system based on fault tree diagnosis and GRNN-based fault diagnosis system. Moreover, we analyzed the vibration signal without faults, gear wearing and teeth-breaking within time and frequency domains, we extracted five characteristic parameter as the input of GRNN and train of the network, established the recognition model of gearbox fault situation based on GRNN, and detected the diagnosis model of GRNN with the reserved signals. The diagnosis result was in conformity with the practical operation, so that the research and development of the gearbox fault diagnosis system has been realized through integrating GRNN model and NET development platform. This fault diagnosis system can recognize different conditions accurately and effectively, then diagnose them quickly and put forward expert solutions.

Key words. GRNN, fault tree analysis, wind turbine gearbox, fault diagnosis.

1. Introduction

Owing to the rapid development of wind turbine industry, fault diagnosis of wind turbine gearbox has always been addressed by the analysis of maintenance staff relying on their experience [1, 2]. The time required for this process is long and the accuracy is low [3]. During the process, the time for addressing the fault accounts for 70 %–90 % of the whole process, whereas the time for maintenance accounts for only 10 %–30 %.

The structure of wind turbine gearbox is complicated, with many subjects involved, so that it is difficult to conduct fault reasoning. Therefore, to relieve the burden of operating and maintenance crew, it is quite necessary to improve the ac-

¹The author acknowledges the National Natural Science Foundation of China (Grant No. 51578109) and National Natural Science Foundation of China (Grant No. 51121005).

²Guangxi University, Guangxi, 530004, China

curacy and rapidity of analysis and judgment, as well as to develop a fault diagnosis system that special to the gearbox. Given this, fault diagnosis expert system can be applied to the wind turbine gearbox to diagnose the fault in time and propose reasonable solutions. We also study the experience from other wind turbine enterprises and try to apply fault diagnosis expert system to the design of gearbox fault diagnosis system. We diagnose the fault of gearbox by integrating the fault tree analysis method with GRNN.

2. Literature review

The fault diagnosis technology of wind turbine gearbox comes from the mechanical fault diagnosis technology, and it will be connected with artificial intelligence technology more and more closely. The present research on the gearbox fault is mainly to detect the operation of the rotor of the wind turbine. The diagnosis is achieved by analysis of the vibration signal spectrum [4]. Howlet et al. [5] proposed a fault diagnosis system of velocity transducers. The signal processing of this system adopts the methods of momentum regression for neural networks and multi-signals processing as well as Fourier variation method. It has been put into use. Moreover, Amirat et al. [6] summarized the monitoring technologies of wind turbine. Zaher et al. [7], through comparing the different research data from three countries, keep the opinion that the most important part of the wind turbine generator system is the gearbox, and also put forward that the operating condition can be accessed by the condition monitoring technologies. Moreover, there are some researches at home that analyze the vibration signals of the main axis and gearbox of wind turbine with the methods like wavelet transform and frequency spectrum analysis. They compare the spectrum under normal and abnormal situations, find out the change of the frequency spectrum and then address the reason and position of the fault [8]. As a result, we try to apply expert system and neural network to the fault diagnosis of wind turbine gearbox.

3. Research method

3.1. *Fault tree analysis*

The fault tree analysis is an interpretation method that refines the reasons for the system fault in dendritic graph progressively [9]. The fault tree analysis method analyzes the possible factors of system fault, draws the fault tree, and refines the fault events in a dendritic shape. Thus, it addresses the reasons and the probability of occurrence, and calculates the importance of each factor leading to system fault [10–11].

Fault tree model sets the most undesirable event in the system as the top event, all possible reasons for the top event as intermediate event, and all possible reasons for the intermediate event as basis event. Logic gate is adopted to show the connection of different events. A schematic diagram is shown in Fig. 1.

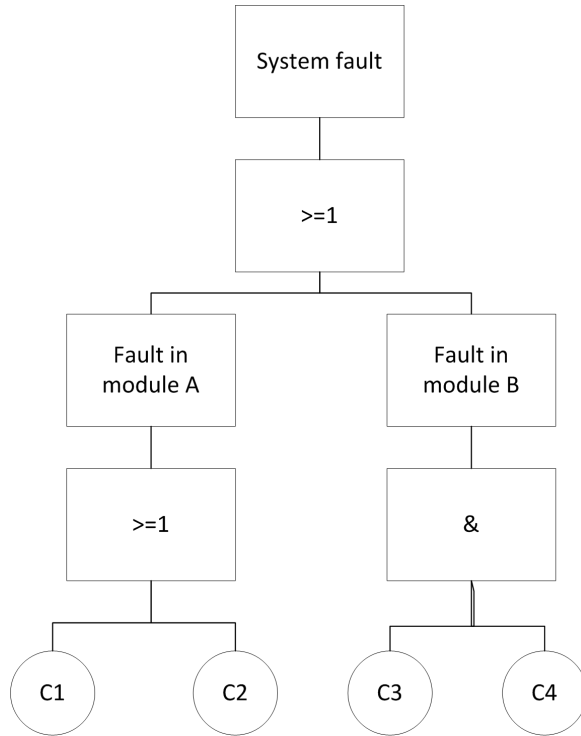


Fig. 1. Schematic diagram of fault tree

In Fig. 1, the top event is system fault, which was caused by the intermediate events (faults in module A or B). Meanwhile, fault in module A was caused by the failure of basis event C1 or C2, while fault in module B was caused by the simultaneous failure of basis event C3 and C4.

In general, most gearbox faults happened in the gears, bearings, shafts and components like cases [12]. Looking at the previous analysis, we can see that the establishment of fault tree can be classified to the establishing of top event (T), intermediate event (M) and basis event (C), as well as the construction of the fault tree. Construction of the fault tree is one of the core parts of fault tree analysis method. Fault in any part of the gearbox may lead to the fault in the system, so the logic relation among different faults refers to the word “or”. The fault tree constructed can be seen in Fig. 2.

In Fig. 2, the top event T refers to the fault in gearbox, intermediate event M1 refers to gear fault, M2–bearing fault, M3–shaft fault, M4–case fault, M5–fastener fault, M6–oil seal fault, and basis event C1–fatigue fracture, C2–overload fracture, ..., C32–rubber aging. Since there exist various basic events, the rest are omitted here.

We add corresponding weight and solution to every basis event of the fault tree. The total weight of all basis events is equal to to 1. Then the expanded fault tree

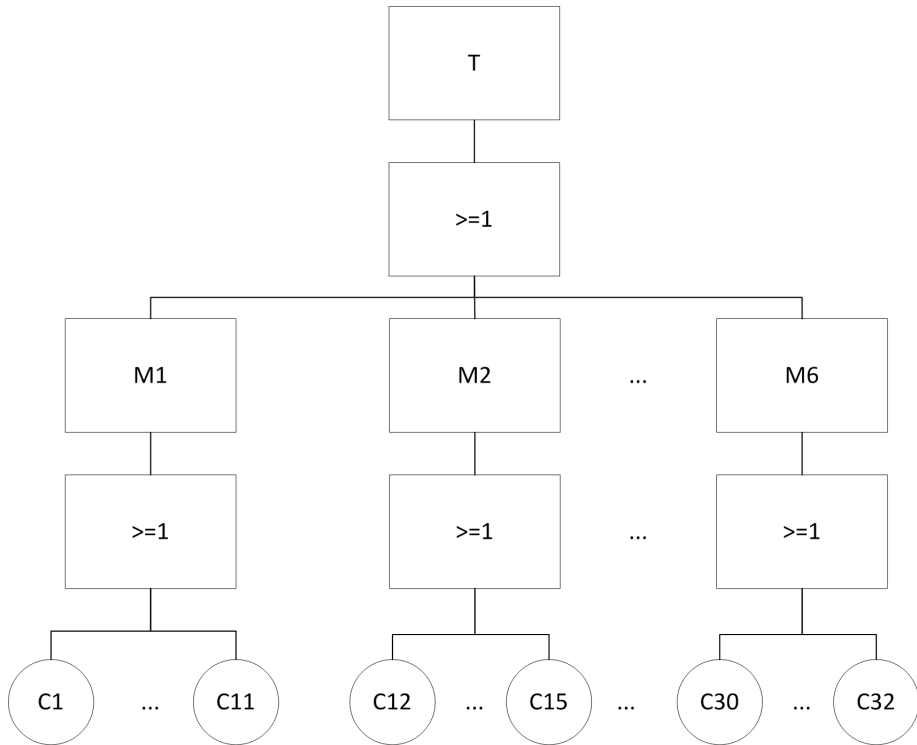


Fig. 2. Fault tree diagram of wind turbine gearbox

can not only help to address the positions of and reasons for the faults, but also figure out the referred solution from the system.

Qualitative analysis of fault tree analysis method aims at searching the minimum cut-set of fault tree, that is the reason for the fault of top event [13]. There are two major methods to search the minimum cut-set: ascending method and descending method [14]. The latter method is adopted this time. The descending method, starting from the top event, supersedes every event with the lower level event from top to bottom, records the events in portrait format when encountering with “or” gate, and records in landscape format when facing “and” gate. The rest can be done in the same manner until all the logical gates were transformed to basis events. Thus, all the cut-set of fault tree are addressed [15].

Given the characteristics of the gearbox, all the cut-set in this research are the minimum cut-sets, denoted as C1, C2, ..., C32. All the minimum cut-sets are independent from each other. If there is any fault in a certain one, the top event related to it will occur, that is, the gearbox will exhibit a fault [16].

The quantitative analysis aims at working out the incidence of the top event and importance of the basis event, which refers to the influence of the basis event occurrence on the top event. The analysis on the probability of top event follows.

When the logical gate refers to “or” gate, the occurrence probability of the top

event is:

$$p(x) = \bigcup_{i=1}^n p(x_i) = 1 - \prod_{i=1}^n [1 - p(x_i)]. \quad (1)$$

When the logical gate refers to “and” gate, the occurrence probability of the top event is:

$$p(x) = \bigcap_{i=1}^n p(x_i) = \prod_{i=1}^n p(x_i). \quad (2)$$

In both above formulae, $p(x)$ is the occurrence probability of the top event, $p(x_i)$ is the probability of the minimum cut-set that ranks as the place of i , while n refers to the total amount of minimum cut-sets. The importance can be expressed as follows:

$$I_i(x) = \frac{\partial p(x)}{\partial p(x_i)}, \quad (i = 1, 2, \dots, n). \quad (3)$$

In this formula, $I_i(x)$ is the probability importance of the basis event which ranks at the i th position. The higher is the value, the greater is its influence on the occurrence of the top event.

When users check the gearbox, they can input the obtained fault phenomenon in the system to search or check them directly. The module of the diagnosis process is shown in Fig. 3. Obtaining of knowledge refers to a transferring process of accessing the professional knowledge from the knowledge source, and then transforming them to the knowledge base. In general, the obtaining methods of knowledge involve three methods, as artificial obtaining, semi-automatized obtaining, and mechanical obtaining.

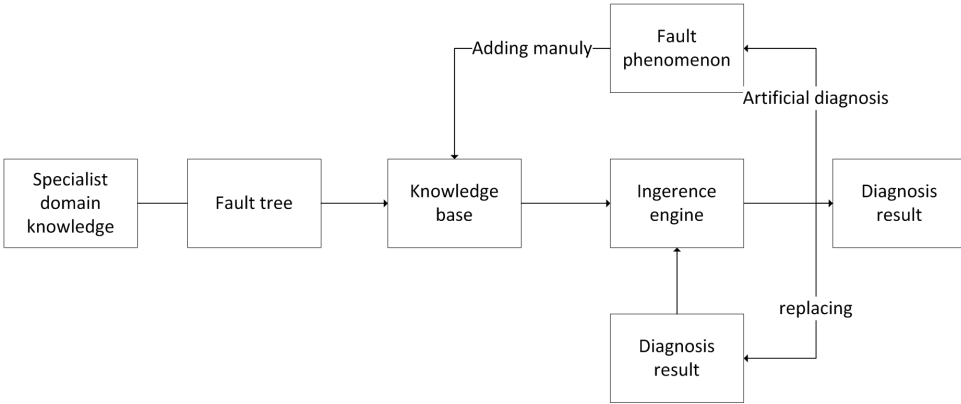


Fig. 3. Diagnosis module

3.2. Fault diagnosis strategy based on GRNN

During the operation of mechanical equipment, their vibration signals vary rapidly, involving many condition information of their operating. When there is any fault

in the equipment, the vibration condition changes, and the vibration signals may include fault information [17–18].

During the process of signals collection, the selection of the measurement point is very important. The principle of this selection is to get as much vibration signals and less loss of vibration transferring path as possible. Yet, as to the gearbox, the measurement point should be placed at the position where damping is low and rigidity is high. The place near the bearing pedestal is good to choose the measurement point.

Any artificial neural network cannot have recognition ability unless learning to do it [19]. So some data samples are needed to train the neural network, and these samples refer to the interpretation on the characteristics of the extracted vibration signals. We will conduct research from aspects of time domain as well as frequency domain.

Extracting signal features within time domain is convenient. The statistical indicators of time domain can be classified as unit characteristic values and unitless characteristic values [20]. A unit characteristic value includes peak value, peak-to-peak value, mean, variance, etc. A unitless characteristic value includes average amplitude, waveform index, peak index, impulsion index and so on. However, in unitless characteristic value, tolerance index, kurtosis index, peak index and impulsion index can indicate the value of impact energy properly, referring to good evaluation index to diagnose faults. Given this, these four indexes are chosen within the time domain to carry out a characteristic extraction on vibration signals.

If $\{x_n|n = 1, 2, 3, \dots, N\}$ is used to show a discrete time sequence, then the unit parameter and the four consequent unitless characteristic values can be shown in Table 1:

Table 1. Unit and unitless characteristic values

Unit characteristic value		Unitless characteristic value	
Peak value	$X_{\max} = x(n) _{\max}$	Tolerance index	$CL_f = \frac{X_{\max}}{X_r}$
Average value	$\mu = \frac{1}{N} \sum_{n=1}^N x(n)$	Kurtosis index	$K_v = \frac{\beta}{\sigma^4}$ (σ —standard deviation)
Variance	$\sigma^2 = \frac{1}{N-1} \sum_{n=1}^N (x(n) - \mu)^2$	Peak index	$C_f = \frac{X_{\max}}{D}$ (usually between 3–6)
Root-mean-square value	$D = \sqrt{\frac{1}{N} \sum_{n=1}^N x^2(n)}$	Impulsion index	$I_f = \frac{X_{\max}}{\mu}$
Root-square magnitude	$X_r = \left[\frac{1}{N} \sum_{n=1}^N \sqrt{ x(n) } \right]^2$		
Kurtosis	$\beta = \frac{1}{N} \sum_{n=1}^N (x(n) - \mu)^4$		

If the gear or bearing is damaged, there will arise impact signals, and the peak value will increase evidently to 10 or more. Along with the expansion of the fault, the peak index will decrease gradually, so changes of the peak index can be used as an early warning for the infancy fault of the gearbox. If the information involved in time signals belongs to numerous components, the waveform index, impulsion index, tolerance index and other unitless indexes can be used to conduct fault diagnosis [21]. The kurtosis index, tolerance index and impulsion index are relatively sensitive to damages like shock pulse; their values will increase obviously, especially at the onset of fault. But when increasing to a certain value, they will start to decrease in turn along with the expansion of fault, which shows that they are highly sensitive to the early fault but their stability is low.

During the process of signal analysis, the time-domain signal has limitations in analyzing complex signals. As a result, time-domain signals are often transformed to those of frequency domain through mathematical methods to obtain more information from the signals. As to the distributing characteristics of signals in frequency domain, information entropy can be adopted as signal signature parameter. We extract the characteristics of information entropy from the signals within frequency domain based on power spectrum analysis.

If $\{x_n|n = 1, 2, 3, \dots, N\}$ is used to show the discrete time sequence, the power spectrum is [22]:

$$S(w) = \frac{1}{2\pi N} |x(w)|^2 . \tag{4}$$

In this formula, $x(w)$ is the Fourier transform of sequence $\{x_n\}$. Through dispersing the Fourier transform, we can draw the spectrum $X(k)$ and power spectrum S_k , $k = 1, 2, \dots, N$. We can derive

$$\sum_{i=1}^N |x(n)|^2 = \sum_{i=1}^N |S(k)|^2 . \tag{5}$$

The power spectrum entropy H_f can be defined as:

$$H_f = - \sum_{k=1}^N p_k \ln p_k , \tag{6}$$

where p_k is the percentage of k th power spectrum to the whole spectrum, and

$$p_k = \frac{S_k}{\sum_{k=1}^N S_k} .$$

The power spectrum entropy indicates the spectral structure of vibration signals. The simpler is the frequency structure of the signals, the lower is the power spectrum entropy, and also the less is the complexity and uncertainty of the signals. In turn, the uncertainty will be increasingly high. As a result, the power spectrum entropy can indicate the distribution complexity of vibration energy on the whole frequency [23].

Now, we start building the fault diagnosis module based on GRNN. If the joint probability density function of random vector x and random variable y is $f(x, y)$, the regression of y to x can be expressed as [24]

$$E(y/x) = \hat{y}(x) = \frac{\int_{-\infty}^{\infty} y f(x, y) dy}{\int_{-\infty}^{\infty} f(x, y) dy}. \tag{7}$$

In formula (7), the estimation of $f(x, y)$ can be accessed by estimating the training data with the application of the Parzen's nonparametric estimation operator. The nonparametric estimation is

$$\hat{f}(x, y) = \frac{1}{(2\pi)^{\frac{m+1}{2}} \sigma^{m+1}} \cdot \frac{1}{n} \sum_{i=1}^n e^{-d(x, x_i)} e^{-d(y, y_i)}, \tag{8}$$

where

$$d(x, x_i) = \frac{(x - x_i)^T(x - x_i)}{2\sigma^2}, \quad d(y, y_i) = \frac{(y - y_i)^2}{2\sigma^2}.$$

In this formula, x_i is the observation vector of x and y_i is the observation value of y . Symbol m denotes the dimensionality of x , σ is the smoothing factor and n is the number of samples. Symbol $\hat{f}(x, y)$ is used to replace $f(x, y)$. substituting it to formula (7), and taking into account that $\int_{-\infty}^{\infty} z e^{-z^2} dz = 0$, we can see that

$$\hat{y}(x) = \frac{\sum_{i=1}^n y_i e^{-d(x, x_i)}}{\sum_{i=1}^n e^{-d(x, x_i)}}. \tag{9}$$

The estimated value $\hat{y}(x)$ is the weighted average of all y_i . Each weighted factor of y_i is the index of squared Euclidean distance between sample x_i and x . Through formula (9), we can see that $\hat{y}(x)$ is within the variation range of y_i , which is the sample observation value of y [25].

Construct now a general regression neural network according to formula (9), whose structure is expressed in Fig. 4. It includes 4 layers of neurons.

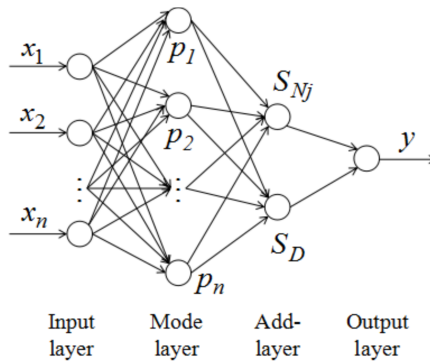


Fig. 4. Structure diagram of GRNN

From the previous analysis, we select the tolerance index, kurtosis index, peak index, impulsion index and power spectrum entropy as the input and output parameters. The settings are as follows:

Normality: Output $Y = (1, 0, 0)$. Abrasion: Output $Y = (0, 1, 0)$. Gear teeth breakage: $Y = (0, 0, 1)$.

The fault diagnosis module based on GRNN is depicted in Fig. 5

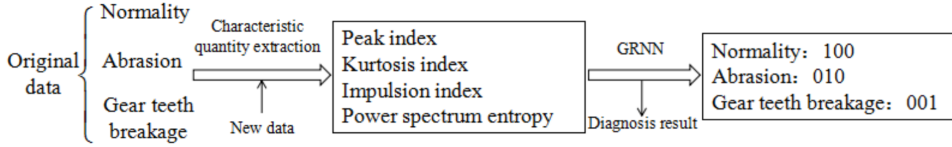


Fig. 5. Fault diagnosis module based on GRNN

4. Experimental results and discussion

4.1. Test on fault diagnosis model

During the training of neural network, the input information data should be within range $[0, 1]$, so the input data used in the neural network should be transformed through normalization processing. The corresponding formula is [26]

$$x_{io} = \frac{x_i - x_{\min}}{x_{\max} - x_{\min}}. \quad (10)$$

In this formula, x_{io} is the i th characteristic parameter after normalization processing, symbol x_i is i th characteristic parameter of the original input data, x_{\min} is the minimum characteristic parameter, and x_{\max} is the maximum characteristic parameter.

General regression neural network will conduct the module recognition on the gearbox with three fault conditions: fault-free, abrasion and gear teeth breakage. The output mode is $y = (a, b, c)$. The ideal output result is that there is one “1”, and two “0”s among these three parameters. However, the real outcome is certainly a little different from the ideal outcome. So we need to judge the simulation result. We judge it with the threshold condition of 0.9 in this research, in the following way: if $0.9 \leq a \leq 1$, it is judged as fault-free, if $0.9 \leq b \leq 1$, it is judged as abrasion of gear surface, and if $0.9 \leq c \leq 1$, it is judged as gear broken. If there is an exception, the case is not evaluated.

There are 25 groups of data under these signal samples of 3 fault conditions, among which 10 data groups are fault-free, 10 are abrasion and 5 are gear broken. To prove the validity of this module, we randomly choose one sample among those three to detect module, and the rest samples are used as module-building, i.e. network training. After modulating and observing the diagnosis outcome for many times, we can see that the training effect is the best when the distributing density is 0.14. The

results of the training process are summarized in Table 2:

Table 2. Training diagram of general regression neural network

Fault type	Sample number	Tolerance index	Kurtosis index	Peak index	Impulsion index	Power spectrum entropy
Fault-free	1	4.5363	2.5926	3.1438	3.8794	3.7556
	2	4.8814	2.6627	3.2776	4.1243	3.9353
	3	4.2038	2.5822	2.9482	3.6025	3.2745
	4	4.2392	2.3255	2.9264	3.6123	3.2972
	5	3.4127	1.6478	2.3685	2.9245	3.3713
	6	4.7188	2.9606	3.1489	3.9878	3.5716
	7	3.8659	2.1607	2.7261	3.3114	3.3946
	8	3.7938	1.9976	2.6339	3.2534	3.9537
	9	4.6521	2.3712	3.2262	3.9764	3.8014
Gear abrasion	11	2.5653	1.2408	1.9142	2.2726	2.9810
	12	3.6127	1.6156	2.2588	2.9465	3.3054
	13	6.0127	2.7246	3.4326	4.7176	3.1076
	14	4.5746	2.3827	3.1072	3.8765	3.4056
	15	3.7716	1.7365	2.5217	3.1726	3.3845
	16	3.1975	1.4945	2.2947	2.7775	3.1727
	17	4.1426	2.5217	2.8128	3.5056	3.3903
	18	3.9175	1.7203	2.5718	3.2642	3.1054
	19	4.1517	2.1987	2.7653	3.4956	3.0656
Gear broken	21	6.3805	2.9665	3.6652	5.0627	4.3424
	22	8.7954	4.7965	6.1554	7.6534	4.9945
	23	7.9436	4.1823	5.3335	6.7365	4.3347
	24	9.8745	4.9345	6.2114	8.1767	6.3665

To detect the fault diagnosis ability of general regression neural network, the network that has been trained needs to be tested. The reserved 3 groups of sample data were used to do module detection. The comparative condition of predicted and real results is shown in Table 3.

Analyzing the data in Table 3 we can see that the fault diagnosis based on GRNN has a high recognition rate on three typical fault modes, all of which are above 90%. It satisfies the threshold conditions set before, and thus, the validity of this module can be declared as verified.

Table 3. Detection result of fault diagnosis module based on GRNN

Fault type	Normality	Abrasion	Teeth breakage
Testing sample	Sample 11	Sample 27	Sample 31
Fault number	100	010	001
Diagnosis result	0.9987, 0.0003, 0.0000	0.0012, 0.9994, 0.0000	0.0000, 0.0004, 0.9996

4.2. The design and implementation of fault diagnosis system

Based on analysis on the gearbox fault, we developed an expert system of gearbox fault diagnosis facing with Web. The system is designed in three levels: page for fault conditions, page for fault reasons and page for solutions. The default page of the system is the one for fault conditions, see Fig. 6.

Fig. 6. Expert system of gearbox fault diagnosis

We developed this system on .NET platform, integrating C programming language. The overall framework of the system is: the left side is the menu of fault types, the right side is the list for fault conditions. Below the page of fault conditions, users can search information page by page, and also can input key words in the box to search what they need. Click the “View detail” in the list of search results, the possible reasons correspondent to various fault conditions can be achieved. Users can also click the correspondent menu of fault conditions, and have access to the list of relative reasons where possible reasons are listed. The list of search result is ranked according to the weight of reasons, those with the higher weight are ranked at a higher position on the list to attract the attention of the maintenance staff immediately.

After having knowledge of fault reasons, users only need to click the “View detail” on the solutions list to obtain the expert solutions. The maintenance staff can choose

relative fault solutions considering the practical fault condition and concerning their own knowledge.

5. Conclusion

Gearbox is an important part of the wind turbine generator system, whose fault will influence the stability and security of the whole wind turbine generator system. We developed a fault diagnosis system based GRNN and fault tree analysis, and applied it to the gearbox of wind turbine. The results show that this system can shorten the time of diagnosing fault, and put forward expert solutions rapidly, thus the gearbox fault can be diagnosed and maintained accurately and effectively.

References

- [1] S. YANG, W. LI, C. WANG: *The intelligent fault diagnosis of wind turbine gearbox based on artificial neural network*. Proc. IC Condition Monitoring and Diagnosis, 21 to 24 April 2008, Beijing, China, 1327–1330.
- [2] Z. FENG, X. CHEN, M. LIANG: *Iterative generalized synchrosqueezing transform for fault diagnosis of wind turbine planetary gearbox under nonstationary conditions*. Mechanical Systems and Signal Processing 52–53 (2015), 360–375.
- [3] M. NIE, L. WANG: *Review of condition monitoring and fault diagnosis technologies for wind turbine gearbox*. Procedia CIRP 11 (2013), 287–290.
- [4] D. ZAPPALAA, P. J. TAVNER, C. J. CRABTREE, S. SHENG: *Side-band algorithm for automatic wind turbine gearbox fault detection and diagnosis*. IET Renewable Power Generation 8 (2014), No. 4, 380–389.
- [5] K. KIM, A. G. PARLOS, R. M. BHARADWAJ: *Sensorless fault diagnosis of induction motors*. IEEE Trans. Industrial Electronics 50 (2003), No. 5, 1038–1051.
- [6] Y. AMIRAT, M. BENBOUZID, B. BENSACE, R. WAMKEUE: *Condition monitoring and fault diagnosis in wind energy conversion systems: A review*. Proc. IEEE International Electric Machines & Drives Conference, IEMDC, 3–5 May 2007, Antalya, Turkey, 1434–1439.
- [7] A. S. ZAHER, S. D. J. MCARTHUR: *A multi-agent fault detection system for wind turbine defect recognition and diagnosis*. Proc. IEEE Power Tech, 1–5 July 2007, Lausanne, Switzerland, 22–27.
- [8] Q. HUANG, D. JIANG, L. HONG, Y. DING: *Application of wavelet neural networks on vibration fault diagnosis for wind turbine gearbox*. Advances in Neural Networks, Lecture Notes in Computer Science 5264 (2008), 313–320.
- [9] Z. FENG, M. LIANG: *Fault diagnosis of wind turbine planetary gearbox under non-stationary conditions via adaptive optimal kernel time–frequency analysis*. Renewable Energy 66 (2014), 468–477.
- [10] Z. FENG, M. LIANG: *Complex signal analysis for wind turbine planetary gearbox fault diagnosis via iterative atomic decomposition thresholding*. J Sound and Vibration 333, (2014), No. 20, 5196–5211.
- [11] H. BOUDALI, P. CROUZEN, M. STOELINGA: *A rigorous, compositional, and extensible framework for dynamic fault tree analysis*. IEEE Trans. Dependable and Secure Computing 7 (2010), No. 2, 128–143.
- [12] Z. DU, X. CHEN, H. ZHANG, R. YAN: *Sparse feature identification based on union of redundant dictionary for wind turbine gearbox fault diagnosis*. IEEE Trans. Industrial Electronics 62 (2015), No. 10, 6594–6605.

- [13] H. YIN, Y. ZHOU, W. LIU, L. L. REN: *Application of fault tree analysis in the investigation of production incidents of oil and gas wells*. Environmental Protection of Oil & Gas Fields 17 (2012), No. 1, 154–169.
- [14] J. KLOOS, T. HUSSAIN, R. ESCHBACH: *Risk-based testing of safety-critical embedded systems driven by fault tree analysis*. Proc. IEEE Fourth IC Software Testing, Verification and Validation Workshops, 21–25 March 2011, Berlin, Germany, 26–33.
- [15] F. A. RAHMAN, A. VARUTTAMASENI, M. KINTNER-MEYER, J. C. LEE: *Application of fault tree analysis for customer reliability assessment of a distribution power system*. Reliability Engineering & System Safety 111 (2013), 76–85.
- [16] F. ZHOU: *Fault diagnosis method of gear of wind turbine gearbox based on undecimated wavelet transformation*. Proc. IC Computer Design and Applications, 25–27 June 2010, Qinhuangdao, China, 4 606–609.
- [17] F. C. ZHOU: *Research on online monitoring and diagnosis of bearing fault of wind turbine gearbox based on undecimated wavelet transformation*. Proc. IEEE Youth Conference on Information, Computing and Telecommunications, 28–30 November 2010, Beijing, China, 251–254.
- [18] X. Y. ZHONG, L. C. ZENG, C. H. FAULT DIAGNOSIS TECHNIQUES FOR WIND TURBINE GEARBOX. Applied Mechanics and Materials 197 (2012), 206–210.
- [19] E. BOUFOUNAS, Y. BERRADA, M. KOUMIR, I. BOUMHIDI: *A robust intelligent control for a variable speed wind turbine based on general regression neural network*. Proc. Intelligent Systems and Computer Vision (ISCV), 25–26 March 2015, Fez, Morocco, 1–6.
- [20] C. M. HONG, F. S. CHENG, C. H. CHEN: *Optimal control for variable-speed wind generation systems using general regression neural network*. IJ Electrical Power & Energy Systems 60 (2014), 14–23.
- [21] J. YOON, D. HE, B. V. HECKE: *On the use of a single piezoelectric strain sensor for wind turbine planetary gearbox fault diagnosis*. IEEE Trans. Industrial Electronics 62 (2015), No. 10, 6585–6593.
- [22] M. SCHLECHTINGEN, I. F. SANTOS: *Comparative analysis of neural network and regression based condition monitoring approaches for wind turbine fault detection*. Mechanical Systems and Signal Processing 25 (2011), No. 5, 1849–1875.
- [23] J. SHELDON, G. MOTT, H. LEE, M. WATSON: *Robust wind turbine gearbox fault detection*. Wind Energy 17 (2014), No. 5, 745–755.
- [24] C. JING, W. Q. WANG, H. E. SHAN: *Noise prediction of wind turbines based on regression analysis and BP neural network*. Noise & Vibration Control 33 (2013), No. 6, 49–52.
- [25] F. C. SICA, F. G. GUIMARAES, R. D. O. DUARTE, A. J. R. REIS: *A cognitive system for fault prognosis in power transformers*. Electric Power Systems Research 127 (2015), 109–117.
- [26] N. D. KAUSHIKA, R. K. TOMAR, S. C. KAUSHIK: *Artificial neural network model based on interrelationship of direct, diffuse and global solar radiations*. Solar Energy 103 (2014), 327–342.

Received November 16, 2016

Robust radar waveform algorithm based on beam steering vector estimation

YINGLIU CUI^{1,2}

Abstract. In view of the problems of traditional adaptive beam-forming algorithm in the practical application, this paper, under the premise of acquisition of expected target angular domain based on the sequence of two quadratic programming method, puts forward the robust adaptive beam-forming based on beam-space steering vector estimation (BA-RAB). First of all, make use of the complement structure in the expected beam domain angle area to form the weights, and then the weights are reversely transformed to matrix domain. As a result, it can obtain adaptive robust with steady performance to form weights on the two occasions of steering vector mismatch and training samples contaminated. Moreover, the effectiveness of the proposed method is verified by computer simulation.

Key words. Radar waveform, algorithm, adaptive beam.

1. Introduction

Although all solid state transmitter and digital receiver greatly improve the stability of radar, the system error is greatly reduced. The significant improvement of the technological level of the antenna makes the channel error further reduced, but it cannot completely eliminate the array channel amplitude and phase error. At the same time, the estimation error and steering vector error of signal co-variance matrix caused by finite samples or small samples will lead to the decrease of the adaptive beam-forming performance.

Reasonable use of angle region information of the target signal can eliminate the impact of training samples being polluted. This paper uses the complement structure beam domain conversion matrix of the desired signal beam domain angle mismatch region, to transform the array domain training data to the beam field, which eliminates the desired signal component in the training samples, and gives the

¹School of Electronic and Optical Engineering, Nanjing University of Science and Technology, Nanjing, 210094, China

²School of Technology, Nanjing Audit University, Nanjing, 211815, China

beam-space steering vector estimation method, using semi definite relaxation planning solution with constant constraint quadratically constrained quadratic programs (QCQP) problem [1].

2. Literature review

The generalized radar waveform includes transmitting wave and receiving wave. Received waveform is the waveform matched with the radar receiver filter. When the radar is carry out mismatch processing with the received signal, the received waveform is different from the transmitted waveform. Radar waveform is of variety, and according to the fuzzy function form, it can be divided into three types: 1. the signal with blade fuzzy function, including constant frequency pulse signal with positive blade fuzzy function and linear frequency modulation pulse signal with inclined blade fuzzy function; 2. the pseudo-random signal with encoding thumbtack fuzzy function; 3. the coherent pulse train signal with the nail bed type fuzzy function. In addition to the constant frequency pulse signal, for other types of signal, the multiple of time bandwidth and bandwidth is greater than 1, referred to as the large time bandwidth product signal. The signal with inclined blade type and thumbtack fuzzy function is the pulse width encoding signal. Due to the introduction of nonlinear phase modulation in the pulse, wide pulse with narrow pulse bandwidth, through the matched filter or related integral processing, can be compressed into a narrow pulse to output, called the pulse compression signal. This signal not only has excellent detection performance and speed performance, but also has high range resolution and ranging performance of narrow pulse waveform. Pulse compression waveform can be divided into two types of frequency modulated pulse compression signal and phase coded pulse compression signal according to the nonlinear phase modulation rule. The former also has the difference in linear frequency modulation and the nonlinear frequency modulation; the latter has the difference in two-phase code, the multiple-phase code and the complementary code.

The traditional adaptive beam-forming algorithm is applied to practical problems, there are two aspects of the problem. On the one hand, the traditional adaptive beam-forming algorithm assume that there is no desired signal in the training data, but in practice, if the desired signal exists in the training data, it will significantly reduce the convergence rate of the adaptive beam-forming algorithm. If the number of samples is very small, it will lead to a serious decline in performance. On the other hand, the traditional adaptive beam-forming algorithm, under non-ideal conditions, such as environmental pollution and the antenna array pollution, it will be affected by the pollution, which will lead to some errors between the steering vector assumed and the actual signal steering vector, and the traditional adaptive beam-forming algorithm is very sensitive to steering vector error. Very sensitive, then the algorithm performance also very serious declines. The researchers showed that the traditional adaptive beam-forming method is sensitive to the steering vector mismatch and array error [2]. To get high performance, it is necessary to know the co-variance matrix of the desired signal steering vector and the interference plus noise. In the actual scene, there is always mismatch reduction between the desired signal steering vector

assumed and the actual steering vector [4]. In addition, in the passive no-source positioning, mobile communication and so on actual application cases, the training sample data will inevitably contain the desired signal component, oriented vector mismatch and the training samples containing the desired signal component, which will cause the decline of the performance of adaptive beam-forming [5]. The research of adaptive beam forming algorithm with steady performance is the problem needed to be solved in engineering application.

There exist many methods used to improve the robustness of adaptive beam-forming algorithm. Literature [3] makes use of diagonally Loaded SMI, LSMI sample matrix inversion method to improve the direct sample matrix inversion (SMI) robust beam-forming, and LSMI, by controlling the diagonal loading to increase artificial white noise variance, alleviates the self-destructive problem of useful signal, suitable for mismatch cases in different types, but the method has an obvious deficiency - it is difficult to determine the amount of diagonal loading. Literature [2], in allusion to the steering vector mismatch, proposed robust beam-forming with mode constraint algorithm, and acquired the robust adaptive algorithm relevant with the uncertainty set, while the method needs appropriate parameters selection to ensure its robustness. Literature [5] studied the robust adaptive beam-forming algorithm under the worst performance (Worst case based RAB, W C-RAB). On the assumption that the mismatch scale limit is known, the approximate analytic formula of the optimal loading amount is obtained, while the limit of mismatch amount in practice is not known. The literature [6] and literature [9] improve the literature [5], and under the assumption that the spatial range of the target signal uses the low resolution method, the iterative sequence of quadratic programming (Sequential Quadratic Programming, SQP) method is used to estimate the actual steering vector. However, since that the impact of the desired signal component in the training samples is not considered, when the signal-to-noise ratio increases, the increase of output SINR will occur bottlenecks.

3. Method

The proposed algorithm is based on the premise of target angular domain known by low resolution method. First of all, use the complement structure beam-space conversion matrix of the desired signal angle area, and then, in the beam domain, deduct the estimation algorithm of the desired steering vector, and calculate beam-space beam-forming weights. At last, the beam-space beam-forming weights are transformed to the element space, which can obtain adaptive beam-forming weight with robust performance on the two conditions for steering vector mismatch and training samples contaminated.

3.1. Robust radar waveform formation algorithm based on beam steering vector estimation

The algorithm consists of six steps:

1. According to the low resolution method, divide the target airspace range Θ

and the interference target airspace $\bar{\Theta}$.

2. Calculate $A = \int_{\bar{\Theta}} a(\theta)a^H(\theta) d\theta$, where $a(\theta)$ is the expected signal steering vector and θ represents the signal location. The number of A 's main feature vectors M' is derived from the minimum description length criterion (MDL) method. Construct the beam transform matrix $B = [u_1, u_2, \dots, u_{M'}]_{M \times M'}$, in which $\{u_i\}_{i=1}^{M'}$ is the M' th main feature vector of A .
3. Calculate the co-variance matrix $R_b = B^H R_\chi B$ of the beam field, and make use of CVX to solve (1) that does not contain rank $(Z_b) = 1$, and obtain the optimal solution in the form

$$\begin{cases} \min_{Z_b} \text{Tr}(\hat{R}_b^{-1} Z_b), \\ \text{s.t. } \text{Tr}(BB^H)^{-1} B Z_b B^H ((BB^H)^{-1})^H = M, \\ \text{Tr}(Z_b) \leq \delta_0, \\ Z_b \succeq 0, \\ \text{rank}(Z_b) = 1, \end{cases} \quad (1)$$

δ_0 being the unknown error between the expected and true steering vectors and

4. Randomly generate L vectors $\xi_l \sim N(0, \hat{Z}_b)$ following zero mean Gauss distribution, $l = 1, \dots, L$. They are normalized, and then $\tilde{a}_l = \xi_l / \|\xi_l\|$ is obtained. The chosen optimal beam steering vector $\hat{a}_b = \tilde{a}_l$ meets the condition $l^* = \arg \min_{l=1, \dots, L} \tilde{a}_l^H R_b^{-1} \tilde{a}_l$ (\hat{a}_b denoting the optimal signal steering vector and \tilde{a}_b denoting the true signal steering vector).
5. After obtaining the optimal estimate beam steering vector \hat{a}_b , make use of (2) to solve the beam domain Capon weight vector W_{b_opt} ;

$$w_b = \frac{\hat{R}_b^{-1} \tilde{a}_b(\theta_s)}{\tilde{a}_b^H(\theta_s) \hat{R}_b^{-1} \tilde{a}_b(\theta_s)}. \quad (2)$$

6. Eventually, make use of the conversion relation $W_{opt} = (B B^H)^{-1} B W_{b_opt}$ between the beam domain Capon vector and right array domain Capon weight vector to solve the domain Capon adaptive weight vector W_{opt} .

3.2. Simulation experiment design

The effectiveness of the proposed method is verified by computer simulation experiments. Assume that the receiving array is a uniform linear array, the number of array elements is $M = 20$, and the array element spacing is half of the wavelength. It is assumed that the two interference sources are incident at 30 degrees and 50 degrees respectively, the dry noise ratio is 30 dB, the actual incident angle of the desired signal is $\theta_P = 5^\circ$, and the space noise is Gauss white noise with zero mean value. All the simulation results are obtained by 200 Monte-Carlo experimental statistics,

and the training snapshot data always contains the desired signal component. The proposed algorithm (BS-RAB) is compared with SMI, LSMI, WC-RAB and SQP-RAB. For BS-RAB and SQP-RAB, the angle domain interval of the desired signal is assumed as $\Theta = [\theta_P + 5^\circ \text{ to } \theta_P - 5^\circ]$, the number of main feature value is $M' = 8$, and the proposed algorithm BS-RAB theory is $N_{3\text{dB}} = 13$. Slack variable of SQP-RAB is $\delta_0 = 0.1$. The upper limit of steering vector mismatch amount in WC-RAB algorithm, is set to $\varepsilon = 0.3M$, and the diagonal loading factor of LSMI algorithm is set to two times of the noise power.

Table Simulation experiments assumptions

Simulation experiments	
Experiment 1	In the case of existing direction mismatch, compare the performance of BS-RAB, SMI, LSMI, WC-RAB and SQP-RAB algorithms. The assumed steering vector is calculated by $\theta_P + \theta_e$, θ_e being observing direction mismatch error, and in the experiment, θ_e is set to evenly distributed in the interval $[-5^\circ, 5^\circ]$.
Experiment 2	In the construction of beam domain conversion matrix, make use of the desired target angle domain Θ and the array element position information without interference. The desired target angle domain is the mismatch region of the target direction, and the selection criteria is only containing the useful signal, but not containing any interference direction. It is assumed that the element position interference caused by antenna position error is evenly distributed in $[-k\lambda, k\lambda]$, where λ is the wavelength.
Experiment 2	Considering the direction mismatch and element position interference, compare the performance of BS-RAB, SMI, LSMI, WC-RAB and SQP-RAB algorithms. Assume that the error between the element and ideal position is evenly distributed in the interval of $[-0.15\lambda, 0.15\lambda]$, where λ is the wavelength. Other simulation conditions are the same as in experiment 1 settings.

4. Results

Experiment 1: set the single element SNR is SNR=10 dB, compares the change relation of 5 algorithms output SINR with the training snapshots, as shown in Fig. 1. As can be seen from the figure, WC-RAB and SQP-RAB, on the condition that the number of snapshots is less than 30, have a similar output SINR; while on the condition that the number of snapshots is larger than 30, the output of SQP-RAB SINR is better than that of WC-RAB, and the algorithm proposed BS-RAB output SINR has basically reached the convergence value in the output snapshots of 20. In the case of small samples, this method has better performance, while the overall output SINR is much higher than the other 4 algorithms.

The number of snapshots is set as 100, then the variation relation diagram of 5 algorithms output SINR with the input SNR is shown in Fig. 2. We can see that, when the input SNR approximation is less than 20 dB, the output of SQP-RABSINR

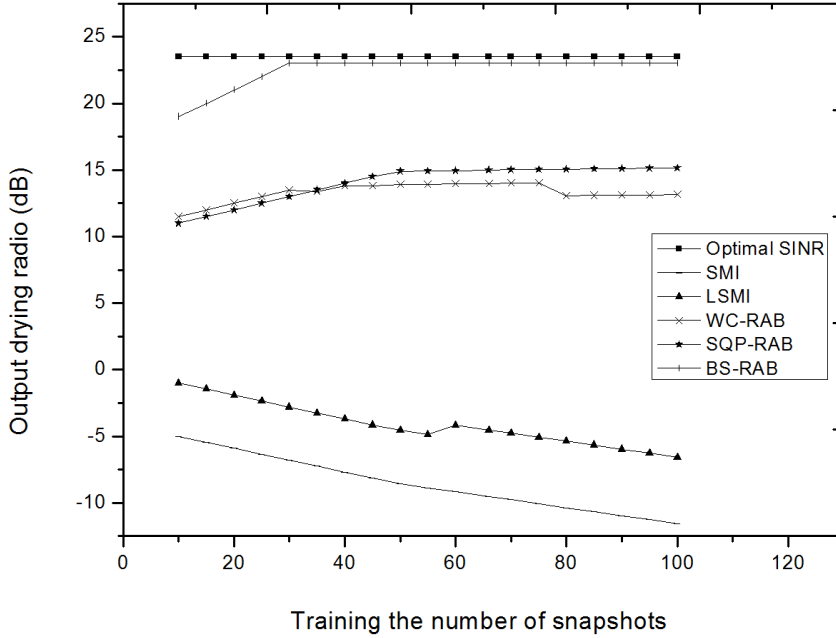


Fig. 1. The variation curves of OSINR with the number of snapshots on the occasion of direction mismatch

SINR is higher than that of WC-RAB; when the input SNR approximation is larger than 20 dB, the output of WC-RAB SINR is higher than that of SQP-RAB. But there is bottleneck in the variation of SINR with the increase of SNR, while the output of BS-RAB SINR has the performance of close to the optimal SINR. It can be seen that BS-RAB has a strong robust performance to signal direction mismatch error, and the output of SINR is superior to other algorithms.

5. Discussion

The method proposed in this paper does not require the upper limit constrain of the steering vector mismatch error, which avoids the modeling of the upper limit of the steering vector mismatch. Compared with the method of literature [6], although all belong to the class of robust adaptive steering vector estimation algorithm, because the proposed method reasonably uses the spatial information of target signal and interference, the proposed method can eliminate the influence of the desired signal contained in the training sample. In addition, since that the steering vector of non-uniform linear array is more general compared with uniform linear array, and there is no limit in the construction of beam-space transformation matrix and the constrain condition of estimation beam-space steering vector in the array type, the proposed method is also applicable to non-uniform linear array.

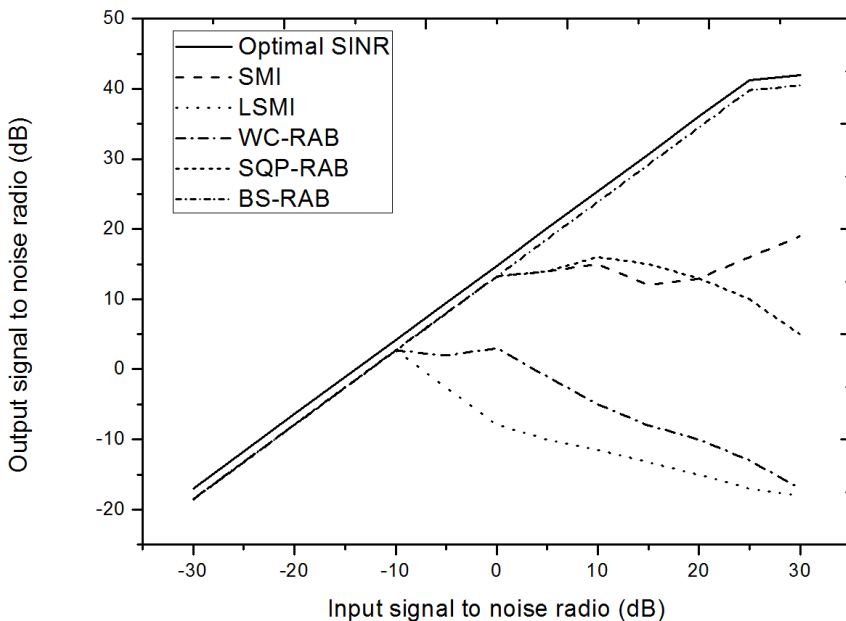


Fig. 2. The performance comparison on the occasion of direction mismatch

Experiment 2: Figure 3 shows the variation curves of constrained region $\hat{\Theta}_k$ deviation degree from $\hat{\Theta}$ with k . It is found that the $\hat{\Theta}_k$ deviation is less than 4% in the presence of the array element, and the influence of the element disturbance on the deviation is not great. Although there is a difference between the use of the steering vector without array position disturbance and the steering vector calculation matrix A in the presence of array element position disturbance, as long as the angle domain $\hat{\Theta}_k$ contains only the desired signal but does not contain any interference signal, the constrain $\|\tilde{a}_b\| \leq \max \|\tilde{a}_b(\theta)\|$, $\theta \in \Theta$ is established. As a result, we can calculate the beam field transformation matrix by the assumption that the array elements are not perturbed.

The simulation experiment 3 showed that the proposed method is suitable for small sample snapshots, and compared with other algorithms, it has more performance advantages.

6. Conclusion

This paper studies the robust adaptive beam-forming method, and for steering vector mismatch and sample co-variance matrix estimation error resulting in adaptive beam-forming performance degradation problems, puts forward a kind of robust adaptive beam-forming method (BA-RAB) based on beam-space steering vector estimation on the condition of training samples contaminated. This method uses the

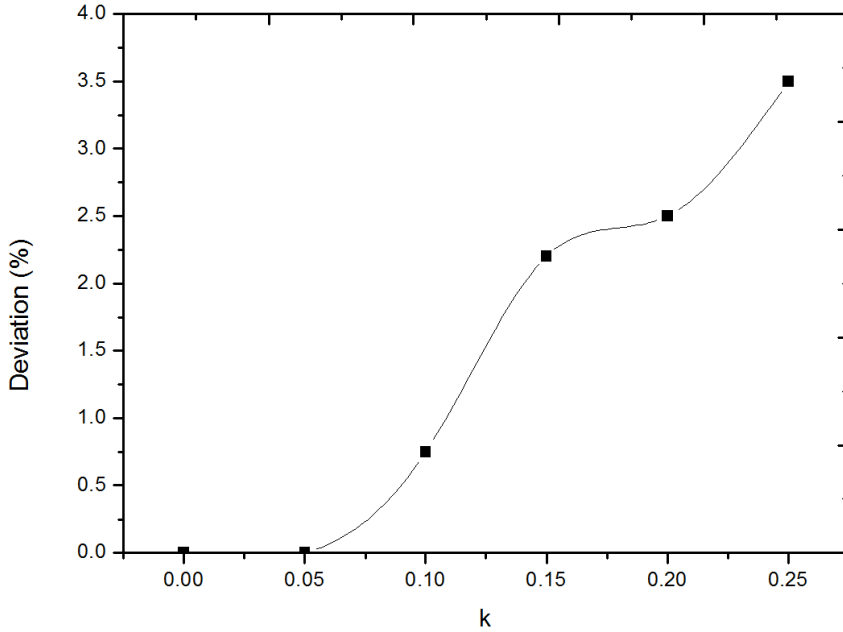


Fig. 3. The variation curve of $\hat{\Theta}_k$ deviation with element disturbance degree

complement structure of the desired signal beam domain angle mismatch area of the conversion matrix, the array domain training data is transformed to the beam field, to eliminate the desired signal component in the training samples, and gives the beam-space steering vector estimation method, using semi definite relaxation planning solving QCQP problem with constant modulus constraint. The proposed method, in the case of training sample contaminated and steering vector mismatched, can effectively improve the robust performance of adaptive beam-forming output SINR, so the output SINR achieves the approximate optimal SINR, and it is suitable for small sample snapshot. It overcomes the shortcomings of the existing algorithms useful signal elimination when the desired signal component exists in the sample covariance matrix. And then the method to estimate the beam-space steering vector is derived, and transformed into quadratic programming problems with two non-convex constant modulus constraint, then the semi definite relaxation planning is used to estimate the actual beam-space steering vector. Finally, the effectiveness of the proposed method is verified by computer simulation.

References

- [1] Y. LIU, H. WANG, J. WANG: *Robust multiple-input multiple-output radar waveform design in the presence of clutter*. IET Radar, Sonar & Navigation 10 (2016), No. 7, 1249–1259.

- [2] B. NUSS, J. FINK, F. JONDRAL: *Cost efficient frequency hopping radar waveform for range and doppler estimation*. IEEE International Radar Symposium (IRS), 10–12 May 2016, Krakow, Poland, 1–4.
- [3] Z. ZHOU, G. HUANG, J. GAO: *A robust radar emitter signals recognition algorithm based on cauchy random projection*. IEEE International Conference on Fuzzy Systems and Knowledge Discovery (FSKD), 15–17 August 2015, Zhangjiajie, China, 644–648.
- [4] A. AUBRY, A. DE MAIO, Y. HUANG, M. PIEZZO, A. FARINA: *A new radar waveform design algorithm with improved feasibility for spectral coexistence*. IEEE Trans. Aerospace and Electronic Systems *51* (2015), No. 2, 1029–1038.
- [5] A. AUBRY, A. DE MAIO, M. M. NAGHSH: *Optimizing radar waveform and doppler filter bank via generalized fractional programming*. IEEE J. Selected Topics in Signal Processing *9* (2015), No. 8, 1387–1399.
- [6] B. JIU, H. LIU, X. WANG, L. ZHANG, Y. WANG, B. CHEN: *Knowledge-based spatial-temporal hierarchical MIMO radar waveform design method for target detection in heterogeneous clutter zone*. IEEE Trans. Signal Processing *63* (2015) No. 3, 543–554.

Received November 16, 2016

Gauge point positioning method based on computer vision

JIAOZHEN ZHAO¹

Abstract. A new effective gauge point positioning is proposed in the paper, which is very crucial from the viewpoint of the safety and reliability of railway transportation. Firstly, framework of the computer vision based track geometric deformation detection system is proposed. In particular, the visual inspection system is made up of four modules, that is, 1) Sensing system, 2) Light source system, 3) Image acquisition system, and 4) Image processing system. Secondly, to tackle the gauge point positioning problem, two conversions should be done in advance, including 1) world coordinate system to camera coordinate system, and 2) camera coordinate system to image coordinate system. Thirdly, in order to accurately position gauge points, a weighted least square based curve fitting algorithm is exploited to choose an appropriate type of curve to fit the observed data. Finally, from the simulation results, it can be observed that the proposed method is able to position gauge points using computer vision.

Key words. Gauge point positioning, computer vision, curve fitting, surface defect repair.

1. Introduction

As the backbone of modern transportation system, railway plays an important role in promoting the development of social economy and improving the utilization of social resources [1], [2]. In recent years, with the rapid development of railway construction, the passenger and freight volume increase rapidly [3]. Particularly, after China comprehensively promoting the construction of high-speed railway passenger and freight traffic, traffic density significantly develops than ever. Furthermore, together with the high quality demand of the railway line, the requirements of track parameter standardization improve as well [4], [5].

Track irregularity mainly contains track longitudinal level, along-track, track level, track twist irregularity, gauge, and so on. In all track parameters, gauge refers to one of the basic rail parameter and it has always been one of the necessary ones which should be measured [6], [7]. However, if the gauge cannot be detected precisely, it will lead to weighty rail hidden trouble. Moreover, when gauge is out of range, not only the stability of vehicle's moving and the comfort of passengers will

¹The College Humanities & Sciences of Guizhou Minzu University, Guizhou, 550025, China

be affected, but also the relationships between wheel and rail may cause security risks of climbing out of track [8]. In order to detect gauge points precisely, high efficiently, and non-contact, there are many difficult problem we should solve [9], [10]. Particularly, to satisfy to the need of speediness and over loading and guarantee the train running safely, it is of great importance to propose an effective gauge point positioning method [11].

The rest of the paper is organized as follows. We illustrate the computer vision based track geometric deformation detection system in section 2. In Section 3, we explain the proposed gauge point positioning method. To test the effectiveness of the proposed method, simulations are conducted to prove the effectiveness of our method in section 4. Finally, section 5 concludes this paper in detail.

2. Computer vision based track geometric deformation detection system

Computer vision products can obtain object information through the image acquisition system, and then convert them into digital signals, which can be widely used in image processing system, image processing system, and so on. After a series of operations and processing steps, the target characteristic information of the position and contour can be obtained. Finally, equipment actions are controlled according to test results. Thus, the visual inspection system is made up by the following parts:

1. Sensing system—relies on various types of sensors to collect information, and then build detection devices.
2. Light source system—provides the linear light source through the light source controller for the detection system.
3. Image acquisition system—contains video camera, image acquisition card, and so on.
4. Image processing system—contains a variety of image processing algorithms, and image processing software.

Early track geometric deformation detection mostly used the contact measurement mode. However, this kind of method mainly depends on the rolling wheel rail contact to obtain valid data. Therefore, measurement accuracy and reliability of are not very ideal. At present, with the rapid development of high-speed railway technology, gauge detection becomes more and more important to track the geometric deformation. In track geometric deformation detection, the geometrical parameters selection is a crucial problem. Particularly, gauge point positioning should be solved in advance. Framework of the computer vision based track geometric deformation detection system is shown in Fig. 1.

The detection system based on machine vision has been widely used in track geometric deformation detection due to its powerful function of perception, analysis and processing of data. Therefore, considering various factors, in this paper, we

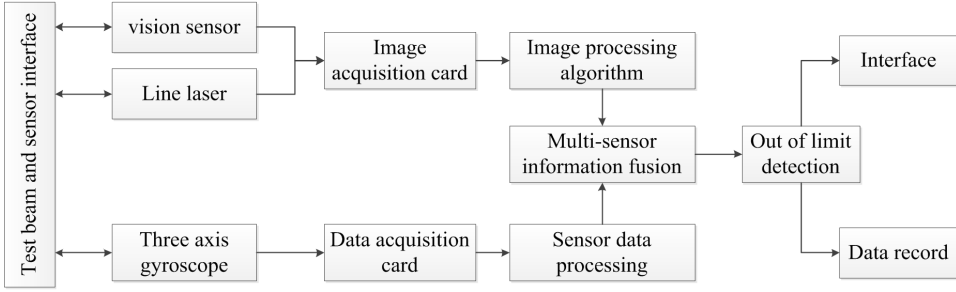


Fig. 1. Framework of the computer vision based track geometric deformation detection system

will use the detection system based on machine vision to realize the track geometry deformation gauge positioning algorithm. Diagram of gauge and gauge point is shown in Fig. 2.

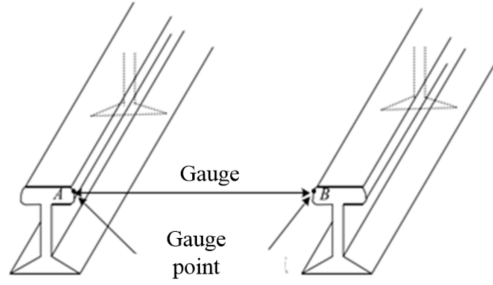


Fig. 2. Diagram of gauge and gauge point

As is shown in Fig. 2, the gauge point is located at the top of the vertical downward 16 mm position, and points A, B denote two gauge points which are corresponding to the left and right rails, respectively. According to the railway gauge corresponding with the international standard in China, the distance between two gauge points is 1435 mm.

3. The proposed gauge point positioning method

For the gauge point positioning problem, we should solve the coordinate system conversion issue. World coordinate system can be converted to the camera coordinate system by the equation

$$\begin{bmatrix} x_c \\ y_c \\ z_c \\ 1 \end{bmatrix} = \begin{bmatrix} R & T \\ 0^T & 1 \end{bmatrix} = \begin{bmatrix} r_{11} & r_{12} & r_{13} & t_x \\ r_{21} & r_{22} & r_{23} & t_y \\ r_{31} & r_{32} & r_{33} & t_z \\ 0 & 0 & 0 & 1 \end{bmatrix}, \quad (1)$$

where R is the rotation matrix, which is computed as follows

$$R = \begin{bmatrix} \cos(\varphi) & -\sin(\varphi) & 0 \\ \sin(\varphi) & \cos(\varphi) & 0 \\ 0 & 0 & 1 \end{bmatrix} \cdot \begin{bmatrix} \cos(\theta) & 0 & \sin(\theta) \\ 0 & 1 & 0 \\ -\sin(\theta) & 0 & \cos(\theta) \end{bmatrix} \cdot \begin{bmatrix} 1 & 0 & 0 \\ 0 & \cos(\phi) & -\sin(\phi) \\ 0 & \sin(\phi) & \cos(\phi) \end{bmatrix}, \quad (2)$$

where symbols φ, θ, ϕ denote the angle between the three axes of the camera and the corresponding world coordinate system, and $T \{t_x, t_y, t_z\}$ refers to the displacement between two different coordinate systems.

Next, we will discuss how to convert the camera coordinate system to the image coordinate system. Suppose that a point of camera coordinate system is represented as $P(x, y, z)$, and the corresponding image coordinate is represented as $p(X, Y)$. The point $P(x, y, z)$ can be converted to $p(X, Y)$ as follows

$$\begin{cases} X = fx/z \\ Y = fy/z \end{cases} \quad (3)$$

Then, the following equation should be satisfied.

$$z \begin{bmatrix} X \\ T \\ 1 \end{bmatrix} = \begin{bmatrix} f & 0 & 0 & 0 \\ 0 & f & 0 & 0 \\ 0 & 0 & f & 0 \\ 0 & 0 & 1 & 0 \end{bmatrix} \begin{bmatrix} x \\ y \\ z \\ 1 \end{bmatrix}. \quad (4)$$

To effectively position gauge points, we utilize curve fitting algorithm to select the appropriate type of curve to fit the observed data. For x, y , the discrete array is represented as (x_i, y_i) , and curve fitting process aims to find a function $y = f(x, c)$. Particularly, we choose the weighted least square method [12–14] to solve the curve fitting problem.

4. Experiment simulation

In this section, we test the performance of the method is by simulations. Particularly, parameters of Laser transmitter, CCD camera, and Image acquisition card, and the detailed experimental settings are shown in Table 1.

For the laser light rail profile image with top surface defects, in order to achieve precise positioning of the gauge point, we should repair defects of the top laser light. To solve this problem we utilize the curve fitting technology to repair surface defects at the top of track. Rail profile image is processed by several steps, such as grayscale, binarization, filtering, contour extraction, camera calibration, image correction, and so on. Next, Matlab is used to extract single pixel laser stripe coordinate. Curve fitting results are shown in Figs. 3 and 4.

Table 1. Experimental settings

Item	Index name	Value
laser transmitter	light source color	red
	angle of sector	eight degrees
	shape	planar array
CCD camera	resolving power	752×582
	working temperature	-9°C to 45°C
	frame rate	80 fps
image acquisition card	interface number	five
	interface type	CoaXPress

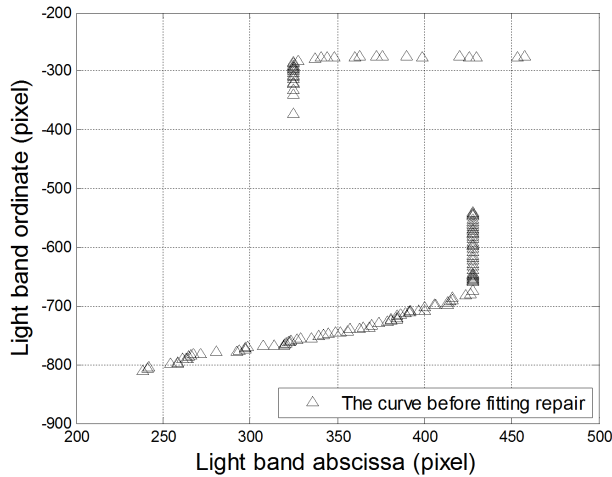


Fig. 3. Diagram of gauge and gauge point

It can be observed from Figs. 3 and 4 that the surface defect at the top of track can be repaired very well, and then the utilization rate of data acquisition can be promoted significantly. Based on the surface defect repair results, accuracy of the gauge point positioning can be enhanced obviously.

5. Conclusion

In this paper, we discuss how to locate gauge points with higher accuracy. The framework of the computer vision based track geometric deformation detection system is proposed at first. To solve the gauge point positioning issue, we explain how to convert world coordinate system to camera coordinate system, and how to convert camera coordinate system to image coordinate system. Based on the above steps, a weighted least square based curve fitting algorithm is exploited locate gauge

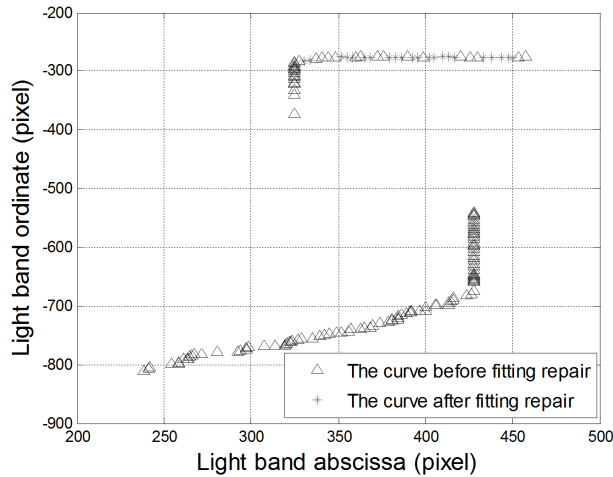


Fig. 4. Repair curve of surface defect at the top of track

points. In the end, experimental results demonstrate the effectiveness of our proposed method.

References

- [1] Y. ZHANG, Q. F. ZENG, D. LEI, X. WANG: *Simulating the effects of noncrossing block sections setting rules on capacity loss of double-track railway line due to the operation of out-of-gauge trains*. *Discrete Dynamics in Nature and Society 2016* (2016), Article ID 2319437.
- [2] S. MIKRUT, P. KOHUT, K. PYKA, R. TOKARCZYK, T. BARSZCZ, T. UHL: *Mobile laser scanning systems for measuring the clearance gauge of railways: State of play*. *Testing and Outlook, Sensors 16* (2016), No. 5, 683.
- [3] B. T. GORRIZ, I. PAYA-ZAFORTEZA, D. B. VILAR, Y. A. ALVARADO, P. A. GARCIA, A. L. LARA, M. S. GARCIA, A. ZORNOZA, S. S. MAICAS: *High-speed railway tunnel monitoring using point, long gauge and distributed strain and temperature fiber optic sensors*. *Informes de la Construcción 67* (2015), No. 538.
- [4] M. MORILLAS-TORNE: *The narrow gauge railway in Spain, 1852–2010. The role of intermodality and the demand in its construction and current status*. *Revista Electrónica De Geografía y Ciencias Sociales 18* (2014), No. 485, 123–130.
- [5] D. MISHRA, E. TUTUMLUER, H. BOLER, J. HYSLIP, T. SUSSMANN: *Railroad track transitions with multidepth deflectometers and strain gauges*. *J Transportation Research Board 2448* (2014), 105–114.
- [6] D. KANG, D. H. KIM, S. JANG: *Design and development of structural health monitoring system for smart railroad-gauge-facility using FBG sensors*. *Experimental Techniques 38* (2014) No. 5, 39–47.
- [7] B. A. PALSSON, J. C O. NIELSEN: *Track gauge optimisation of railway switches using a genetic algorithm*. *IJ Vehicle Mechanics and Mobility 50* (2012), No. 1, 365–387.
- [8] I. GUZMAN, J. L. MONTAYA: *Technical efficiency and productive change in the Spanish wide gauge railroad sector (1910-1922)*. *Innovar, Revista de Ciencias Administrativas y Sociales 21* (2011), No. 40, 219–234.

- [9] A. VELKAR: *Tracks across continents, paths through history: The economic dynamics of standardization in railway gauge*. J Economic History 70 (2010), No. 1, 262–263.
- [10] A. J. VEENENDAAL: *Tracks across continents, paths through history: The economic dynamics of standardization in railway gauge*. Technology and Culture 51, (2010), No. 2, 511–513.
- [11] T. GOURVISH: *Tracks across continents, paths through history: The economic dynamics of standardization in railway gauge*. The Economic History Review 63 (2010), No. 1, 278–280.
- [12] K. R. RIDGWAY, J. R. DUNN, J. L. WILKIN: *Ocean interpolation by four-dimensional weighted least squares—application to the waters around Australasia*. J Atmospheric and Oceanic Technology 19 (2002), No. 9, 1357–1375.
- [13] D. RUPPERT, M. P. WAND: *Multivariate locally weighted least squares regression*. The Annals of Statistics 22 (1994), No. 3, 1346–1370.
- [14] J. A. FESSLER: *Penalized weighted least-squares image reconstruction for positron emission tomography*. IEEE Transactions on Medical Imaging 13 (1994), No. 2, 290 to 300.

Received November 16, 2016

Research on hand movement recognition based on static image decomposition

JUN HE¹

Abstract. Estimation of human hand movement state is studied, that is, estimate the global pose of the human hand and the state of each local joint angle from the visual observation. In this paper, the static image sequence acquired by the camera is used as the observation input. Based on the improved Particle Swarm Optimization (PSO) particle filter algorithm study the human hand movement recognition, realize the interaction between the hand movement and the sphere.

Key words. Image sequence, particle filtering, human hand movement.

1. Introduction

It is an important research topic to use computer vision to analyze and recognize the multijoint hand movement. The main goal of this research is to detect and recover the human motion from the sequence of video images, and then to describe and understand the human hand movement behavior on this basis [1–2]. The visual analysis of the human hand movement can be applied to many fields, such as robot teaching and learning, human-computer interaction, virtual reality or three-dimensional animation [3]. At the same time, the visual analysis of human hand movement is a very challenging research topic, which involves image processing, computer vision, computer graphics, pattern recognition and artificial intelligence and other disciplines. In the past few decades, researchers at home and abroad have carried on a great deal of research around this subject. However, due to the inherent complexity of the project, the research results so far cannot meet the requirements of real-time, accuracy and robustness, and there is a certain distance from the practical application.

At present, some relatively mature mobile analysis systems in the market most need people to wear sensors or optical markers on the hand [4]. The sensor system (such as a data glove) acquires motion data by placing a sensor on a tracked object,

¹Guizhou Electronic Information Career Technical College, Guizhou, 550000, China

such systems can guarantee a certain accuracy, but the equipment is often expensive, require complex calibration steps, and it can impede the movement of the object being tracked. The optical marking system places the optical mark on the joint of the human hand, then these markers are tracked by the camera, but in the movement, blocking will cause some of the mark is not visible, therefore, the system needs manual post-processing of the captured data. In comparison, the unmarked motion tracking method of computer vision is a more natural, more applicable and non-contact method. With the rapid increase of computer hardware processing capacity and the popularization of digital video equipment, the unmarked visual analysis of manpower moving has attracted the attention of many researchers both at home and abroad because of its wide application prospect, which has gradually become a research focus in computer vision field.

2. Methods

2.1. Algorithm

One of the main problems of the standard particle filter algorithm is the use of state transition prior model $p(x_i | x_{i-1})$, which does not consider the latest observation z_i , as the important density function, so the importance of the particle sampling process is suboptimal. In the tracking process, the standard particle filter algorithm needs to collect a large number of samples in order to approximate the true posteriori probability density distribution of the system state. The sample set too small will produce sample poor phenomenon, reduce the estimation accuracy, and even lead to sample set divergence and estimate failure. The three-dimensional human motion tracking is a high-dimensional problem, in the premise of calculation, due to the extreme sparsity of particle sampling in high-dimensional space, it is impossible to use a finite number of particles to effectively express the true posteriori distribution of human hand-like disease, which can easily lead to tracking failure.

The Gaussian particle swarm optimization (PSO) algorithm is an improved PSO algorithm [5], which uses the Gaussian distribution to generate the velocity vector. Its convergence is better than that of the classical PSO algorithm. Its particle velocity and position update equation is as follows:

$$v_{k+1}^i = |\text{randn}| (p_k^i - x_k^i) + |\text{randn}| (g_k - x_k^i) \quad (1)$$

$$x_{k+1}^i = x_k^i + v_{k+1}^i \quad (2)$$

where $|\text{randn}|$ is a positive Gaussian random number that can be generated by the absolute value of the standard Gaussian distribution $N(0, 1)$.

Particle Swarm Optimization Particle Filter (PSOPF) algorithm [6] is an algorithm that integrates the PSO algorithm into PF and optimizes the sampling process of PF. In this paper, the PSOPF algorithm is applied to human motion tracking in high-dimensional state space. The Gaussian PSO algorithm is used to optimize the

matching error function $E(z, x)$. In the inter-frame state transition process, the $t - 1$ th moment convergence of the individual optimal position $p_{t-1, K}^i$ is to initialize the particles at time t

$$x_{t,0}^i = p_{t-1, K}^i + r \quad (3)$$

where $r \sim N(0, \Sigma)$ is the mean multidimensional Gaussian noise and Σ is the covariance matrix. Its diagonal elements are determined according to the maximum interface angle or displacement variation.

However, Gaussian PSO algorithm with the standard PSO algorithm by updating the global extreme and extreme values of the particles themselves can search for the optimal solution only when a better solution is encountered. Then, the extreme value will be updated, thus narrowing the search neighborhood of the particle and making it easy to converge. In the process of particle swarm pursuit of the best particles, as it is getting closer to the best particles, the speed is getting smaller and smaller, and the entire group gradually shows a strong convergence. Therefore, the algorithm is easy to fall into the local optimum in the middle and late stages of the search process, resulting in the premature convergence phenomenon. This problem is particularly acute for high-dimensional multimodal problems such as hand motion tracking. In this paper, two improved methods are used to overcome the premature convergence of the algorithm and improve the diversity of the particle to enhance the global search ability of the algorithm.

First, introduce the simulated annealing into Gaussian PSO; use the simulated annealing algorithm to improve the updating condition of the extreme value of the particle. It cannot only accept the optimal solution, but also accept the degenerate solution to expand the global searching range. It is given by the formula

$$p_{k+1}^i = \begin{cases} x_{k+1}^i & \text{if } r^i \min(1, \exp(-\Delta D/T_{k+1})), \\ p_k^i & \text{otherwise,} \end{cases} \quad (4)$$

where T_{k+1} is the annealing temperature of the $(k + 1)$ th iteration. The value of $T_{k+1} = \alpha T_k$, α being the cooling coefficient that lies in interval $(0, 1)$. In all the experiments described in this paper, the values of α are 0.8. Symbol ΔD is the particle distortion change defined as $\Delta D = 1/f(x_{k+1}^i) - 1/f(p_k^i)$, where $f(x_{k+1}^i)$ and $f(p_k^i)$ are the new particle fitness value and old best individual fitness value, respectively. In this paper $f(x) = p(z|x)$, that is, the fitness value $f(x)$ of the particle is calculated using the observation likelihood $p(z|x)$ defined by $p(z|x) \propto \exp(-\lambda_e \cdot E(z, x))$. Finally, r^i is a uniformly distributed random number from the interval $[0, 1]$.

Secondly, starting from the third iteration of Gaussian PSO, local randomization is performed on the corresponding dimension of the finger joint angle according to the method in [7]. More specifically, in each iteration process, after the particle position update calculation, the particle position is recalculated with a small probability, which is selected as uniform sampling in the corresponding dimension value range.

It is shown in the formula

$$x_k^{ij} = \begin{cases} U(x^{j,\min}, x^{j,\max}) & \text{if } \text{rand}^{ij} < \text{Pr} \\ x_k^{ij} & \text{otherwise} \end{cases} \quad (5)$$

Here, $x^{j,\min}$ and $x^{j,\max}$ are the minimum and maximum values defined by the j th dimension of the search space, respectively, while $U(x^{j,\min}, x^{j,\max})$ is a random number evenly distributed in interval $[x^{j,\min}, x^{j,\max}]$. Symbol $\text{rand}^{ij} = U(0, 1)$ is a random number evenly distributed over the interval $[0, 1]$. Finally, Pr is a probability wide value constant for the treatment of particles, in this experiment its value is 0.01.

In this paper, the modified PSOPF is used as the tracking algorithm to search the human hand and object state parameters in $32(26 + 6)$ -dimensional state space. In the particle filter framework, the convergence of the particle set is accelerated by optimizing the matching error of the Gaussian PSO, at the same time, using simulated annealing method to avoid the premature convergence of the particle, but canceling the local optimization in the process of randomization steps. Although the localized randomization method is suitable for tracking a variety of flexible movements individually, it does not apply to the tracking of hand-to-object interaction (such as human hand-crawling objects).

In the initial stage, due to the lack of time domain continuity information, this paper uses manual and object in their respective calibration positions to manually initialize the tracking process. The specific algorithm steps are as follows:

- Initialization: From the prior distribution of $p(x_{h-o,0})$ sampling N particles, the weights are $1/N$, which is expressed as $\left\{x_{h-o,0}^i, 1/N\right\}_{i=1}^N$.
- Particle state transfer: This process is an important sampling process. The particle initial position is acquired using (3). With the newest observing value, (1) and (2) are used to iteratively evolve the particle set. The iteration will drive the particle to the high likelihood region. The particle diversity and mature convergence is assured through (4).
- Weight update: The observation likelihood is used to update the particle weight $w_t^i \propto w_{t-1}^i p(z_t | x_{h-o}^i)$ and weight normalization. The maximum post-calibration is utilized to output the system state estimation value.
- Resampling: To avoid the degradation of particle weights, the sample set $\left\{x_{h-o,t}^i, w_t^i\right\}_{i=1}^N$ is resampled according to the weights. The new equal-weight sample set is $\left\{x_{h-o,t}^i, 1/N\right\}_{i=1}^N$.
- Is the judgment over? If yes, exit this algorithm, otherwise go to step 2.

2.2. Relevant models

This paper focuses on the interactive process between human hand and sphere. The method used in this paper is also applicable to the tracking of human hand

interaction with other objects.

After defining the state variable (hand-sphere variable x_{h-o}), the matching error is defined as

$$E(z, x_{h-o}) = \lambda_d E_d(z, x_{h-o}) + \lambda_s E_s(z, x_{h-o}) + \lambda_m E_m x_{h-o}. \quad (6)$$

The above equation shows that the matching error with the current observation input z is determined by the human hand motion state and object motion state. For the state transition model of human hands and objects, the first-order linear model is adopted in this chapter, and the multidimensional Gaussian noise is used as the disturbance.

3. Results and discussion

This experiment system is developed on the Visual Studio 2010 platform using open source cross platform 3D graphics engine Open Scene Graph (OSG) 3.0.0. The three-dimensional human hand and object model with DOF degrees of freedom nodes are loaded into the OSG. The control the movement of hands and objects is realized through `osgSim::DOFTransform`. In addition, in each iteration, the depth image of human hand and object model is generated by using Frame Buffer Object (FBO) in OSG, which is used to calculate the particle matching error and observation likelihood value in the algorithm.

In this paper, the experiments on the synthetic and real sequences are performed to verify the effectiveness of the hand-object tracking method. In all experiments, the improved PSOPF tracking method used in this chapter works with 60 particles, and for each image input, iterations are optimized 40 times. Experiments were run on an ordinary PU machine with dual-core Core 2 2.0 GHz CPU, 2.0GB of RAM and Nvidia GeForce 8400M GS GPU.

3.1. Synthesis of sequence experiments: Relevant models

Since it is not possible to obtain the real pose data directly from the sequence of images captured by the camera, this chapter uses a synthetic sequence with realistic pose data to further evaluate the algorithm quantitatively. The real value data for the synthesis sequence is the tracking result of the tracking system in the real sequence experiment, and the synthetic sequence of the human hand and the sphere is generated by the tracking result of the real sequence. The synthetic sequence is used as the input of the tracking system, and then for carrying out the experiments. Figures 1–7 show the results of tracking method proposed in this paper for a part of the tracking parameters and corresponding value of the comparison. The solid line depict the tracking results, while the dotted lines show the real values.

Figures 1-7 show the recognition results of human hand from a video frame by frame. The human hand captured in the video is permanently interactive with a sphere object. The sphere object works as an interference in the human hand recognition. When the palm moves along axis x , the actual movement and the recognition

results converge perfectly in Fig. 1, indicating that the method can keep a high degree of consistency with the real situation. In Fig. 2, the actual movement is compared with the recognition results as the palm moves along axis y . Figure 2 also shows very good convergence of the actual results and tracking results. Figures 3–5 show the recognition results of PIP (proximal interphalangeal), MCP (metacarpophalangeal), TM (trapeziometacarpal) joint movement measured in angles.

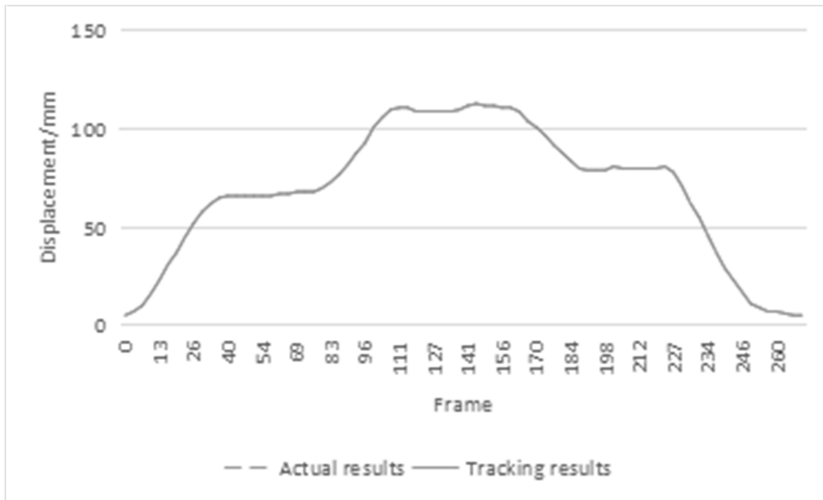


Fig. 1. Comparison of tracking results and real values of synthetic sequences between human hand and sphere: palm displacement along axis x

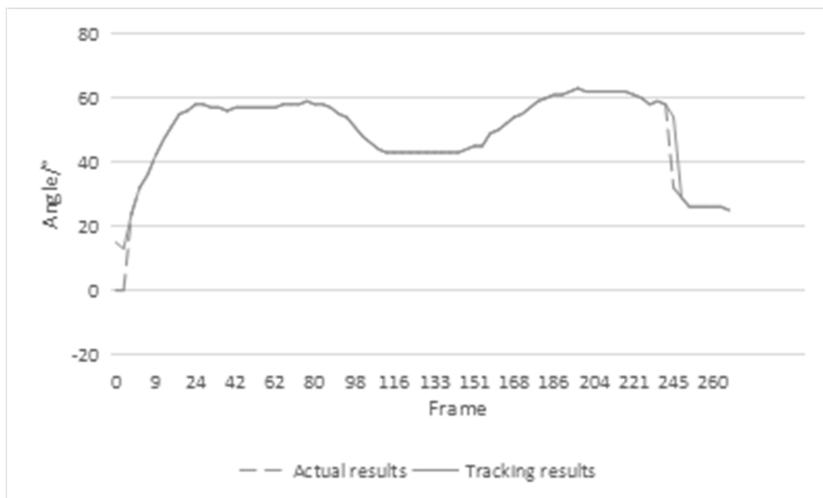


Fig. 2. Comparison of tracking results and real values of synthetic sequences between human hand and sphere: palm displacement along axis y

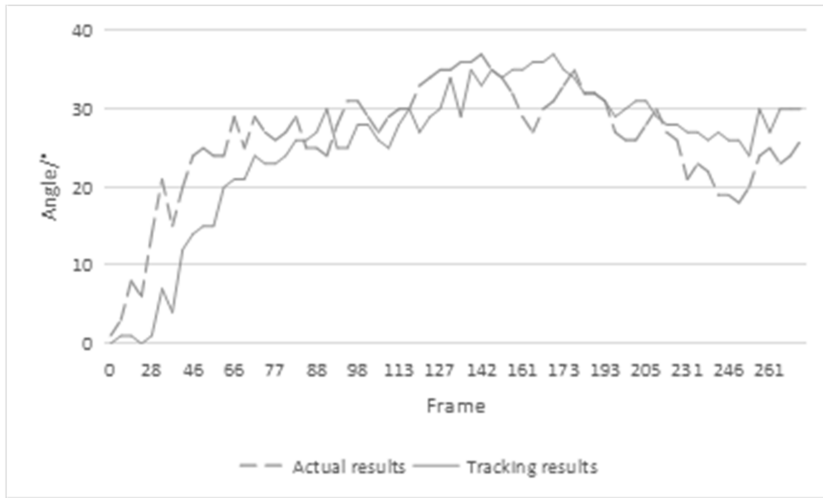


Fig. 3. Comparison of tracking results and real values of synthetic sequences between human hand and sphere: angle of ring finger PIP joint flexion



Fig. 4. Comparison of tracking results and real values of synthetic sequences between human hand and sphere: angle of thumb MCP joint flexion

4. Conclusion

Aiming at the difficulty of particle sampling in three-dimensional space, this paper integrates the swarm intelligence optimization method into particle filter, and using its powerful global optimization ability to improve the distribution of parti-



Fig. 5. Comparison of tracking results and real values of synthetic sequences between human hand and sphere: angle of thumb TM joint flexion

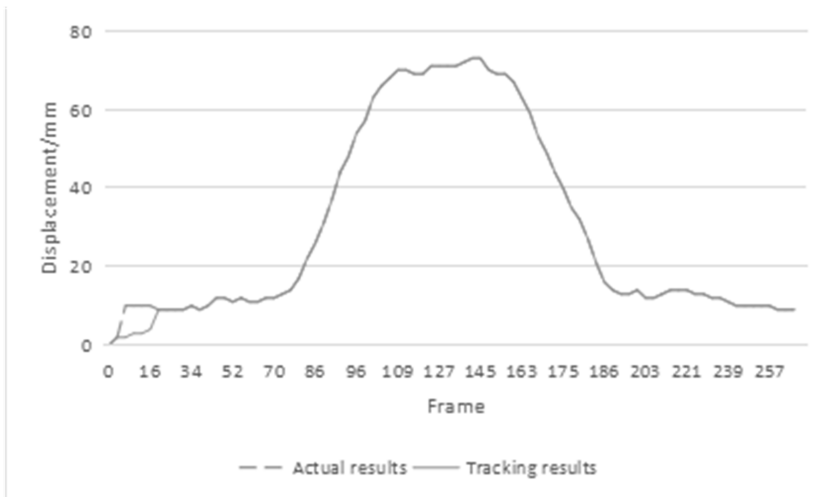


Fig. 6. Comparison of tracking results and real values of synthetic sequences between human hand and sphere: object displacement along axis x

cle filter samples, it proposes a specific three-dimensional hand tracking algorithm. This algorithm applies an existing Particle Swarm Optimization (PSO) particle filter algorithm to hand motion tracking in high-dimensional space, and in order to solve the problem of premature convergence in high dimensional-space, it uses simulated annealing and local randomization to improve the convergence of the algorithm. The improved algorithm can track the free movement of human hands and interaction between human and object.

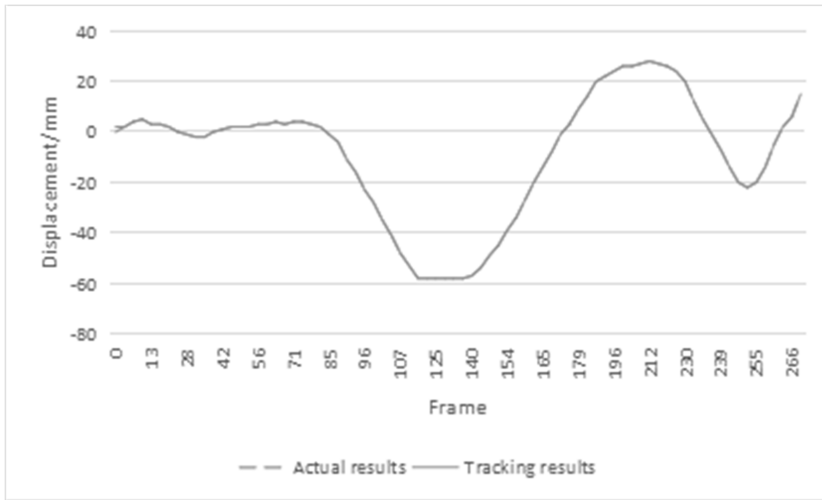


Fig. 7. Comparison of tracking results and real values of synthetic sequences between human hand and sphere: object displacement along axis y

Table 1 summarizes the results of the statistical analysis of the attitude parameters error on the whole sequence.

Table 1. Tracking error of synthetic sequences between human hand and sphere

Attitude parameter	Error mean	Standard deviation
Palm displacement along x	0.3453	0.2896
Palm displacement along y	0.6655	1.1481
Angle of ring finger PIP joint flexion	3.5181	2.5534
Angle of thumb MCP joint flexion	2.2100	1.8216
Angle of thumb TM joint flexion	0.7944	0.8104
Object displacement along x	0.6265	1.3522
Object displacement along y	0.3121	0.5192

References

- [1] M. PROTTER, M. ELAD: *Image sequence denoising via sparse and redundant representations*. IEEE Trans Image Process 18 (2009), No. 1, 27–35.
- [2] E. KALOGERAKIS, O. VESSELOVA, J. HAYS, A. A. EFROS, A. HERTZMANN: *Image sequence geolocation with human travel priors*. Proc. IEEE IC Computer Vision (ICCV), 29 Sept.–2 Oct. 2009, Kyoto, Japan, 253–260.
- [3] M. LINDERMAN: *EMG measured during controlled hand movement for biometric analysis, medical diagnosis and related analysis*. Patent US 8280503 B2, 2012.

- [4] B. J. GALVAN, A. S. MARCO, J. F. ROLIN, L. DELAUNEY: *NeXOS contribution to the adaptation of system analysis engineering tools for mature and reliable ocean sensors*. Proc. IEEE Sensor Systems for a Changing Ocean (SSCO), 13–17 Oct. 2014, Brest, France, 1–6.
- [5] X. ZHANG, P. WANG, J. C. XING, Q. L. YANG: *Particle swarm optimization algorithms with decreasing inertia weight based on Gaussian function*. Application Research of Computers 29 (2012), No. 10, 3710–3712.
- [6] T. KRZESZOWSKI, B. KWOLEK, K. WOJCIECHOWSKI: *Articulated body motion tracking by combined particle swarm optimization and particle filtering*. Lecture Notes in Computer Science 6374 (2010), 147–154.
- [7] T. YASUDA, K. OHKURA, Y. MATSUMURA: *Extended PSO with partial randomization for large scale multimodal problems*. Proc. World Automation Congress (WAC), 19–23 Sept. 2010, Kobe, Japan, 1–6.

Received November 16, 2016

A study on control system of electronic treadmill based on neural network theory

YUN MIAO¹

Abstract. The control system of electronic treadmill is researched on the basis of neural network theory so as to provide theoretic bases for the research and development of new electronic treadmill. Firstly, studies are carried out on the composition of brushless DC motor and its operating principle and neural network as well as PID control to establish mathematical model of motor and confirm the program for single closed loop speed regulation of motor and PID control method based on neural network. Secondly, hardware architecture is researched and designed according to the control needs of electronic treadmill. The whole hardware system is divided into main control board and function board with function board researched and designed. In succession, $\mu\text{C}/\text{OS-II}$, the embedded real time operating system is chosen as the target platform for product development and transplanted to the main control board. Finally, tests are made for the control system of the treadmill. It can be seen that, when the performance index of the speed of running belt meets no-load condition, the deviation is lower than 5% and when meeting load condition, the deviation is lower than 10%; the deviation of slope regulation is less than 5%. the deviation of heart rate is less than 5%. Control system of treadmill designed in the study can meet everything what the design requires.

Key words. Electronic treadmill, neural network theory, $\mu\text{C}/\text{OS-II}$, $\mu\text{C}/\text{GUI}$, PID control method.

1. Introduction

With the development of economy and improvement of living standard, people pay more and more attention to their health [1]. In the present modern life with rapid pace, the chances and places for people to doing physical labor and exercise are lessened, giving rise to the decreasing of the amount of exercise and people's subhealth. Doing exercise on electronic treadmill is unaffected by the limitation of weather and takes up small space, which solve problems about people's unwillingness to expose to bad air, insufficient exercising time and space. In addition, the price of electronic treadmill is acceptable, and general people can afford it. Scientific

¹North China University of Water Resources and Electric Power, Henan, 450000, China

researches show that running is the most effective and scientific aerobic exercise for people to keep health [2], which is vigorously advised in sports and medical filed. From the point view of kinematics, the posture of walking on treadmill are the same as that on ground. As walking on treadmill does not need a posture of stretching, users may feel it is easier to doing exercise on treadmill.

$\mu\text{C}/\text{OS-II}$ real time operating system is applied in the control system of electronic treadmill for the first time. On the basis that hardware and software architecture of the control system are confirmed, with with $\mu\text{C}/\text{OS-II}$ as the development platform, functions of electronic treadmill are realized on it [3], which provides a new way of thinking for the development of control system of electronic treadmill.

2. Literature review

Treadmill product has been updated for four generations in less than 40 years from the 1980s [4]. The popularity of embedded system overcomes such problems as large size and poor stability of PC terminal. Reference [5] proposes that streaming media technology can be introduced in control system of electronic treadmill. When runners are running, they can choose videos and audios to play. Reference [6] puts forward a adaptive control method that follows the speed of treadmill and can be used in the system of lower limbs rehabilitative robot. According to structure features of lower limbs rehabilitative robot, a force measuring device is adopted to test runner's acting force on treadmill. The acting force is also used to reflect the motion state of runners in real time and control the speed of treadmill. Tests on physical prototype show that this control method works in making treadmill follow and adapt to runner's speed. Reference [7] designs a adjustable speed treadmill based on the principle of computer vision gesture recognition, which collects gestures of runners through camera. Users can control the speed of the treadmill by making gestures in front of camera. References [8, 9] combine virtual reality technology with treadmill to provide a virtual sports ground and interactive entertainment functions for users, thus improving motion perception. In a word, electronic treadmill tends to be digital, intellectual and networked with more improved functions and it also develops more human [10].

3. Methodology

4. Control technologies of electronic treadmill

The brushless DC motor consists of motor body, electronic commutating device and rotor position detecting device [11]. DC motor is made up of stator and rotor. The armature of the general DC motor is mounted on the rotor and the main pole is on the stator, as shown in Fig. 1.

We established a mathematical model for the three-phase and six-state brushless DC motor. The assumed conditions are as follows [12]: the effect of gear slot, commutation process and armature reaction is ignored; three-phase winding is completely

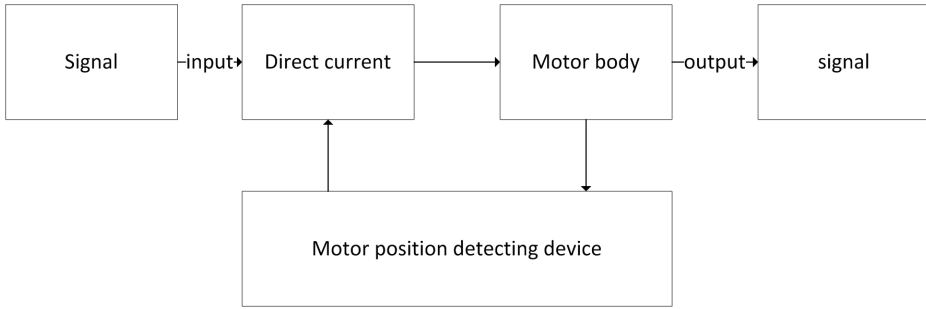


Fig. 1. Schematic diagram of brushless DC motor

symmetrical, the air gap magnetic field has the form of a square wave, and the distribution of stator current and rotor magnetic field is symmetrical; the distribution of armature winding on the surface of stator is uniform and continuous; magnetic circuit is not saturated and eddy currents and hysteresis loss are ignored. The mathematical model of brushless DC motor is composed of voltage, torque and motion equation [13]. When each switch and conduction pressure drop of anti-parallel diode is ignored, the voltage equation can be expressed in the form

$$\begin{bmatrix} u_a \\ u_b \\ u_c \end{bmatrix} = \begin{bmatrix} R_a & 0 & 0 \\ 0 & R_b & 0 \\ 0 & 0 & R_c \end{bmatrix} \cdot \begin{bmatrix} i_a \\ i_b \\ i_c \end{bmatrix} + \frac{d}{dt} \begin{bmatrix} L - M & 0 & 0 \\ 0 & L - M & 0 \\ 0 & 0 & L - M \end{bmatrix} \cdot \begin{bmatrix} i_a \\ i_b \\ i_c \end{bmatrix} + \begin{bmatrix} e_a \\ e_b \\ e_c \end{bmatrix}, \quad (1)$$

where u_a , u_b and u_c refer to voltages of three-phase stator, R_a , R_b and R_c refer to resistances of three-phase stator winding, i_a , i_b and i_c refer to currents of three-phase stator, and e_a , e_b and e_c refer to induced back electromotive force. Finally, symbol L denotes the inductance of each phase winding and M refers to mutual inductances of the phase windings.

Current and rotor magnetic field in each phase of winding of the brushless DC motor interact with each other and produce electromagnetic torque

$$\frac{T_e}{\Omega} = \frac{e_a i_a + e_b i_b + e_c i_c}{\Omega}. \quad (2)$$

Here, P denotes the electromagnetic power of the motor and Ω stands for the mechanical angular velocity of rotor.

From (2), the equation of electromagnetic power is

$$P = e_a i_a + e_b i_b + e_c i_c = 2E_s I_s, \quad (3)$$

where E_s is the overall induced back electromotive force of the brushless DC motor and I_s is the overall current of the three-phase stator.

From (2), we can also obtain the motion equation in the form

$$J \frac{d\Omega}{dt} = T_e - T_L - B\Omega, \quad (4)$$

where J refers to rotor inertia, $d\Omega/dt$ refers to angular acceleration of rotor, B denotes the damping coefficient and T_i stands for the load torque.

The PID control principle of K_P , K_I , and K_D consists in self-learning established on the basis of BP neural network: the output state of neural network is in line with three above mentioned parameters of PD controller. By making use of self-learning ability, neural network constantly adjusts weighing factor, and its stable state is consistent with the parameter of PID controller under the optimal control law.

BP neural network has the ability to approximate any nonlinear function whose structure and learning algorithm are simple and clear. It is easy to know P, I, D parameters under the optimal control law by adopting the self-learning property of network. Typical incremental digital PID control algorithm is

$$\begin{aligned} \Delta u(k) &= u(k) - u(k-1) = \\ &= K_P \Delta e(k) + k_I e(k) + K_D [e(k) - 2e(k-1) + e(k-2)], \end{aligned} \quad (5)$$

where k denotes the index of the step.

4.1. Hardware system of electronic treadmill

The hardware system of electronic treadmill consists of main control board and function board. The main control board is in charge of commanding works of each parts and it functions in controlling the touch screen, playing and recording audios as well as recording motion data of users. It also extends interface to send control signals to function board. Function board mainly works in driving speed motor and lift and drop motor and detecting heart rate.

Mini 2440 development board, from Friendly ARM, is used as the main control board in the hardware system aiming to save the underlying development time. The development board has abundant resources meeting function needs of the main control board. And external extended port on the development board can be used to control signals for function board. S3C2400 is adopted as the main controller, a microprocessor chip generally applied in handheld devices with low cost, consumption and high performance or other electronic products. Audio circuit is designed for the purpose of playing background musics and related warning tones, which employs solution of embedded audio system based on IIS bus. As a human-computer interaction interface, the touch screen can be used as the display interface, and operates the control system. It shows the current speed, slope, heart rates, distance and calorie consumption and other parameters. Users also can set parameters on it, such as speed and slope. SD card is applied in SD card interface circuit, which is a multi-functional memory card widely used in portable devices based on semiconductor flash memory technology.

Function board includes modules such as speed motor driving, lift and drop

motor driving and heart rate detecting. It functions in adjusting speed and slope and detecting heart rate controlled by control signals from the main control board. The main control board and function board are connected through extended port, where control signals of the main controller and feedback signals of each modules in function board transfer.

Adjusting speed is one of the basic function of treadmill, so speed adjustment is one of the most important part of brushless DC motor in treadmill control system. A special chip for regulating speed is chosen when controlling rotary speed of motor, which simplifies hardware circuit and achieves higher control accuracy. Hand heartbeat detection module TM998 is adopted as heart rate detection device which works by using the ECG principle [14]. Heart beatings produce electrophysiological changes and conduct to body surface. Heart beating signals can be obtained through laying electrodes on skin and measuring potential differences. Arunning asynchronous motor drive with single phase capacitor is used to adjust the running slope. To increase or decrease the running slope can be achieved by controlling the positive inversion of motor. The lift and drop motor is actually a two-phase motor, which produces elliptical rotating magnetic potential in air gap of the motor when it performs, dragging the rotor to rotate. Motor leads to red, white and black lead wires. Windings can be switched by using electric relay. The capacity of the actual selected relay is 250 AC/3 A and coil voltage is 12 VDC.

4.2. Software system of electronic treadmill

$\mu\text{C}/\text{OS-II}$ is a multitask real time kernel provided by Micrium which can be applied in many microprocessors. Main features of it are: source code is open; it can be transplanted, cured and cut; it has preemption and can manage 64 tasks at most; function call of most $\mu\text{C}/\text{OS-II}$ and function time of service are certain; ever task has its stack space. The system provides many kinds of service such as signal quantity, mutual exclusion semaphores, event flag group, message mailboxes and message queue, which is stable and reliable and can be managed in interruption.

$\mu\text{C}/\text{OS-II}$ can just read and write processor register through assembler language, codes related with register hardware, thus, is written in assembler language. If $\mu\text{C}/\text{OS-II}$ is to be successfully transplanted, the compiler and register need to meet some preconditions. The compiler is required to create reentrant code. Compiler ADS is used in the development, which meets the requirement. Processor ARM9 is adopted and requirements it meets are as follows [15].

1. The processor supports interruption and can produce timer interruption in the frequency range of 10 Hz–100 Hz.
2. CPSR in the core of ARM processor and global interruption disable bit in the register can manage the global interruption. Its state can be changed to enable and disable interruption through the use of C language.
3. The processor supports data storage and hardware stack.
4. Assembler command `stmfd` in ARM processor can push all registers into the

stack and command `ldmfd` makes all register pop from the stack.

5. Transplanting can be completed just by revising codes `OS_CPU.H`, `OS_CPU_A.S`, `OS_CPU_C.C` [16] related with the processor.

The task is of three basic characteristics, namely, dynamic, independence and concurrency. When tasks are assigned, comparisons are made among all feasible assignment plans, from which the optimal plan is selected to achieve the expected goal. The method of assigning tasks is as follow[16]: Functions relative with IO device are set as independent tasks, which is a kind of device-relied task. For a function, the assigned key or emergent functions should be realized respectively by an independent task (or ISR) or independent higher priority task(or ISR), and the rest of which can be completed by another task. The two tasks synchronize and exchange information with each other by using the communication mechanism. The emergent and key task should be considered as a emergent task. Data processing function which costs much more time can be combined into a lower priority task. Functions, which are closely connected, triggered by the same event, completed in a certain order and has the same execute cycle, should be integrated into a task so as to conglomerate functions and exempt event and time distribution mechanism and synchronous relay communication.

As a graphic support system in embedded applications, μ C/GUI [17] provides GUI for all applications adopting LCD graphic display, has high efficiency and is independent from the processor and LCD controller, which also simplifies the design process of LCD and shortens production time. It can be compatible with single or multiply tasks environment, special operating system or any RTOS with any commercial nature, whose production type is source code of C language.

μ C/GUI can be applied in S3C2440, but a series of configurations need to be carried out on it before use. μ C/GUI is transplanted to modify head documents `GUIConf.h`, `GUITouch Conf.h` and `LCDDConf.h` in the content of `\Config` and C documents `GUI_X_u COS.candLCDWin.cin` the content of `GUI\LCDDriver`.

5. Result analysis and discussion

5.1. Hardware debugging

Problems appearing in the process of hardware debugging are mainly from motor driver chip LB11820M. Because of deficient knowledge about features of LB11820M, the allowed voltage range of monitoring end LVS protecting low voltage is ignored. The working voltage inserted in LVS end is less than 3.6 V and as a result, the motor halts when it is started for a while. After related analyses and investigations, the problems is found out and settled down by changing voltage regulator tube in the LVS end.

5.2. Software debugging

After hardware debugging is accomplished, software debugging is to be carried out. The most critical drivers are: driver of speed motor, lift and drop motor and heart rate detection. Speed motor is the brushless DS motor, whose operating condition can be evaluated through its input driving waveform and input of correspondent Hall sensor. Driving module of lift and drop motor is tested. When control command is signaled to control running slope from control board, the electric relay can correctly pull and disconnect operation according to operation demand. Two electrodes of heart rate module are respectively held by hands and oscilloscope is connected to the output end of TM998 in order to observe output pulse waveform.

5.3. Tests on performance of the complete motor

The system works at the speed of 1 km/h when it begins to operate. Step speed regulation is tested at first at the increasing speed from 1 km/h to 20 km/h and later decreasing speed back to 1 km/h. It can be observed that the speed of running belt is changing with changing demands from main board. Speed direct shortcut is, in the following, tested. Low, middle and fast speed shortcut is pressed in order and another same test is carried out in a converse order. It is observed that the speed of running belt is slowly changing to the set speed. Table 1 shows the record of tests on the speed of treadmill.

Table 3. Record of speed test

Set speed (km/h)	Speed of running belt (no-load, km/h)	No-load deviation	Speed of running belt (load, 100 kg, km/h)	Load deviation
1.0	0.99	-1.0%	0.95	-5.0%
3.0	2.88	-4.0%	2.90	-3.3%
6.0	5.78	-3.7%	5.73	-4.5%
9.0	8.65	-3.9%	8.51	-5.4%
12.0	11.48	-4.3%	11.39	-5.1%
15.0	14.33	-4.5%	14.24	-5.1%
18.0	17.28	-4.0%	17.16	-4.7%
20.0	19.19	-4.1%	19.06	-4.7%

From Table 1, it can be seen that when the performance index of the speed of running belt meets no-load condition, the deviation is lower than 5% and when meeting load condition, the deviation is lower than 10%. In the testing process, if speed changes suddenly, the motor should be stopped and checked. From what are tested, it is known that both hardware and software of the speed motor are correct.

The range of slope regulation is $0^{\circ} - 26^{\circ}$ and uniform quantization is 0–13, namely 14 grades with 2 degrees in each grade. The slope can be adjusted in grades and grades are 3, 6, 9 and 11. When the system is restarted, the running slope is always set to grade 0. When the slope adjustment is tested in grades, it is adjusted from grade 0 to 13 and back to grade 0. It can be seen that the slope changes according to changing demands. When the test is made on slope shortcut, direct shortcuts are pressed from the low to the high and in the converse order, and the running slope is slowly changing to the set one. Test record of typical slope is shown in Table 2.

Table 2. Record of slope test

Grade	Set slope ($^{\circ}$)	Slope measurement ($^{\circ}$)	Deviation
0	0	0	0%
3	6	5.9	-1.6%
6	12	11.7	-2.5%
9	18	17.4	-3.3%
11	22	21.5	-2.3%
13	26	25.6	-1.5%

The test on heart rate is conducted as heart rate monitor is the reference standard. Metal electrode is held by two hands, and heart rate display window in the touch screen shows the current value of heart rate. When indication of heart rate monitor is up to the value needing to be recorded, value displayed in the heart rate display window of the touch screen is read.

Table 3. Record of heart rate test

Heart rate reading	Show value	Deviation
80	82	+2.5%
100	103	+3.0%
120	117	-2.5%
140	137	-2.1%

Table 3 indicates that the deviation of heart rate is less than 5%.

6. Conclusion

According to the current development situation of electronic treadmill combining with multi-disciplinary knowledge and technologies and the trend of digital intelligence, for the first time, $\mu\text{C}/\text{OS-II}$ system is introduced in software system of electronic treadmill control system, which is considered as a new attempt. It turns out that, when the performance index of the speed of running belt meets no-load condition, the deviation is lower than 5% and when meeting load condition, the deviation is lower than 10%; the deviation of slope regulation is less than 5%. the

deviation of heart rate is less than 5%. Control system of treadmill designed in the study can meet everything what the design requires.

References

- [1] E. GILBERTHORPE, E. POPYRAKIS: *The extractive industries and development: The resource curse at the micro, meso and macro levels*. The Extractive Industries and Society 2 (2015), No. 2, 381–390.
- [2] K. J. REID, K. G. BARON, B. LU, E. NAYLOR, L. WOLFE, P. C. ZEE: *Aerobic exercise improves self-reported sleep and quality of life in older adults with insomnia*. Sleep Med 11 (2010), No. 9, 934–940.
- [3] K. SOGA, T. SHISHIDO, R. NAGATOMI: *Executive function during and after acute moderate aerobic exercise in adolescents*. Psychology of Sport and Exercise 16 (2015), No. 3, 7–17.
- [4] J. J. DALY, J. ZIMBELMAN, K. L. ROENIGK, J. P. MCCABE, J. M. ROGERS, K. BUTLER, R. BURDSALL, J. P. HOLCOMB, E. B. MARSOLAIS, R. L. RUFF: *Recovery of coordinated gait: Randomized controlled trial of functional electrical stimulation (FES) versus no FES, with weight-supported treadmill and over-ground training*. Neurorehabil Neural Repair 25 (2011), No. 7, 588–596.
- [5] R. STOJANOVIC, S. KNEZEVIC, D. KARADAGLIC, G. DEVEDZIC: *Optimization and implementation of the wavelet based algorithms for embedded biomedical signal processing*. Computer Science and Information Systems 10 (2013), No. 1, 503–523.
- [6] W. CUI, F. LI: *An adaptive speed control method for running machine in lower extremity rehabilitation robot system*. Modern Manufacturing Engineering (2013) No. 9, 30–34.
- [7] L. V. NGUYEN-DINH, A. CALATRONI, G. TRÖSTER: *Robust online gesture recognition with crowdsourced annotations*. Journal of Machine Learning Research 15 (2015), No. 1, 3187–3220.
- [8] T. NING, H. B. MA, L. HUO, F. ZHAO: *Virtual environment interactive system of treadmill*. Proc. IEEE Fourth International Conference on Information and Computing, 25–27 April 2011, Phuket Island, Thailand, 240, No. 5, 933–939.
- [9] H. HU, Y. CUI, B. X. HUANG: *Game system of treadmill based on video capture*. Proc. IEEE/ACM IC Cyber, Physical and Social Computing & Computing and Communications (CPSCom), 18–20 Dec. 2010, Hangzhou, China, 836–839.
- [10] A. J. STEVENSON, S. S. GEERTSEN, T. SINKJR, J. B. NIELSEN, N. MRACHACZKERSTING: *Interlimb communication following unexpected changes in treadmill velocity during human walking*. Journal of Neurophysiology 113, (2015), No. 9, 3151–3158.
- [11] J. H. PARK, J. H. CHANG, G. H. JANG: *Development of the starting algorithm of a brushless DC motor using the inductance variation*. J. Korean Society for Precision Engineering 17 (2000), No. 8, 157–164.
- [12] S. SONG, Y. XU, H. TIAN, X. GONG: *Design and simulation of dual rotor permanent magnet brushless DC motor*. Proc. IEEE International Conference on Electrical Machines and Systems (ICEMS), 22–25 Oct. 2014, Hangzhou, China, 1591–1595.
- [13] C. S. R. REDDY, M. S. KALAVATHI: *Improved performance of a novel SMC-fuzzy controller for DTC brushless DC motor drive for precise speed regulation*. Proc. IEEE Ninth International Conference on Power Electronics and Drive Systems, 5–8 Dec. 2011, Singapore, 873–880.
- [14] X. X. CAO, S. Q. ZHU, Z. P. CUI: *Control system of intelligent treadmill based on sensor application technology*. Transducer and Microsystem Technologies 2 (2011), 97–100.
- [15] G. SUN, F. S. NAME, B. SHENG: *Performance test of an embedded real-time operating system based on a new high-security network computer*. IJ Digital Content Technology and its Applications 4 (2010), No. 8, 252–259.

- [16] L. YUAN, G. ZHANG, H. GAO: *Implementation of a multifunction black-box for tower crane based on ARM and $\mu C/OS-II$* . Proc. IEEE World Congress on Intelligent Control and Automation (WCICA), 25–27 June 2008, Chongqing, China, 7681–7685.
- [17] Y. LIU, X. J. WANG, X., W. KONG, C. C. ZHOU: *Touch screen display design based on UCGUI*. Chinese Journal of Liquid Crystals and Displays 5 (2014), 739–744.

Received November 16, 2016

Key technology simulation of equipment anomaly detection based on image processing

BAOYING LI¹, JIANGUANG QI¹

Abstract. With the deepening of automation of electric network management in our country, more and more substations are equipped with video monitoring system and various alarm systems to realize unattended operation. Therefore, the equipment images collected by the monitoring system are processed, and the equipment anomaly is fast and accurately detected by the monitoring images for early warning of potential hazards, which has an important practical value to the safe operation of the power system. The related algorithms of the image processing are applied to the substation electrical equipment image to analyze and study the characteristics of images when the electrical equipment is abnormal and the related detection techniques and methods. At the same time, a detection method of the power transformer oil leakage is proposed. We first use the difference method on the sample images and monitoring images to get the abnormal region, and the noise of it will be eliminated and it will be segmented. Then the H-S color histogram of the abnormal region corresponding to the sample image and the monitoring image is extracted. The oil leakage condition is detected by observing the change of the gray-brown part of the H-S color histogram. Through experiments, we find that this method can more accurately detect the oil leakage anomalies of the transformer.

Key words. Image processing, equipment anomaly, color histogram.

1. Introduction

The unattended operation of substation has become the trend of power system development, and the electric power departments around the country have basically realized the functions of "four remote" (remoter metering, remote signaling, remote control and remote regulation). However, for the status of fire, the state of the disconnecting link, the oil leakage of the transformer and other equipment anomaly, the monitoring of abnormal conditions is "four remote" cannot be achieved, therefore, remote sensing system will emerge as the times require, it is necessary supplement

¹School of Information Science and Engineering, Dalian Polytechnic University, Dalian, 116034, China

for the unattended substation. Due to the complexity and technical limitations of the equipment anomaly detection process, traditional algorithms are often used to detect the abnormalities of equipment, which often require a lot of manpower and financial costs, and the collected image of the abnormal parts cannot be identified, which cannot ensure the reliability of the results, and then a satisfactory test results cannot be obtained.

Based on image processing, we present an equipment anomaly detection method. The H-S color histogram is extracted by denoising and segmenting the abnormal region of the sample image and the monitoring image. It is found that this method can detect the oil leakage abnormality of the transformer more accurately and realize the effective anomaly detection of the transformer equipment to ensure the accuracy of the detection and meet the actual demand of the equipment anomaly detection automation.

2. Summary

The application of image processing in the monitoring system is also called intelligent video surveillance. It uses image processing, computer vision and pattern recognition, etc., in the case of almost no human intervention, to analyze the image sequence by using the correlation method of the moving target detection in image processing technology to extract the moving target, and then analyzes and predicts to the behavior of the moving target in the images on the basis of following and recognition [1]. Compared with the traditional monitoring system, the main advantage of intelligent video surveillance system is lies in its "intelligence", simply, the intelligent video surveillance system instead of the human eye in a sense. The computer can help to complete a series of tasks through the analysis and judgment of the collected images sequence to greatly reduce the burden on people, and improve the recognition efficiency [2].

With the widely using of video technology and infrared imaging technology in this area, the image processing technology in power system applications become increasingly widespread. For the substation, the main content of video surveillance includes the detection of moving objects, on-site smoke, flames, water, gas and other unusual circumstances. In some research abroad proposed that two matching algorithms are used to identify the casing of the power transformer, and the correlation between the template image and the image to be matched is calculated to determine the matching. In order to improve the speed of matching, two matching strategies are proposed: one is rough, and the other is exact match, but this algorithm has some limitations, the matching image and template image must be the same size and the same direction, and it will fail when the image is zoomed or there is jitter or rotation in the camera acquisition.

With the higher degree of the scale and automation of modern industrial production, the requirements of equipment anomaly detection technology are ever higher. In the production process, the equipment failure will cause unpredictable hazards, thereby affecting production efficiency. Therefore, in-depth exploration of equipment anomaly detection has become a hot research topic in this field [3]. At present, the

traditional method of equipment anomaly detection mainly includes optimization method based on machine learning [4]. Because the effectively improvement of the key technology of the equipment anomaly detection system can improve the detection rate of the equipment, reduce the detection time-consuming and avoid the harm caused by the fault to the production. Therefore, it has been paid close attention by relevant experts and scholars, and has very broad development potential [5].

3. Methods

In the unattended substation, power transformers as a common and major equipment, its operating conditions must be monitored timely. When abnormal conditions happen, the corresponding alarm should be given. The accuracy of the method that detect the transformer will have abnormal conditions by detecting the composition of the gas should be improved. When the gas composition changes, it does not necessarily indicate the occurrence of oil spills; and the method of detecting oil droplets in the water method is not applicable to the detection of oil leakage of power transformer. Taking into account the color of the power transformer oil is generally taupe, you can observe the abnormal characteristics of the oil leakage from the perspective of the image, and the abnormal area of the gray level will appear in the surface of the transformer compared with the normal condition, and the color of the abnormal area is taupe, and the shape of the abnormal region is different with the different parts of the oil spill. So the abnormal of the transformer only can be detected by extracting the color characteristics of abnormal areas. Based on this idea, a color histogram-based transformer oil leakage detection method is proposed. Firstly, the abnormal region is detected, and the abnormal region is denoised. Then, the color histogram of the abnormal region of two images is compared. When the taupe part has large changes, the transformer has oil spill.

RGB color space is a cube, and the origin corresponds to black, the vertex farthest away from the origin corresponds to the white. In this model, the gray-scale values from black to white are distributed over the line connecting the origin to the vertices furthest from the origin. The rest of the points in the cube correspond to different colors, and can be represented by vectors from the origin to the point. So each color can be represented by a point in colorized cube in RGB space.

HSV color space is a color space based on human visual characteristics. Parameter H represents color information, that is, the location of the spectral color, the parameter is expressed as an angle, red, green and blue are separated by 120°, the difference of the complementary colors respectively is 180°. Purity S is a proportional value, ranging from 0 to 1, and it represent the ratio between the purity of the selected color and the maximum purity of the color, when $S = 0$, there is only gray. Symbol V represents the bright degree of the colors, ranging from 0 to 1. It is not directly related to light intensity. Unlike the RGB color space, the coordinate system of the HSV color space is a cylindrical coordinate system, but is generally represented by a hexcone. HSV color model is a uniform color space, using a linear scale, and the distance of the color perception is proportion to the Euclidean distance of HSV color model coordinates. The R , G and B values (in the interval

[0,255]) at any point in the RGB space can be converted to the HSV space to obtain the corresponding values of H, S and V, and the conversion formula is as follows:

$$H = \left\{ \begin{array}{l} \arccos \left\{ \frac{(R-G)+(R+B)}{2\sqrt{(R-G)^2+(R-B)(G-B)}} \right\} B \leq G \\ 2\pi - \arccos \left\{ \frac{(R-G)+(R+B)}{2\sqrt{(R-G)^2+(R-B)(G-B)}} \right\} BG \end{array} \right\}, \quad (1)$$

$$S = \frac{\max(R, G, B) - \min(R, G, B)}{\max(R, G, B)}, \quad (2)$$

$$V = \frac{\max(R, G, B)}{255}. \quad (3)$$

The global summed histogram is based on the color value as the abscissa and the frequency of the color accumulation as the ordinate. Therefore, the accumulated histogram H of the image is defined as:

$$\bar{H} = \{ \bar{h}[c_1], \bar{h}[c_k], \dots, \bar{h}[c_k] \mid 0 \leq \bar{h}[c_k] \leq 1 \}. \quad (4)$$

where $\bar{h}[c_k] = \sum_{c_i \leq c_k} h(c_i)$ represents the cumulative frequency of pixels in c_i to c_k colors, and n denotes the number of quantized colors. In the global cumulative histogram, the adjacent colors are relevant on the frequency.

In the process of converting the RGB color space to the HSV color space, H , S , and V are usually quantized with non-equally spaced, and the hue H , saturation S , and luminance V are divided into eight, three and three, respectively. In the later experiment, we find that the effect of quantization detection is not very good. So, we divide the H space quantization into 16 parts, the saturation S is divided into 4 parts, and the brightness V is divided into 4 parts. Since the hue and color saturation components are closely connected to the way the human perceives the color, only the intuitive color needs to be considered here, the luminance information is temporarily ignored, and only the H component and the S component are taken into account. Since the H component has 16 equal parts, and the S component has 4 equal parts, so the combination of them is 64 kinds. The characteristics of its color is summed up and converted to the RGB model and observed with the naked eye, we can find that the color of the brown part of the color is in the seventh group, but in fact, because the degree of oil spill is different, the color will appear a certain deviation, so the scope of consideration is extended, and the gray-brown of the 7–14 groups is similar, their information are also considered and tested. So the follow-up detection can detect the color histogram information changes of 7–14 groups to determine the oil leakage anomalies of the transformer. Figure 1 is flow chart of the transformer oil leakage detection based on the color histogram.

The specific algorithm is as follows:

1. The sample image and the monitoring image are grayed separately to obtain the difference image.
2. Abnormal areas will be detected and the small particles noise is removed by

morphological open operation.

3. The sample image and the monitoring image will be converted into the HSV space, and the H-S color histogram of each abnormal area detected by (2) will be done.
4. The change of the number of the pixels in the 7–14 groups which belongs to taupe in the HS color histogram is determined. When the difference value of the data of the monitoring image and the sample image will be a certain value (it is 75 in this paper), it can be considered as abnormal oil leakage anomalies in abnormal area.

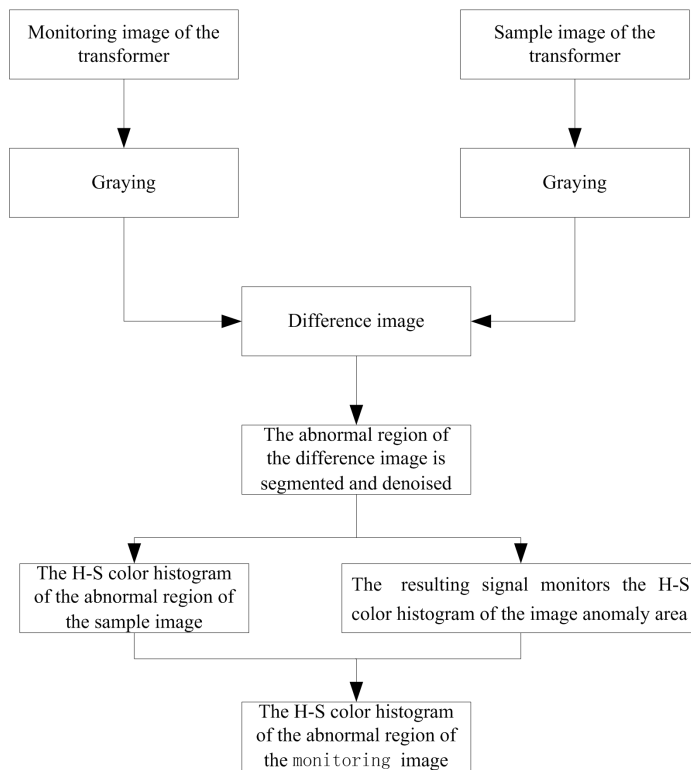


Fig. 1. Transformer oil leakage detection flow chart

4. Results

Three groups of 420×420 pixels of the picture are used to simulate in MATLAB 8.5 environment to verify the effectiveness and correctness of the algorithm, in which the oil pillow part of the transformer occurred abnormal oil leakage in pictures of two

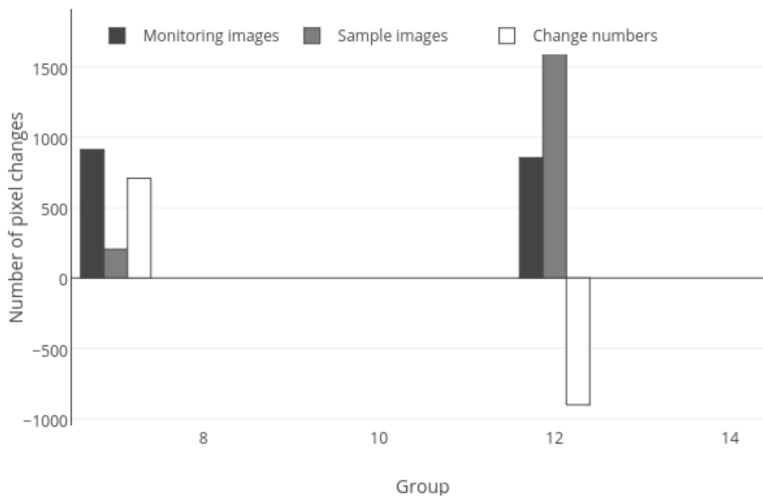


Fig. 2. Number of pixel changes in 7–14 group

groups. The detection results of oil leakage occurred in the transformer oil pillow part are as follows

From Fig. 2, we can see that the pixels of HS color histogram of the 7th and 12th group change greatly. As the specific situation of transformer oil leakage is uncertain, so the group where the taupe of the HS color histogram is located should be expanded. The color of the group 7 in Table 1 is similar to the color of the oil leakage zone. There are negatives in 12th groups, and the reason for this is that the data of the color in the 12th group in the sample image are more, and the color of the 7th group in the monitoring image after the oil leakage covers it.

Table 1. The number of pixels in groups 7 to 14

Group	Monitoring images	Sample images	Change numbers
7	912	204	708
8	0	0	0
9	0	0	0
10	0	0	0
11	0	0	0
12	853	1754	-901
13	0	0	0
14	0	0	0

5. Discussion

From the above experimental results, we can see that this method can detect the transformer oil leakage anomalies more accurately. From Table 1, we can find that the number of pixel changes have negative in the color group where the brown color

is located. This is because the colors before and after the oil spill are likely to be close to each other. A certain group or several groups of pixels will inevitably cause reduction of pixels of other groups. Only the change of the group whose number of pixels is positive is detected here, and the detection result is not affected.

The disadvantage of this method is that when the detection interval is too long, the detection image relative to the rust of the sample image transformer part may fail, and the corresponding alarm is given here when the processing results of the transformer monitoring image of the unattended substation meet the above conditions. The staff needs to do further determine for this anomaly and the extent of the oil leakage.

6. Conclusion

We firstly denoise and segment the sample image and the monitoring image. The original image is transformed from the RGB space to the HSV space based on the visual feature, and then the corresponding HS color histogram of the anomaly area of the sample image and the monitoring image is extracted. The oil leakage abnormality of the transformer is detected by observing the change of the gray-brown part of the HS color histogram. It is found through the experiment that this method can detect the oil leakage abnormality of the transformer more accurately. We proposed a new HS color histogram-based anomaly detection method for oil leakage in power transformers. It is found that this method can detect the abnormal oil leakage of transformer effectively and realize the effective anomaly detection of transformer equipment to ensure the accuracy of detection. At the same time, it meets the actual needs of equipment anomaly detection automation.

References

- [1] M. D. ABRAMOFF, P. J. MAGALHAES, S. J. RAM: *Image processing with imageJ*. *Biophotonics International* 11 (2004), No. 7, 36–42.
- [2] H. FOROUGHI, B. S. ASKI, H. POURREZA: *Intelligent video surveillance for monitoring fall detection of elderly in home environments*. Proc. IEEE International Conference on Computer and Information Technology (ICCIT), 24–27 Dec. 2008, Khulna, Bangladesh, 219–224.
- [3] M. KASKA, O. MARECEK: *Utilization of data communication according to the IEC61850 standard for nuclear power plant electrical equipment testing*. *J. Energy and Power Engineering* 8 (2014), No. 4, 765–769.
- [4] M. MOSBAH, B. BOUCHEHAM: *The influence of the color model on the performance of a CBIR system based on color moments*. *J. Communication and Computer* 11 (2014), No. 3, 266–273.
- [5] J. CARREIRA, C. SMINCHISESCU: *CPMC: Automatic object segmentation using constrained parametric min-cuts*. *IEEE Trans. Pattern Analysis and Machine Intelligence* 34 (2012), No. 7, 1312–1328.

Underwater robots detection based on image segmentation¹

JISONG BAI², LONGJIE PANG², QIANG ZHANG²

Abstract. The segmentation and detection technology of underwater image under the condition of lighting environment is analyzed. Firstly, the basic process of image segmentation based on grey scale is proposed. Secondly, on the basis of the traditional grey processing and Hough transform circle detection method, we propose improvements of the image segmentation method based on improved grey processing, multi-threshold segmentation method based on sliding window, and traditional point Hough transform circle detection method. Finally, the methods proposed in the paper are tested according to contrast experiments under uniform light and uneven illumination and also contrast experiments of circle detection method before and after improvement. In the contrast experiment under uniform illumination, the segmentation results based on the grey method indicate that indexes FOM (Figure of merit), UM (Uniformity measure) and GC (Gray-level contrast) are higher than those of the image segmentation results after grey processing of (National Television System Committee) method. In the contrast experiment under uneven illumination, multi-threshold segmentation of sliding window method can reduce the error caused by the similar grey values and refine the difference among the grey values around the target area. In the contrast experiments of circle detection method before and after improvement, the improved method can completely eliminate image edge distortion. Compared with the traditional technology, the improved method is more effective in underwater light image detection.

Key words. Image segmentation, target location, underwater robot, illumination image.

1. Introduction

Accounting for nearly 3/4 of the earth's area, the ocean is rich in biological resources, mineral resources and so on, thus it is a very important resource treasure for human beings [1–2]. For China, which is not rich in per capita resources, the development of marine resources is of special significance [3]. As the important tool for ocean development, the underwater robot has become increasingly important in recent years' study. The main task of underwater robot is to get various kinds of

¹The authors acknowledge the National Natural Science Foundation of China (Grant: 51578109) and the National Natural Science Foundation of China (Grant: 51121005).

²Science and Technology on Underwater Vehicle Laboratory, Harbin Engineering University, Heilongjiang, 150001, China

information in the underwater environment. Moreover, getting excellent shot of the target information is essential to make the corresponding operating decision [4–5]. For the target detection system of underwater robot, it can accurately and quickly separate the object from the image sequence and extract the target information, which is the premise of the target location and target tracking [6]. Therefore, in this paper, the underwater robot acquisition image research is mainly including two aspects as underwater light image segmentation and target circle detection.

Researches on the image segmentation technology and underwater robot target detection technology are not uncommon at home and abroad. Image segmentation is a basic machine vision technology, which is the research foundation of the target detection technology. The study of underwater image segmentation methods by many scholars at home and abroad are mainly focused on the research and improvement of the following methods: adaptive threshold method, segmentation method based on edge detection, region growing method, watershed method and method based on Fuzzy Theory [7–9]. Usually, there are taken overall consideration of the computation and segmentation of the above five methods, developed the improvement method of the grey progressing based on minimum calculating volume of adaptive threshold method to increase the grey level difference between target area and background area in the image, and then obtained the final image segmentation results by using the method of double spike threshold segmentation. In order to detect man-made objects in underwater video images, a lot of researches have been done in recent years: Kamal et al. [10] proposed target extraction algorithm taking use of the invariant features and Barat et al. [11] used the visual attention mechanism to form a saliency map for obtaining the possible target area.

Owing to the existence of suspended matter, scattered refraction and absorption effect of aqueous medium on light, the underwater illumination image is often shown as low contrast value and low signal-to-noise ratio, with partial color distortion of the image and other features. When underwater robot is doing image acquisition, the illumination conditions are different. So, this paper will study the image segmentation method in two conditions as uniform illumination and uneven illumination. Under uniform illumination, the image segmentation based on the adaptive threshold method of the NSTC method has problems as adhesion of target and background, emerging more interference area, etc. To solve these problems, this paper proposes a new method of underwater image segmentation based on the improved image grey progressing. In the condition of uneven illumination, the global adaptive threshold method for image segmentation will cause incomplete segmentation of the object and other problems [12]. A method of multi-threshold segmentation based on sliding window is proposed in this paper to solve the problems. Meanwhile, due to the local distortion of the image edge in the image segmentation results, the precision of the circle detection is low, which will further affect the precision of the final target location. In order to improve the accuracy of circle detection, this paper improves the traditional point Hough transform circle detection method to eliminate irregular edge lines, which can reduce the effect of irregular edge segment of circle detection results. Finally, this paper lists the results of a contrast experiment among the proposed three methods and verifies the validity of the three methods.

2. Methodology

2.1. Underwater image segmentation based on the improved image grey progressing

The flow diagram of the proposing method of underwater image segmentation based on the improved image grey progressing is shown in Fig. 1.

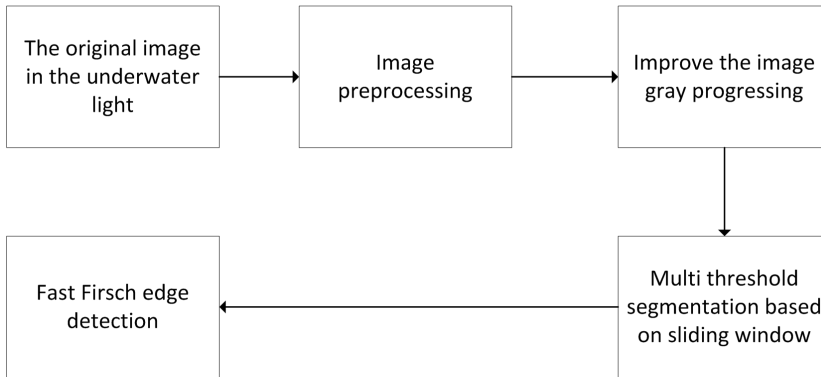


Fig. 1. Flow diagram of image segmentation based on image grey progressing

In this paper, the particular steps are changing the grey weight value of R, G, B to increase the difference of grey level between target and background, then doing threshold value segmentation to the grey image by using the classical double spike method and getting the final image segmentation results. The specific implementation steps are like this: Classification of object and background \rightarrow image information statistics \rightarrow three channel weight adjustment. The following understanding can be done from these three steps. Classification of target and background: The underwater light image is converted into the HSI (Hue, Saturation, Intensity) model [13]. Firstly, in the HSI model, the H and I channel information are quantized, respectively, to the range of [0,225]. Then, the classical Otsu threshold method is used to roughly classify the target and background of the pseudo grey level image of the H and I channels respectively. Image information statistics: Do image information statistics [14] of underwater light image in RGB model to get the grey average and standard deviation of all the pixels in the target area of the R, G, B three channels and background area. Weight adjustment of the three channels: Set the grey level differential measure threshold as T_{\max} and T_{\min} . Then compare the difference between the average value of the target area and the background area in the three channels to T_{\max} and T_{\min} , respectively. Combine the concentration degree of grey value in the region reflected by the standard deviation and change the values of r , g , and b

$$Y = [r \ g \ b] [R \ G \ B]^T \quad (1)$$

so as to meet the formula of $r + g + b = 1$. Determined from experiment, T_{\max} is set as 120 and T_{\min} is set as 50.

On the basis of the traditional method, this paper proposes a multi-threshold image segmentation method based on sliding window. Compared with the former method, the improved method can only handle the pixels of target area within the scope of the processing, greatly reducing the scope of the image processing needs handling, which can save the processing time to a great extent, specific steps are as follows:

Firstly, determine the range of the target area and set up the sliding window. The target area is the classification result of the target and background in H channel, which is shown as $O_{(iH,jH)}$ hereinafter. Gradually expand the scope of the target area on the basis of $O_{(iH,jH)}$, which ensures the relative integrity of the segmentation results. According to the camera imaging model, the calculation formula of the sum of the number of pixels in the image under different distances is obtained on the basis of the size of the sphere object:

$$A = \pi \left(\frac{f \cdot r}{Z_C \cdot k} \right)^2. \quad (2)$$

In the formula, r represents the real radius of the object, f expresses the camera focus and k is the scale factor of camera. The parameters f and k can be acquired by camera calibration; Z_C indicates the distance of camera and the object, and as the distance can be changed, it is the critical factor affecting the value of A . A large number of experiments show that the light condition in the process of imaging is relatively uniform when the distance Z_C between the camera and target is greater than or equal to one meter, the light condition in the process of imaging is more uniform.

According to whether the illumination is uniform, the threshold value segmentation of double spike method and the multi-threshold segmentation method based on sliding window are respectively used for image segmentation, getting the final segmentation results.

2.2. Research on circle detection method of underwater sphere target

Hough transform is a widely used circle detection method at present, which can make use of the target area that is composed of the target edge pixels, or detect the object with known shape in the image [15]. The classical thought of Hough transform is that it implements image segmentation, edge detection and other operations to the underwater original image, forming a closed curve that is similar to the circle by connecting the edge pixels of the target. A set of points on the circumference in the image space forms a set $\{(x_i, y_i), i = 1, 2, 3, \dots, n\}$ that is transformed to the parameter space (a, b, r) according to the formula

$$(x - a)^2 + (y - b)^2 = r^2. \quad (3)$$

It is known from the above formula that the equation can be represented as a three-dimensional cone in the spatial coordinate system, and the corresponding

relationship between the image space and parameter space is that an arbitrary point (x_i, y_i) on the circumference in the image space corresponds to a three-dimensional cone in the parameter space (a, b, r) , forming a conical surface cluster.

2.3. Improvement of circle detection method

In this paper, the traditional Hough transform circle detection method has been improved. Firstly, segment the edge of the target. As shown in Fig.2 below, the edge of the image is segmented to prepare for the next step firstly. In Fig. 2, taking the point O (which can be any point) in the target area as the benchmark, the target edge angle is divided into 16 sections. Picking point O as the center point of the target edge, the formula mode of the coordinate value in the image is

$$\begin{cases} \bar{x} = \frac{1}{A_r} \sum x, \\ \bar{y} = \frac{1}{A_r} \sum y. \end{cases} \quad (4)$$

In the formula, A_r represents the number of all pixels on the edge of target, and x, y are the coordinate value of the target edge pixels in the image.

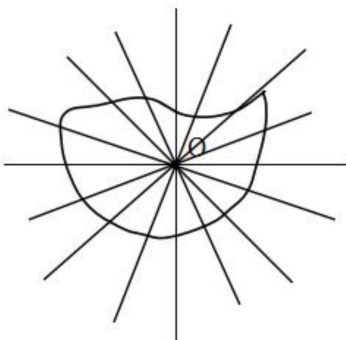


Fig. 2. Fragment diagram of the target edge

Secondly, judgment of sectional edge: judge each section of the edge to achieve the purpose of distinguishing the deformation edge and the edge area that meeting the requirements of the circle detection. Thus reduce the influence of the deformation edge on the accuracy of circle detection [16]. The specific steps are as follows.

Start from the pixel at the bottom left corner, the initial position of the line segment the pixel belongs to is determined, scanning the line segment point by point. In this paper, the circle fitting method is used to judge whether the current edge meets the circle detection requirements. Set the coordinate values as $\{x_i, y_i\}, i = 1, 2, 3, \dots, n\}$ of the pixel points on the edge of any segment. Conducting circle fitting to the pixel points on the same edge, that is, evaluating the center point (x_O, y_O) and the radius R corresponding to these points to minimize

the objective target functional formula

$$F = \sum_{i=0}^n \left((x_i - x_O)^2 + (y_i - y_O)^2 - R^2 \right)^2. \quad (5)$$

Calculating the partial derivative of F with respect to x_O , y_O and R separately and solving the following equations we obtain

$$x_O = \frac{A_2 C_2 - B_2 C_1}{A_1 B_2 - A_2^2}, \quad y_O = \frac{A_2 C_1 - A_1 C_2}{A_1 B_2 - A_2^2}, \quad (6)$$

$$R^2 = \frac{1}{n} \sum_{i=0}^n \left((x_i - x_O)^2 + (y_i - y_O)^2 \right). \quad (7)$$

Here, A_1 and A_2 are the minimal and maximal distances between the pixel and target point, B_1 and B_2 are the minimal and maximal regional areas, and C_1 and C_2 are the average tray-level of background and target regions.

In the same way, the center point (x_O, y_O) and radius R of the circle corresponding to the sixteen line segments can be obtained, respectively.

To determine whether the current edge meets the requirements of the arc segment, that is, if the conditions of $R < R_{\max}$, and $F < R_T$ (the set threshold) are met, the current edge is acceptable, otherwise, the edge is not acceptable. After scanning the sixteen edges, cluster all the parameters of the arc section that meets the requirements, and then conduct Hough transform circle detection to the clustered image pixel point, finally get the target circle detection results.

3. Result analysis and discussion

3.1. Contrast experiment under uniform illumination

Employing the underwater color camera OUTLAND UWC325, the size of the acquisition image was 352×288 , and the experiment was carried out in $4 \text{ m} \times 3 \text{ m} \times 2 \text{ m}$ water tank. In the experiment, the sphere object was suspended at 1 m from the water surface, and the same conditions were set in the following experiments. When the image is collected, open the two underwater lamps that have equal distance to the camera, to ensure adequate and uniform illumination. Figure 3 shows the contrast experiment results of red image segmentation. Diagram (a) represents the original light image, and diagrams (b) and (c) respectively show the grey results by using NTSC method and corresponding threshold segmentation results of double spike method, and diagrams (d) and (e) express the grey results by using the improved grey method and the corresponding threshold segmentation results of double spike method.

As can be seen from the diagrams, there are adhesions and distractors on the red sphere in the background after the threshold segmentation of the grey image by using NTSC method, and the edge of the sphere is rough. The diagram (e) shows

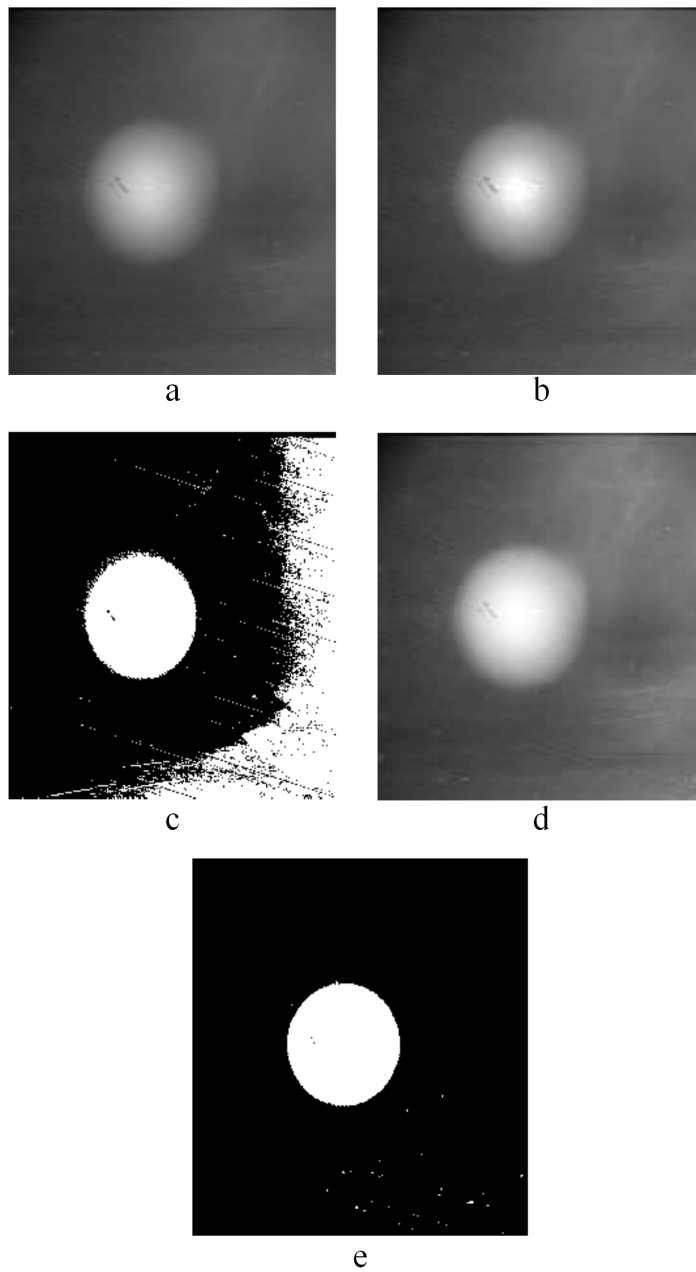


Fig. 3. Segmentation results of double spike method: a–original image of the red sphere in light, b–TNSC method, c–segmentation results of double spike method, d–improved grey progressing, e–segmentation results of double spike method

that the image contrast is enhanced, and the red sphere is completely segmented after threshold segmentation. What is more, the edge of the sphere is smooth, and the noise point is significantly reduced comparing to that of the diagram (c). At the same time, this paper uses segmentation evaluation indexes of FOM, UM and GC on the diagrams (c) and (e), and the performance evaluation results are shown in Table 1.

Table 1. The values of $f''(0)$ for various values of β

	Evaluation criterion		
	FOM	UM	GC
Grey progressing method			
NTSC method	0.0380	0.4738	0.1521
Method of improving the image grey progressing	0.1062	0.8643	0.7172

Analyzing the data in Table 1, the segmentation results show that three indicators FOM, UM and GC were significantly improved on the basis of the improved grey progressing method, illustrating that the improved grey progressing method is more suitable for underwater red light image segmentation than NSTC method.

3.2. Contrast experiment under uneven illumination

Turn to one of the two underwater lights with the same path to the camera. When collecting the image, move the support of the mobile camera and the underwater lamp to ensure that the illumination is not uniform. Taking the red sphere image as an example, Fig. 4 shows contrast experiments of red sphere segmentation under uneven illumination

As can be seen from the diagrams (b)–(d), the difference between the target and the background grey level of the improved grey progressing is larger than that of the NTSC method. Because of uneven illumination, the grey level of the red sphere region (target area) is close to that of the surrounding pixels, and it fails to segment by using double spike method. In the diagram (e), the target area of the image is processed by sliding window, reducing the segmentation error caused by the similar grey values, and the difference between the grey values around the target area can be obviously refined to segment the object. All of these indicate the effectiveness of the multi-threshold image segmentation method based on sliding window.

3.3. Contrast experiments of circle detection method before and after improvement

In the experiment, the binary image after edge detection is processed, respectively, by the traditional point Hough transform and the improved method in this paper. The results of the experiment are depicted in Fig. 5.

In Fig. 5, there is partial deformation on the edge of the sphere in the diagram (a). As can be seen in the diagram (b), after the process of the traditional point

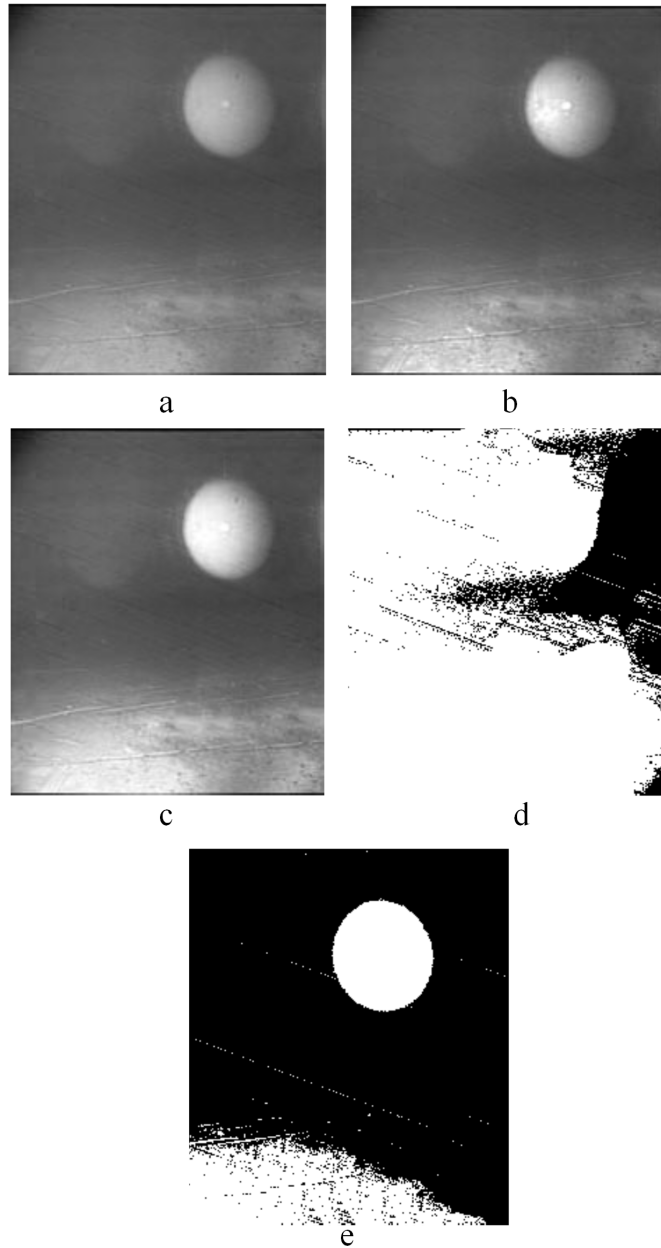


Fig. 4. Contrast experiment results of red sphere segmentation under uneven illumination: a–original image of the red sphere in underwater light, b–TNSC method, c–improved grey progressing, d–segmentation results of double spike method, e–results of multi-threshold segmentation based on sliding window

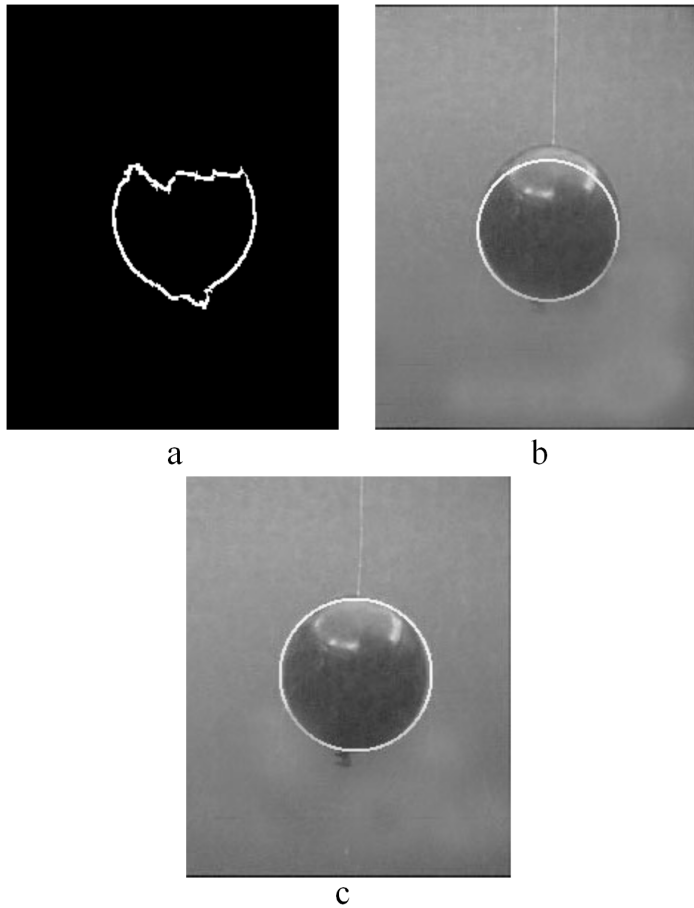


Fig. 5. Contrast experiment results of circle detection: a-partial deformation on the edge of the object , b-traditional point Hough transform , c-Improved method of circle detection

Hough transform circle detection, the results of the circle detection have obvious difference with the true value in the Y direction because of the irregular edge of the upper part of the sphere.

4. Conclusion

In this paper, it is studied the detection technology of underwater robot based on image segmentation. By improving the traditional technology, it is proposed that image segmentation method based on the improved grey progressing and multi-threshold segmentation method uses the sliding window. The traditional Hough transform circle detection method, and also three improvements of the feasibility

and effectiveness of the method are verified by experiments. Finally, the following conclusions are drawn:

As to the problems of the threshold segmentation method based on the NTSC method, this paper proposed and verified an underwater image segmentation method on the basis of improving the grey progressing. The experimental results show that there is less interference and noise in the improved segmentation results, and the three evaluation indexes FOM, UM, GC have a certain degree of improvement. In the uneven illumination conditions in the water, this paper proposes multi-threshold image segmentation method based on sliding window, which is obvious for the existing problems such as incomplete target separation in the image segmentation results. And the experimental results show that the multi-threshold segmentation of sliding window method can effectively separate out the object. There are partial deformations of the target sphere image edge and other problems in image segmentation results, the traditional Hough transform circle detection method is improved and tested to solve the referring problems. Similarly, the underwater experiment results also show that the improved circle detection results has better accuracy than that of the tradition point Hough transform circle detection results. The experimental results show that the improved technology in this paper can make the work of underwater robots more smoothly, and provide convenience for the exploration of marine resources.

However, due to the limited time, the paper takes merely consideration of the conditions under uniform illumination and uneven illumination, which is not sufficient for the actual underwater working. And the experiment is too single, without taking into account the image color of this piece of content. Therefore, it is recommended that the light source structure can be taken as a breakthrough point, focusing on the process of the robot gradually closing to the target, and changing the color of the target, which makes the experiment more rigorous.

References

- [1] C. A. STOCK, M. A. ALEXANDER, N. A. BOND, K. M. BRANDER, W. W. L. CHEUNG, E. N. CHURCHITSER, T. L. DELWORTH, J. P. DUNNE, S. M. GRIFFIES, M. A. HALTUCH, J. A. HARE, A. B. HOLLOWED, P. LEHODEY, S. A. LEVIN, J. S. LINK, K. A. ROSE, R. R. RYKACZEWSKI, J. L. SARMIENTO, R. J. STOUFFER, F. B. SCHWING, G. A. VECCHI, F. E. WERNER: *On the use of IPCC-class models to assess the impact of climate on living marine resources*. Progress in Oceanography 88 (2011), Nos. 1–4, 1–27.
- [2] M. A. PECK, S. NEUENFELDT, T. E. ESSINGTON, V. M. TRENKEL, A. TAKASUKA, H. GISLASON, M. DICKEY-COLLAS, K. H. ANDERSEN, L. RAVN-JONSEN, N. VESTERGAARD, S. F. KVAMSDAL, A. GARDMARK, J. LINK, J. C. RICE: *Forage fish Interactions: A symposium on "Creating the tools for ecosystem-based management of marine resources*. ICES Journal of Marine Science 71 (2014), No. 1, 1–4.
- [3] M. ZHAO, D. YANG, P. WANG, P. SHIA: *A market-based approach to marine sand resource management in the Pearl River estuary, China*. Ocean & Coastal Management 105 (2015), 56–64.
- [4] X. LIN, S. GUO: *Development of a spherical underwater robot equipped with multiple*

- vectored water-jet-based thrusters*. Journal of Intelligent & Robotic Systems 67 (2012), No. 3, 307–321.
- [5] M. DONIEC, C. DETWEILER, D. RUS: *Estimation of thruster configurations for re-configurable modular underwater robots*. Experimental Robotics, Springer Tracts in Advanced Robotics 79 (2014), 655–666.
- [6] I. C. RUST, H. H. ASADA: *A dual-use visible light approach to integrated communication and localization of underwater robots with application to non-destructive nuclear reactor inspection*. Proc. IEEE IC Robotics and Automation (ICRA), 14–18 May 2012, St. Paul, Minnesota, USA, 2445–2450.
- [7] R. KUMARI, N. SHARMA: *Improved Felicm based underwater color image segmentation by using L0 gradient minimization and DBPTGMF*. International Journal of Computer Applications 105 (2014), No. 16, 32–37.
- [8] X. LI, J. SONG, F. ZHANG, X. G. OUYANGA, S. U. KHAND: *Mapreduce-based fast fuzzy C-means algorithm for large-scale underwater image segmentation*. Future Generation Computer Systems (Special Issue on Big Data in the Cloud) 65 (2016), 90–101.
- [9] H. B. WANG, Y. R. WU, J. SHEN, Z. CHEN: *Slip magnetohydrodynamic viscous flow over a permeable shrinking sheet*. Applied Mechanics and Materials 347–350 (2013), 2178–2184.
- [10] S. KAMAL, S. K. MOHAMMED, P. R. S. PILLAI, M. H. SUPRIYA: *Deep learning architectures for underwater target recognition*. Proc. IEEE Ocean Electronics (SYMPOL), 23–25 Oct. 2013, Cochin, Kerala, India, 48–54.
- [11] C. BARAT, R. PHLYPO: *A fully automated method to detect and segment a manufactured object in an underwater color image*. EURASIP Journal on Advances in Signal Processing (Special issue on advances in signal processing for maritime applications) (2010), paper No. 10.
- [12] J. LI, J. M. BIUCAS-DIAS, A. PLAZA: *Spectral-spatial hyperspectral image segmentation using subspace multinomial logistic regression and markov random fields*. IEEE Trans. Geoscience and Remote Sensing 50 (2012), No. 3, 809–823.
- [13] M. BRACH, J. KACZMAROWSKI: *Suitability of the HSI model for the analysis of the forest fire spread*. Sylwan 158 (2014), No. 10, 769–778.
- [14] J. BENDIG, A. BOLTEN, S. BENNERTZ, J. BROSCHEIT, S. EICHFUSS, G. BARETH: *Estimating biomass of barley using crop surface models (CSMs) derived from UAV-based RGB imaging*. Remote Sensing 6 (2014), No. 11, 10395–10412.
- [15] R. EBRAHIMPOUR, R. RASOOLINEZHAD, Z. HAJIABOLHASANI, M. EBRAHIMI: *Vanishing point detection in corridors: Using hough transform and K-means clustering*. IET Computer Vision 6 (2012), No. 1, 40–51.
- [16] J. CHEN, J. LI, D. PAN, Q. ZHU, Z. MAO: *Edge-guided multiscale segmentation of satellite multispectral imagery*. IEEE Trans. Geoscience and Remote Sensing 50 (2012), No. 11, 4513–4520.

Received November 16, 2016

Home control system design based on internet of things¹

HONGLIAN WANG², HU CHEN³, WEI HE²

Abstract. In order to realize the remote management and wireless transmission function of the intelligent home system, Samsung's S3C2440 chip and the related peripheral devices are used to form a home gateway control platform of the entire system and home internal control network is designed based on ZigBee wireless network technology. The Texas Instruments CC2530 chip is used to achieve the functions of the coordinator node and the end node in the family internal control network. Finally, the experiment testing verifies that this system is feasible.

Key words. Home control system, Internet of things, ZigBee.

1. Introduction

With the rapid socio-economic development and Internet technology, control technology, information and communication technology and other advances in technology, and the sustained improvement of people's living standards, the relationship between people's daily life and information is becoming closer [1, 2]. How to make people have a safe, comfortable, energy-saving and convenient home environment has become the development trend of future household life, hence smart home control system came into being [3]. Smart home control system is based on the residential district as a platform environment, combined with computer technology, automatic technology, embedded software and hardware technology, wireless communication technology at an organic whole [4]. Achieve the goal of in close or remote control home appliance equipment and real-time monitoring the status of home appliance by users.

Based on the analysis of the shortcomings and development process of domes-

¹This work is supported by 2014 provincial quality engineering projects, the project name is automation comprehensive reform pilot and project number is 2014zy074. It is also supported by universities national quality engineering projects in Anhui province and the project name is new fire extinguishing car based on STC12 single chip microcomputer.

²Chongqing Electric Power College, Chongqing, 400053, China

³Chongqing Rail Transit Corporation (Group) CO., LTD, Chongqing, 400042, China

tic and foreign smart home control system, an ARM9 processor-based smart home control system is proposed in this work [5, 6]. It has changed the characteristics of traditional smart home control system of writing difficulties, poor mobility, high cost of design system complexity and inhuman.

This system uses S3C2440 microprocessor chip as the family gateway controller module and family internal control network module adopts ZigBee as a communication module [7–9]. The system hardware circuit design mainly follows three basic principles. The first is to try to use the typical application circuit to avoid unnecessary mistakes happening. The second is that it can be used for simulating the operation of the system and is convenient for system development and debugging. The third point is the reserved corresponding expansion interface, providing the needed for future expansion.

2. Hardware design

For the design requirements of family gateway in this paper, some corresponding peripheral devices have been designed, including the power module, the module reset button, touch screen module, LED display module, alarm module, storage circuit module, communication interface module, etc. Power supply is the core part of the whole system, which is related to the normal operation of the whole system. The design of power circuit in the system mainly considers the following two aspects. In order to improve the stability of the whole system, power filter circuit and voltage stabilizing circuit are designed in the power supply module. Power circuit is shown in Fig. 1. In this design, in order to ensure the circuit in the system stable and reliable and monitor the power supply voltage and carry out reset operation, we select MAX811S reset chip having the relatively high cost performance specially used for system monitoring. As long as the system's power value is less than the threshold of system reset, the chip will immediately reset the system.

Nand Flash contains a number of bytes in one page and one storage block is made up of several pages. One Nand storage block size ranges from 8 to 32 kB. The biggest advantages of this structure is that the capacity can be extended and now capacity of more than 512 MB Nand Flash products are quite common. Owing to the high density of Nand Flash unit, the cost is low, erasing speed is fast and is commonly used to store the large capacity data. Of course, it can also be used to run the program. Nand Flash devices are prone to bad block and is a random distribution. Once occurs, it will not be able to be repaired. So when it is used, an initialized medium scan should be carried out to find bad block and mark it as unavailable. Nand Flash circuit is shown in Fig. 2.

WM8731 is a kind of audio codec module with integrated headset drive produced by Wolfson. The voice prompt module circuit's ADC and DAC is 24 bit, the chip price is low, it has good quality, low power consumption and internal integrated optional ADC high-pass filter, which can directly provide 50 mW output power for 16-ohm load. S3C2440 IIS interface support left alignment mode and IIS mode, at the same time, it has the IIC bus interface and greater flexibility when being programmed. The chip also integrates the headphone amplifier to direct drive head-

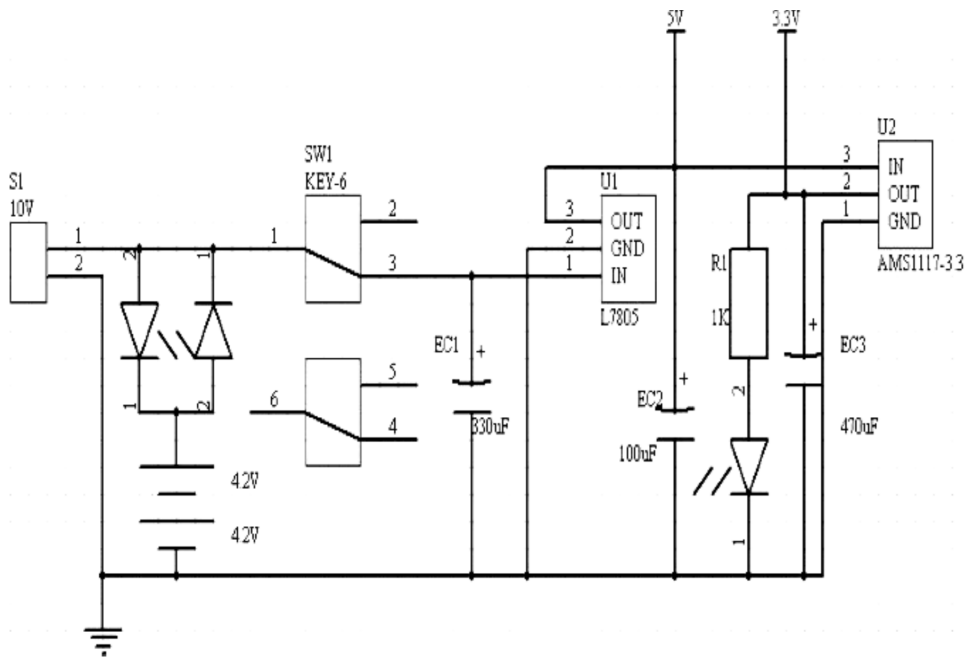


Fig. 1. Power circuit

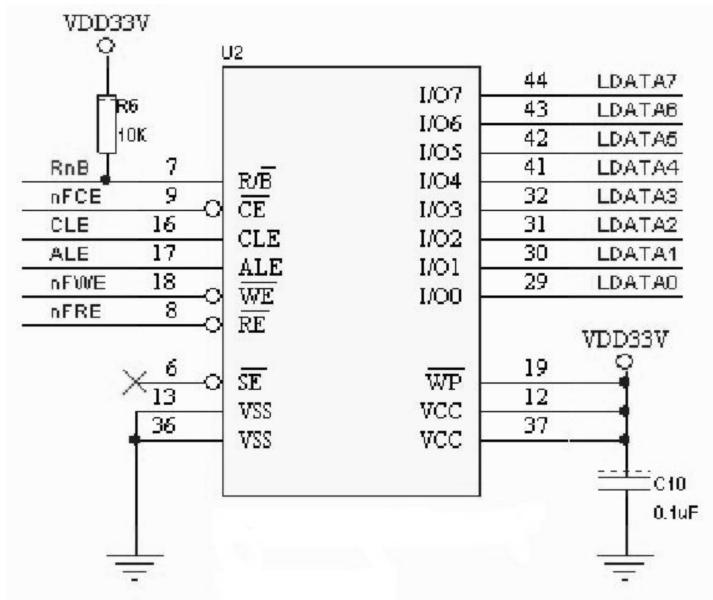


Fig. 2. Nand flash circuit

phones, so as to omit the headphone amplifier circuit. S3C2440 IIS coding system clock output is selected as clock in order to obtain more accurate clock. Subsequent circuit adopts TDA2822M as power amplifier chip to drive the speakers.

This family internal control network adopts the ZigBee wireless technology supported by the star network topology structure, mainly involving the two logical device types of ZigBee coordinator node and end node in the network. Coordinator achieves data transmission to the home gateway through RS232 serial interface, which is mainly responsible for the wireless control network within the family and searches the effective channel and terminal nodes to complete data forwarding function. Terminal node is mainly responsible for receiving command from the coordinator, which realizes the control of temperature sensors and household appliances and feedbacks the corresponding information to the coordinator node and then transmits the information to the home gateway through the coordinator node.

CC2530 chip uses a new generation of SOC system of 2.4 GHz and also combines TI company's gold unit ZigBee protocol and Remo TI, which can support the IEEE 802.15.4 standard. So we can build a more powerful network at low cost. CC2530 integrates a more perfect RF transceiver in sensitivity and anti-jamming, and standard enhanced 8051 microprocessors. In order to shorten the development cycle for developers, we also can use a good network protocol stack of TI company to simplify their own product development. Temperature control circuit is shown in Fig. 3. This circuit is connected to CC2530.

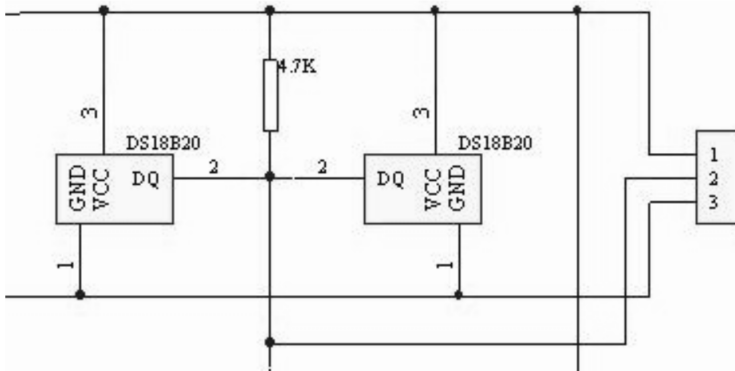


Fig. 3. Temperature control circuit

3. Workflow of Z-stack

The whole process of Z-stack is roughly divided into system and driver initialization, OSAL initialization and starting and entering task round. The focus of the system design is to carry out the ZigBee node related hardware initialized. The hardware initialization needs necessary configuration in Z-Stack protocol. The Z-Stack protocol can realize flexible, stable and energy efficient ZigBee wireless self-organizing network. In the application layer, it adds specific events and writes the

corresponding event handlers, in order to achieve specific functions. As the coordinator, routers and terminal node hardware design, it has different function in the ZigBee network. In the software design, there are the three kinds of nodes.

The implementation process of smart home application system based on ZigBee wireless network is as follows.

1. The coordinator system is initialized to set up the ZigBee wireless network.
2. Routers and terminal node system are initialized to join the established network and send the corresponding node number and web address information to the coordinator. Terminal node initializes the relevant sensors at the same time, the router waits for forwarding information and terminal nodes wait for control information.
3. As the coordinators set up the network successfully, after terminal nodes or routers joining the established ZigBee network, the coordinator will save the address of node in the address table.
4. Terminal node collects report on trigger events, reads sensor information and sends it to the coordinator.
5. Coordinator receives information and sends the upper machine via a serial port. Upper machine receives serial data, analyzes data and displays it on the interface.
6. Triggering the corresponding control information, and the control information is sent to the coordinator through the PC serial port.
7. The coordinator serial port receives information to produce a serial port interrupt, parses serial data and control information is sent to the corresponding terminal nodes.
8. Terminal nodes receive control information, parse and control curtain, light switches or opening and closing operation of sensors of the control nodes, etc.
9. Remote node is initialized and lights and appliances as well as curtain switches are controlled through remote control.

In the node initialization, the hardware initialization and the initialization of OSAL task is important. In the task initialization, we mainly consider ZDApp initialization in ZDO layer and initialization of the application layer. If we do not define `HOLD_AUTO_START` compiler options, in ZDApp task initialization, function `ZDOInitDevice()` is called to initialize the network. When `HOLD_AUTO_START` compiler option is undefined, the equipment general startup process is shown in Fig. 4. If `HOLD_AUTO_START` compiler option is defined, in ZDApp task initialization, network is not initialized. After the application layer task initialization, initialization of network is completed in the event of tasks. When the compiler option `HOLD_AUTO_START` is defined, equipment general startup process is carried out. Due to different configuration files, equipment `ZDO_StartDevice()` initialization step is different. `ZDO_StartDevice()` starts the equipment according to

the different equipment types. In `ZDO_StartDevice()`, the coordinator carries out `devState=DEV_COORD_STARTING` to set equipment's status as the coordinator starting and call the `NLME_NetworkFormationRequest()` to form network. In `ZDO_StartDevice()`, the router executes `devState=DEV_NWK_DISC` to set the status of equipment as finding network status and then calls `NLME_NetworkDiscoveryRequest()` in the network layer to discovery network. It also performs `NLME_StartRouterRequest()` to start the routing function, eventually it joins the network established by the coordinator.

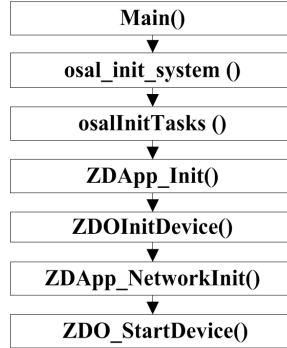


Fig. 4. Equipment general startup process when `HOLD_AUTO_START` is not defined

In `ZDO_StartDevice()`, terminal equipment executes `devState = DEV_NWK_DISC` to set the status as finding network status of equipment, and then call `NLME_NetworkDiscoveryRequest()` to discover network and join the network built up by coordinator eventually. If it does not join in the network successfully, a certain delay time is set and then reset the network initialization event `ZDO_NETWORK_INIT` to initialize the network.

4. System performance testing

Overall system performance testing is to test household system comprehensively. We mainly test o network stability, and power consumption. The chip itself has low power consumption, and the protocol stack can set terminal node in power saving mode. In power saving mode, when the terminal node will not send and receive data, it is in the sleep mode. Sleep mode has low power consumption, which almost can be ignored. Taking standby time as measurement of power consumption is not better. So we test power consumption when node is working. The node sends data continuously in the experiment. Two 1300 mAh rechargeable batteries can make the node keep sending data about 2600 to 3400 times or so. Because the battery charging has difference, average values of the sixty times measured results are shown in Table 1. The node does not send data most of the time, and we can ignore its low power consumption in the sleep mode. If data sending times is 20, battery life

of the node can reach about 150 days.

Table 1. Times of node sending data

Testing node	node 1	node 2	node 3	node 4	node 5
Times of sending data	3400	2850	2650	2600	2650

In the laboratory environment, tested ZigBee network includes a coordinator, two routers and five terminal nodes. It can keep connection with coordinator for 8 days. In 14 days, a terminal node disconnects the connection with the coordinator, but later it can access the network successfully. After four weeks of continuous testing, coordinator and routers basically are stable. Only the terminal nodes had a few broken accidents due to interference, but it basically can be recovered soon. After testing, it proves that this system has stable performance.

5. Conclusion

On the basis of the existing smart home system, we put forward a kind of home control system based on S3C2440 processor and ZigBee wireless technology. The design achieves the co-ordinate management of smart home system through a unified wireless protocol and the different control protocol. The structure is mainly four parts composed of family gateway, terminal controlled equipment, family internal control network and external communication network.

References

- [1] P. BARONTI, P. PILLAI, V. CHOOK, S. CHESSA, A. GOTTA, Y. F. HU: *Wireless sensor networks: A survey on the state of the art and the 802.15.4 and ZigBee standards*. Computer Communications 30 (2007), No. 7, 1655–1695.
- [2] C. LI, J. ZHANG: *Research of ZigBee's data security and protection*. Proc. IEEE International Forum on Computer Science-Technology and Applications (IFCSTA), 25–27 Dec. 2009, Chongqing, China, 1, 298–302.
- [3] S. O. AL MEHAIN, H. BARADA, M. AL QUTAYRI: *Integration of technologies for smart home application*. Proc. IEEE/ACS International Conference on Computer Systems and Applications, 13–16 May 2007, Amman, Jordan, 241–246.
- [4] H. ERDEM, A. UNER: *A Multi-Channel Remote Controller For Home and Office Appliances*. IEEE Trans. Consumer Electronics 55 (2009), No. 4, 2184–2189.
- [5] R. KADOUCHE, B. CHIKHAOUI, B. ABDULRAZAK: *User's behavior study for smart houses occupant prediction*. Annals of Telecommunications 65 (2010), No. 9, 539–543.
- [6] P. RASHIDI, D. J. COOK: *Keeping the resident in the loop: Adapting the smart home to the user*. IEEE Trans. Systems, Man, and Cybernetics - Part A: Systems and Humans 39 (2009) No. 5, 949–959.
- [7] S. MONCRIEFF, S. VENKATESH, G. WEST, S. GREENHILL: *Incorporating contextual audio for an actively anxious smart home*. Proc. IC Intelligent Sensors, Sensor Networks and Information Processing, 5–8 Dec. 2005, Melbourne, Australia, 373–378.
- [8] J. WU, H. QIN.: *The design of wireless intelligent home system base on ZigBee*. proc. IEEE IC Communication Technology, 10–12 Nov. 2008, Hangzhou, China 73–76.

- [9] W. BAO, W. CHEN, X. ZHU: *Design and implementation of wireless meter reading system based on ZigBee*. *Industrial Instrumentation & Automation* 20 (2013), No. 2.

Received November 16, 2016

Research on time optimal trajectory planning of 7-DOF manipulator based on genetic algorithm

JIANRONG BU¹, JUNYAN XU¹

Abstract. Trajectory planning is the basis of robot control. A robot with seven degrees of freedom is the object of study. The shortest time is taken as the trajectory optimization target. The joint trajectory planning is carried out by using B-spline curve. Under the constraint of kinematics parameters, the time optimization of the motion trajectory is realized by using the improved genetic algorithm. The results show that the total time of manipulator is reduced obviously, and the motion trajectory of each robot joint is continuous after optimization, which verifies the effectiveness and practicability of the algorithm.

Key words. 7-DOF, genetic algorithm, time optimization, trajectory planning.

1. Introduction

Trajectory planning is the movement trajectory of the robot in the process of movement, that is, the curve of the movement of the displacement, velocity, acceleration of the joints changing with time. The trajectory planning of robot is the basis of robot control and represents the research hotspot in the field of robotics in recent years. There are many performance indexes of trajectory planning, including time optimal trajectory planning, energy optimal trajectory planning, impact optimal trajectory planning and mixture optimal trajectory planning. Among them, time optimal trajectory planning is of great significance to improve the working efficiency of robots, and has been the focus of robot trajectory planning research.

The time optimal trajectory planning problem belongs to the nonlinear dynamic optimization problem. Its constraint conditions are generally nonlinear, the calculation process is complicated and the computation time is very long. For solving optimization of such problem, intelligent optimization algorithm are developed. The genetic algorithm has a good global searching ability and the advantage of inherent parallelism, so it has higher computational efficiency. In this study, the basic genetic

¹Zhejiang Industry Polytechnic College, Shaoxing, 312000, China

algorithm is improved, and a time optimal trajectory planning method based on the B-spline technique is established.

2. Research overview of optimal trajectory planning

There are many different methods for time optimal trajectory planning of robots at home and abroad [1–5], such as quadratic programming method, dynamic target programming method, PID control method and iterative method. Liu et al. [6] proposed 3 -5 -3 spline function for the trajectory planning of the robot, which effectively avoids the vibration of the acceleration. Zhu et al. [7] used the B-spline curve interpolation method to construct the planned trajectory, and used the sequential quadratic programming method to solve the optimal moving time node, and then the time-optimal continuous trajectory was formulated that met the constraint of the nonlinearity kinematics. However, the interpolation time of polynomials is difficult to be optimized by traditional methods.

In the process of the conventional trajectory planning, the angular velocity, angular acceleration of the joint and joint torque and other variables generally usually take a relatively conservative value, so that it works under the rated value to avoid the robot beyond its maximum load capacity. Although this can ensure the safe and reliable operation of the robot, but this method can not make the robot fully perform its performance and its working efficiency is relatively low, because it does not consider the dynamic characteristics of the robot.

GUOTY uses PSO algorithm for the optimal trajectory planning of the space robot under the dynamics constraints. Based on the consideration of joint velocity, acceleration and acceleration constraints, Karami et al. [8] used genetic algorithm to plan the running time interval of each key point in joint space. However, there are some problems such as slow convergence rate, low accuracy, and local optimality in simple genetic algorithm.

We proposed a time-optimal trajectory planning method based on the improved genetic algorithm, which takes the optimal time in the working process of the robot as the objective function, considering the path constraints, the maximum angular velocity, the maximum angular acceleration and the maximum joint torque as a constraint to complete the task of trajectory planning.

3. Time optimal trajectory planning of seven-DOF manipulator based on genetic algorithm

3.1. Problem description

When the genetic algorithm is used to describe the optimization problem, the first thing to be solved is to encode the individual in the real problem, which is the basis of selecting, crossover and mutation in the process of genetic operation. In the case of a population of N individuals, this population needs to be given at the beginning of the genetic algorithm. In general, the value of the initial population object is given

randomly. The population size N value generally takes 20 to 100, when N is large, the diversity of individuals in the population may increase. The initial population is equivalent to the given initial state in the genetic algorithm. Starting from the initial state, the solution is gradually optimized through the screening of the fitness function and the various operations of the genetic operator.

The genetic algorithm is a general method to solve the optimization problem. The design flow is basically the same for different optimization problems. The only difference is the parameter setting of the specific problem (including coding mode, genetic operator design, running competition value etc.). The general genetic algorithm design process is shown in Fig. 1.

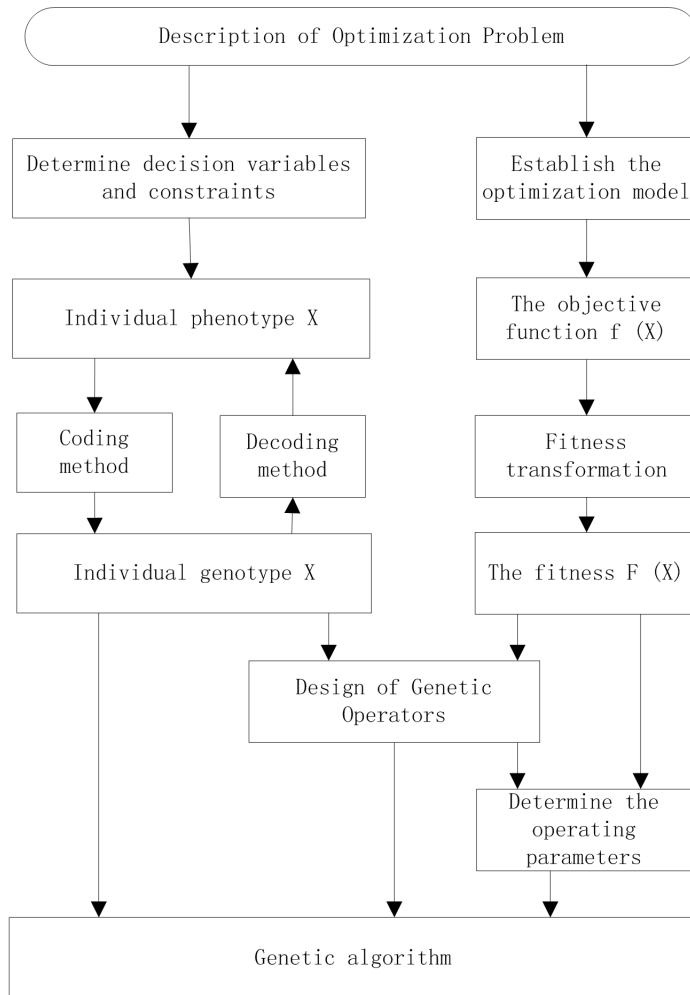


Fig. 1. Genetic algorithm design process diagram

3.2. Genetic algorithm optimization mathematical model

The genetic algorithm based on B-spline time optimization mainly includes the establishment of mathematical model of optimization problem and the design of genetic algorithm parameters. The general time optimization is carried out in the joint angular velocity and angle constraints, the advantages of this is less constraint, and the calculation is relatively simple, but the constraints of the joint torque is not considered, which may lead to large joint torque when the angular acceleration is large, so the actual capabilities cannot be realized. In order to solve this problem, the recurrence Newton-Euler algorithm is used to solve the joint torque, and the time optimal programming method under the constraint of joint torque is considered.

The mathematical model of genetic algorithm optimization problem is established, whose objective function is

$$T = \min \sum X_i \quad (i = 1, 2, \dots, m - 1), \quad (1)$$

where T is the total time of trajectory planning, m is the number of data points, and X_i is the time of the i th trajectory. In (1), X_i is an independent variable, which is chosen as the decision variable. In the study, B-spline programming is adopted as the constraint condition.

Assuming that the joint angular velocity in i th segment, $i = 1, 2, \dots, m - 1$ is $\dot{q}_i(u)$. According to the B-spline in the three average B-spline trajectory plannings we can get

$$\dot{q}_i(u) = \frac{dq}{dt} = \frac{dq/du}{dt/du} = \frac{a_1u^2 + a_2u + a_3}{b_1u^2 + b_2u + b_3}, \quad (2)$$

where

$$a_1 = \frac{-q_{i-1} + 3q_i - 3q_{i+1} + q_{i+2}}{2}, \quad a_2 = q_{i-1} - 2q_i + q_{i+1}, \quad a_3 = \frac{-q_{i-1} + q_{i+1}}{2},$$

$$b_1 = \frac{-t_{i-1} + 3t_i - 3t_{i+1} + t_{i+2}}{2}, \quad b_2 = t_{i-1} - 2t_i + t_{i+1}, \quad b_3 = \frac{-t_{i-1} + t_{i+1}}{2}.$$

The joint angular velocity in the i th segment obtained through (2) is $\dot{q}_i(u)$. For the maximum value $\dot{q}_i(u)_{\max}$ of the $\dot{q}_i(u)$, the $\dot{q}_i(u)$ can be obtained, respectively, through selecting limited discrete points in the section $u \in [0, 1)$, and $\dot{q}_i(u)_{\max}$ is approximated by the larger one to establish the speed constraint equation

$$\dot{q}_i(u)_{\max} \leq \Theta, \quad (3)$$

where Θ is the maximum angular velocity allowed by joints.

Assuming that the joint angular acceleration in i th segment is $\ddot{q}_i(u)$, then

$$\ddot{q}_i(u) = \frac{d\dot{q}}{dt} = \frac{d\dot{q}_i(u)/du}{dt/du} = \frac{q''t' - q't''}{t'^3}, \quad (4)$$

where

$$\begin{aligned}
 q' &= a_1 u^2 + a_2 u + a_3, \\
 t' &= b_1 u^2 + b_2 u + b_3, \\
 t'' &= 2b_1 u + b_2 = c_1 u + c_2, \\
 c_1 &= 2b_1, \\
 c_2 &= b_2, \\
 \ddot{q} &= (-q_{i-1} + 3q_i - 3q_{i+1} + q_{i+2})u + q_{i-1} - 2q_i + q_{i+1} = d_1 u + d_2, \\
 d_1 &= -q_{i-1} + 3q_i - 3q_{i+1} + q_{i+2}, \\
 d_2 &= q_{i-1} - 2q_i + q_{i+1}.
 \end{aligned}$$

In this way we obtain

$$\ddot{\theta}(u) = \frac{(d_1 u + d_2)(b_1 u^2 + b_2 u + b_3) - (c_1 u + c_2)(a_1 u^2 + a_2 u + a_3)}{(b_1 u^2 + b_2 u + b_3)^3}. \quad (5)$$

The method is the same as getting the maximum angular velocity. The value of $\ddot{q}_i(u)_{\max}$ is approximated by getting the maximum of the limited discrete point in $u[0, 1)$ section. The constraint condition of the acceleration is established as follows

$$\ddot{q}_i(u)_{\max} \leq \dot{\Theta}, \quad (6)$$

where Θ is the maximum angular velocity allowed by joints.

In the constraint condition of the torque, according to the inverse kinetic Newton-Euler algorithm, the joint torque can be obtained according to the angular acceleration, angular velocity and angle of the joint at a certain moment. The time of the track passing through the i th segment is continuous. Therefore, in order to find the maximum joint moment during the i th segment, we need to discretize it and get the joint torque of a finite point. The maximum value of the joint torque is approximated as the maximum joint moment. The constraint condition of the joint torque is

$$\tau_{\max} \leq \tau_a, \quad (7)$$

where τ_a is the maximum torque allowed by joints.

4. Genetic algorithm design

In the task of designing genetic algorithm suitable for the optimization problem, the appropriate operating parameters are selected to complete the optimization of genetic algorithm. We first need to encode the chromosome. The choice of chromosome coding method is based on the constraints of this optimization problem. Because the inverse kinematics algorithm is used in the joint torque constraint, it needs to be called repeatedly. The constraint condition is complex and the computation requires a large capacity. Therefore, the floating-point coding method is suitable for solving the optimization problem.

The population size is always 20–100. In this algorithm, 20, 50, and 100 individ-

uals are used to analyze the optimization results and verify the effect of population size on the precision of the algorithm. For the initial population value, the random variable between [30–50] is taken as the initial population (this is a very safe value according to the constraint of angular velocity and angular acceleration). In order to guarantee the accuracy of the algorithm, different interval is taken as the initial population to optimize the optimal solution. For the fitness function of individual fitness, we use Rank Fitness scaling in Matlab Genetic Algorithm Toolbox. The main principle is that the original fitness of the individual is calculated firstly, then the individual fitness ranges from large to small values $1, 2, \dots, n$, and the new fitness of each individual is $\sqrt{1/n}$. The advantage is that the expansion effect of the original fitness is eliminated, so that the new fitness will be more concentrated, and it can reduce the probability of "premature" phenomenon.

The design of the selection operator is based on the "Stochastic uniform" method in the Matlab genetic algorithm toolbox. The principle of the algorithm is to draw a line in the proportion to the fitness of the dataset after the normalization. Then, the line moves according to certain criteria, and each time it stops the algorithm picks an individual dataset. Each time the individual that inherits to next generation accounted 0.2 of the population size. Mutation operator and crossover operator use the default operator in the toolbox, and the crossover probability is 0.8.

The above completes the genetic algorithm design for the optimization problem. It should be noted that there are more variables in genetic algorithms, and many variables are based on actual experience to determine, therefore, in the actual optimization process, it is necessary to repeatedly test. A variety of different parameters should be tested until you find the optimal solution. The flow chart of the genetic algorithm for optimization is shown in Fig. 2.

5. Results

The time optimal genetic algorithm proposed in this paper is validated by simulation, and the effect of optimization parameters and different parameters in the algorithm on the precision of the algorithm are analyzed. In the case of the same parameters, different population size and initial population were set respectively, and their effects on the efficiency and accuracy of genetic algorithm were compared. Under the premise that the initial population take the random number in interval [20–30], 20, 50 and 100 are respectively taken as the population size to compare the different optimization results, as shown in Figs. 3–6.

Figure 3 depicts the optimization process when the population size of genetic algorithm is 20. It can be found that when the optimization to the seventh generation meets the constraints of evolutionary condition, the evolution stops. In the figure, the dashed line represents the average value of objective function of each generation individual in the process of the evolution, and realizes the objective function value that represents the optimal individual. From the figure, we can see that as the evolution proceeds, the mean value gradually approaches the optimal solution. Finally, Fig. 4 shows the value of the fitness function when the evolution stops.

Figures 5 and 6 show individual values of optimal solution and evolution of pop-

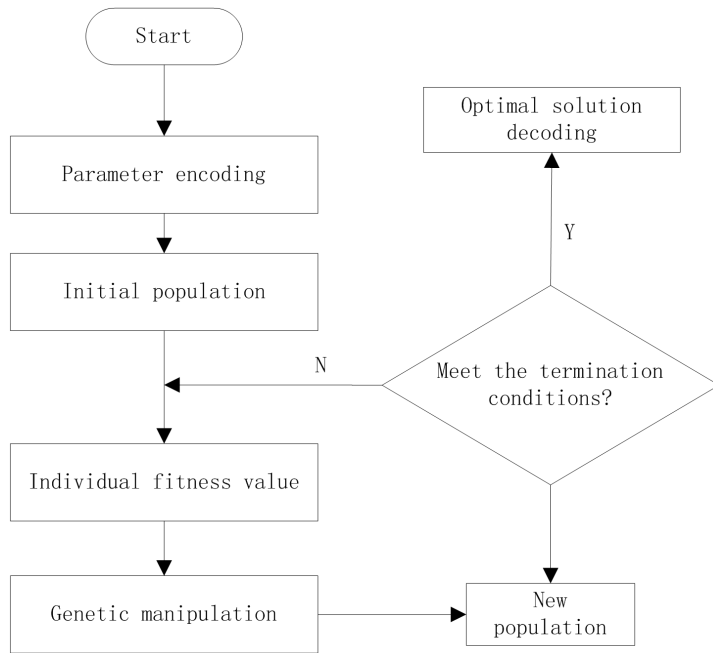


Fig. 2. Flow chart of genetic algorithm design

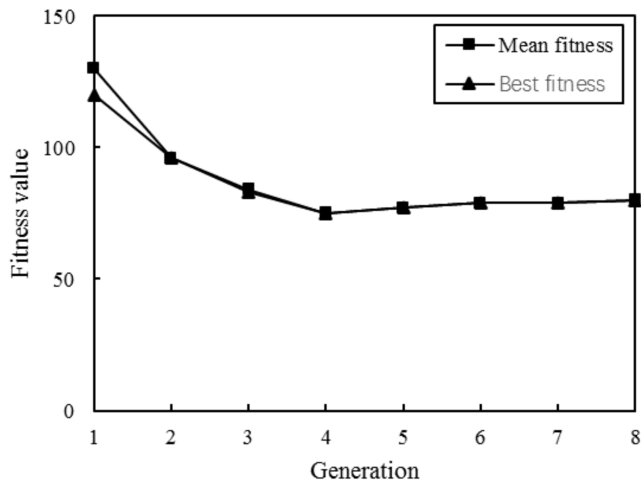


Fig. 3. Effect of population size on genetic algorithm: population size is 20

ulation size at 20, 50 and 100. From Fig.5 we can see that the evolution process can approach the final optimal solution quickly when the population size is large. However, the different population sizes are optimized to the same result, finally.

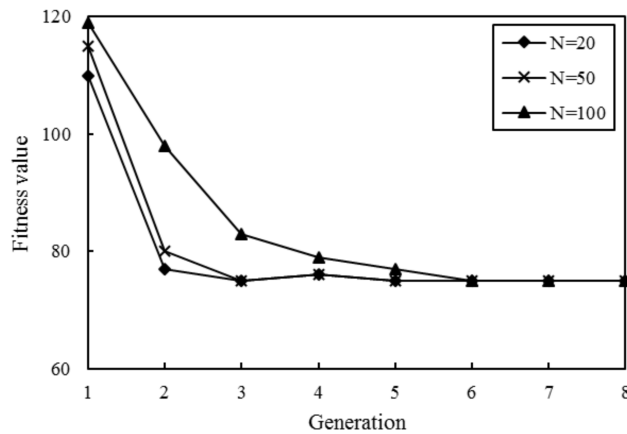


Fig. 4. Effect of population size on genetic algorithm: fitness value when the evolution stops

When the size of the population is large, the population diversity is better and the algorithm is more accurate. But the computational efficiency is sacrificed. In order to balance the two cases in the optimization process, the population size was selected to be 50.

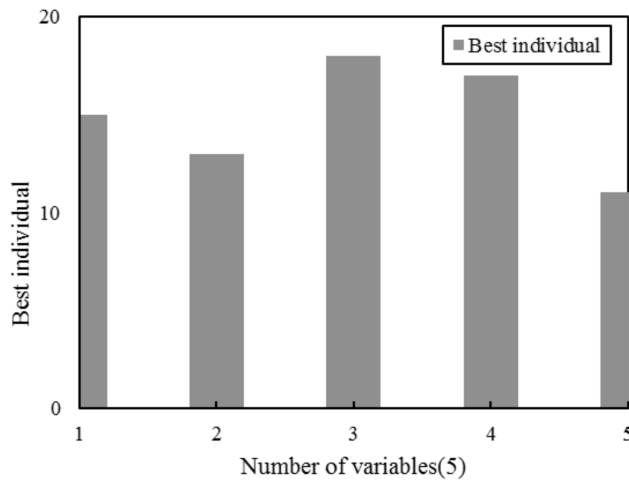


Fig. 5. Effect of population size on genetic algorithm: best individuals

In the genetic algorithm, the initial population value range is [20–30], which is a larger value that meets the condition based on the constraint of the speed and angular velocity. In order to verify the effects of data range of the initial population on the algorithm, the following groups of random number within range are taken respectively to carry out the simulation test, and the section range, respectively, is

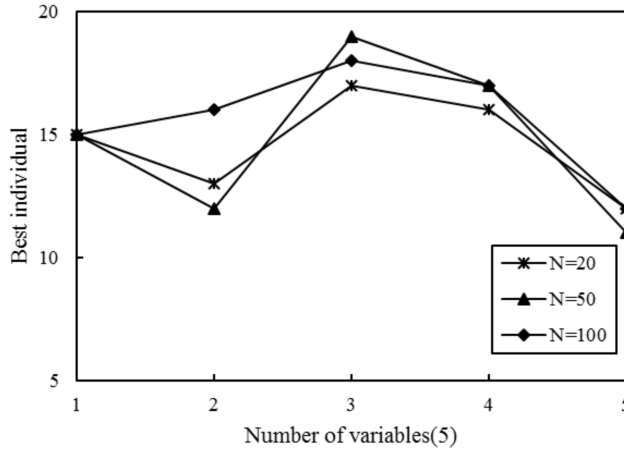


Fig. 6. Effect of population size on genetic algorithm: evolution of population size at 20, 50 and 100 individuals

[20–30], [30–40], [40–50], [20–50] and [10–30], and the population size is 50. The optimization of different interval is shown in Figs. 7 and 8. Figure 7 shows the variation of each generation and Fig. 8 shows the optimal values of different individuals in different intervals.

The results of optimization are summarized in Table 1.

Table 1. Effect of population size on genetic algorithm

Population size	X_1	X_2	X_3	X_4	X_5	T
$N = 20$	14.40	13.81	17.22	15.79	11.40	72.69
$N = 50$	14.20	12.92	18.21	16.45	9.90	71.67
$N = 100$	14.81	14.89	16.89	15.23	10.00	72.09

6. Discussion

In the study of seven-degree-of-freedom manipulator based on genetic algorithm, a seven-degree-of-freedom robot is used as the object of study. The trajectory is constructed by B-spline curves. Taking the shortest time as the optimization target, the coding scheme, selecting operator, crossover probability and mutation probability of the traditional genetic algorithm are improved for the simulation experiment of the trajectory optimization.

From the result analysis we can see that the process of evolution evolves to the optimal solution with the increase of the mean value of the range. For example, when the interval is [40–50], and the fourth generation is evolved, the individual

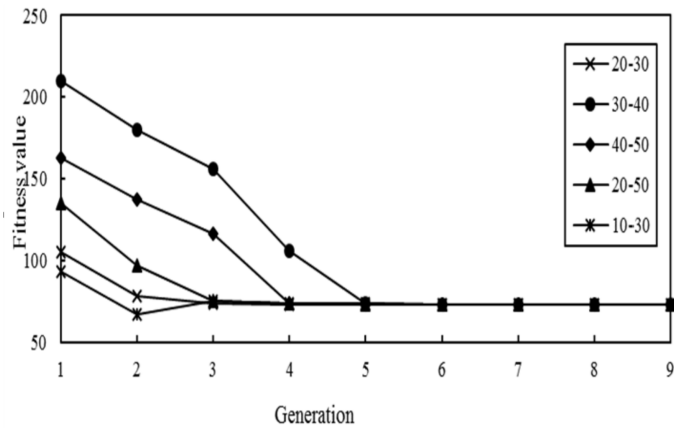


Fig. 7. Influence of initial population value on the algorithm: variation of each generation

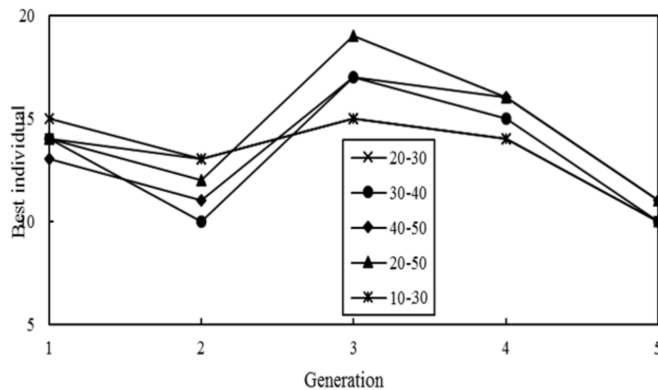


Fig. 8. Influence of initial population value on the algorithm: optimal values of different individuals in different intervals

converges to the optimal solution.. When the interval is $[30-40]$, it will be close to the optimal solution when it evolves to the third generation, and only needs to evolve to two generations to reach the optimum when the interval is $[20-30]$. Interval $[20-30]$ is closer to the optimal solution than the intervals $[30-40]$ and $[40-50]$, and when the interval $[10-30]$ is taken into account, it can be seen from the figure that the solution of the evolution to the first generation is smaller than that of the later generations, so the individual values of the initial interval can be described as small. From the previous analysis, we can see that in the optimization problem, the initial value interval taken as $[20-30]$ can not only guarantee the accuracy of the algorithm, but also improve its computational efficiency. The experimental results show that the manipulator's movement time is optimized from 107.52 s to 70.03 s by optimizing the genetic algorithm, which improves the operating efficiency of the manipulator and optimization of the trajectory time.

7. Conclusion

In this study, a genetic algorithm optimization model is established for the time optimal trajectory planning problem based on B-splines. The objective function, decision variables and constraints are determined. Constraints of angular velocity, angular acceleration and joint torque are considered in the constraint condition, the chromosome encoding method, the initial population, evaluation function, genetic operators and other parameters in the genetic algorithm are established, and finally the algorithm is realized through Matlab genetic algorithm toolbox to verify the genetic algorithm can effectively optimize the B-spline curve. The simulation results of the trajectory optimization simulation show that the time optimal trajectory planning of the seven-DOF manipulator based on genetic algorithm achieves the goal of optimizing the trajectory time. The results show that the proposed method is effective and reliable. The changing curve of the angular velocity, acceleration and acceleration of the robot joints has no abrupt change, which proves that the proposed method is effective and reliable.

References

- [1] E. BARNETT, C. GOSSELIN: *Time-optimal trajectory planning of cable-driven parallel mechanisms for fully specified paths with G1-discontinuities*. Journal of Dynamic Systems, Measurement, and Control *137* (2015), No. 7, paper 071007.
- [2] M. YUAN, B. YAO, X. ZHU: *An efficient computation algorithm for time optimal trajectory planning with physical constraints*. Proc. IEEE IC Information and Automation (ICIA), 8–10 Aug. 2015, Lijiang, Yunnan, China, 3100–3105.
- [3] B. LI, K. WANG, Z. SHAO: *Time-optimal trajectory planning for tractor-trailer vehicles via simultaneous dynamic optimization*. Proc. IEEE/RSJ IC Intelligent Robots and Systems (IROS), 28 Sept.–2 Oct. 2015, Hamburg, Germany, 3844–3849.
- [4] A. BERGER, I. IOSLOVICH, P. O. GUTMAN: *Time optimal trajectory planning with feedforward and friction compensation*. Proc. American Control Conference (ACC), 1–3 July 2015, Chicago, Illinois, USA, 4143–4148.
- [5] Y. KIM, B. K. KIM: *Efficient time-optimal two-corner trajectory planning algorithm for differential-driven wheeled mobile robots with bounded motor control inputs*. Robotics and Autonomous Systems *64* (2015), 35–43.
- [6] H. LIU, X. LAI, W. WU: *Time-optimal and jerk-continuous trajectory planning for robot manipulators with kinematic constraints*. Robotics and Computer-Integrated Manufacturing *29* (2013), No. 2, 309–317.
- [7] S. ZHU, X. JIN, B. YAO, Z. PAN: *Non-linear sliding mode control of the lower extremity exoskeleton based on human-robot cooperation*. IJ Advanced Robotic Systems *13* (2016), No. 5, paper 1729881416662788..
- [8] A. H. KARAMI, M. HASANZADEH: *An adaptive genetic algorithm for robot motion planning in 2D complex environments*. Computers and Electrical Engineering *43* (2015), 317–329.

A local location-based self-adjusting deployment algorithm for MSN

REN DUAN^{1,2}, DINYI FANG¹, KAIGUO QIAN³

Abstract. Aimed at maximizing coverage area and minimizing coverage gaps, we propose a deployment algorithm named local location based self-adjusting deployment (LLSAD) for mobile sensor network. Based on the analysis of the theory on optimal nodes layout with full coverage, a rule of sensors adjusting and location update is established. According to the rule, the sensor nodes can move close to the position of layout with full coverage in task region. The LLSAD algorithm realizes local optimal coverage by updating the local nodes' location to achieve required coverage. The simulation results have demonstrated that LLSAD can rapidly improve the coverage and achieve convergence under several different initial deployments to provide guarantee of coverage (quality of service-QoS). Moreover, sensor nodes do not need to maintain global sensor nodes' location data. It is highly applicable for sensor network, which has limited resources.

Key words. Local location, self-adjusting deployment, mobile sensor network, coverage QoS.

1. Introduction

Wireless Sensor Network (WSN) consists of many sensor nodes, which have capabilities of perceiving, computing and communicating. As an sensing infrastructure of Cyber Physical Systems (CPS) [1], WSN relies on all sensor nodes to cooperatively monitor physical world and gather the conditions of things. Coverage performance is a crucial quality of service (QoS) metric of WSN, which is the capacity of perceiving and collecting the status information of monitored objects in task region. Node deployment has much influence on the coverage performance. For a task in a specific region, deployment algorithm determines the number of nodes as well as their positions, to meet the application's requirement of coverage quality.

With the increasing popularization of CPS, WSN has been widely used in several fields including some fields where human access rarely, such as forewarning of forest fire, volcano monitoring, wetland monitoring, etc. In generally, a large and

¹School of Information Science and Technology, Northwest University, Shaanxi, 710000, China

²Information School, Yunnan University of Finance and Economics, Yunnan, 650221, China

³Department of Physics Science and Technology, Kunming University, Yunnan, 650214, China

redundant number of nodes are deployed randomly in task regions, to obtain a high coverage rate. However, it is still hard to guarantee the nodes distributed uniformly and meet the applications' coverage requirements. Thus, the nodes need redeployment [2]. In addition, some nodes exhaust will break the network structure and decrease coverage capacity [3]. Redeployment could optimize the layout of the remaining alive nodes to maintain a good coverage rate. Mobile sensor nodes [4, 5] can update their position dynamically to meet coverage requirement. What is more, mobile WSN can track the change of the target events' area and redeploy nodes correspondingly, such as pollution diffusion, fire spread monitoring, etc. Hence, the deployment based on mobility is a key support for QoS guarantee in WSN.

In this paper, we propose a self-adjusting deployment algorithm LLSAD for Mobile Sensor Network (MSN). Each sensor node updates position based on the layout with full coverage in task region that references greedy ideas, which adjusts the distance to its adjacent neighbors to achieve required coverage in global. It improves the coverage rate rapidly with no need to exchange and maintain global sensor position information.

2. Related works

One crucial deployment mechanism of sensor nodes is virtual force algorithm (VFA), which is proposed in [6]. Each pair of nodes exerts positive force if they are too far apart from each other in VFA, or exerts negative forces if they are too close. A node will move unless the net force from all neighbors is not zero. By using a force-directed approach, VFA improves the coverage provided by an initial random placement. An improvement of VFA [7] is used to deploy sensors in a region with obstacles and guarantee connectivity. However, the algorithm in [7] did not take into account redeployment of residue sensor node in operation. Some mobile sensor nodes are added to a static sensor network to improve performance by moving them to locations of a coverage hole based on the VFA [8]. Besides, there are some variations [9, 10] of VFA that are presented for mobile sensor network. Although the algorithms-based virtual force improves coverage in sensor network, the collisions of nodes occurs occasionally due to varied direction of net force and indefinite destination position. Moreover, the number of nodes needed to achieve required coverage in theoretical is not taken into account in the algorithms and evaluations are operated in some experienced and random situations.

Many redeployment strategies based on Voronoi diagram are proposed to optimize coverage of sensor nodes. Three algorithms of VEC, VOR and Minimax are presented in [11] to relocate sensors to build a Voronoi diagram and reach a high coverage rate. VEC can disperse dense nodes, VOR and Minimax are used to repair coverage hole. By calling Minimax and calculating Maxim-Edge of Voronoi directly, VEDGE [12] can enhance coverage at a high cost of computation. CBS [13] is a deployment algorithm which transforms the coverage problem of a network into the optimization problem of Voronoi polygon corresponding to each node. CBS algorithm has a low complexity, but there exist some small coverage holes inside the Voronoi polygons. The deployment algorithms-based Voronoi polygon can deter-

mine exact position of each node on the premise of all nodes' location data. The cost of exchanging location data is too high to afford in a sensor network without power harvesting.

There are other strategies [14, 15] that exploit mobility of sensor to improve coverage. A technique for k -coverage is proposed [14] in a grid-divided network, in which a few weak-mobility sensors are controlled to migrate from a grid to the adjacent one and collaborate with pre-placed static sensors to realize k -coverage. An algorithm based on the divide-and-conquer approach is proposed in [15]. By dividing task region into sub-regions and selecting the minimum connected sensor cover set for each sub-region considering the energy, a mobility assisted minimum connected sensor cover is achieved. It can significantly increase the capability of a remainder network with loss of connectivity as failure of some sensors. The methods above provide a fixed degree of coverage with no adaptive reconfiguration, in which the mobility of sensors is weak.

Based on the theoretical analysis on number and layout of nodes with full coverage, our LLSAD algorithm adopts self-adjusting to meet required coverage relying on the locations of sensors.

3. System model

3.1. Network and coverage model

In generally, WSN can be described as an undirected graph $G = (V, E)$, where V is the set of sensor nodes deployed in monitoring region, and E is the set of the links between two adjacent nodes. Assume that all nodes have the same communication radius R and sense radius r . It requires network keep connectivity when the nodes deployment is done, which means there are no isolated nodes. According to literature [16], if the sensor nodes' communication radius R is twice of sense radius r , the deployed nodes can fully cover the monitoring convex region and communicate with their neighbor nodes. Assuming n nodes are deployed in a monitoring region A , some definitions are as follows:

3.1.1. Neighbor set. The neighbor set of node v_i consists of all nodes located in its communication range. This is defined as follows:

$$N(v_i) = \{v_j | \text{dist}(v_i, v_j) \leq R, i \neq j\}. \quad (1)$$

Here, $\text{dist}(v_i, v_j)$ denotes the distance between node i and node j .

3.1.2. Coverage disk area. The sense coverage area of v is called the coverage disk area. If the coordinates of node v are x, y , the coverage disk area is a circle centered at x, y with radius r . It is defined as follows:

$$ca(v) = \{q | \text{dist}(v, q) \leq r\}, \quad (2)$$

where q is a point located in region A .

3.1.3. Coverage model. Can be defined using the Boolean disk model, i.e., any location $q(x_q, y_q)$ in the coverage disk area of sensor node $v(x_v, y_v)$ that is covered by v , others not.

3.1.4. Coverage rate. Divide region A into $a \times b$ grids. Coverage rate CR is the ratio of the number of covered grids to the number of all grids, defined as

$$CR = \frac{\sum_{i=1}^{a \times b} g_i}{a \times b}, \quad (3)$$

where $g_i = 1$ if grid i is covered by a node and $g_i = 0$ if grid i is not covered by any node.

3.1.5. Coverage efficiency. The coverage efficiency CE is the ratio of the union covered area by all sensor nodes in A and the sum of all nodes' coverage disk areas

$$CE = \frac{\bigcup_{v \in V} ca(v)}{\sum_{v \in V} ca(v)}. \quad (4)$$

The value of CE is an indicator of the redundancy of all nodes. The larger is CE , the higher is redundancy.

3.2. The node layout for full coverage

Obviously, single node's sensing area coincides with the coverage disk. However, the union sensing area of multiple nodes is determined by the layout of nodes.

There exist three layouts of two neighboring nodes' coverage disk area. It is just as shown in Fig. 1. The nodes v_2, v_3 and v_4 are neighbors of node v_1 . The distance d_1 between node v_1 and v_2 is shorter than sense radius r . There is overlapping sensing coverage area between these two nodes. The distance d_2 from node v_1 to node v_3 is twice the sense radius r , i.e. communication radius R . Then two coverage disks are tangent each other. There is only one point on the mutual tangent and no overlapping coverage area. The distance d_3 from node v_4 to node v_1 is longer than r and shorter than R . It causes blind zone which is not covered by any node. Thus, the coverage capacity is related to the layout of nodes. If the number of nodes $n \leq 2$ and there is no overlapping coverage area, the coverage is not affected by the nodes layout. If the node number $n \geq 3$, it could form coverage blind zone among the disjointed coverage disks (the shadow area in Fig. 2). It requires deploying more nodes in order that the blind zone is covered totally.

The blind zone can be eliminated by using multiple nodes' overlapping coverage. As shown as Fig. 3, upper part, three nodes' coverage disks intersect at a same point. The segments between any two nodes form an equilateral triangle. When the triangle sides length, i.e. the nodes' distance $d_0 = \sqrt{3}r$, the coverage efficiency of these three

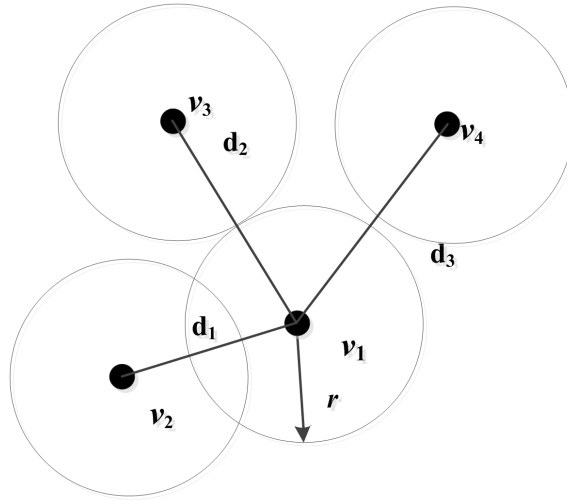


Fig. 1. Different layouts of two coverage disks

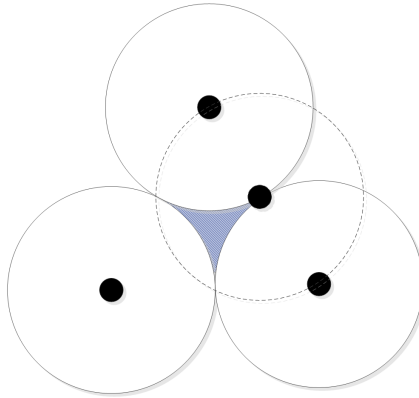


Fig. 2. Blind zone among disjointed coverage disks

nodes is the best. In this case, the overlapping area is calculated by formula

$$S_b = 6 \left(\frac{1}{6} \pi r^2 - \frac{\sqrt{3}}{4} r^2 \right). \quad (5)$$

An optimal layout of sensor nodes offering full coverage can be obtained by a triangular lattice [16], as shown in Fig. 3, bottom part. In this case, the effective coverage area of a node is calculated by formula

$$S_n = \frac{3\sqrt{3}}{2} r^2. \quad (6)$$

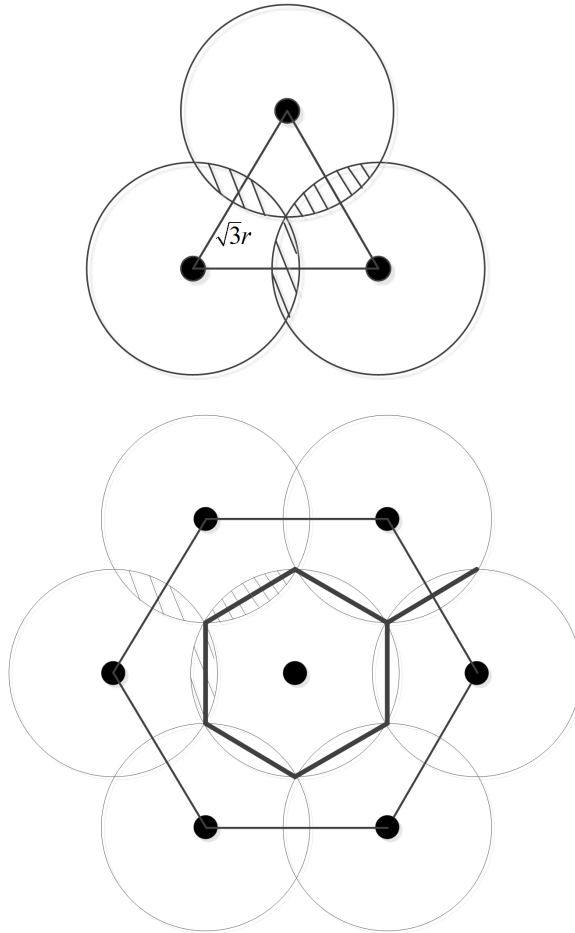


Fig. 3. Layout for full coverage: up-layout for full coverage of three nodes, bottom-triangular lattice layout

Let n denote the number of nodes using triangular lattice deployment which offers full coverage in region A of $L \times W$. Now n can be expressed as

$$n = \frac{2M \times N}{3\sqrt{3}r^2}. \quad (7)$$

However, due to the shape and side length factor, it is more likely that n nodes cannot cover the region of $L \times W$ fully. First of all, it is necessary to ensure that every point on the border is covered by a rectangle monitoring region. Therefore, nodes can be deployed as in Fig. 4 to cover border as few as possible. We can estimate the node number of full coverage on this condition. First, we have to determine the number w of nodes covering the side of length W in the horizontal dimension and

then the number l of nodes in vertical dimension. We use the formulae

$$w = \left\lfloor \frac{W}{\sqrt{3}r} \right\rfloor \quad (8)$$

and

$$l = 2 \left\lceil \frac{L}{3r} \right\rceil + \alpha, \quad (9)$$

where

$$\alpha = \begin{cases} 1 & \text{if } (L \bmod 3r) \leq r, \\ 2 & \text{if } (L \bmod 3r) > r. \end{cases}$$

According to formula (8) and (9), the number of nodes offering full coverage in monitoring region A is given by the formula

$$N_{fc} = l \times w. \quad (10)$$

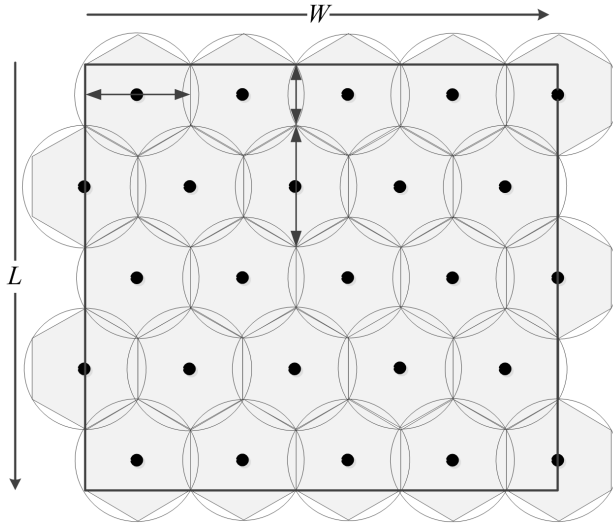


Fig. 4. Ideal node layout offering full coverage in a rectangular region

4. Computations

4.1. Judgment rule of self-adjusting

From the above discussion, we know that the ideal distance between two nodes to obtain the best coverage is $\sqrt{3}r$, denoted as d_0 . Thus, the nodes can be adjusted as follows to close the triangular lattice layout based on the local location of neighbors.

Let v_i denote a scheduling node, v_j being a v_i 's neighbor. If the distance between

the two nodes is less than d_0 , it means that there is too much coverage overlap between them. Thus, v_j will be moved opposite to v_i to reduce the coverage overlap area. Otherwise, if the distance is greater than the threshold d_0 , v_j will move towards v_i to fully cover the gap between them. As shown in Fig. 1, node v_2 should move oppositely to v_1 , on the contrary, v_4 should move toward v_1 .

4.2. Node position updating

Assume that node v_j is a neighbor of node v_i . If $d(v_i, v_j) \neq d_0$, then let node v_j move by $d_m = d_0 - d(v_j, v_i)$. When $d_m < 0$, the movement of node v_j should be opposite to node v_i . When $d_m > 0$, node v_j will move towards node v_i . The direction of movement depends on the angle θ from v_j to v_i . The value of θ can be calculated according to the position of the two nodes. The coordinate of node v_j is then updated in the following way:

$$\begin{cases} x_j' = x_j + \varepsilon \cdot d_m \cdot \cos \theta, \\ y_j' = y_j + \varepsilon \cdot d_m \cdot \sin \theta. \end{cases} \quad (11)$$

Here, ε represents the movement coefficient, that is given as

$$\varepsilon = 1 - \frac{7}{24}CR$$

in this paper.

4.3. LLSAD algorithm

From the above analysis, LLSAD algorithm we proposed is shown in Fig. 5. First of all, it initializes task region border parameter as $L \times W$, and determines the sensor node number n by the formulae (9) and (10). And then, randomly deploys the nodes in the task region (line 1). The operation of LLSAD is divided into rounds where each round is further divided into 4 steps as follows from Fig. 5.

1. Calculate the current coverage rate CR . If $CR > C0$ ($C0$ denoting the required coverage ratio), the algorithm will quit, otherwise it will perform step 2 (lines 3–6 in Fig. 5).
2. Traverse every node and exchange latest location information between every two nodes via broadcast (lines 7–8 in Fig. 5).
3. For each neighboring node v_j of node v_i , calculate their distance $d(v_j, v_i)$. According to the adjusting judgment rule determine, whether to update the nodes' location or not (lines 9–14 in Fig. 5).
4. After scheduling all the nodes (line 15), every node moves to the new location. And then it begins the new round and jump to Step 1.

```

1   Initialize the network in region  $A$ ;
2   For each round
3     Calculate the coverage rate  $CR$ ;
4     If ( $CR > CR_{req}$ )
5       break;
6     end if
7     For each node  $v_i (i=1:n)$ 
8       Exchange location message with all neighbors in
      one-hop range;
9       for each neighbor  $v_j (j=1:N(v_i))$ 
10        if ( $d(v_j, v_i) \neq d_0$ )
11          Calculate the azimuth angle  $\theta$  that  $v_j$  relative to  $v_i$ ;
12          Calculate the movement and update location of  $v_j$ .
13        end if
14        move to next neighbor
15        move to next node
16      Each node moves to latest location;
17  move next round;

```

Fig. 5. Flowchart of LLSAD algorithm

5. Performance evaluations

The algorithm evaluation is simulated in the MATLAB R2013a. The evaluation metrics includes coverage rate CR and coverage efficiency CE as well as average running rounds to meet the coverage rate required CR_{req} . In order to evaluate the algorithm performance under different conditions, we tested LLSAD in two initial scenarios. One scenario is S_1 where all nodes are initially randomly deployed in the whole monitoring region, as shown in Fig. 6. In another scenario S_2 , all nodes are split in half and initially randomly deployed in the two 1/4 diagonal area of task region, as shown in Fig. 7. Besides, we compared LLASD and VFP algorithms under the scenario S_1 .

We set two task region sizes corresponding to each case in formulae (9) and (10), including $80\text{ m} \times 80\text{ m}$ and $100\text{ m} \times 80\text{ m}$. Thus, we can build many settings of different scenarios and sizes of region. The details of settings and CR requirements are shown as Table 1. The initial coverage rate of each random network in scenario S_1 is less than 80%, and is not larger than 60% in S_2 .

Table 1. Simulation settings

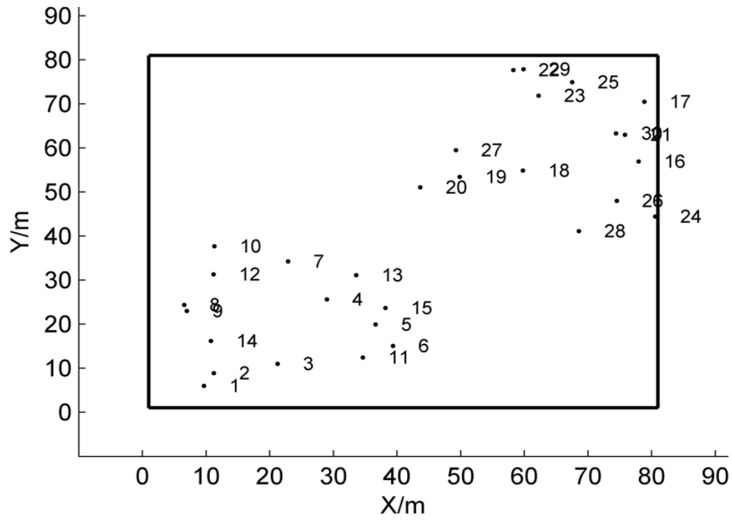


Fig. 6. Nodes are randomly deployed in the whole region

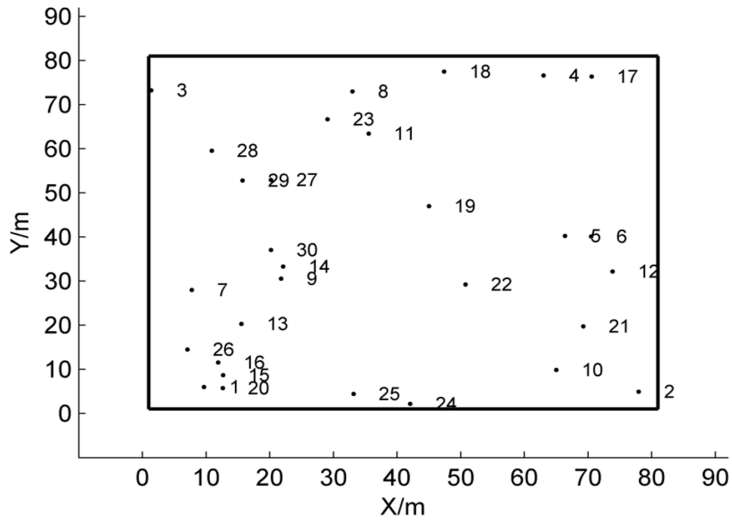


Fig. 7. Nodes are deployed on the two opposite angles

settings	scenario S_1 nodes/ CR_{req}	scenario S_2 nodes/ CR_{req}	region size $L \times W$	sensing radius r
1	28/94 %	28/93 %	80 m \times 80 m	10 m
2	29/95 %	29/94 %	80 m \times 80 m	10 m
3	30/95 %	30/95 %	80 m \times 80 m	10 m
4	30/95 %	36/95 %	100 m \times 80 m	10 m

Table 2. Results of simulation under scenario S_1

settings	nodes	CR_{req}	rounds	CR	CE	region size
1	28	>94 %	9.4348	0.9421	0.6854	80 m×80 m
2	29	>95 %	9.1986	0.9539	0.6701	80 m×80 m
3	30	>95 %	6.8482	0.9553	0.6487	80 m×80 m
4	36	>95 %	9.2758	0.9540	0.6749	100 m×80 m

Table 3. Results of simulation under scenario S_2

settings	nodes	CR_{req}	rounds	CR	CE	region size
1	28	>93 %	10.9627	0.9341	0.6797	80 m×80 m
2	29	>95 %	12.1865	0.9445	0.6635	80 m×80 m
3	30	>95 %	11.3478	0.9543	0.6481	80 m×80 m
4	36	>95 %	14.9953	0.9532	0.6743	100 m×80 m

According to the formula (8) and (9), it needs to deploy 30 nodes in 80 m×80 m and 36 nodes in 100 m×80 m region to obtain full coverage. Under every configuration, the algorithm operates 100 runs, respectively. The evaluation results are as shown in Table 2 and Table 3 under different settings of region size and initial deployment.

In all settings, the maximum of average iterating rounds to meet the coverage requirement is 14.9953, and the minimum is only 6.8482. This illustrates that LLSAD is able to improve the coverage by redeploying under these two scenarios.

Under scenario S_1 , LLSAD improves network coverage rate rapidly when sensor nodes are placed randomly in whole monitoring region at initialization. In the region of 80 m×80 m deployed randomly 28 nodes (93.5 % of N_{fc}), LLSAD only runs for 9.4348 rounds in average when the CR increases to 94 %. If the number of nodes increases to N_{fc} , the average rounds are not more than 10 in the two regions. There are only 6.8482 rounds, 9.2785 rounds in the regions of 80 m×80 m, 100 m×80 m respectively. LLSAD provides an effective redeployment for improving coverage.

Under scenario S_2 , LLSAD runs more rounds to achieve CR_{req} (see Table 3). It runs nearly 15 rounds in average in the worst case to obtain CR_{req} . This is because the nodes are only placed in half area at initialization so that the nodes are dense with a low coverage rate. The movement of one node affects the coverage of multiple neighbors. Hence, the nodes have to adjust over and over to form a uniform distribution with higher coverage rate. Even if the number of nodes is N_{fc} , the algorithm runs more rounds under scenario S_2 . In the settings of line 3 and 4 in Table 4, there is 5 %–6 % of the simulations have run more than 40 rounds to reach CR_{req} . What is more, the algorithm achieves much better average coverage efficiency when the number of node is less than N_{fc} . The small number is, the higher CE is. It is just because the overlaps between the nodes are reduced by LLSAD to achieve the CR_{req} .

In a word, the LLSAD algorithm has the capacity to enhance coverage by self-

adjusting based on the local locations of the nodes under two scenarios. And it will run fewer rounds to achieve the required coverage rate if the nodes are placed uniformly with a relative high coverage rate in initial deployment.

In addition, we compare LLSAD and virtual force (VF) position algorithm in term of convergence and coverage rate. We evaluate the two algorithms in $80\text{ m} \times 80\text{ m}$ region deployed 30 nodes under the scenario S_1 . Both average results of 25 rounds calculated from 20 random initial deployment are shown in Fig. 8. The LLSAD algorithm only runs 5 rounds in average to reach the required coverage rate 95% and keeps stable after 10 rounds. In contrast, VF's coverage rate increases slowly and only reaches 92% after 25 rounds. LLSAD is a very fast and efficient deployment for MSN, which defeats VFP in terms of convergence and coverage capacity.

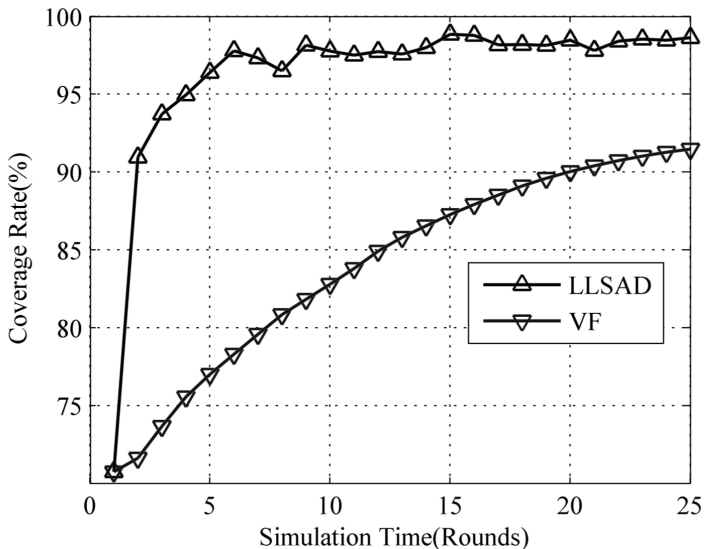


Fig. 8. Comparison of LLSAD and VF under scenario S1

6. Conclusion

The issue of deployment and coverage is fundamental in WSN, which is basic to data fusion, routing techniques as well as management in upper application. In this paper, we have proposed a new adaptive deployment algorithm for mobile sensor networks, namely, local location based self-adjusting deployment algorithm. By using only location information of local neighbors for the self-adjustment of each node, sensor nodes can move to close optimum location of the perfect coverage layout. The results of the simulations show that LLSAD is a fast, efficient redeployment for mobile sensor networks. Without getting and maintaining the global topology information of sensor nodes, each node runs the algorithm with low cost. Therefore,

LLSAD is applicable to mobile sensor network with constrained resources.

References

- [1] J. A. STANKOVIC: *Research directions for the internet of things*. IEEE Internet of Things Journal 1 (2014), No. 1, 3–9.
- [2] K. MOUGOU, S. MAHFOUDH, P. MINET, A. LAOUITI: *Redeployment of randomly deployed wireless mobile sensor nodes*. Proc. IEEE Vehicular Technology Conference (VTC Fall), 3–6 Sept. 2012, Quebec City, Canada, 1–5.
- [3] S. CHELLAPPAN, X. BAI, B. MA, D. XUAN, C. XU: *Mobility limited flip based sensor network deployment*. IEEE Trans. Parallel and Distributed Systems (TPDS) 18 (2007), No. 2, 199–211.
- [4] A. CHEN, Z. LI, T. H. LAI, C. LIU: *One-way barrier coverage with wireless sensors*. Proc. IEEE IC Computer Communications (INFOCOM), 10–15 April 2011, Shanghai, China, 626–630.
- [5] S. HE, J. CHEN, X. LI, X. SHEN, Y. SUN: *Cost-effective barrier coverage by mobile sensor networks*. Proc. IEEE IC Computer Communications (INFOCOM), 25–30 March 2012, Orlando, Florida, USA, 819–827.
- [6] Y. ZOU, K. CHAKRABARTY: *Sensor deployment and target localization based on virtual forces*. Proc. IEEE IC Computer Communications (INFOCOM), 30 March–3 April 2003, San Francisco, California, USA, 2 1293–1303.
- [7] G. TAN, S. A. JARVIS, A. M. KERMARREC: *Connectivity-guaranteed and obstacle-adaptive deployment schemes for mobile sensor networks*. J IEEE Trans. Mobile Computing 8 (2009), No. 6, 836–848.
- [8] T. ZHOU, B. HONG, S. PIAO: *Hybrid sensor networks deployment based on virtual force*. J Computer Research and Development 44 (2007), No. 6, 965–972.
- [9] N. AITSAADI, N. ACHIR, K. BOUSSETTA, G. PUJOLLE: *Potential field approach to ensure connectivity and differentiated detection in WSN deployment*. Proc. IEEE International Conference on Communications, 14–18 June 2009, Dresden, Germany, 1–6.
- [10] L. TAN, C. YU, M. YANG: *Self-deployment algorithm of mobile sensor network based on uniform density cluster*. Proc. IC Wireless Communications Networking and Mobile Computing (WiCOM), 23–25 Sept. 2010, Chengdu City, China, 1–4.
- [11] G. WANG, G. CAO, T. F. LA PORTA: *Movement-assisted sensor deployment*. J IEEE Trans. Mobile Computing 5 (2006), No. 6, 640–652.
- [12] H. MAHBOUBI, J. HABIBI, A. G. AGHDAM, K. SAYRAFIAN-POUR: *Distributed deployment strategies for improved coverage in a network of mobile sensors with prioritized sensing field*. IEEE Trans. Industrial Informatics 9 (2013), No. 1, 451–461.
- [13] H. J. LEE, Y. KIM, Y. H. HAN, C. Y. PARK: *Centroid-based movement assisted sensor deployment schemes in wireless sensor networks*. Proc. IEEE Vehicular Technology Conference, 20–23 Sept. 2009, Anchorage, Alaska, USA, 1–5.
- [14] W. WANG, V. SRINIVASAN, K. C. CHUA: *Coverage in hybrid mobile sensor networks*. IEEE Trans. Mobile Computing 7 (2008), No. 11, 1374–1387.
- [15] A. M. KHEDR, W. OSAMY: *Mobility-assisted minimum connected cover in a wireless sensor network*. J Parallel and Distributed Computing 72 (2012), 827–837.
- [16] M. MA, Y. YANG: *Adaptive triangular deployment algorithm for unattended mobile sensor networks*. IEEE Trans. Computers 56 (2007), No. 7, 946–957.

Received November 16, 2016

A hybrid model for scale forecast of regional highway network¹

HANG YANG², XIAOQING LI², BING WU²

Abstract. A hybrid method for improvement of accuracy and reliability of scale-forecast and obtaining the optimal hierarchical structure of highway network in Hangzhou is proposed. Firstly, drawbacks of traditional scale-forecast methods of highway network are illustrated. Then, a novel prediction method which is based on BPNN and Markov chain is proposed. After that, a multi-objective programming (MOP) model is established to obtain the optimum technical grade structure of highway network. Finally, the scale of highways and their optimal hierarchical structure in the year of 2015, 2020 and 2025 is obtained.

Key words. Highway transportation, highway network, scale forecast, BP neural network, Markov chain, multi-objective programming.

1. Introduction

The forecast of regional highway network is an important part of regional transportation planning. The study by Chen et al. [1] revealed that scale forecast was of great importance in the planning of regional highway network. Qi and Chen [2] indicated that development of highway network should fit into location characteristics of regional transportation and functional requirements for highway traffic. Marin [3] showed that rational scale of a highway system referred to efficient configuration of the transportation system in which supply and demand reach the equilibrium state.

Rational highway network scale should meet the demands of regional economic and social activities by relatively small total mileage, and make the configuration

¹This research is sponsored jointly by the National Natural Science Foundation of China (grant No. 51608386) and Shanghai Sailing Program (grant no. 16YF1411900). Authors appreciate the support of the Planning and Research Institute of the Ministry of Transport of the People's Republic of China as well as the Highway Bureau of Hangzhou. Authors also appreciate the abundant data given by the Statistical Bureau of Hangzhou. Finally, authors would like to thank Dr. Linbo Li, Dr. Yajie Zou, Mr. Zhongyu Wang, Mr. Jiajun Yin, Ms. Zhen Chen and Ms. Xiaohe Zhang, for giving recommendations which helped to consolidate the final paper from its earlier versions.

²Key Laboratory of Road and Traffic Engineering of Ministry of Education, Tongji University, No. 4800 Cao'an Road, Shanghai, 201804, China, wubing@tongji.edu.cn

of highway in all grades optimized, which was conducted by Nogués and González-González [4] and Wang and Han [5].

Li and Chen [6] listed methods mainly incorporate territory coefficient method, connectivity method, analogy method, and time series method, etc. Jha et al. [7] pointed out that such methods go against the evolution rule of highway network, and the thought was proved wrong by Tsou et al. [8]. Traditional prediction methods attach little importance to the grade structure and give little consideration to influences of grade structure of highway on supply capacity, as concluded by Aldrich et al. [9] and Bonnafous et al. [10]. Li and Chen [6] concluded that the relevance of influence factors, subjectivity in the weight-determination and other issues would affect the evaluation accuracy of the traditional methods.

Our work in this paper is to build a model which can be applied to both the prediction and the analysis of regional highway network's rational scale. In the meantime, the model to optimize the technical grade structure of highway network are used.

2. Hybrid forecast method

2.1. Highway network scale forecast model based on BP neural network and Markov chain

2.1.1. Construction of forecast model based on BP neural network. In order to improve the convergence rate and reduce convergence error, sample data is normalized before training so that values of this data lie in the interval [0,1] which was put forward by Xu et al. [11] and Du et al. [12].

2.1.2. Result correction. According to the fitting error margin of BP Neural Network (the percentage that absolute error takes in actual value), Markov's status area can be classified by 5 states:

1. Extremely overvalued state (α^+).
2. Overvalued state (α).
3. Normal state (β).
4. Undervalued state (γ).
5. Extremely undervalued state (γ^+).

If the system's initial state vector is S_0 and the state vector is S_k after k steps of transfer, then $S_k = S_{k-1}p = \dots = S_0p^k$, which is based on C-K Equation listed in Iwankiewicz [13] and Khmel et al. [14].

The state vector of predicted highway network scale can be achieved by One-step State Transfer Probability Matrix in the first place, which was conducted by D'Amico et al. [15] and Mukherjee et al. [16].

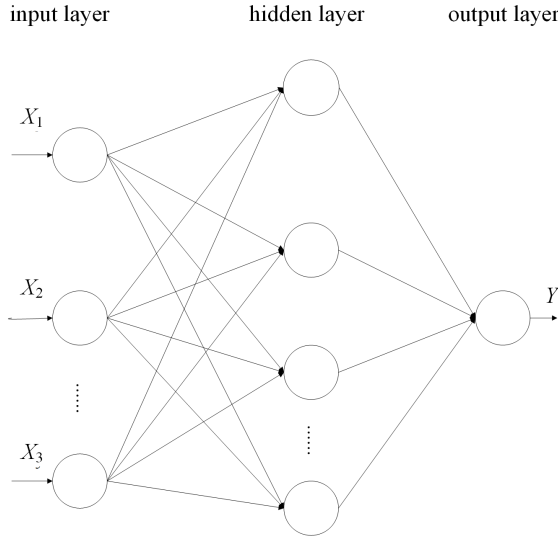


Fig. 1. BP neural network model

2.2. Multi-objective prediction method

According to the work done by Yang et al. [17] and Ojalehto et al. [18], the multi-objective programming method could take requirements put forward by highway planners and the users into consideration at the same time, and also reflect the multiple factors affecting highway network grade structure optimization. The mathematical description of highway network's technical grade structure optimization model is as follows:

2.2.1. Objective function.

- The minimum of highway network construction funds given by the formula

$$\min \left\{ \sum_{j=0}^2 p_j(t) [l_j(t) - l_j(t-1)] + \sum_{j=3}^5 q_j(t) [l_j(t-1) - l_j(t)] \right\}, \quad (1)$$

where l_j is the mileage of j th class highways, $p_j(t)$ is the construction cost of unit mileage for j th class highways which are newly built in year t and $q_j(t)$ is the construction cost of unit mileage for j th class highways which is rebuilt into second-class highways.

- Making the highest utilization rate of highway network highest, that can be expressed as

$$\min |S_N(t) - 1|, \quad (2)$$

where $S_N(t)$ is the traffic saturation degree in t th year.

- The maximum traffic capacity of highway network, that is,

$$\max C_N(t) = \sum_{j=0}^5 C_j(t)P_j(t), \quad (3)$$

where $C_j(t)$ is the traffic capacity (capacity per day) of j th class highway in highway network in t th year. Symbol $P_j(t)$ denotes the mileage weight of its j th class highway that is given by the relation

$$P_j(t) = l_j(t)/L(t), \quad L(t) = \sum_{j=0}^5 l_j. \quad (4)$$

- The highest average technical level of highway network expressed as

$$\min J_N(t) = \sum_{j=0}^5 J_i(t)P_j(t), \quad (5)$$

where $J_i(t)$ represents the technical level of j th section in t th year.

- And finally, the minimum average vehicle travel time of highway network expressed as

$$\sum_{j=0}^5 K_j l_j(t) \leq Q_{\text{NTF}} T_N. \quad (6)$$

Here, K_j is the designed traffic density of j th class highway (capacity per day); Q_{NTF} denotes the average daily amount of vehicles and their daily average kilometers in planning year(s) within the highway network. Its value can be determined from the formula

$$Q_{\text{NTF}} = \left(\frac{W_1}{n_1 a_1} + \frac{W_2}{n_2 a_2} \right) \times \frac{\beta}{365}. \quad (7)$$

Symbols W_1 and W_2 refer to freight and passenger turnover within a region respectively, while n_1 and n_2 is the average rated tonnage and the average number of seats of both trucks and buses separately; a_1 and a_2 are the actual load rates of trucks and buses; β is the integrated correction coefficient which is related to through traffic, and T_N is the average travel time in unit mileage within a highway network.

2.2.2. Constraint conditions

- Sum of mileage

$$\sum_{j=0}^5 l_j = L(t). \quad (8)$$

- Mileage $L_{\text{eq}}(t)$ of highways with different technical levels

$$L_{\text{eq}}(t) = \sum_{j=0}^5 l_j(t) \mu_j, \quad (9)$$

where μ_j is the conversion factor given as $\mu_j = C_j/C_2$. Symbols C_j and C_2 are the traffic capacity of j th class and secondary highways, respectively.

- Key projects

$$\alpha_j(t) \leq l_j(t) \leq \beta_j(t), \quad j = 0, 1, 2, 3, 4, 5. \quad (10)$$

Here, $\alpha_j(t)$ and $\beta_j(t)$ represent the lower and upper bounds used as standards for j th class highway construction.

3. Experimental tests and analysis

3.1. Scale forecast of highway network based on BP neural network

GDP, total population, the number of civil motor vehicle ownership, passenger capacity and volume of freight traffic are regarded as nodes in the input layer of Back-Propagation Neural Network (BPNN); the total mileage of highway network is chosen as the output node. The 13th Five-Year Development Plan of Highway Transportation in Hangzhou began in 2015, ends in 2020, and looks forward to 2025. The simulation and the predicted values of BPNN are showed in Table 1 and the plot of training regression is presented Fig. 2. More information about TCM can be obtained in the research done by Yi et al. [19]. The mean absolute error (MAE), the mean absolute percentage error (MAPE), and the root mean square error (RMSE) are used to compare the prediction performance between these three methods. The comparing results which shows the advantage of BPNN in dealing with nonlinear problems are shown in Table 2.

3.2. Result correction

Markov state transfer situation and Markov state transfer probability matrix P are showed in Table 3 and holistic prediction result are listed in Table 4.

3.3. Technical grade structure optimization for highway network

Data such as the average cost invested in highways of all grades, adaptable traffic and designed traffic density, etc., are derived from various surveys, statistics and related norms. All of the norms come from the newly published Technical Standard of Highway Engineering of People's Republic of China, which was compiled by Wu et al. [20]. The objective functions of the model and also constraint conditions are listed below. The input parameters are listed in Tables 5–8.

Table 1. Actual length (km) of highway network and predicted length (km) with BPNN

year	actual value (Av)	predicted value (Pv)	absolute error	relative error (%)
1994	5227	5216	11	0.21
1995	5360	5488	-128	-2.30
1996	5376	5500	-124	-2.20
1997	5570	5548	22	0.39
1998	5756	5712	44	0.77
1999	6407	6320	87	1.37
2000	6339	6422	-83	-1.29
2001	6396	6498	-102	-1.56
2002	6560	6712	-152	-2.26
2003	6793	6916	-123	-1.78
2004	7758	7590	168	2.21
2005	10644	10875	-231	-2.12
2006	12181	12108	73	0.60
2007	13463	13329	134	1.00
2008	13700	13497	203	1.50
2009	14265	13922	343	2.46
2010	14399	14143	256	1.81
2011	14586	14688	-102	-0.69
2012	14938	15074	-136	-0.90
2013	15900	15741	159	1.01
2014	16024	16197	-173	-1.07
2015		16244		
2016		16340		
2017		16424		
2018		16536		
2019		16647		
2020		16713		
2021		16815		
2022		16903		
2023		16997		
2024		17082		
2025		17169		

Table 2. Comparison between BPNN, 2-dimensional autoregressive model (AR(2)) and travel cost prediction method (TCM)

	BPNN	AR (2)	TCM
MAE	135.9	775.4	385.2
MAPE ($\times 100\%$)	1.4	7.3	3.8
RMSE	156.0	1192.5	428.7

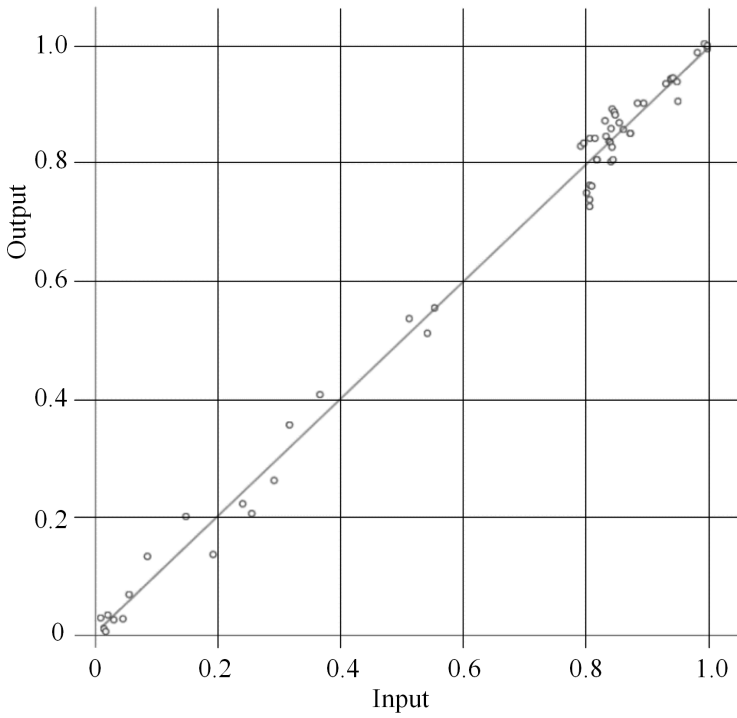


Fig. 2. Training regression of BP neural network model

Table 3. Status transfer of Markov chain

state	α	β	γ	total
α	4	1	1	6
β	1	2	3	6
γ	3	2	3	8
total	8	5	7	20

3.3.1. Objective function.

1. The minimum of highway network construction funds:

$$\begin{aligned} \min f_1 = & 5000(l_0 - l_0^0) + 1200(l_1 - l_1^0) + 300(l_2 - l_2^0) + 120(l_3 - l_3^0) + \\ & + 70(l_4 - l_4^0) + 30(l_5 - l_5^0) = 5000l_0 + 1200l_1 + 300l_2 + 120l_3 + 70l_4 + 30l_5 - \\ & - (5000l_0^0 + 1200l_1^0 + 300l_2^0 + 120l_3^0 + 70l_4^0 + 30l_5^0), \end{aligned} \quad (11)$$

where l_j^0 denotes the mileage of j th class highways in the last year.

2. The maximum traffic capacity of highway network:

$$\begin{aligned} \max f_2 = & 55000 \frac{l_0}{16406} + 30000 \frac{l_1}{16406} + 15000 \frac{l_2}{16406} + 6000 \frac{l_3}{16406} + \\ & + 2500 \frac{l_4}{16406} + 400 \frac{l_5}{16406} = 3.352l_0 + 1.828l_1 + 0.914l_2 + 0.366l_3 + \\ & + 0.152l_4 + 0.024l_5. \end{aligned} \quad (12)$$

3. The minimum average vehicle travel time of highway network:

$$\min f_3 = 45l_0 + 30l_1 + 20l_2 + 10l_3 + 3.5l_4 + 1.2l_5, \quad (13)$$

4. The highest average technical level of highway network:

$$\max f_4 = \frac{l_1}{16406} + 2 \frac{l_2}{16406} + 3 \frac{l_3}{16406} + 4 \frac{l_4}{16406} + 5 \frac{l_5}{16406}. \quad (14)$$

Table 4. Modified forecast value of highway scale of Hangzhou

year	predicted value	state vector	state vector value	predicted value interval	probability (%)
2015	16244	α	0.17	15756.7–16081.6	17
	16244	β	0.33	16081.6–16406.4	33
	16244	γ	0.50	16406.4–16731.3	50
2020	16813	α	0.46	16308.6–16644.9	46
	16813	β	0.23	16644.9–16981.1	23
	16813	γ	0.31	16981.1–17317.4	31
2025	17169	α	0.46	16653.9–16997.3	46
	17169	β	0.23	16997.3–17340.7	23
	17169	γ	0.31	17340.7–17684.1	31

3.3.2. Constraint conditions.

1. The total mileage:

$$l_0 + l_1 + l_2 + l_3 + l_4 + l_5 = 16406. \quad (15)$$

2. The mileage of expressway in the Year 2015 is more than 583 km:

$$l_0 \geq 583. \quad (16)$$

3. The mileage of secondary and above class highways:

$$l_0 + l_1 + l_2 \geq 2790, . \tag{17}$$

4. The mileage of fourth and above class highways

$$l_0 + l_1 + l_2 + l_3 + l_4 \geq 13125. \tag{18}$$

Table 5. Upper bound of traffic volume for the different grade highways

Grade	Upper traffic volume (converted to standard passenger car, vehicle/day)
Highway	55000
First-grade	30000
Second-grade	15000
Third-grade	6000
Fourth-grade	2500
Substandard	400

Table 6. Planned traffic density for different grade highways in Hangzhou

Grade	Density (converted to standard passenger car, vehicle/kilometer)
Highway	45.0
First-grade	30.0
Second-grade	20.0
Third-grade	10.0
Fourth-grade	3.5
Substandard	1.2

Table 7. Turnover volume of freight and passenger for regional development planning of Hangzhou

year	W_1	W_2
2015	315.6	160.2
2020	545.8	320.8
2025	860.2	684.7

Table 8. Other related parameter values

year	n_1	a_1	n_2	a_2	β	Q_{NTF}	T_N (h/km)
2015	4.8	0.56	40	0.35	2.4	847256360	0.0172
2020	5	0.6	40	0.35	2.4	1346943249	0.0164
2025	5.2	0.64	40	0.35	2.4	2021133373	0.0156

3.3.3. *Multi-objective programming model.* The multi-objective programming model consists of the following relations:

$$\begin{aligned}
 & \min R_1 d_1^+ + R_2 d_2^- + R_3 d_3^+ + R_4 d_4^-, \\
 & 5000l_0 + 1200l_1 + 300l_2 + 120l_3 + 70l_4 + 30l_5 + d_1^- - d_1^+ = e_1, \\
 & 3.352l_0 + 1.828l_1 + 0.914l_2 + 0.366l_3 + 0.152l_4 + 0.024l_5 + d_2^- - d_2^+ = e_2, \\
 & 45l_0 + 30l_1 + 20l_2 + 10l_3 + 3.5l_4 + 1.2l_5 + d_3^- - d_3^+ = e_3, \\
 & \frac{l_1}{16406} + \frac{2l_2}{16406} + \frac{3l_3}{16406} + \frac{4l_4}{16406} + \frac{5l_5}{16406} + d_4^- - d_4^+ = e_4, \quad (19) \\
 & l_0 + l_1 + l_2 + l_3 + l_4 + l_5 = 16406, \\
 & l_0 \geq 583, \\
 & l_0 + l_1 + l_2 \geq 2790, \\
 & l_0 + l_1 + l_2 + l_3 + l_4 \geq 13125.
 \end{aligned}$$

Here, e_1 denotes the funds invested in the Hangzhou's transportation planning, e_2 is the desired traffic capacity of highway network within the planning period e_3 is calculated as $Q_{\text{NTF}} \cdot T_k$, and e_4 stands for the lower bound of the average technical grade of highways. The corresponding parameters and optimized values are summarized in Tables 9 and 10, respectively.

Table 9. Parameter values

year	e_1	e_2	e_3	e_4
2015	10000000	24000	14572809.39	3.10
2020	15000000	30000	22089869.28	3.06
2025	12000000	32000	31529680.63	3.02

Table 10. Highway grade optimization

Year	Highway	First grade	Second grade	Third grade	Fourth grade	Substandard	Total
2015	590	808	1550	1120	11544	794	16406
2020	650	830	1610	1260	12294	0	16644
2025	705	885	1700	1457	12250	0	16997

4. Results and discussion

It can clearly be seen from the outcome that the growth rates of highway-scale with different grades, except for the fourth grade and substandard highway, are steady. This growth trend is reasonable by comparatively analyzing the city's economic and social development status and planning under the condition of "new normal". And the growth rate of the total scale between 2020 and 2025 is faster than that between 2015 and 2020 due to the fact that Hangzhou was the host city of G20 summit in 2016 and the Asian Games in 2022 may account for it. Heggie [21] showed the impacts which was brought by Olympic Games on highway construction. In other words, the objective functions and the constraints set in the paper is rational.

The substandard highway is diminished to 0, it is in accordance with the initial 13th Five-Year Plan of Hangzhou. It reflects that the content of key projects in the constraints is acceptable. In the year of 2020, the scale of fourth grade will rise to 12294, while this figure will decrease to 12250 five years later. All substandard highways convert to the fourth grade highway in 2020, and it may explain the reason why the scale of the fourth grade highway has an increase. In this 10-year period of time, the scale of the fourth grade highway represents a declining trend. It conforms to the expectation of the optimal structure of regional highway network. So the model built in this paper can be applied to both the prediction and analysis of regional highway network's rational scale.

5. Conclusion

This article adopts the method of hybrid forecast and comprehensively utilizes Back-Propagation Neural Network, Markov chain and multi-objective programming method to improve the accuracy and the reliability of forecasting. Highway network mileage and its grade structure are both predicted, which can better reflect the quantity and quality requirements of the development of the regional highway network. As a result, regional highway network planning method is optimized.

In view of the complexity of highway network, more improvements should be made when deciding the nodes in the input layer of BPNN as well as the classification of Markov's status area. Meanwhile, some related factors, such as land use and natural resources, are not considered in the presented model. Further researches may focus on taking these factors into consideration when set objective functions and constraints. In addition, different prediction approaches (statistical methods (Zou et al. [22], Zou et al. [23]) and other machine learning methods (Jiang et al. [24]) will be considered to evaluate the performance of the proposed model.

References

- [1] J. CHEN, J. CHEN, Y. MIAO, M. SONG, Y. FAN: *Unbalanced development of inter-provincial high-grade highway in China: Decomposing the gini coefficient*. Transporta-

- tion Research Part D: Transport and Environment 48 (2016), 499–510.
- [2] A. QI, H. CHEN: *Research on China construction project management paradigms change and development in the last 30 years*. Procedia– Social and Behavioral Sciences 119 (2014), 321–328.
 - [3] E. MARIN: *Demand forecast, congestion charge and economic benefit of an automated highway network for the Paris agglomeration*. Transport Policy 10 (2003), 107–120.
 - [4] S. NOGUÉS, E. GONZÁLEZ-GONZÁLEZ: *Multi-criteria impacts assessment for ranking highway projects in Northwest Spain*. Transportation Research Part A: Policy and Practice 65 (2014), 80–91.
 - [5] F. WANG, X. HAN: *Research on the optimal density of highway network*. Procedia–Social and Behavioral Sciences 96 (2013), 1556–1565.
 - [6] M. LI, W. CHEN: *Application of BP neural network algorithm in sustainable development of highway construction projects*. Physics Procedia 25 (2012), 1212–1217.
 - [7] M. K. JHA, H. G. OGALLO, O. OWOLABI: *A quantitative analysis of sustainability and green transportation initiatives in highway design and maintenance*. Procedia–Social and Behavioral Sciences 111 (2014), 1185–1194.
 - [8] K. W. TSOU, H. T. CHENG, F. Y. TSENG: *Exploring the relationship between multi-level highway networks and local development patterns—a case study of Taiwan*. Journal of Transport Geography 43 (2015), 160–170.
 - [9] R. P. ALDRICH, J. EL-ZABET, S. HASSAN, J. BRIGUGLIO, E. ALIAJ, M. RADCLIFFE, T. MIRZA, T. COMAR, J. NADOLSKI, C. D. HUEBNER: *Monte Carlo tests of small-world architecture for coarse-grained networks of the United States railroad and highway transportation systems*. Physica A: Statistical Mechanics and its Applications 438 (2015), 32–39.
 - [10] A. BONNAFOUS: *The economic regulation of french highways: Just how private did they become?* Transport Policy, Special Issue 41 (2015), 33–41.
 - [11] Y. XU, T. YOU, C. DU: *An integrated micromechanical model and BP neural network for predicting elastic modulus of 3-D multi-phase and multi-layer braided composite*. Composite Structures 122 (2015), 308–315.
 - [12] S. DU, R. XU, D. HUANG, X. YAO: *Markov modeling and analysis of multi-stage manufacturing systems with remote quality information feedback*. Computers & Industrial Engineering 88 (2015), 13–25.
 - [13] R. IWANKIEWICZ: *Integro-differential Chapman–Kolmogorov equation for continuous-jump Markov processes and its use in problems of multi-component renewal impulse process excitations*. Probabilistic Engineering Mechanics 26 (2011), No. 1, 16–25.
 - [14] V. KHMEL, S. ZHAO: *Arrangement of financing for highway infrastructure projects under the conditions of Public–Private Partnership*. IATSS Research 39 (2016), No. 2, 138–145.
 - [15] G. D’AMICO, F. PETRONI, F. PRATTICO: *Reliability measures for indexed semi-Markov chains applied to wind energy production*. Reliability Engineering & System Safety 144 (2015), 170–177.
 - [16] I. MUKHERJEE, S. ROUTROY: *Comparing the performance of neural networks developed by using Levenberg–Marquardt and Quasi-Newton with the gradient descent algorithm for modelling a multiple response grinding process*. Expert Systems with Applications 39 (2012), 2397–2407.
 - [17] N. YANG, M. W. KANG, P. SCHONFELD, M. K. JHA: *Multi-objective highway alignment optimization incorporating preference information*. Transportation Research Part C: Emerging Technologies 40 (2014), 36–48.
 - [18] V. OJALEHTO, D. PODKOPAEV, K. MIETTINEN: *Agent assisted interactive algorithm for computationally demanding multiobjective optimization problems*. Computers & Chemical Engineering 77 (2015), 105–115.
 - [19] J. YI., L. LI, B. WU, Y. WANG: *Research on scale forecast of regional highway network*. Transportation Science and Technology 34, (2011), No. 1, 100–103.
 - [20] Y. WU, T. LIU: *Technical standard of highway engineering*. Beijing, China Communications Press (2014).

- [21] T. W. HEGGIE: *Traveling to Canada for the Vancouver 2010 Winter olympic and paralympic games*. *Travel Medicine and Infectious Disease* 7 (2009) No. 4, 207–211.
- [22] Y. ZOU, X. HUA, Y. ZHANG, Y. WANG: *Hybrid short-term freeway speed prediction methods based on periodic analysis*. *Canadian Journal of Civil Engineering* 42 (2015), No. 8, 570–582.
- [23] Y. ZOU, X. ZHU, Y. ZHANG, X. ZENG: *A space-time diurnal method for short-term freeway travel time prediction*. *Transportation Research Part C: Emerging Technologies* 43 (2014), 33–49.
- [24] H. JIANG, Y. ZOU, S. ZHANG, J. TANG, Y. WANG: *Short-term speed prediction using remote microwave sensor data: Machine learning versus statistical model*. *Mathematical Problems in Engineering* (2016), paper 9236156.

Received November 16, 2016

Cascade design and optimization for hydraulic torque-retarder assembly

JINGYAN WU¹, QINGDONG YAN¹, CHENG LIU¹, WEI WEI¹

Abstract. In order to improve the power density of transmission system, a hydraulic torque-retarder assembly, which is a combination of torque converter and hydraulic retarder, is proposed. The parameterized torus and blade design approach is carried out, and CFD analysis processes are automated by programs and secondary development technique. Geometry modeling, mesh generating and CFD analysis are integrated and a 3D flow design platform is built, thus the combination of CFD and optimization is realized. The 3D flow design platform is employed to design a hydraulic torque-retarder assembly and the results show that the new approach is able to optimize the cascade of hydraulic torque-retarder. A high brake torque is achieved without sacrificing too much power and efficiency.

Key words. Hydraulic torque-retarder assembly, cascade construction, design optimization..

1. Introduction

Hydraulic transmission, using fluid as the working medium transform between mechanical energy and fluid kinetic energy, can achieve the purpose of flexible transmission power and auxiliary braking. Since 1905 by the German Hermann Fottinger invention, after more than one hundred years' development, at present it has been widely used in ships, locomotives, engineering machinery, drilling equipment, fans and various military and civilian vehicles.

The main form of hydraulic transmission is the hydraulic torque converter and hydraulic coupling (as shown in Fig. 1). The typical automotive torque converter includes pump wheels, turbine and wheel guided three impellers, wherein the pump wheel is connected with the power source, the turbine and load side are connected, and due to the presence of the guide pulley, the torque converter has torque capacity, which can broaden the stable working range and adaptability of the engine. At the same time, in order to improve efficiency, integrated hydraulic torque converter is also equipped with one-way coupling and locking clutch. The hydraulic coupling

¹Beijing Institute of Technology, Beijing, 100081, China

consists of a pump impeller and a turbine, and the blades are mostly simple straight blades. This can ensure that the active and passive flexible connection between the shaft, when the hydraulic coupling is fixed at one end, can play the role of deceleration brake, known as the hydraulic reducer.

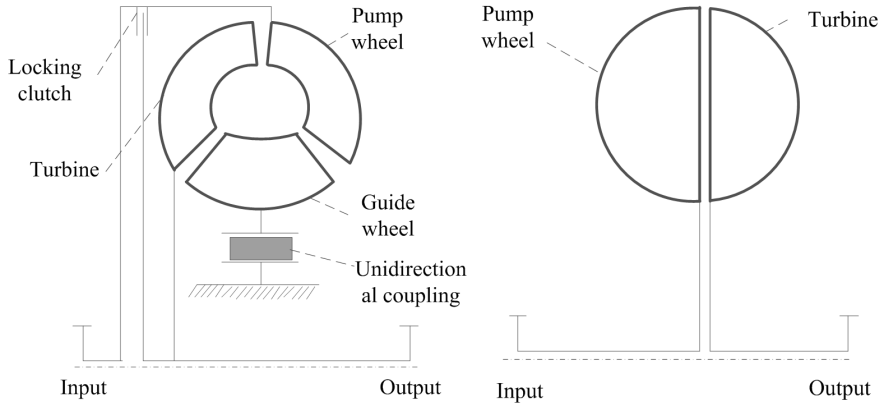


Fig. 1. Typical hydraulic transmission structure diagram

In order to improve the vehicle power density and simplify the transmission system structure, the researchers proposed the hydraulic torque converter and hydraulic reducer function integration program, mainly including the guide wheel reverse type, such as VOITH DIWA gearbox hydraulic components, as well as the division of wheel-type hydraulic torque reduction device. A model of traction and braking characteristics of hydraulic torque reduction device based on one-dimensional beam flow theory [1]. The flow field analysis of hydraulic torque reduction device is carried out and its integrated design method is explored. The idling characteristics of the guide pulley on the basis of CFD, and determined the reasonable boundary conditions of the flow field analysis [2]. With the development of computer technology and CFD, the design method of hydraulic components is also changed from the traditional one-dimensional beam theory to three-dimensional flow design. Establishment of integrated three-dimensional flow design platform, which includes integrates cascade system modeling, CFD analysis and intelligent optimization algorithms, is the development trend of hydraulic component design at present [3–5].

2. Geometric design of cascades for hydrodynamic torque reducer

The design of the circulation circle of the hydraulic torque reduction device is carried out by dividing the work wheel form. There exist two types of structure: split pump wheel type and split turbine type (as shown in Fig. 2). By adding two rigidly connected large and small brake wheels, the brake will clutch. In the traction condition, the brake clutch will separate, and the brake wheel enter the idling state.

While the brake clutches, the oil flow in the circulation forms a large number of vortices. Compared with the splitter pump wheel-type hydraulic torque reduction device, the split-turbine type requires more than one layer of sleeve shaft, the structure is more complex, which increases the radial size. Therefore, the design method of the cascade system is designed, based on the segmented pump wheel-type torque converter.

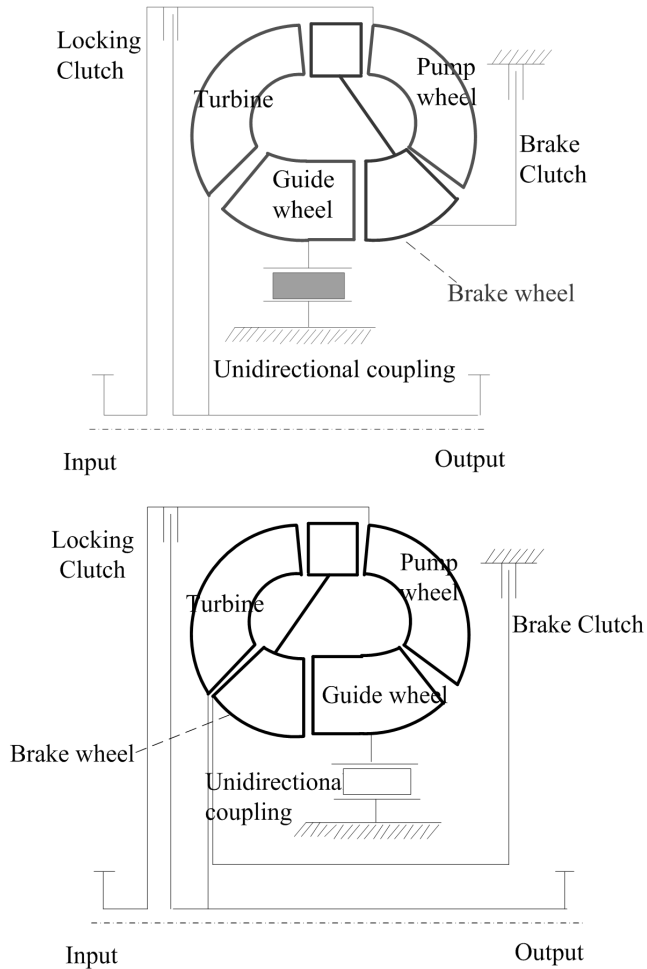


Fig. 2. Hydraulic torque reduction gear structure diagram: up-split pump wheel type, bottom-split turbine type

2.1. Hydrodynamic torque deceleration device cyclical circle parametric design

Split pump wheel-type hydraulic torque reduction device cyclic circle is obtained in the original three-component torque converter on the basis of the pump wheel division, its pump wheel, turbine circular shape and prototype to keep consistent, guide wheel circle from the center of the circle. The divided circle of the guide wheel generates a small braking wheel near the pump impeller part. The part near the turbine part is reserved as a guide wheel. In the middle, a straight line is used. The straight line is tangent to the arc, so that the first derivative of the circle is continuous, thus ensuring good flow characteristics.

In general, the hydraulic torque converter guide wheel circle consists of a circular arc, and the circular circle is mostly symmetrical. Suppose the prototype torque converter pulley width is b_s , then the hydraulic torque reducer's axial increment is defined as the inlet and outlet of the impeller being aligned while the impeller is divided by 2–3 mm and the wheel is in symmetrical movement. In order to ensure traction performance after the redesign of the torque converter, the axial increment must satisfy the guide wheel's width that still remains b_s .

2.2. Hydraulic torque reduction device blade parametric design

Hydraulic torque device installs speed blade design process shown in Figure 3, Firstly, the design of circular circle and the development of blade are designed. Then the conformal transformation method is used to map the two-dimensional blade line to space to form three-dimensional blade.

In order to reduce the impact and minimize the energy loss, we change the current mainstream hydraulic retarder blade shape. The straight brake wheel blades are used, that is, their inlet angle and the outlet angle are equal ($\beta_1 = \beta_2$) and blade bone line is a straight line. The thickening rule adopts the streamlined thickening, and the thickness is superimposed on the blade bone line to obtain the two-dimensional profile of the blade.

Split pump wheel type hydraulic torque reduction gear brake wheel according to the radius can be divided into large braking wheel and small brake wheel, the cascade can be regarded as an extension of the pump wheel blades (as shown in Fig. 4), the large and small brake wheel blades are parameterized by means of deflection angle. The blade angles are

$$\beta_S = \beta_{P1} - \Delta\beta_S, \quad \beta_B = \beta_{P2} - \Delta\beta_B,$$

where $\Delta\beta$ is the brake wheel blade bone line deviation from the pump wheel blade into and out of the angle: clockwise is positive, counterclockwise is negative. The subscript S represents a small braking wheel, the subscript B represents a large braking wheel. The subscript P represents the pump impeller, 1 represents the inlet and 2 represents the outlet.

The large and small brake wheel blades are modeled with different blade angles,

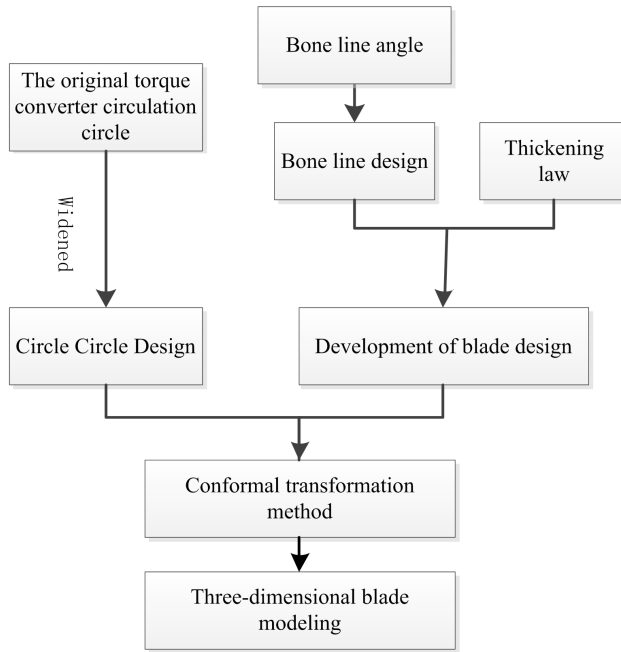


Fig. 3. Blade design flow of hydraulic torque reducer

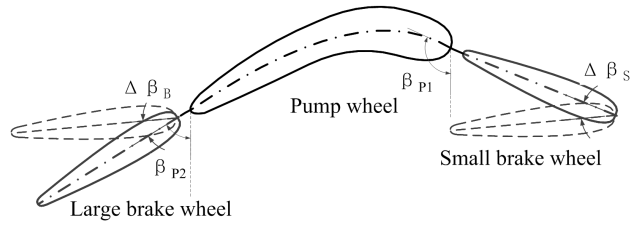


Fig. 4. Brake wheel and pump wheel blade expansion diagram

and their 3D solid shapes are shown below (Figs. 5 and 6).

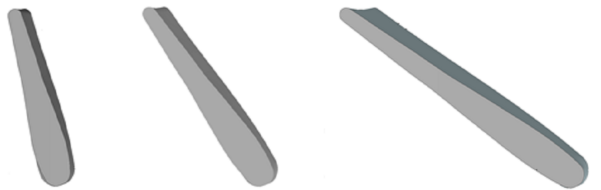


Fig. 5. Examples of large brake wheel blades: left $-\Delta\beta_B = 15^\circ$, middle $-\Delta\beta_B = 0^\circ$, right $-\Delta\beta_B = -15^\circ$



Fig. 6. Examples of small brake wheel blades: left $-\Delta\beta_S = 15^\circ$, middle $-\Delta\beta_S = 0^\circ$, right $-\Delta\beta_S = -15^\circ$

3. Optimal design of cascades for torque converter based on CFD

The hydraulic torque device can realize the torque function under the traction condition and the deceleration function under the braking condition. In the traction conditions, the brake clutch separates and the brake wheel enters the idling state. The idling state has an additional impact and friction with hydraulic power losses. In the braking state, the brake clutch bites and oil serves for the purpose of deceleration. The design of the hydraulic torque reduction gears needs to be based on the traction performance as far as it is possible to get good braking performance.

3.1. Optimization design system of hydraulic torque reducer

In order to realize the optimization design of the hydraulic torque reduction device based on the three-dimensional flow field analysis, a set of integrated optimization system of hydraulic torque reducer with integrated geometric modeling, flow channel division, CFD analysis and intelligent optimization algorithm was established (as shown in Fig. 7).

As shown in Fig. 7, in the case of the torque converter, the main design variables include the parameters of the circular wheel and cascade brake gears. The cascade brake gears' parameters are designed with the above method. Through the blade modeling and geometric modeling and CFD analysis, the traction and braking performance is optimized. Finally, the optimization algorithm is used to optimize the design goal by changing the design variables, so as to form the complete design flow. The concrete realization process is shown in Fig. 8, first of all, using Matlab program to achieve the parameterization of the brake wheel blade generation, the blade profile and circular circle are introduced into the TurboGrid for flow channel geometry modeling, and then the flow channel geometry is introduced into ICEM-CFD to automatically divide the unstructured grid. At last, the CFD calculation model and the CFD calculation model of braking condition are set up respectively. The characteristics of the hydraulic torque reduction device are calculated to obtain the performance index. The entire process is supplemented with the script file, command line, batch processing and other automated processing. By using the platform, the performance evaluation, parameter sensitivity analysis and optimization design

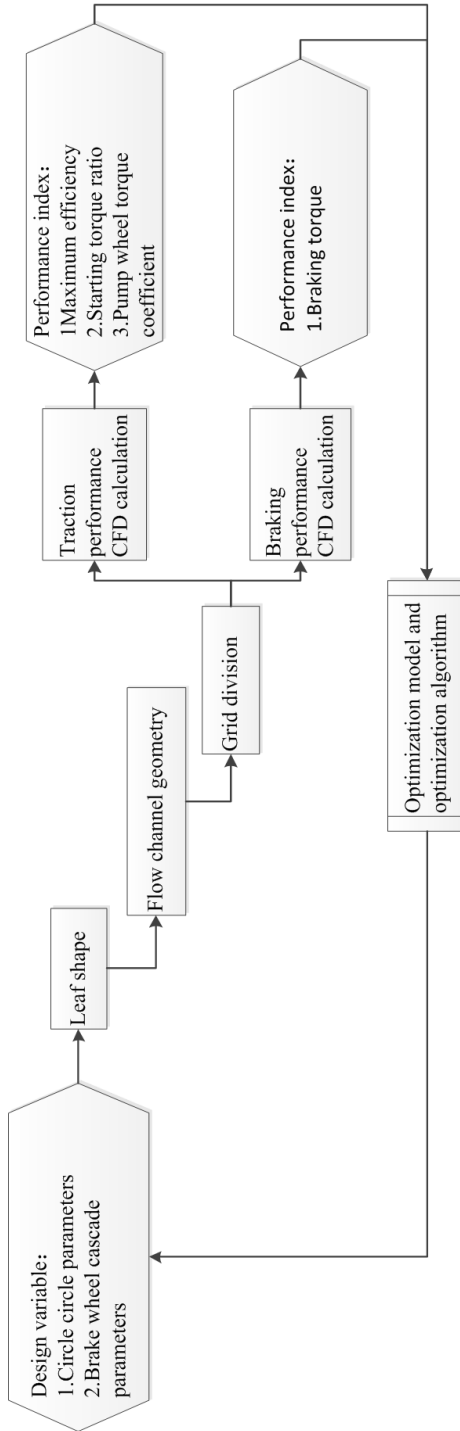


Fig. 7. Framework of 3D flow optimal design system

of the hydraulic torque reduction device can be realized [6].

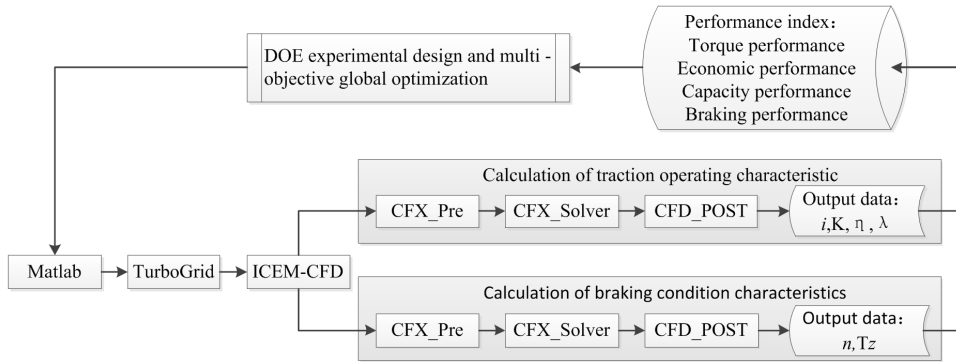


Fig. 8. Three-dimensional flow optimization design platform

3.2. CFD calculation model and verification

CFD calculation can directly obtain the internal velocity field, pressure field and other flow field state parameters distribution of the hydraulic element, and also extract its torque and other external characteristics. In order to facilitate the construction of the computational model of the flow field and automatic processing of the calculation process, the periodic steady state method is used to calculate the traction working condition of the hydraulic torque-retarder and the characteristics of the braking working condition.

The geometrical runner model of $1/z$ (z being the number of blades) was established and covered by unstructured mesh. The calculation model of the hydraulic torque-retarder was established, as shown in Fig. 9. Based on the analysis of the mesh independence, the number of the mesh cells of each impeller is about 200000 and the total number of cells is 1486276.

Because of the different rotational speeds of impellers in hydrodynamic torque-retarder, the mixed plane model is used to deal with the boundary conditions of the impeller inlet and outlet interfaces. The different velocity regions are simulated as "mixed plane" in the interface. The calculated total pressure, velocity, turbulence kinetic energy, and dissipation rate in the upstream are averaged and then passed to the downstream region to be a boundary condition for the downstream channel inlet face. While the average value of the static pressure calculated at the downstream channel inlet face can be taken as the boundary conditions of the upstream runner exit, so the above process will be iterated until it converges. In the inner and outer rings and the blade surface are used no sliding boundary conditions, that is, the normal and the tangential velocities and solid velocity of the fluid near the wall surface are equal. The blades of each impeller of the hydrodynamic torque-retarder are evenly distributed. The single blade flow channel model is adopted in the calculation model. The periodic boundary conditions are imposed on both sides of the flow channel, and the impeller is given the boundary condition of speed [3]. CFXTM

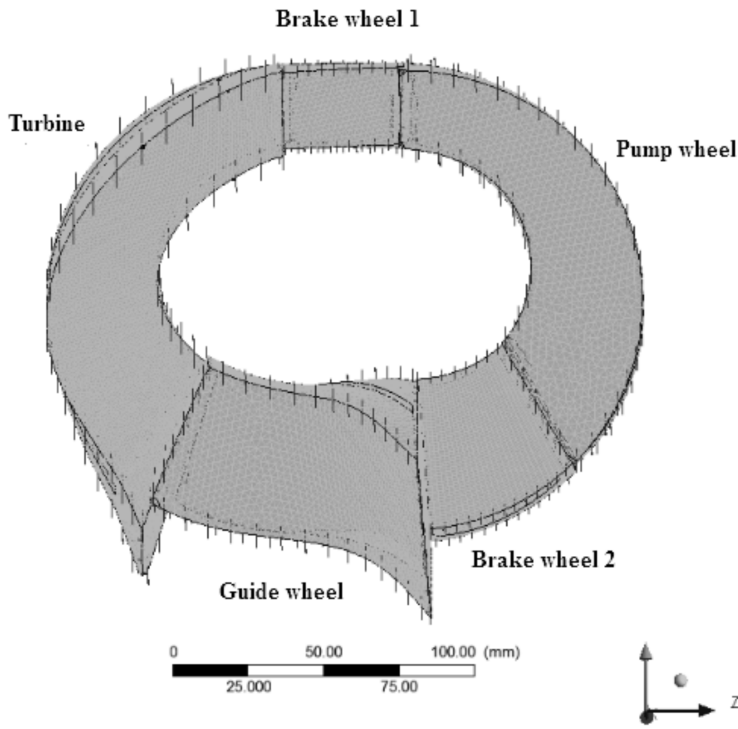


Fig. 9. Computer model of hydraulic torque reduction device

is used to build the CFD model of the hydraulic torque reduction device, and the CFD model attributes and other settings are shown in Table 1 below.

Table 1. CFD model settings

Analysis of types	Steady state calculation
Fluid property	Density: 860 kg m^{-3} , dynamic viscosity: $2 \times 10^{-4} \text{ kg m}^{-1} \text{ s}^{-1}$
Turbulence model	SST (Shear stress transport model)
Interface model	Stage (Mixed plane model)
Wall boundary	No sliding wall, periodic boundary

The hydraulic torque converter was designed with the 375 mm diameter three-component integrated torque converter as the prototype. The increment of the circular axial is $\Delta b = 50 \text{ mm}$ and the braking wheel blade angle is $\Delta\beta_B = \Delta\beta_S = 0$. The above method is used to design the cascade system of the hydraulic torque-retarder, and the prototype is processed to test the performance of the traction and braking working conditions. The results of the CFD model are depicted in Fig. 10.

It can be seen from the comparison chart that the CFD models of the traction

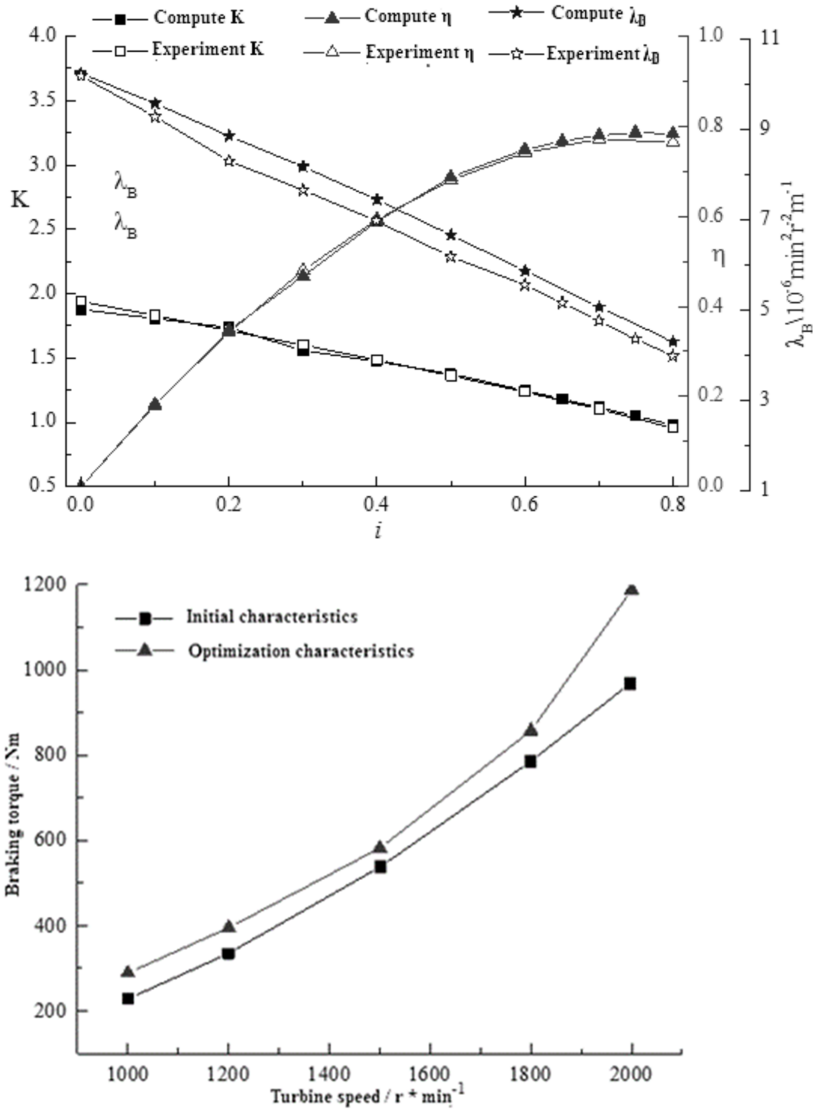


Fig. 10. Comparison of calculation characteristics and experimental characteristics of the hydraulic torque-retarder: up-traction working conditions, bottom-braking working conditions

and braking working conditions have higher precision. The torque ratio of traction working condition and the efficiency prediction precision are higher. The maximum torque error is less than 3%, and the torque coefficient of the pump pulley is slightly higher than the experimental value. The maximum error is less than 7%, and the

prediction error of the braking torque is within 10 %.

The initial prototype test data comparison of the prototype three-component integrated torque converter and hydraulic torque-retarder is in Table 2 showing that the hydraulic torque converter power and economy decline after adding brake wheel, especially the efficiency, the maximum efficiency is less than 80 %. The initial cascade system needs to be optimized and designed.

Table 2. Comparison of performance of the prototype hydraulic torque converter and hydraulic torque-retarder

	K_0	λ_0 ($\text{min}^2\text{r}^{-2}\text{m}^{-1}$)	η_{max} (%)	λ_z ($\text{min}^2\text{r}^{-2}\text{m}^{-1}$)
Prototype torque converter test data	2.02	8.7×10^{-6}	85.1	
Test data of initial hydraulic torque reducer	1.88	10.2×10^{-6}	78.5	3.98×10^{-6}

3.3. Hydraulic torque-retarder optimization design

Hydrodynamic torque-retarder adds the brake wheel on the basis of the torque converter, and it will have a certain impact on the performance of traction conditions. The performance indexes of traction torque converter have many conditions under a variety of indicators, and the most common are starting torque ratio K_0 , starting pump wheel torque coefficient λ_0 and maximum efficiency η_{max} . The braking conditions of braking performance can be described by index λ_z , which is the coefficient expressing the average braking torque and can be used to characterize the braking capacity. In the design of hydraulic torque-retarder, the principle is as follows: 1) The original hydraulic torque converter traction performance is affected as little as possible. 2) The brake torque is as large as possible. In order to simplify the optimization model, the main performance indicators in the traction conditions are normalized and then synthesized into the overall performance index F of the traction condition by using the linear weighting method. The expression is as follows:

$$F = \sum_{i=1}^3 m_i f_i,$$

where the subscripts 1, 2 and 3 represent, in turn, K_0 , λ_0 and η_{max} , m_i is a weighting coefficient given according to the importance degree of each performance index, and symbols f_i represent the difference values between the performance of the hydraulic torque-retarder and the original torque converter, calculated as

$$f_1 = \frac{K_{0\text{TC}} - K_{0\text{TCR}}}{K_{0\text{TC}}} \text{ if } K_{0\text{TC}} > K_{0\text{TCR}}, \text{ otherwise } f_1 = 0,$$

$$f_2 = \frac{\lambda_{0TC} - \lambda_{0TCR}}{\lambda_{0TC}} \text{ if } \lambda_{0TC} > \lambda_{0TCR}, \text{ otherwise } f_2 = 0,$$

$$f_3 = \frac{\eta_{\max TC} - \eta_{\max TCR}}{\eta_{\max TC}} \text{ if } \eta_{\max TC} > \eta_{\max TCR}, \text{ otherwise } f_3 = 0.$$

The subscript TC denotes a prototype torque converter, and TCR denotes a hydraulic torque-retarder.

The overall performance index of the traction condition F represents the degree of deterioration of the performance of the hydraulic torque converter in comparison with the prototype torque converter. The larger the value is, the more serious is the deterioration of the traction performance. If the traction condition performance does not deteriorate, then $F = 0$. After the establishment of the comprehensive index, the optimization goal of the hydraulic torque-retarder is reduced to two, and the optimization design model is simplified to two objectives optimization problem, namely

$$\min F(f_i), \quad \max \lambda_z.$$

3.4. Hydraulic torque-retarder optimization design example

Based on the initial prototype of the hydraulic torque converter with 375 mm diameter, the index weight coefficients m_i , $i = 1, 2, 3$ of the traction working condition are taken, and the optimal parameters are set as Δb , $\Delta\beta_S$ and $\Delta\beta_B$. The design model is as

$$\min F(f), \quad \max \lambda_z, \quad \text{S.T. } 50 \leq \Delta b \leq 65,$$

$$-15^\circ \leq \Delta\beta_B \leq 15^\circ, \quad -15^\circ \leq \Delta\beta_S \leq 15^\circ.$$

The AMGA algorithm is a typical second-generation multi-objective genetic optimization algorithm, which uses the small population genetic algorithm (AMGA) based on the archive to optimize the model based on the three-dimensional flow optimization platform of the hydraulic torque-retarder. It uses an external population to archive the elitist solutions, which can use small populations and calculated quantity to obtain a large number of non-inferior solutions. The main parameters of AMGA algorithm are listed in Table 3.

Table 3. AMGA algorithm parameter setting table

Crossover probability	Mutation probability	Population size	Algebra	External archive size
1	0.02	24	20	60

A total of 240 searches were conducted. The result is shown in Fig. 11. In total, 31 non-dominated solutions were obtained. Compared with the performance of the initial hydrodynamic torque-retarder, a series of non-inferior solutions were obtained and the performances were greatly improved. Selected are the typical four groups for analysis, as shown in Table 4.

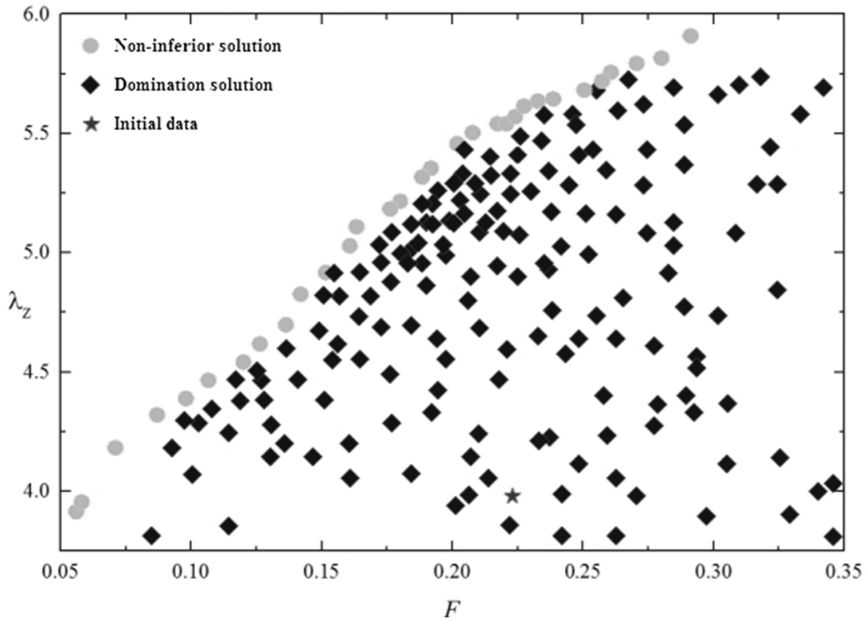


Fig. 11. AMGA optimization results

Table 4. Typical non-dominated solution

	0	1	2	3	4
F	0.223	0.056	0.098	0.121	0.282
λ_z	3.98	3.915	4.389	4.542	5.816

The 0th group in the table is the objective function value obtained from the initial prototype test data of the hydraulic torque-retarder, and 1–4 are the typical non-inferior solutions. It can be seen from the table that there is a contradiction between the overall performance indexes and braking performance of the traction conditions, that is, the pursuit of high braking performance is at the expense of the corresponding sacrifice of the traction performance, so its multi-objective optimization results is a series of non-inferior solutions rather than a single optimal solution. The fourth group solution is characterized by the highest braking torque coefficient, i.e. the best braking performance, but the expense of traction characteristics is larger. The deterioration of traction performance of the first group solution is the smallest, but the braking performance is poor. The two solutions are characterized by the fact that one of the two objective functions is optimal, but the sacrifice of the other one is great. In the second and third groups, there is no index which is optimal, but which is still non-inferior solution. The second group of solutions sacrifices the traction characteristics of the original torque converter little, and the third group has good braking performance. Designers can choose different non-inferior solutions

according to the actual needs. Because the efficiency of the initial hydrodynamic torque-retarder is low, so in order to improve the traction performance of the hydraulic torque-retarder, the parameters of the cascade system of the second group are selected, and the brake pulley width and blade angle parameters are used to optimize the braking pulley ruled vane modeling. The large and small brake pulley three-dimensional models are shown in Figs. 12. Figures 13 and 14 and Table 5 show the characteristics of the optimized hydraulic torque converter.

The results show that the dynamic property and economy of hydrodynamic torque-retarder is improved after transformation, and its maximum efficiency is improved by 5.2%. The torque performance of the hydraulic torque converter is close to that of the original three-component torque-retarder. The braking torque coefficient is also increased by 10.3%.

4. Conclusions

At present, the design method of the hydraulic torque-retarder is still 1D calculation method based on the beam theory. In order to improve the design precision, a 3D flow design platform of hydraulic torque-retarder is established for the optimal design of the hydraulic torque torque-retarder, which is combined with CFD simulation and intelligent optimization. The main conclusions are as follows:

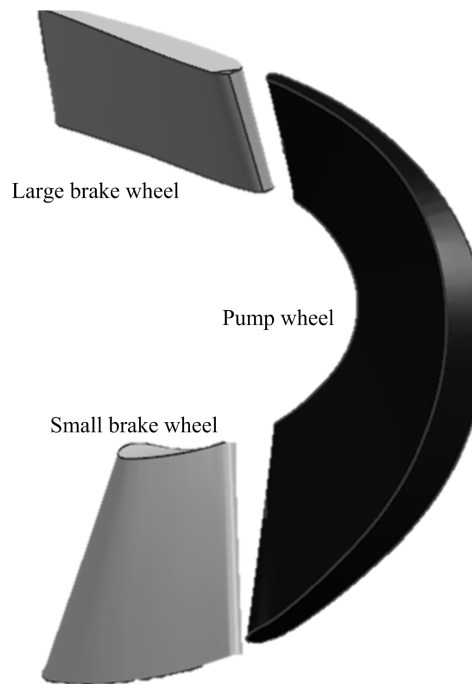


Fig. 12. 3D solid of brake pulley and pump pulley blade

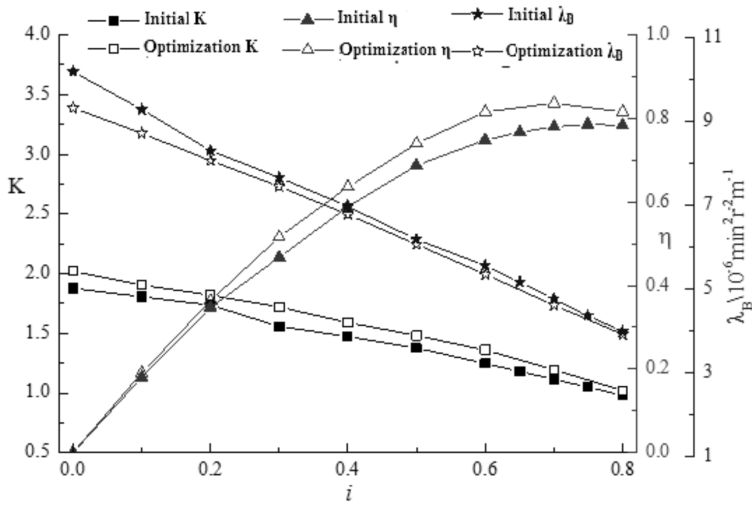


Fig. 13. Contrast of hydraulic torque reduction device characteristics after optimization: traction working condition

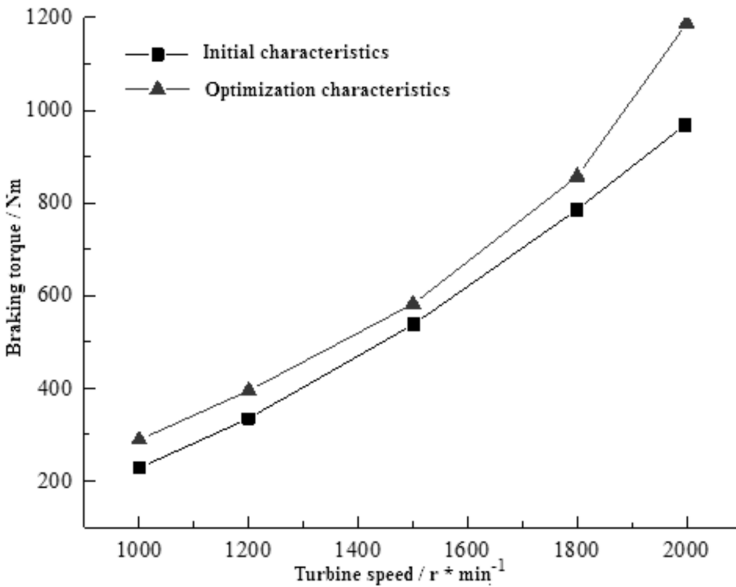


Fig. 14. Contrast of hydraulic torque reduction device characteristics after optimization: braking working condition

Table 5. Comparison of optimization results

	K_0	λ_0 ($\text{min}^2\text{r}^{-2}\text{m}^{-1}$)	η_{\max} (%)	λ_z ($\text{min}^2\text{r}^{-2}\text{m}^{-1}$)
Optimization results of hydraulic torque reducer	2.02	9.3×10^{-6}	83.7	4.39×10^{-6}
Initial data of hydraulic torque reduction device	1.88	10.2×10^{-6}	78.5	3.98×10^{-6}

1. The parameterized design method of the circulating circle of the division pump wheel-type hydraulic torque-reducing device based on prototype hydraulic torque converter is proposed, and parametric configuration method of the brake disc is established, which achieves the parametric design of the braking pulley cascade.
2. The CFD calculation model of the hydraulic torque converter is established under the braking condition in the traction condition, and the model is validated by the prototype test. It is proved that the CFD calculation has high precision and can be used for the design calculation of hydraulic torque-retarder.
3. The 3D flow design platform of the automatic hydraulic torque-retarder with integrated geometric modeling, channel division, mesh generation and CFD analysis is constructed, and the 3D flow design of the hydraulic torque-retarder is realized.
4. The optimization model of hydraulic torque-retarder based on traction working condition comprehensive performance index F and braking torque coefficient λ_z is established. On the 3D flow design platform of hydraulic torque-retarder, the optimization design of the hydraulic torque-retarder is carried out combined with genetic algorithm, and a series of non-inferior solutions are obtained. The results show that the hydrodynamic torque-retarder has been greatly improved in power, economy and braking after being optimized by 3D flow design.

References

- [1] K. YANG, M. ZHENG, Q. YAN: *Technical development of hydraulic retarder in vehicle drive line*. Construction Machinery and Equipment 32 (2001), No. 6, 32–35.
- [2] W. WEI, Q. YAN: *Study on hydrodynamic torque converter parameter integrated optimization design system based on tri-dimensional flow field theory*. SAE IJ Fuels and Lubricants 1 (2009), No. 1, 778–783.
- [3] C. B. LIU: *Research on flat hydrodynamic torque converter for passenger car*. Jilin University, Changchun, China (2009).
- [4] T. SHIEH, C. PERNG, D. CHU, S. MAKIM: *Torque converter analytical program for blade design process*. Proc. 2000 SAE World Congress, 6–9 March 2000, Detroit, Michigan, USA, 2000–01–1145.

- [5] C. LIU, X. PAN, Q. D. YAN, W. WEI: *Effect of blade number on performance of torque converter and its optimization based on DOE and response surface methodology*. Trans. Beijing Institute of Technology 21 (2012), No. 3, 689–693.
- [6] Y. X. CHU, C. WEI, Z. ZHONG, X. SUN: *Optimization design of the cascade system of dual-turbine hydrodynamic torque converter*. Proc. IEEE IC Mechatronic Science, Electric Engineering and Computer (MEC), 19–22 Aug. 2011, Jilin, China, 154–157.

Received November 16, 2016

Research on virtual technology of data caching and data real-time allocation in cloud computing

ZEYU YU¹, HUAYUN YU¹, YUNCAI ZHOU¹

Abstract. A distributed caching technology based on cloud computing is proposed in order to enable massive data processing and high concurrent access. On this basis, the LAB equalization algorithm is used to distribute equally the intermediate data output by the Map output to improve the load imbalance of the processing data in Reduce end. Through the parallel sampling test for each block data set, it is found that the distributed caching technology can relieve the server pressure. The MapReduce model can effectively reduce the running time of the system, which not only improves the system performance, access speed, reliability and response delay, but also makes the input data of the Reduce side achieve load balancing.

Key words. Cloud computing, distributed caching technology, massive data, data distribution, Map Reduce.

1. Introduction

With the development of cloud computing, more and more enterprises will build their own cloud platform, while more and more applications are supported by the cloud platform to provide users with cloud services [1]. With the increase in the number of users accessing the Internet and the large amount of data generated by sales promotion of certain e-commerce websites at certain times, making the cloud services popular, at the same time, the needs of the data visits, access speed and access security rapidly increase. And the distributed processing, distributed database and cloud storage, virtualization technology of the cloud computing for provide technical support and basic guarantee for the massive data analysis and processing [2].

Cloud computing system usually uses MapReduce model to realize the parallel computing and processing of large-scale data sets. The system uses virtual technology to generate virtual resource pool which can be configured and managed independently. Virtual resources and computing services are provided for various application

¹Yangtze University, Hubei, 434023, China

systems according to actual demand. MapReduce model is a simplified distributed programming model and efficient task scheduling model, the model allows developers do not need to perceive the complex parallel computing and task scheduling of the background, thereby reducing the programming complexity [3]. For the processing of the large-scale data accessing the database with high real-life solution, it needs to be based on the guiding research of the distributed cache technology research and the integration of the related content. The following topics are discussed in this paper.

2. Literature review

In recent years, caching system technology has caused quite a stir at home and abroad, such as virtual data caching technology, cooperative data caching technology, network shared caching technology and other distributed caching technology. At present, the main study focus on two main aspects, the first is that the technical research of cache theory—to improve the cache algorithm and the innovative application of architecture, and the second is that theory is applied to the actual environment, that is, the verification process.

Colorado University in the United States proposed a cache structure, known as hierarchical cache architecture harvest, the main purpose was to greatly increase the hit rate range, but the response time to the user also increased [4]. A high-performance distributed architecture was mentioned, it was a Web proxy server based on a global memory object buffer pool, the buffer pool was established, in which data can be shared [5]; Duke University in the Crisp project proposed a theoretical method based on central map cooperative cache, but at present only in the theoretical research stage. Sinisa Sribljic et al. [6] used a distributed network caching technique to avoid the conflict of network congestion and the excessive load of proxy proxy [7]. The aim was to find out the optimal number of Proxy Server. Distributed caching technology is applied to distributed spatial database, P2P, SOA and many other applications [8].

For Google, Amazon, Alibaba and others Internet companies provide hundreds of millions of users at all times with demand, so in this case, it will bring massive data storage and processing problems, but also is an important moment that test database load balancing ability. Therefore, the demand in this case, just relying on a few servers is far from being able to meet these data storage and processing requirements, if only enhancing the server performance can not change the requirements of this case. Google and Amazon are the national top technology aggregation, their solution is to abandon the traditional relational database, and use the storage with the key/Value form. Because the distributed cache system of key/Value pair slowly enter People's attention due to Google's big data epoch-making announcement, and the corresponding papers published by Dynamo which is launched by Amazon and Cassandra which is published by FaceBook, the Tair cache system developed independently by Alibaba plays a decisive role in the domestic In [9]. These successful practices of the top Internet giants in the distributed cache system make the distributed cache system technology become one of the core technology of cloud

computing.

At present, the distributed cache system products have been quite mature and complete, the static cache products are more than the dynamic cache products in quantity, and the technology is relatively mature than the dynamic. Although the dynamic cache technology obtain some achievements in some ways, but still in a stage of exploration and development, namely the confused period, the current products are mainly JCS, OSCache and Memcached, etc. [10]. From the emergence of distributed cache technology until now, the technology is mature, the products are constantly updated, in fact, they emerge because a scientific problem cannot be solved, and Memcached is a key/value caching system which is wildly used and emerges to solve these problems.

3. Research contents and methods

3.1. *Distributed caching technology*

Distributed cache has high performance, dynamic scalability, ease of use, high availability, distributed code execution and other characteristics [11]. And in order to solve the performance problem under large concurrent and avoid high response latency, distributed cache abandons the original relational database, and uses the key/value form of data storage, accompanied by high-speed memory as storage medium, which can guarantee the high performance, dynamic scalability of the system. Moreover, the distributed cache uses multiple copies of NRW mechanism to avoid the cache single point failure, so as to further ensure the data reliability, and ultimately data consistency on the basis of improving the speed of data access. Distributed caching system should also implement the data redundancy mechanism, which ultimately ensure the security of the system [12].

3.2. *MapReduce data distribution problems*

MapReduce model take a key value pair (keyin, valuein) as input to output another key value pairs (keyout, valueout), the above operation is achieved by the user-defined Map function and Reduce function. The existing processing mechanism first splits the input data of each Map task, the slice data blocks are executed in parallel on different nodes, and the slice size is specified by the user according to the actual situation. Therefore, the data size processed by each Map task is determinate and basically the same [13]. Based on the intermediate results generated in the calculation, the Map tasks are partitioned by the default Hash allocation algorithm. The data set under the same key value are assigned to the same Reduce node to deal with. Since the size of the data set can be determined after the Map phase is completed. Therefore, the data volume of each Reduce task has dynamic uncertainties which shows that the intermediate data output by the Map end is unbalanced, which leads to the imbalance of the data processing load of the Reduce end [14].

3.3. Data allocation algorithm

We use the above principle to evaluate the locality of the data, which is the ratio of the number of key_s at the local node to the number of key_s distributed at each node. Locality of the LAB data allocation algorithm is:

$$\text{Locality}_{\text{LAB}} = \frac{\sum_{i=1}^N (k_i)^j}{\sum_{i=1}^K c(k_i)}, \quad (1)$$

where $(k_i)^j$ is the number of key_i at the n_j th node and $c(k_i)$ is the sum of the number of key_i at all nodes.

The balance of input data of the Reduce shows that the data size processed by Reduce end is basically the same. In the MapReduce system, the end of the job depends on the slowest sub-tasks, so the operating efficiency is limited by the slowest Reduce tasks. In the LAB algorithm, the difference in the balance of D_{overload} is expressed with overload data, the size is the largest input data volume of the Reduce end minus the average.

$$D_{\text{overload}} = \max(\text{Data}_i^j) - \frac{\text{TotalData}}{M}, \quad (2)$$

where Data_i^j represents the amount of data at the node n_j after assigning the key_i , which is calculated as follows:

$$\text{Data}_i^j = \begin{cases} \text{Sum } N^j = \sum_{i=1}^N c(k_i)^j, \\ \text{Data } N_{i-1} + (c(k_i) - c(k_i)^j), \\ \text{Data } N_{i-1} - c(k_i)^j. \end{cases} \quad (3)$$

Here $\text{Sum } N^j$ is the sum of all keys at node n_j , and when the key is assigned to a node, the standard deviation of each node is used to evaluate the equalization of the assignment, expressed as:

$$\text{Balance - score } N_i = \sqrt{\frac{\sum_{i=1}^M (\text{Data } N_i - \text{Mean})^2}{M}}. \quad (4)$$

The LAB algorithm assigns keys with different sets of numbers to the nodes with the smallest standard deviation. The key_s are arranged in descending order of $c(k_i)^j$ values. In order to improve the locality of data allocation, the key is assigned to the node with the largest number of key_s . After the completion of a key value distribution, the new data on each node is calculated, and then is the next key allocation. the heuristic method is used to assign the data set in turn which is correspond to the N key values distributed in the M nodes to the desired Reduce nodes.

4. Results analysis

4.1. Distributed cache

4.1.1. *Overall structure diagram.* Considering the function of distributed caches and the model architecture of distributed memory data, the specific and effective concordance is achieved by the distributed and coordinated mechanism of Zookeeper, and a distributed cache architecture is realized. Distributed cache overall structure is shown in Fig. 1 [15].

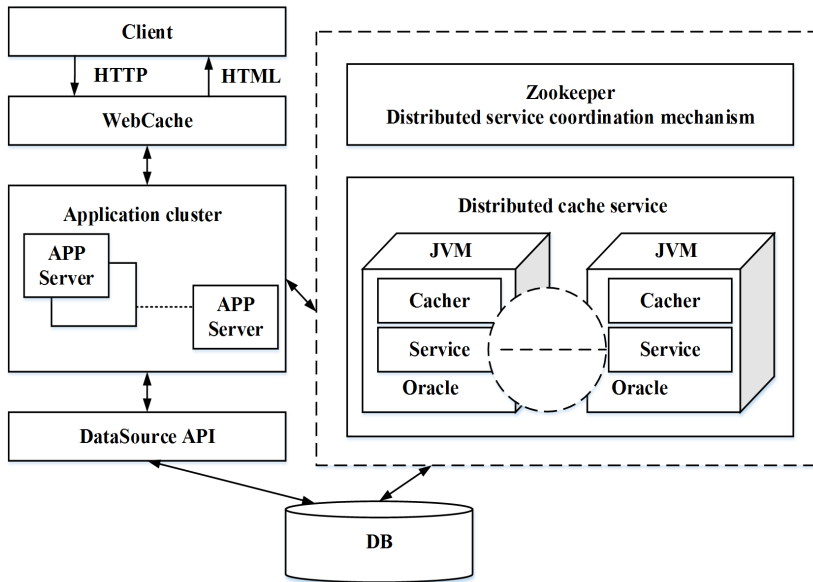


Fig. 1. Distributed cache overall architecture diagram

4.1.2. *Reliability testing.* The distributed cache system environment is tested for reliability, including data recovery and data integrity testing for each cache node. The test results are shown in Table 1.

Table 1. Data recovery time table

Add or delete the cache nodes	Data recovery time (s)
No-operation	About 2.2
Commodity fuzzy query	About 3

It can be seen that the distributed cache system can meet the requirements of application and meet the system performance requirements. The distributed memory data management has high reliability and high expansibility, and contains powerful fault tolerance and self-repair function.

4.2. Data distribution

4.2.1. *Working time.* In different allocation strategies, the execution time of the system varies with the inclination of the data set, as shown in Fig. 2. The data set size is 1 G, and depicted is an enlarged view of the LABWC working change curve.

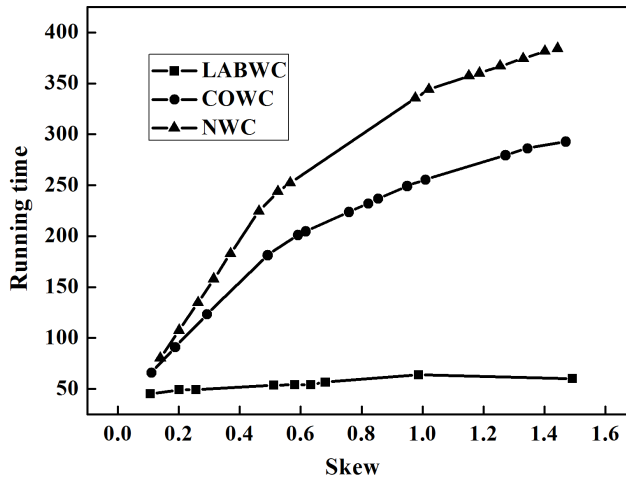


Fig. 2. Running time under different inclination

It can be seen that for different size of data set the running time increases with increasing tilt and the time difference tends to increase. This is due to the increase of the inclination. In the NWC mode, it takes more time to wait for the data from the Reduce side to complete the job. The COWC method needs to merge more data sets, and the LABWC method needs to balance the more inclined data. At the same time, the overall operation time of LABWC operation mode is smaller than that of NWC and COWC, and the change of the time difference of the different inclination is small, and the time difference shows a decreasing trend.

WordCount experiment was conducted on the data set with 1.5 degree inclination. The relationship between the running time of the system and the size of the data set is shown in Fig. 3.

It can be seen that the run-time increases with the increase of data set for data sets with different data set but different inclination. The run-time gap between LABWC and NWC and COWC is significantly increased with the increase of processing data set. It can be seen from the 2G data set experiment that the LABWC running time is about half of the NWC running time and about one third less than the COWC operation. It is shown that the improved LAB algorithm can effectively improve the efficiency of parallel operations.

4.2.2. *Load balancing.* The standard deviation is used to evaluate the load balance. The ordinate Stdev represents the standard deviation. The abscissa is the

inclination of the data set. The smaller the value of Stdev, the better the load balance of the processed data. The data set with the size of 1 G and the inclination between 0.1 and 1.5 was used to carry out the WordCount experiment. The experimental results show that the load balance results are shown in Fig. 4.

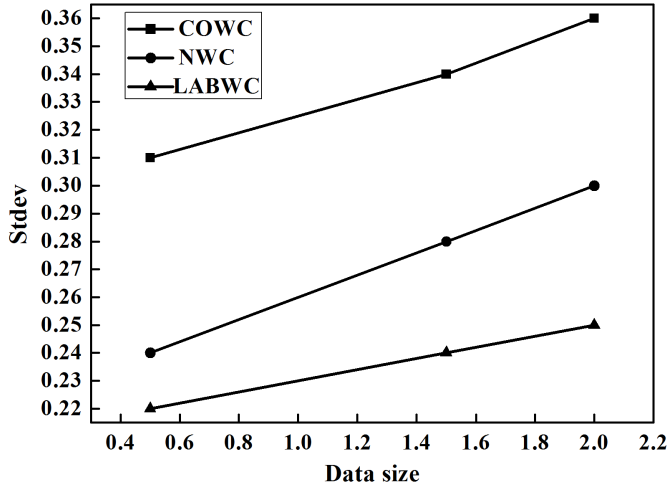


Fig. 3. Running time of data sets of different sizes

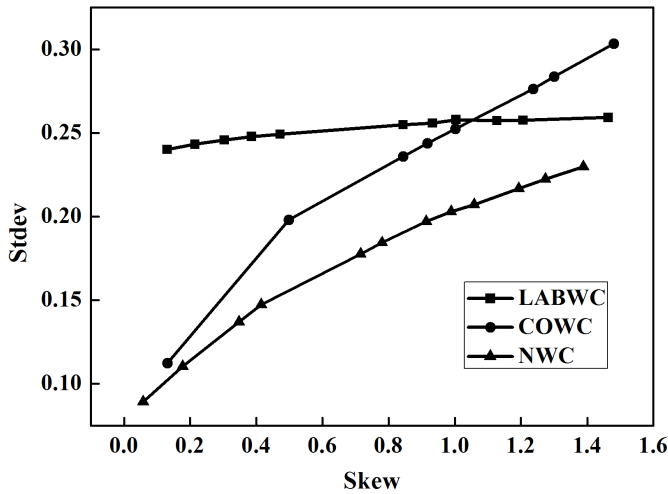


Fig. 4. Load balance of reducing end with different inclination

It can be seen from the figure, Stdev's change trend and execution time trends are basically consistent, while reflecting that the smaller degree of tilt, the load balance of the difference smaller. With the increase of the inclination degree, the

advantage of load balancing of Reduce end under LABWC mode appears. The results show that the LAB allocation strategy based on the sampling results can effectively improve the balanced distribution of the intermediate data of the Map end, and make the Reduce end handle the data size balance. When the inclination is 1.5, the load balance of different size data set is shown in Fig. 5.

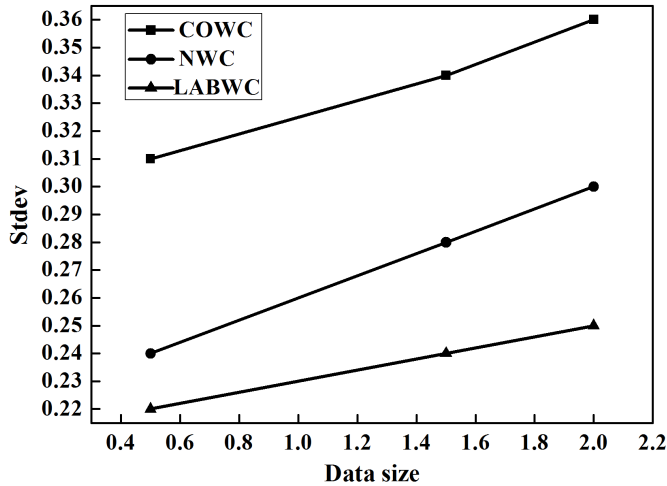


Fig. 5. 5 Load balance of different size data set

It can be seen from the figure that the Stdev values of LABWC under different data sets are smaller than those of other methods. With the increase of data set, the Stdev values of different operation modes show an increasing trend, but the increase of NWC and COWC modes is significantly greater than the LABWC operation mode, therefore, LABWC operation mode has obvious advantages of load balancing.

5. Conclusion

We studied how to use distributed caching technology in cloud computing to solve the problem in the massive data processing platform to ensure high performance, high access speed, low latency and high reliability of the system. The deployment and the overall architecture design of distributed caching system is proposed and discussed

The LAB algorithm is used to optimize the unbalanced distribution of the intermediate data. The improved LAB algorithm can balance the locality of the data and input of the Reduce end, which greatly improves the efficiency of parallel operations. Performance verification is performed on the distributed cache open source platform through an experimental cluster. The experimental results show that this method can distribute the load balance data for the Reduce end, and can solve the performance bottleneck of the unbalanced input data in the Reduce side.

References

- [1] Y. ZHAO, J. WU, C. LIU: *Dache: A data aware caching for big-data applications using the MapReduce framework*. Tsinghua Science and Technology 19 (2014), No. 1, 39–50.
- [2] C. L. P. CHEN, C. Y. ZHANG: *Data-intensive applications, challenges, techniques and technologies: A survey on big data*. Information Sciences 275 (2014), 314–347.
- [3] K. KAMBATLA, G. KOLLIAS, V. KUMAR, A. GRAMA: *Trends in big data analytics*. J. Parallel and Distributed Computing 74 (2014), No. 7, 2561–2573.
- [4] H. CAI, B. XU, L. JIANG, A. V. VASILAKOS: *IoT-based big data storage systems in cloud computing: Perspectives and challenges*. IEEE Internet of Things J. PP (2016), No. 99, 1–1.
- [5] S. JIANG, T. CHEN, J. DONG: *Application and implementation of private cloud in agriculture sensory data platform*. Computer and Computing Technologies in Agriculture IX, IFIP Advances in Information and Communication Technology 479 (2016), 60–67.
- [6] K. GAI, M. QIU, H. ZHAO: *Security-aware efficient mass distributed storage approach for cloud systems in big data*. Proc. IEEE 2nd International Conference on Big Data Security on Cloud (BigDataSecurity), IEEE International Conference on High Performance and Smart Computing (HPSC), and IEEE International Conference on Intelligent Data and Security (IDS), 8–10 April 2016, New York, USA, 140–145.
- [7] E. C. PETERS, S. RABINOWITZ, H. R. JACOBS, P. J. FASCIANO: *Computer system and process for transferring multiple high bandwidth streams of data between multiple storage units and multiple applications in a scalable and reliable manner*. Patent US 9432460 B2 (2016).
- [8] Y. SHEN, P. LU, X. QIN, Y. QIAN, S. WANG: *Efficient query algorithm of coallocation-parallel-hash-join in the cloud data center*. Cloud Computing and Security, series Lecture Notes in Computer Science 9483 (2016), 306–320.
- [9] H. DUAN, S. YU, M. MEI, W. ZHAN, L. LI: *CSTORE: A desktop-oriented distributed public cloud storage system*. Computers & Electrical Engineering 42 (2015), 60–73.
- [10] A. UTA, A. SANDU, T. KIELMANN: *Overcoming data locality: An in-memory runtime file system with symmetrical data distribution*. Future Generation Computer Systems 54, (2016), 144–158.
- [11] D. DEV, R. PATGIRI: *A survey of different technologies and recent challenges of big data*. Proc. 3rd International Conference on Advanced Computing, Networking and Informatics, series Smart Innovation, Systems and Technologies, 23–25 June, Bhubaneswar, Orissa, India, 537–548.
- [12] A. A. YILDIRIM, D. A. WATSON: *A cloud-aware distributed object storage system to retrieve large data via HTML5-enabled web browsers*. Managing Big Data in Cloud Computing Environments (2016), Chapter 2, 25–45.
- [13] K. ZHENG, Z. YANG, K. ZHANG, P. CHATZIMISIOS, K. YANG, W. XIANG: *Big data-driven optimization for mobile networks toward 5G*. IEEE Network 30 (2016), No. 1, 44–51.
- [14] I. STEFANOVICI, E. THERESKA, G. O’SHEA, B. SCHROEDER, H. BALLANI, T. KARAGIANNIS, A. ROWSTRON, T. TALPEY: *Software-defined caching: Managing caches in multi-tenant data centers*. ACM Symposium on Cloud Computing, 27–29 Aug. 2015, Kohala Coast, Hawaii, 174–181.
- [15] C. VITOLO, Y. ELKHATIB, D. REUSSER, C. J. A. MACLEOD, W. BUYTAERT *Web technologies for environmental Big Data*. Environmental Modelling & Software 63 (2015), 185–198.

Research on the winding control system in winding vacuum coater

WENBING JIN¹, SUO ZHANG¹, YINNI JIN²

Abstract. A method of control of the winding speed and rewinding or unwinding tension of the rolling high-vacuum continuous coating machine is proposed. The method is based on control of the armature current of the DC motor. Its time variation is caused by a lot of factors, such as the film winding tension, motor constant friction, electrical load that can change with the speed of the friction, unload acceleration and deceleration resistance, acceleration and deceleration with a load resistance, current introduced by the rolling tension of the film and others. All these factors may influence the tension. Thus, the control of the rolling tension can be achieved through control of the armature current. In order to find the relation between this current and tension, we first established a mathematical model in accordance with the principle of the rewinding system. Based on its analysis, we designed an alternative rewinding automatic control system. Our work shows that the proposed automatic control system exhibits a quite satisfactory performance and properties. This is also confirmed by its successful application in industry.

Key words. Winding control, rewinding; unwinding, tension, armature current, speed.

1. Introduction

There are three schemes of existing winding control for selection: one is the tension closed-loop control scheme (speed mode). A feedback signal derived from the tension detecting device cooperates with the tension setting value to constitute a PID closed-loop control circuit, which adjusts motor speed to achieve the purpose of tension control. The second kind is tension open-loop control scheme (torque mode). By controlling the output torque of the motor, the objective tension can be controlled. The principle is that by setting the value of tension and volume, the torque can be calculated. This scheme does not need tension detection feedback, but for frequency converter working method and closed-loop vector control mode, a speed measuring coder and a reel diameter sensor must be equipped. In addition, the influence of rotational inertia in acceleration and deceleration process should be considered. The third kind is the tension closed-loop control scheme (torque mode).

¹Zhejiang Institute of Mechanical & Electrical Engineering, Hangzhou, 310000, China

²School of Lehigh University, 27 Memorial Drive West, PA 18015-3086, USA

The tension detection feedback closed-loop control is added on the open-loop tension control scheme to realize the technique. The working principle is that PID closed-loop circuit can be obtained and output torque command can be adjusted by tension detection feedback signal and tension setting value, which would guarantee the high precision of tension control. These above control methods all should be equipped with a feedback sensor measuring the tension or radius.

Usually, the winding part is installed in the vacuum chamber, and vacuum degree is there high when working. The more components installed in vacuum chamber, the more poles elicited from the lead wires can greatly influence the vacuum degree. In addition, sensor could cause discharge when the tension or speed increases in high-vacuum environment. A control system without rewinding/unwinding tension sensor and reel diameter sensor was proposed to meet the requirements of the performance. The tension values can be obtained and controlled by two parameters: DC motor output torque and winding diameter.

2. Methods

2.1. Profile of continuous high-vacuum winding coater

Winding control plays an important part in control of continuous high-vacuum winding coating machine, whose structure diagram is shown in Fig. 1.

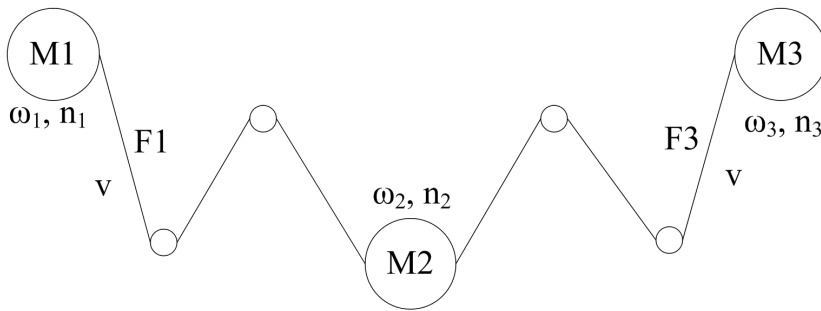


Fig. 1. Structure of winding or unwinding system

The corresponding components M1 and M3 are rewinding and unwinding motors, respectively and M2 is a water-cooled main roller motor. Symbols ω_1 , ω_2 and ω_3 are the angular velocities of the three electric motors and n_1 , n_2 and n_3 , respectively, are their revolutions. Symbol v denotes the line speed of film winding, and symbols F_1 and F_3 stand for the rewinding and unwinding tensions, respectively.

In order to ensure a constant value of the line speed and tension in the winding process, both these quantities should be adjusted appropriately.

2.2. Analysis of winding motor

We take DC motor M1 for example. The motor is described by several equations. The equation for voltage can be written in the form

$$U_{a1} = R_{a1}i_{a1} + L_{a1}\frac{di_{a1}}{dt} + E_1 = R_{a1}i_{a1} + L_{a1}\frac{di_{a1}}{dt} + K_{e1}\Phi_1n_1, \quad (1)$$

where U_{a1} is the armature voltage, R_{a1} denotes the armature resistance, L_{a1} stands for the armature leakage inductance, E_1 represents the armature electromotive force, Φ_1 is magnetic flux, n_1 stands for the motor speed and K_{e1} represents the torque constant.

As quantities R_{a1} , L_{a1} , K_{e1} and Φ_1 may be considered constant, we can put $K_{e1}\Phi_1 = K_1$, so that

$$U_{a1} = R_{a1}i_{a1} + L_{a1}\frac{di_{a1}}{dt} + K_1n_1. \quad (2)$$

The effective torque of rewinding control is described by the equation

$$T_{L1} = F_1R_1. \quad (3)$$

The relationship between motor rotation angular velocity ω_1 and motor speed n_1 is

$$\omega_1 = \frac{2\pi}{60}n_1. \quad (4)$$

Now, we will deal with the analysis of the load of M1. There are many parameters we should consider, for example the film winding tension, constant friction force of load, variable friction coming from the rotation of load, no-load speed resistance, loading speed resistance, etc. Symbol i_{a1} denotes the armature current, which is the sum of the currents passing through the 5 parts.

$$i_{a1} = i_{T1} + i_{FC1} + i_{F\omega_1} + i_{JC1} + i_{J\omega_1}, \quad (5)$$

where

1. Current i_{a1} varies with the change of tension and coil diameter by the formula

$$i_{T1} = \frac{F_1R_1}{K_{T1}\Phi_1} = \frac{1}{K_{T1}\Phi_1} \frac{30v}{\pi n_1} F_1. \quad (6)$$

2. Current i_{FC1} can be obtained when the system is to overcome the constant friction; the current is derived when the system is under the no-load working state, and when the speed is a stable low speed. It is normally obtained when the system is working at the minimum speed (close to 0 rpm) and in a no-load working state, which is of the constant character.
3. Current $i_{F\omega_1}$ is obtained when the system is to overcome variable friction force: the current and motor speed n_1 have a linear curve in a certain speed

range. There holds

$$i_{F\omega_1} = K_2 n_1, \quad (7)$$

where K_2 is a constant value.

4. Current i_{JC1} is an inherent acceleration and deceleration current of machine caused by load inertia, which is proportional to variation rate of the motor speed; it is given by the formula

$$i_{JC1} = J_{c1} \frac{1}{K_{T1}\Phi_1} \frac{d\omega_1}{dt} = J_{c1} \frac{1}{K_{T1}\Phi_1} \frac{2\pi}{60} \frac{dn_1}{dt}, \quad (8)$$

where J_{c1} is the no-load inherent inertia. Its value is constant and can be obtained from the no-load test. The rated voltage is added to the no-load motor, the time t is calculated when the rewinding system accelerates from 0rpm to the nominal speed ω_N . The current i_{Jc} can be obtained when the motor works at the rated speed according to the formula

$$i_{Jc} = i - i_{Fc} - i_{F\omega}, \quad (9)$$

where i_{Fc} refers to the current when the no-load motor works at a stable minimum speed and $i_{F\omega}$ is the current obtained when the motor works at the rated speed ω_N to overcome the variable friction force. The value of current $i_{F\omega}$ may be obtained from the relation

$$J_{c1} = i_{F\omega} \frac{t}{\omega_N} K_{T1}\Phi_1. \quad (10)$$

5. Current $i_{J\omega_1}$ is an acceleration and deceleration current caused by the change of winding inertia of the film coater in the process of winding. It is given by the formula

$$\begin{aligned} i_{J\omega_1} &= \frac{J_1}{K_{T1}\Phi_1} \frac{d\omega_1}{dt} = \frac{1}{2} \frac{\sum(m_i r_i^2)}{K_{T1}\Phi_1} \frac{d\omega_1}{dt} = \\ &= \frac{1}{2} \frac{R_1^2 \pi R_1^2 L_1 \rho_1}{K_{T1}\Phi_1} \frac{d\omega_1}{dt} = \frac{\pi^2}{60} \frac{\rho_1 L_1 R_1^4}{K_{T1}\Phi_1} \frac{dn_1}{dt}. \end{aligned} \quad (11)$$

Here, ρ_1 is the density of winding film, L_1 is the width of the winding film, R_1 is the radius of winding film roll. The numerical value of R_1 is continuously changeable in the winding process.

When the minimal volume diameter of the core is $R_{\min 1}$, then

$$i_{J\omega_1} = \frac{\pi^2}{60} \frac{\rho_1 L_1}{K_{T1}\Phi_1} \frac{dn_1}{dt} (R_1^4 - R_{\min 1}^4), \quad (12)$$

and after substitution $R_1 = 30v/(\pi n_1)$ we finally obtain

$$i_{J\omega_1} = \frac{\pi^2}{60} \frac{\rho_1 L_1}{K_{T1}\Phi_1} \frac{dn_1}{dt} \left(\frac{30^4 v^4}{\pi^4 n_1^4} - R_{\min 1}^4 \right). \quad (13)$$

Substitution of (6), (7), (10) and (13) into (5) provides

$$\begin{aligned}
 i_{a1} &= \frac{1}{K_{T1}\Phi_1} \frac{30v}{\pi n_1} F_1 + i_{FC1} + K_2 n_1 + J_{c1} \frac{1}{K_{T1}\Phi_1} \frac{2\pi}{60} \frac{dn_1}{dt} + \\
 &+ \frac{\pi^2}{60} \frac{\rho_1 L_1}{K_{T1}\Phi_1} \frac{dn_1}{dt} \left(\frac{30^4 v^4}{\pi^4 n_1^4} - R_{\min 1}^4 \right) = i_{FC1} + \frac{30}{K_{T1}\Phi_1 \pi} \frac{v}{n_1} F_1 + K_2 n_1 + \\
 &+ \frac{J_{c1}}{K_{T1}\Phi_1} \frac{\pi}{30} \frac{dn_1}{dt} + \frac{30^4}{60\pi^2} \frac{\rho_1 L_1}{K_{T1}\Phi_1} \frac{v^4}{n_1^4} \frac{dn_1}{dt} - \frac{\pi^2}{60} \frac{\rho_1 L_1 R_{\min 1}^4}{K_{T1}\Phi_1} \frac{dn_1}{dt}. \quad (14)
 \end{aligned}$$

2.3. Analysis of winding motor and main rolling motor

A similar equation for motor M3 can be obtained as above

$$\begin{aligned}
 i_{a3} &= i_{T3} + i_{FC3} + i_{F\omega 3} + i_{JC3} + i_{J\omega 3} = \frac{1}{K_{T3}\Phi_3} \frac{30v}{\pi n_3} F_3 + i_{FC3} + K_4 n_3 + \\
 &+ J_{c3} \frac{1}{K_{T3}\Phi_3} \frac{2\pi}{60} \frac{dn_3}{dt} + \frac{\pi^2}{60} \frac{\rho_3 L_3}{K_{T3}\Phi_3} \frac{dn_3}{dt} \left(\frac{30^4 v^4}{\pi^4 n_3^4} - R_{\min 3}^4 \right) = \\
 &= i_{FC3} + \frac{30}{K_{T3}\Phi_3 \pi} \frac{v}{n_3} F_3 + K_4 n_3 + J_{c3} \frac{1}{K_{T3}\Phi_3} \frac{2\pi}{60} \frac{dn_3}{dt} + \\
 &+ \frac{30^4}{60\pi^2} \frac{\rho_3 L_3}{K_{T3}\Phi_3} \frac{v^4}{n_3^4} \frac{dn_3}{dt} - \frac{\pi^2}{60} \frac{\rho_3 L_3 R_{\min 3}^4}{K_{T3}\Phi_3} \frac{dn_3}{dt}. \quad (15)
 \end{aligned}$$

Finally, the revolutions of the main rolling motor are described by the following differential equation

$$T_{m2} T_{a2} \frac{d^2 n_2}{dt^2} + T_{m2} \frac{dn_2}{dt} + n_2 = \frac{u_{a2}}{K_{e2}\Phi_2} - \frac{1}{K_{T2}K_{e2}\Phi_2^2} \left(T_{a2} \frac{dT_{L2}}{dt} + T_{L2} \right), \quad (16)$$

where T_{m2} , T_{a2} and T_{L2} represent the electric time constant of main rolling motor M2, armature circuit and winding vacuum coater with the winding film width of L , respectively. These parameters are given by the formulae

$$T_{m2} = \frac{J_{G2} R_{a2}}{K_{T2} K_{e2} \Phi_2^2}, \quad T_{a2} = \frac{L_{a2}}{R_{a2}}.$$

3. Results

The main rolling motor is used to keep the film linear velocity constant. The mechanism design considered that when the tension of winding/unwinding motor is above 50 N and when winding tension F_3 is slightly higher than 5%–10% of unwind tension F_1 in actual use, the film coater would not slip in the main rolling motor. Thus, we can draw the conclusion that a constant line speed could be kept in film winding process as long as the rotation speed of main rolling motor is constant.

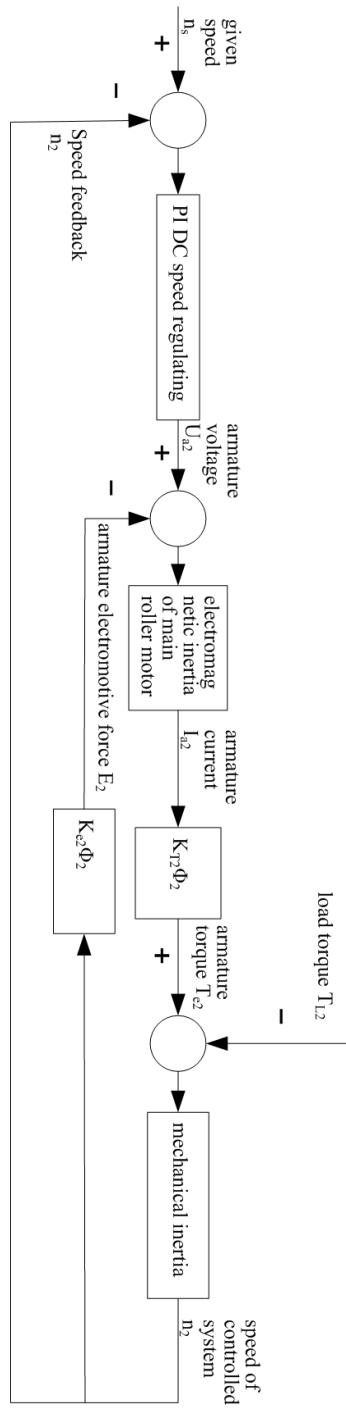


Fig. 2. Control functional block diagram of the home roll motor

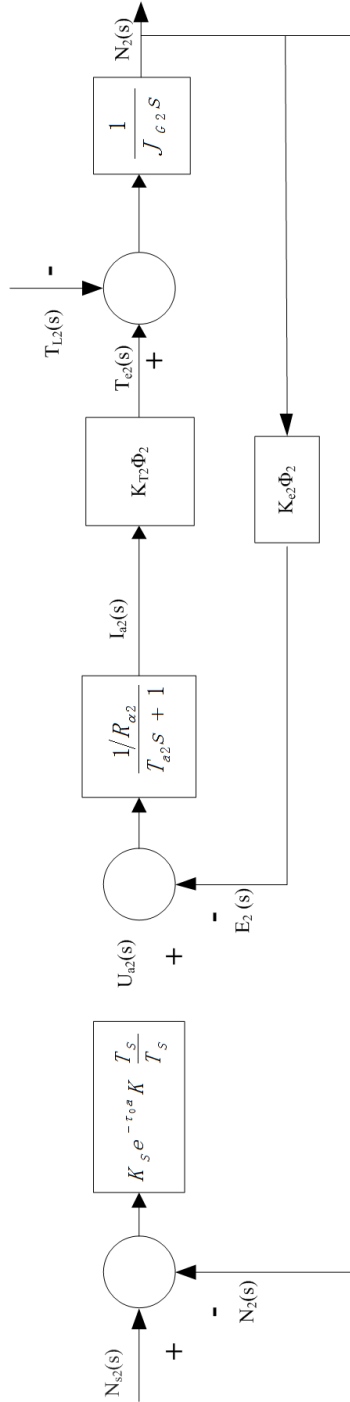


Fig. 3. Control system block diagram of the home roll motor

Line speed V , main rolling motor revolutions n_2 and angular velocity ω_2 are connected by the relation

$$V = \omega_2 R_2 = \frac{2\pi}{60} R_2 n_2, \quad (17)$$

where R_2 is the radius of main rolling motor, which is a constant value.

The control scheme of the main roller motor is PI control of DC speed regulating system. The control principle block diagram is shown in Fig. 2, and the transfer function block diagram is shown in Fig. 3.

4. Discussion

According to formula (14), the working current of the motor is determined by detecting the rotate speed of the motor n_1 and linear velocity v of the film coater, when a certain value of unwinding motor tension is given. So the tension control would be turned to the working current control. The control system block is shown in Fig. 4, where, I_{a1s} is the given working current of the motor calculated from equation (14) for the given tension value F_1 .

The tension control in the winding part could be transformed to the current control which is similar to the unwinding part. The motor working current I_{a3s} was calculated from equation (15).

The parameters of control system wiring are shown in Table 1, and the flow chart is shown in Fig. 5.

Table 1. Parameters of control system wiring

HMI touch pad	S7-200 CPU226CN	EM235 4AI/1AQ	EM232 2AQ
No	Address	Function	Component model
1	I0.0–I0.2	winding rotate speed	optical encoder TRD-J-S
2	I0.3–I0.5	unwinding rotate line speed	optical encoder TRD-J-S
3	I0.6–I1.0	winding rotate line speed	optical encoder TRD-J-S
4	AIW0	main roller speed	4-20 mA
5	AIW2	winding motor real armature current	4-20 mA
6	AIW4	unwinding motor real armature current	4-20 mA
7	AIW0	unwinding motor given armature current	4-20 mA
8	AIW4	winding motor given armature current	4-20 mA

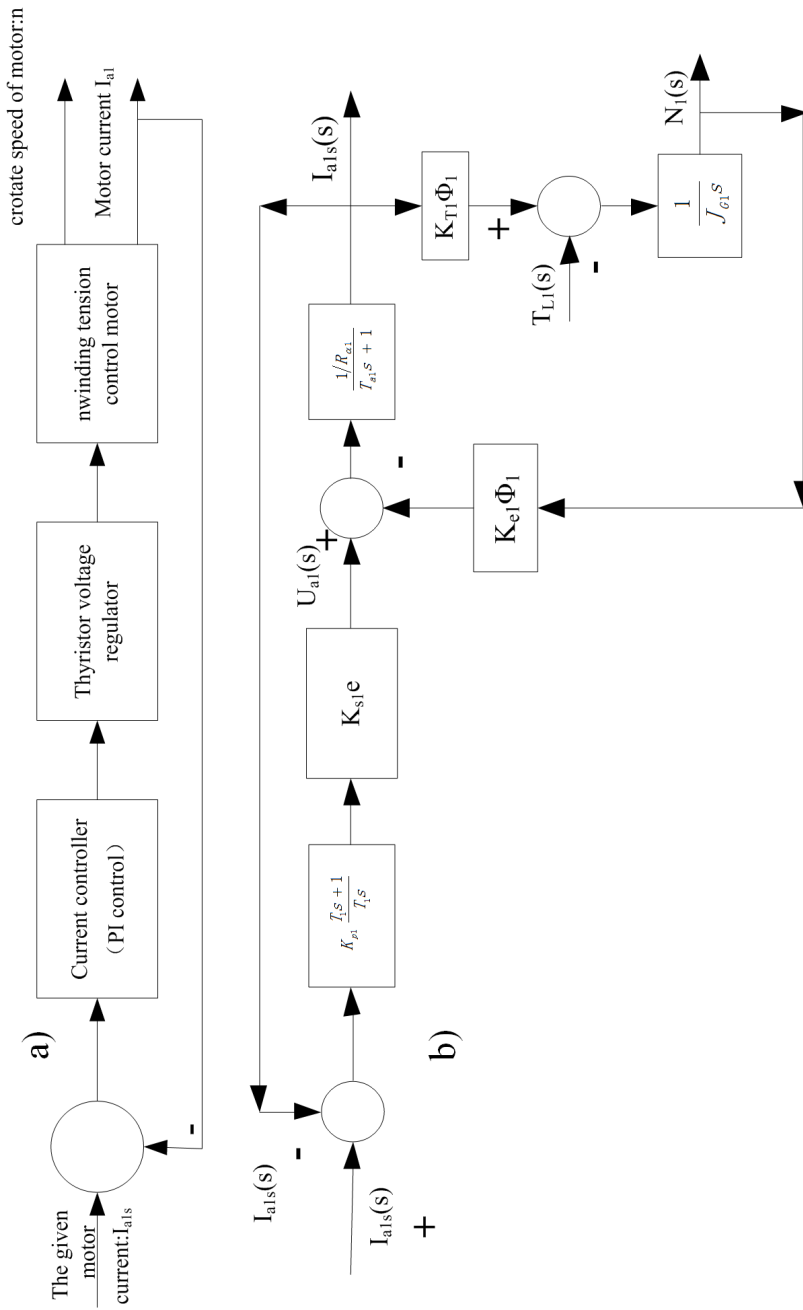


Fig. 4. Control system block diagram of the unwinding roller motor

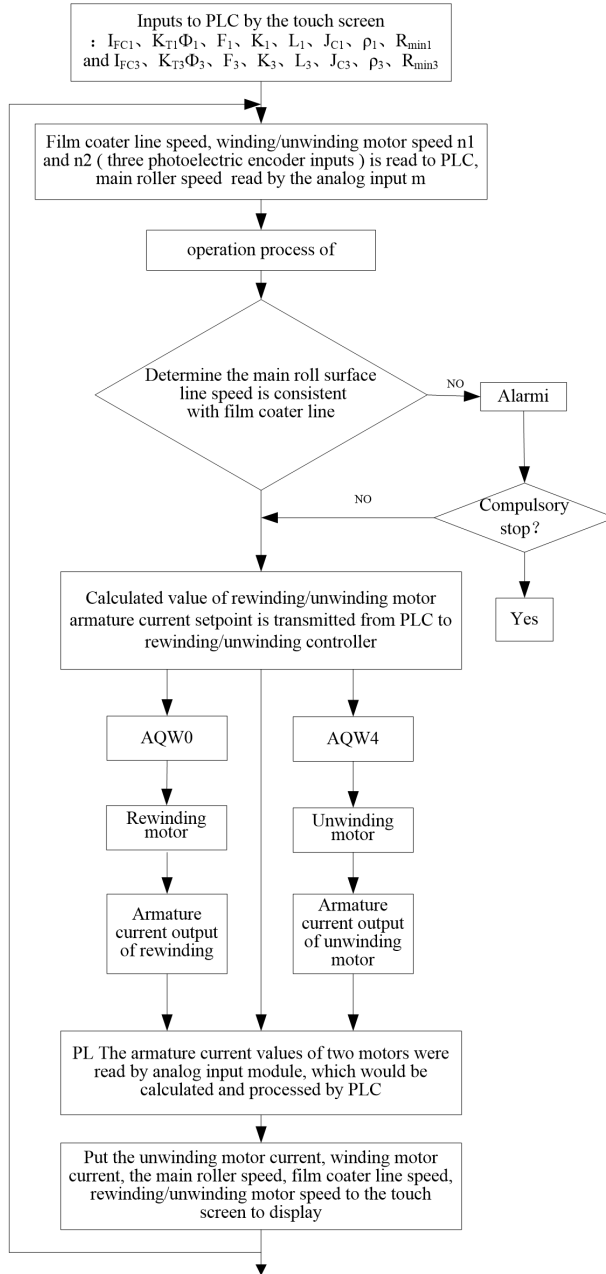


Fig. 5. Functional block diagram of the control program

5. Conclusion

The relative difficulty of system debugging was caused due to the lack of tension sensor or direct measurement to the roll diameter sensor. A high system reliability and normal working state can be obtained after more than half a year operation, In the debugging process, two control systems have been compared: one is the system with tension sensor and the other without it. The two systems both work under the standard atmospheric pressure. The result shows that tension control uniformity of the control system without tension sensor can reach the accuracy of about 3%, which has been able to meet the actual needs of reflective film coating.

References

- [1] GROUP SCHNEIDER: *Three phase digital variable speed controllers for DC motors interface extension option board VW1-RZD101*. User's manual EB (2012), 32–45.
- [2] J. C. PONSART, D. THEILLIOL, C. AUBRUN: *Virtual sensors design for active fault tolerant control system applied to a winding machine*. Control Engineering Practice 18 (2010), No. 9, 1037–1044.
- [3] S. J. DODDS, G. SOORIYAKUMAR: *Observer based robust tension control for a segmented stator coil winding machine*. Proc. IEEE International Symposium on Industrial Electronics, 27-30 June 2011, Gdansk, Poland, 1925–1930.
- [4] L. WANG, W. Y. LU, L. WANG: *A study of the tension-observer-based winding tension control system*. Computer Engineering and Science 30 (2008), No. 4, 56–67.
- [5] L. MORRONE, P. A. FRIGERI, J. BERTOMEU: *Low cost vacuum web coating system*. Vacuum, Part B 122 (2015), 337–341.
- [6] G. H. S. SCHMID, C. EISENMENGER-SITTNER: *A method for uniformly coating powdery substrates by magnetron sputtering*. Surface and Coatings Technology 236 (2013) 353–360.
- [7] L. CHEN, K. K. CHANG, Y. DU, J. R. LI, M. J. WU: *A comparative research on magnetron sputtering and arc evaporation deposition of Ti–Al–N coatings*. Thin Solid Films 519 (2011), No. 11, 3762–3767.
- [8] F. S. LE BLANC, J. FLEISCHER, M. SCHMITT, M. UNGER, J. HAGEDORN: *Analysis of wire tension control principles for highly dynamic applications in coil winding: Investigation of new tension control devices for noncircular orthocyclic coils*. Proc. IEEE International Electric Drives Production Conference (EDPC), 15-16 Sept. 2015, Nürnberg, Germany, 1–8.
- [9] V. T. DUONG, P. T. DOAN, J. H. MIN, H. K. KIM, S. B. KIM, J. H. JEONG, S. J. OH: *Active real-time tension control for coil winding machine of BLDC motors*. Proc. IEEE International Conference on Advances in Computing, Communications and Informatics (ICACCI), 24-27 Sept. 2014, Delhi, India, 765–770.
- [10] F. HE, J. HAN, Q. WANG: *Fuzzy control with adjustable factors in tension control system*. Advanced Materials Research 902, (2014), 201–206.

Received November 16, 2016

Hybrid discrete-time modelling and explicit model predictive control for brushed DC motor speed control¹

ZHAOZHUN ZHONG^{2*}, MIAO GUAN², XINPEI LIU³

Abstract. The development of an innovative EMPC (Explicit Model Predictive Control) scheme for brushed DC (Direct Current) motor speed control is traced to overcome the control difficulties encountered in practice. Based on multi-parametric linear/quadratic programming, EMPC moves the online iteration algorithm of optimal control problem off-line to reduce the online computation time. By dividing the switching period into subperiods, a hybrid discrete-time model of the brushed DC motor system, which reflects the switching and hybrid nature of the system, is derived for EMPC controller design. The proposed EMPC scheme achieves better performance by coordinate control and the steady state error is eliminated by feedback correction. In addition, EMPC is more suitable for implementation on digital controllers compared with existing continuous controllers. Simulations show the effectiveness of the proposed method compared with conventional ones under unmodelled disturbances.

Key words. Explicit model predictive control, brushed DC motor, speed control.

1. Introduction

With the advantages of torque coefficient, high reliability and excellent overload capacity, brushed DC motors are widely used in industry [1, 2]. The motor control system plays an important role in the smooth and rapid operational performance of the brushed DC motor system. When working at low speed, many problems, such as steady state error, instability, oscillation and so on, can be caused by unmodelled disturbances [3].

In the literature, the speed control of the brushed DC motor has been studied for

¹This work was partially supported by National Natural Science Foundation of China (61304095 & 61403254), Natural Science Foundation of Jiangsu Province (BK20130317), Shanghai Natural Science Foundation of China (13ZR1428500) and Jiangsu Planned Projects for Postdoctoral Research Funds (1302103B).

²School of Iron & Steel, Soochow University, Suzhou, Jiangsu, 215000, China

³School of Urban Rail Transportation, Soochow University, Suzhou, Jiangsu, 215000, China

decades, and many methods have been proposed. PID control schemes are widely used in the speed control of the brushed DC motor due to its simplicity and reliability. However in the case of unmodelled disturbances, the performance of the PID is deteriorated [4]. The unmodelled disturbances, such as input source voltage variations, frictions, load torque variations and so on, are major problems remain unsolved in the speed control of the brushed DC motor. Many researchers have proposed new methods for the speed control. The support vector machines are studied in [5] to meet the design requirements. Wiener-type neural network is studied in [6] to improve the speed control performance of the system. An adaptive robust speed control is proposed in [7] based on a disturbance observer. Backstepping-based output feedback controller is studied in [8]. The performance of the above mentioned modern controllers have been verified by simulations and experiments.

Among these modern control strategies, one research direction with significant potential is coordinated control using a MPC (Model Predictive Control) algorithm which have already been proposed in the brushed DC motor control [9]. In the literature, MPC is regarded as an efficient control strategy based on the completely multivariable system framework [10]. There are several aspects, such as the ability to perform optimization and constraint handling, make MPC strategy attractive to both practitioners and academics. Relying on a dynamic model of the process, the traditional MPC schema uses a receding horizon control principle and the optimal control problem is solved by on-line iteration. As a result, the application of MPC strategy needs expensive on-line computation power and MPC is labeled as a technology for slow processes. Recently, EMPC is proposed to handle this problem [11–13]. EMPC moves all the computations necessary for the implementation of MPC off-line using multi-parameter programming, while preserving all its other characteristics. EMPC divide the state space into critical regions off-line and for each critical region the optimal control law is fixed and given. Therefore, EMPC reduces on-line computation time and renders MPC suitable for fast systems such as switched power converters. For power electronics, EMPC has been studied in some electrical drives [14]. As for brushed DC motor speed control, the application of EMPC strategies is still under investigation.

According to the circuit topology and switching philosophy, this paper proposes a hybrid discrete-time modelling method for brushed DC motor speed control which is simple and adequate as a predictive model. Based on the discrete-time model, EMPC strategy is developed to reduce the on-line computation time and regulate the output voltage under a wide range of operating conditions. As a result, the dynamic performance is developed and the complexity of controller is greatly reduced [15].

Besides these benefits, the proposed EMPC respects all the constraints of the brushed DC motor speed control system including the current constraint of the armature, the input constraint, the input rate constraint, which is difficult to handle in the conventional control strategies.

2. Physical structure and mathematical model

2.1. Physical structure

An overview of the brushed DC motor is given in this section to illustrate the background of the control problem. Fig. 1 depicts the circuit topology and physical setup of the brushed DC motor where ω represents the angular speed, u denotes the input voltage, L , i , R , and E are equivalent inductance, current, equivalent resistance, back-EMF of armature respectively. Symbol J denotes the total inertia of the system, f is the friction coefficient, E_s and i_s are the excitation voltage and current, respectively.

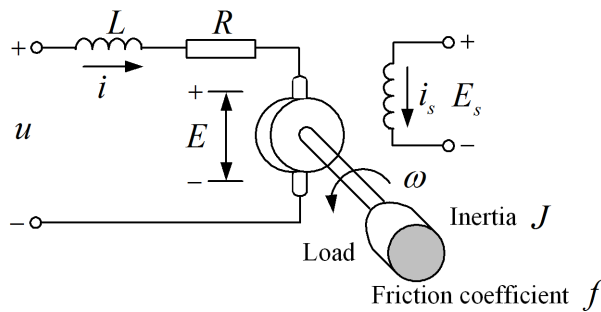


Fig. 1. Physical setup of brushed DC motor

As stated in introduction, angular speed control of the brushed DC motor is an important topic. There are main three kinds of angular speed control method in practice: change of the input voltage u , tuning of the resistance R , and change of the excitation voltage E_s . The first method is the most frequently used for small and medium brushed DC motors. Changing of the input voltage is usually accomplished by the PWM (Pulse Width Modulation) method. A switch is inserted into the power supply circuit, the power supply is turned on and off periodically with fixed frequency. The averaged input voltage U_d is determined by the percent of T_{on} with respect to switching period T (i.e., T_{on}/T), which is called the duty cycle d . As a result, the angular speed of the brushed DC motor can be controlled by the duty cycle d .

2.2. Mathematical model

Mathematical model of the brushed DC motor can be derived by choosing $x(t) \in [i, \omega]^T$ as the state vector. For each switching period T , the system has different dynamics in T_{on} and T_{off} , which are referred to as different modes. By applying Kirchhoff's Voltage and Current Laws, and Newton's Dynamic Law, we have the continuous time state space model for each mode.

2.2.1. Model 1 (T_{on}).

$$\dot{x} = Fx + g = \begin{bmatrix} -\frac{R}{L} & -\frac{C_e}{L} \\ \frac{C_M}{J} & -\frac{f}{J} \end{bmatrix} \cdot x + \begin{bmatrix} \frac{1}{L} \\ 0 \end{bmatrix} \cdot u, \tag{1}$$

$$y = [0 \ 1]x. \tag{2}$$

2.2.2. Model 2 (T_{off}).

$$\dot{x} = Fx = \begin{bmatrix} -\frac{R}{L} & -\frac{C_e}{L} \\ \frac{C_M}{J} & -\frac{f}{J} \end{bmatrix} \cdot x, \tag{3}$$

$$y = [0 \ 1]x. \tag{4}$$

where C_e and C_M are the voltage coefficient and torque coefficient of the brushed DC motor, respectively.

For the optimal control problem formulation, a discrete-time prediction model is needed. The model should be beneficial to capture the evolution of the states not only at time instant kT but also within the switching period which would be able to impose system constraints on intermediate samples. This could be done by dividing the period length T into v subperiods T_0 , which is shown in Fig. 2 (take $v = 3$ for example).

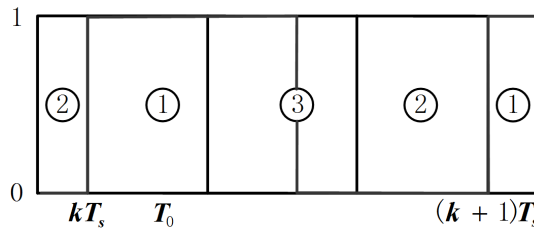


Fig. 2. Position of the switch and active mode in the respective subperiod

According to the switch position and continuous time model, we have different models for the three different modes of subsystems.

Mode 1: $\xi(n + 1) = \Phi\xi(n) + \Psi, \quad d(k) \geq (n + 1)/v,$

Mode 2: $\xi(n + 1) = \Phi\xi(n), \quad d(k) \geq n/v,$

Mode 3: $\xi(n + 1) = \Phi\xi(n) + \Psi(vd(k) - n), \quad n/v \leq d(k) \leq (n + 1)/v,$ where

$$\Phi = e^{FT_0}, \tag{5}$$

$$\Psi = \int_0^{T_0} e^{F(T_0-t)} dt \cdot g = \int_0^{T_0} e^{Ft} dt \cdot g. \tag{6}$$

The corresponding matrices F and g are given in (1)–(4).

3. Proposed control schema: EMPC

3.1. Hybrid discrete-time modelling

In order to implement the EMPC scheme, an adequate discrete-time model should be derived at first step. The discrete-time model must be accurate enough to guarantee satisfactory performance and sufficiently simple for controller design.

Start from the normalized continuous state space model (1)–(4). Divide the switching period into three equal intervals as shown in Fig. 2. We have the hybrid discrete time state space model of the brushed DC motor in hybrid (piecewise affine) form given as follows

$$x(k+1) = \begin{cases} \Phi^3 x(k) + 3\Phi^2 \Psi d(k) & d(k) \in [0, 1/3]. \\ \Phi^3 x(k) + \Phi^2 \Psi + 3\Phi \Psi (d(k) - 1/3) & d(k) \in [1/3, 2/3]. \\ \Phi^3 x(k) + \Phi^2 \Psi + \Phi \Psi + 3\Psi (d(k) - 2/3) & d(k) \in [2/3, 1]. \end{cases} \quad (7)$$

where matrices Φ and Ψ are given by (5) and (6).

3.2. EMPC based on multi-parametric programming: a brief review

For the sake of the readers' convenience, a brief review of EMPC based on multi-parametric programming, which has been applied to typical linear quadratic control for constrained systems [15], is given in this section.

Consider a discrete-time MIMO LTI (Linear Time-Invariant) system of the regular form:

$$\begin{cases} x(k+1) = Ax(k) + Bu(k) \\ y(k) = Cx(k) \end{cases} \quad (8)$$

subjected to the constraints

$$x_{\min} \leq x(k) \leq x_{\max}, y_{\min} \leq y(k) \leq y_{\max}, u_{\min} \leq u(k) \leq u_{\max} \quad (9)$$

at all time instants $k \geq 0$. In equations (8)-(9), the state vector $x(k) \in \mathbb{R}^n$, output vector $y(k) \in \mathbb{R}^q$, and the input vector $u(k) \in \mathbb{R}^p$, the state space matrices A , B and C are of proper dimension.

In the literature, for system (8), MPC solves the following optimization problem

$$\begin{aligned} & \min \\ & U \triangleq \{u_k, \dots, u_{k+N_u-1}\} \\ & \left\{ J(U, x(k)) = x'_{k+N_p} P x_{k+N_p} + \sum_{j=0}^{N_p-1} \left[x'_{k+j} Q x_{k+j} + u'_{k+j} R u_{k+j} \right] \right\} \end{aligned} \quad (10)$$

subjected to system dynamics and constraints.

The idea of MPC is the construction of an optimal control input sequence $U^* = \{u_k^*, u_{k+1}^*, \dots, u_{k+N_u-1}^*\}$, which minimizes the cost function J in (10) with respect

to the state, output and input constraints (9). And MPC employs the receding horizon control principle, only the first step of the control input U^* (i.e., $u^*(k)$) is taken into the system at the time instant k . As for $k + 1$, the whole procedure will be repeated once again, that is, this optimal programming will be taken over and over again along the control time sequence. MPC has been regarded as one of the practical modern control strategies. However, it usually has the drawback of heavy on-line computational burden. As a result, the application of MPC strategy needs expensive on-line computation power and MPC is labeled as a technology for slow processes. In this paper, we adopt a recently proposed EMPC strategy based on multi-parametric programming which is able to move all the computations of MPC off-line. And the resulting controller is an explicit piecewise affine function of the states which is suitable for the discrete-time hybrid model of the brushed DC motor derived in Section 3.1.

By substituting $x_{k+j} = A^j x(k) + \sum_{m=0}^{j-1} A^{j-m-1} B u_{k+m}$, the optimal problem (10) can be rewritten in compact form as

$$V^*(x_k) = \frac{1}{2} x'_k Y x_k + \min_U \left\{ \frac{1}{2} U' H U + x'_k F U, \text{ s.t. } G U \leq W + E x_k \right\}, \quad (11)$$

where $U = [u'_k, u'_{k+1}, \dots, u'_{k+N_u-1}]'$ is the optimization vector, and H, F, Y, G, W, E are obtained from Q and \tilde{R} in (10). As proposed in [10], the quadratic problem (11) can be solved by multi-parametric quadratic programming. By setting $z \triangleq U + H^{-1} F' x_k$, (11) can be transformed into the form

$$V_z^*(x_k) = \min_z \frac{1}{2} z' H z \text{ s.t. } G z \leq W + S x_k, \quad (12)$$

where $S \triangleq E + G H^{-1} F'$ and $V_z^*(x_k) = V^*(x_k) - \frac{1}{2} x'_k (Y - F H^{-1} F') x_k$.

For the multi-parametric quadratic programming of problem (12), we introduce the following result which is the key to construct a piecewise affine state-feedback control law for EMPC.

Lemma 1 [11]: For a quadratic programming problem stated in (12), let $z = z_0^*$ be the optimal solution for a given state x_k^0 and $\{\tilde{G}, \tilde{W}, \tilde{S}\}$ is the uniquely determined set of active constraints $\tilde{G} z_0^* = \tilde{W} + \tilde{S} x_k^0$. Assume that the rows of \tilde{G} are linearly independent, and let CR_0 be the set of all vectors x_k for which the combination of constraints $\{\tilde{G}, \tilde{W}, \tilde{S}\}$ is active at the optimum (CR_0 being referred to as critical region). Then, the optimal solution z^* of (12) is a uniquely defined affine function of x_k

$$z^* = H^{-1} \tilde{G}' \left(\tilde{G} H^{-1} \tilde{G}' \right)^{-1} \left(\tilde{W} + \tilde{S} x_k \right) \quad (13)$$

over the polyhedral region CR_0 defined by

$$GH^{-1}\tilde{G}' \left(\tilde{G}H^{-1}\tilde{G}' \right)^{-1} \left(\tilde{W} + \tilde{S}x_k \right) \leq W + Sx_k^0 \quad (14)$$

and

$$\left(\tilde{G}H^{-1}\tilde{G}' \right)^{-1} \left(\tilde{W} + \tilde{S}x_k \right) \leq 0. \quad (15)$$

To summarize, multi-parametric quadratic programming systematically subdivides the space X of parameters x_k into critical regions (CRs). For every CR , the optimal solution z^* is an affine function of x_k . Once the critical region CR_0 has been defined, the rest of the space $CR^{\text{rest}} \triangleq X \setminus CR_0$ can be explored and new critical regions will be generated by an iterative algorithm which partition CR^{rest} recursively. As for the iterative algorithm, interested readers may refer to related articles of EMPC [11].

As a result, the state space X is divided into critical regions, and in each region, the optimal solution $z^*(x_k)$ is an affine function of x_k (i.e., $z^*(x_k)$ is piecewise affine) which can be calculated off-line.

3.3. EMPC controller design

A simple brushed DC motor is taken as an example to the implementation of EMPC strategies. Its parameters are given as follows: $u = 12\text{ V}$, $L = 0.329\text{ mH}$, $R = 1.4\ \Omega$, $C_e = 0.06\text{ V}\cdot\text{s}/\text{rad}$, $C_M = 0.08\text{ N}\cdot\text{m}/\text{A}$, $J = 0.0137\text{ g}\cdot\text{m}^2$, and $f = 0.008\text{ N}\cdot\text{m}\cdot\text{s}/\text{rad}$. The hybrid discrete-time model can easily be derived from these parameters.

The control objectives are to regulate the output voltage to its reference, or in other words, to minimize the output voltage error $\omega_{o,\text{err}} = \omega_o - \omega_{o,\text{ref}}$ with respect to the constraints on the armature current, input duty cycle and input rate. Additionally, we introduce the difference of two consecutive duty cycles

$$\Delta d(k) = d(k) - d(k-1).$$

Define now the penalty matrix $Q = \text{diag}(q_1, q_2)$ and vector $\varepsilon(k) = [\omega_{o,\text{err}}(k), \Delta d(k)]$. The performance index function is given as

$$J = \sum_{k=0}^{N-1} \varepsilon^T(k) Q \varepsilon(k). \quad (16)$$

Based on the piecewise affine discrete-time linear model (7) and performance index function (16), piecewise affine EMPC controllers can be designed according to the standard procedure discussed in Section 3.2.

4. Simulation and experiment results

Dynamic simulations using Matlab were carried out to evaluate the performance of the proposed EMPC strategy. The simulations were performed on a mathematical model which is tuned in agreement with the real plant and adequately grasps the dynamic behavior of the brushed DC motor. Therefore, they are very useful for tasks such as high performance controller design and evaluation.

For the sake of comparison, we also report simulation results of the conventional PI algorithm which adjusts the control input of the PWM according to the difference between the output angular speed and the reference speed. The PI regulators are of the form

$$d(k) = 0.02(\omega_{o,\text{ref}} - \omega_o) + 0.004 \int (\omega_{o,\text{ref}} - \omega_o) dt,$$

which were developed by on-line tuning.

As far as the characteristics of the brushed DC motor system are concerned, we choose prediction horizon $N = 6$ for EMPC. The weight matrices are selected as $Q = \text{diag}(0.01, 5)$. The constraints are taken from the parameters $0 \leq d \leq 1$, $|\Delta d| \leq 0.2$. As for system model mismatches and sustaining disturbances, the predictive model will be inadequate, which will cause steady state error. A feedback correction algorithm is proposed to eliminate the steady state error, that is

$$y_p(k+i|k) = y_M(k+i|k) + h_i e(k), \quad i = 1, \dots, N, \quad (17)$$

$$e(k) = y(k) - y_M(k), \quad (18)$$

where $e(k)$ is the prediction error at time instant k , $y_M(k+i|k)$ is the predicted output based on predictive model, h_i is the feedback correction coefficient which can be determined by trade-off or online identification, $y_P(k+i|k)$ is the corrected predictive output, which is finally taken into account in the EMPC strategy.

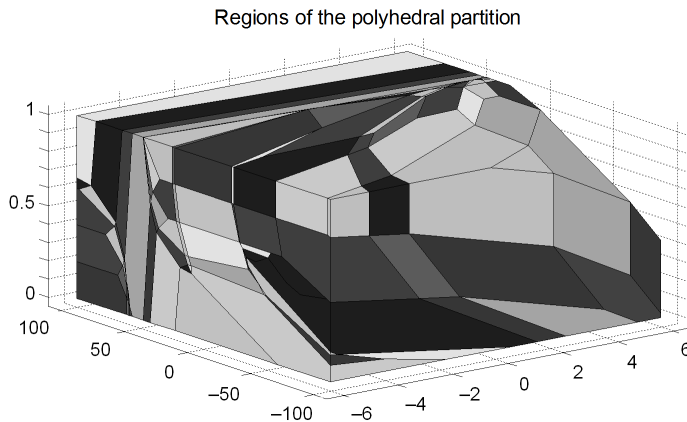


Fig. 3. Regions of the polyhedral partition

Simulation results considering the startup, step disturbance and input voltage step down of the brushed DC motor system are given in Figs. 3–6, where the results of EMPC controllers are drawn in solid lines and PI controllers in dashed lines.

The regions of the polyhedral partition are shown in Fig. 3. For each critical region, the optimal EMPC control law is an affine function of the states and the previous control input. Figure 4 gives the system trajectories during startup under EMPC and PI controllers. As we can see from the trajectories, the EMPC controller derives the angular speed to the reference quickly and with small overshoot whereas the PI controller reacts slowly and results in big overshoot. With the help of system constraint handling, EMPC control strategy respects the input and armature current constraint. Conventional PI controller deal with the input constraint by saturation but fail to handle armature current constraint. As far as the difference of two consecutive inputs is concerned, EMPC successfully restricts the difference within the constraint $[-0.2, 0.2]$. Figure 5 gives the state and input trajectories of the system in presence of angular speed step disturbance active for $t \geq 80$ s after startup. As we can see from the figures, the EMPC strategy settles down the system in presence of step disturbance quickly compared with the conventional PI schema. Figure 6 gives the closed-loop responses to the step-down change in the input voltage active for $t \geq 80$ s. It also shows that both EMPC and conventional PI can derive the angular speed to the reference, however, the deviations of angular speed and armature current is smaller under EMPC.

As we can see from the simulation results, EMPC improves the closed-loop performance systematically and the controller is easy to tune by adjusting the weight matrices.

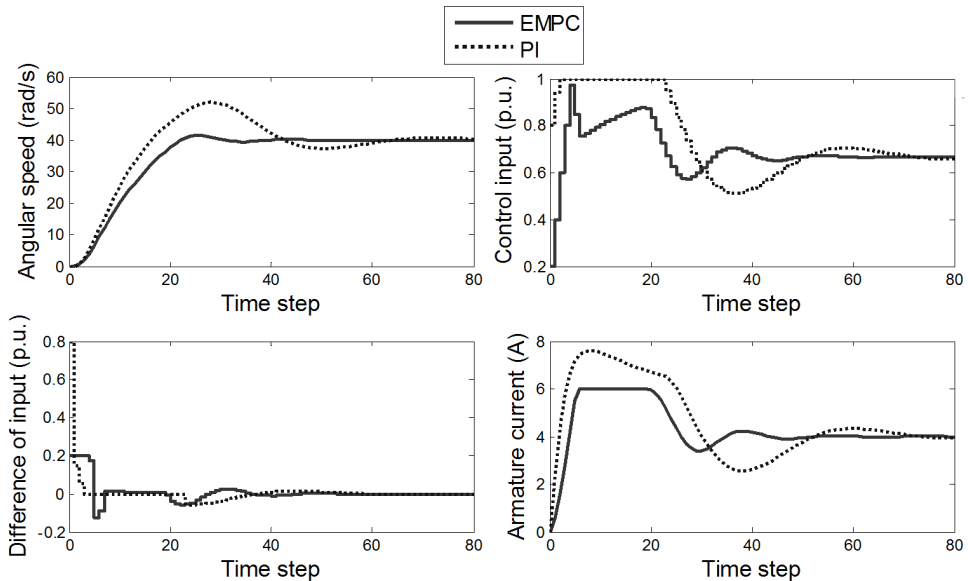


Fig. 4. Closed-loop responses during startup

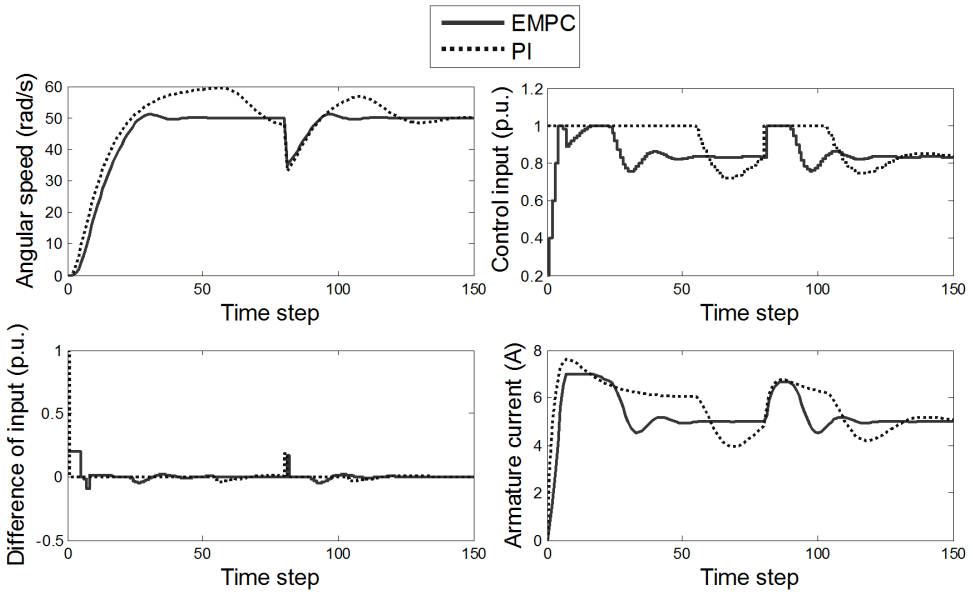


Fig. 5. Closed-loop responses to the step disturbance active for $t \geq 80$ s

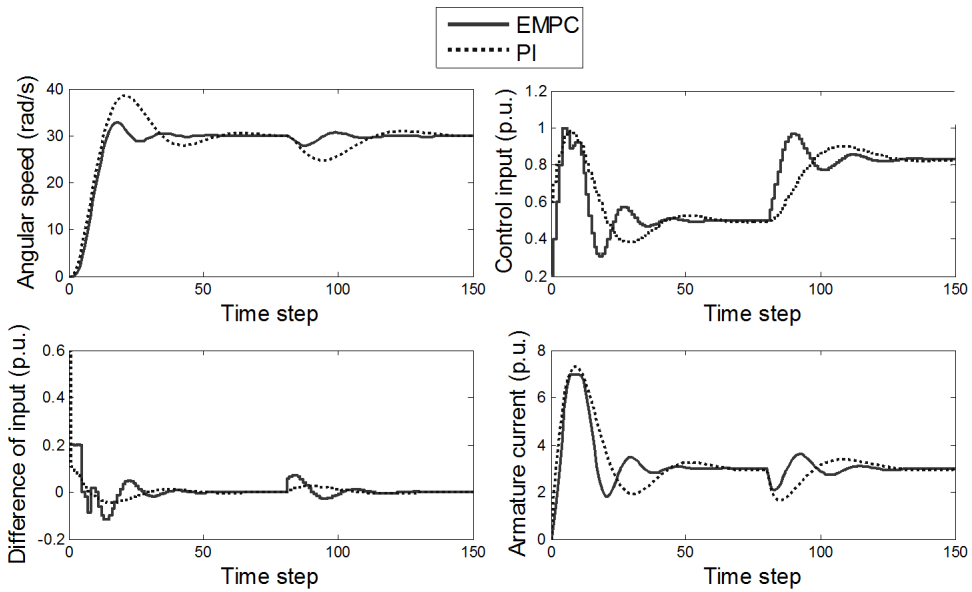


Fig. 6. Closed-loop responses to the step-down change in the input voltage active for $t \geq 80$ s

5. Conclusion

EMPC is proposed for brushed DC motor speed control under unmodelled disturbances. The EMPC strategy divides the state space into critical regions. For each critical region, the optimal control law is an affine function of the states and previous control input which could be calculated off-line. The constraint optimal speed control of brushed DC motor is transformed into a table look-up algorithm and the on-line computation time is greatly reduced. As a result, the brushed DC motor system is coordinately controlled and can easily be tuned by adjusting the weight matrices. EMPC improves the closed-loop performance remarkably compared with conventional PI regulator. Inspired by this benchmark example, EMPC can be extended to power electronic converters, electrical drives and related fields for constraint handling and optimal control. However, in order to apply this scheme to industry practice, a major and important work to be done is realization of the algorithm in the embedded system which has limited computation power and hardware resources.

References

- [1] J. RUIZ-ROSETO, E. TORRES, E. VILLARREAL: *Design and construction of a mobile robot with regenerative brake on DC motors*. IJ Materials Science and Engineering 2 (2014), No. 1, 6–9.
- [2] P. RADCLIFFE, D. KUMAR: *Sensorless speed measurement for brushed DC motors*. IET Power Electronics 8 (2015), No. 11, 2223–2228.
- [3] Y. LIU, J. ZHAO, M. XIA, H. LUO: *Model reference adaptive control-based speed control of brushless DC motors with low-resolution hall-effect sensors*. IEEE Trans. Power Electronics 29 (2014), No. 3, 1514–1522.
- [4] S. SHEEL, O. GUPTA: *High performance fuzzy adaptive PID speed control of a converter driven DC motor*. IJ Control and Automation 25 (2012), No. 1, 71–88.
- [5] E. VAZQUEZ-SANCHEZ, J. GOMEZ-GIL, J. C. GAMAZO-REAL, J. F. DIEZ-HIGUERA: *A new method for sensorless estimation of the speed and position in brushed DC motors using support vector machines*. IEEE Trans. Industrial Electronics 59 (2012), No. 3, 1397–1408.
- [6] J. PENG, R. DUBAY: *Identification and adaptive neural network control of a DC motor system with dead-zone characteristics*. ISA Transactions 50 (2011) No. 4, 588–598.
- [7] Y. YANG, Y. WANG, P. JIA: *Adaptive robust control with extended disturbance observer for motion control of DC motors*. Electronics Letters 51 (2015), No. 22, 1761 to 1763.
- [8] F. S. AHMED, S. LAGHROUCHE, M. HARMOUCHE: *Adaptive backstepping output feedback control of DC motor actuator with friction and load uncertainty compensation*. IJ Robust and Nonlinear Control 25 (2015), No. 13, 1967–1992.
- [9] M. RIVERA, J. RODRIGUEZ, S. VAZQUEZ: *Predictive control in power converters and electrical drives - Part I*. IEEE Trans. Industrial Electronics 63 (2016), No. 6, 3834 to 3836.
- [10] J. B. RAWLINGS: *Tutorial overview of model predictive control*. IEEE Trans. Control Systems 20 (2000), No. 3, 38–52.
- [11] A. BEMPORAD, M. MORARI, V. DUA, E. N. PISTIKOPOULOS: *The explicit linear quadratic regulator for constrained systems*. Automatica 38 (2002), No. 1, 3–20.

- [12] A. BEMPORAD, F. BORRELLI, M. MORARI: *Model predictive control based on linear programming—The explicit solution*. IEEE Trans. Automatic Control *47* (2003), No. 12, 1974–1985.
- [13] F. BAYAT, T. A. JOHANSEN: *Multi-resolution explicit model predictive control: Delta-model formulation and approximation*. IEEE Trans. Automatic Control *58* (2013), No. 11, 2979–2984.
- [14] S. MARIETHOZ, A. DOMAHID, M. MORARI: *High-bandwidth explicit model predictive control of electrical drives*. IEEE Trans. Industry Applications *48* (2012), No. 6, 1980 to 1992.
- [15] M. A. MOHAMMADKHANI, F. BAYAT, A. A. JALALI: *Design of explicit model predictive control for constrained linear systems with disturbances*. IJ Control, Automation and Systems *12* (2014), No. 2, 294–301.

Received November 16, 2016

Batch delivery scheduling with simple linear deterioration on a single machine¹

JUAN ZOU^{2,3}

Abstract. Several single machine scheduling problems are solved, in which n independent jobs are available simultaneously and delivered to the customer together upon the completion time of the last job in the batch. The processing time of a job is a simple linear increasing function of its starting time. The objective is to minimize the scheduling cost plus the delivery cost, using several classical scheduling objectives. The several problems are to determine the optimal number of batches, the assignment of jobs to the batches and the job processing sequence so that the sum of cost is minimized. For each problem, we either derive an efficient dynamic programming algorithm that minimizes total cost, or provide some basic properties of the intractable problem.

Key words. Scheduling, batch delivery, linear deterioration, dynamic programming.

1. Introduction

Batch scheduling problems, as combinations of sequencing and partitioning problems, have attracted much attention of researchers in recent years. Motivation for the batch delivery problems comes from the assembly stage in manufacturing of very large-scale integrated circuits. In this stage, chips of various types are attached and placed on a circuit board by a pick and insertion machine. Each circuit board represents a job, upon completion, it is loaded onto a pallet. Intermittently, pallets are moved to the soldering machine and then to the test area. A set of circuit boards loaded on a pallet corresponds to a batch. In practice, however, the number of pallets in use is a cost factor which has to be taken into account. Then we obtain a situation which can be modelled as a batch delivery problem formulated. Batch delivery problems were first introduced by Cheng and Kahlbacher [1], who studied single machine batch delivery scheduling to minimize the sum of the total

¹This paper is supported by the Science and Technology Projects of Qufu Normal University (xkj201516&sk201507).

²School of Mathematics and Statistics, Zhengzhou University, Zhengzhou, 450001, China

³School of Mathematical Sciences, Qufu Normal University, Shandong, 273165, China

weighted earliness and delivery costs. They showed that the problem is NP-complete in the ordinary sense, and the equal weight case is solved in polynomial time. Ahmadizar and Farhadi [2] studied the single machine scheduling problem in which jobs are released in different points in time but delivered to customers in batches. A mathematical formulation is developed and dominance properties providing necessary conditions for any solution to be optimal are established. Hall and Potts [3] analyzed the complexity of some single machine scheduling problems with deliveries. Yin, Ye and Zhang [4] considered the problem of scheduling n non-resumable and simultaneously available jobs on a single machine, the jobs are delivered in batches to the customers. The objective is to minimize the sum of total flow time and batch delivery cost. They proved the problem is NP-hard and developed two fully polynomial time approximation schemes. Mor and Mosheiov [5] studied a single machine batch scheduling problem with unit time jobs and an optional maintenance activity, the objective function is minimum total flowtime. They proposed a simple rounding procedure that guarantees an integer solution. Selvarajah and Zhang [6] considered supply chain scheduling problem, the objective is to minimize the sum of weighted flow time and the batch delivery costs. They analyzed some polynomially solvable problems and developed a heuristic algorithm for the general problem. Rostami et al. [7] proposed a single-machine scheduling problem that involves minimizing the maximum tardiness plus delivery costs in a batched delivery system with release times. They developed a MIP model and proposed a B&B algorithm with a heuristic upper bound and the LP relaxation technique was developed.

In the classical scheduling theory, the processing times of jobs are considered to be constant and independent of their starting times. However, this assumption is not appropriate for the modelling of many modern industrial processes where the processing time of a job may deteriorate while waiting to be processed. Machine scheduling problems with time dependent processing times have received increasing attention in the recent years. This model reflects some real-life situations in which the expected processing time of a task increases/decreased linearly with starting time. In fact, such situations can be found in maintenance scheduling, steel production, cleaning assignment, fire fighting, resource allocation, where any delay in processing a job may increase the time necessary for its completion. Scheduling deteriorating jobs was first considered by Browne and Yechiali [8] who assumed that the processing times of jobs are non-decreasing, start time dependent linear functions. They provided the optimal solution when the objective is to minimize the expected makespan. Mosheiov [9] considered simple linear deterioration where jobs have a fixed job-dependent growth rate but no basic processing time. He showed that most commonly applied performance criteria, such as the makespan, the total flow time, the total lateness, the sum of weighted completion times, the maximum lateness, the maximum tardiness, and the number of tardy jobs, remain polynomial solvable. Since then, Machine scheduling problems with time dependent processing times have received increasing attention. Cheng, Ding and Lin [10] presented a survey of the results on scheduling problems with time-dependent processing times. Pei et al. [11] considered serial batching scheduling problem with deteriorating jobs in a two-stage supply chain. The objective is to make decisions on job batching and batch sequenc-

ing so as to minimize the makespan. They presented some useful properties and a heuristic for solving it. Yin et al. [12] studied a new deterioration model, the objective is to find the optimal schedule such that makespan or total completion time is minimized. They showed that both problems are solvable in polynomial time.

In this paper, we assume that the actual processing time of each job is a simple linear increasing function of its starting time. The actual processing time of job j in a schedule is given by $p_j = b_j t$, where t represents its starting time. Note that the assumption $t_0 > 0$ is made here to avoid the trivial case of $t_0 = 0$ (when $t_0 = 0$, the completion time of each job will be 0). Each batch is to be assigned a delivery date upon which all jobs within the batch are to be delivered to the customer together. The delivery time of the batch is equal to the completion time of the last job in the batch. There is also a batch delivery cost which is a non-negative function that depends on the number of batches formed to process all the jobs. The problem is to determine simultaneously the optimal number of batches, the assignment of jobs to the batches and the job processing sequence so that the sum of batch delivery cost and the scheduling cost is minimized.

This paper is organized as follows. In section 2, we describe our notation and our scheme for the scheduling and batch delivery problems. In section 3, we provide dynamic programming algorithms for the minimization of total scheduling cost and delivery cost. For the total weighted completion time and delivery cost, we discuss several basic properties. In section 4, we conclude the paper and suggest some topics for future research.

2. Preliminaries

In this section, we describe our notation and assumptions. We begin with some notation. The jobs are processed on a single machine. Let $J = \{1, 2, \dots, n\}$ denote the set of jobs to be processed. For job $j \in J$, let p_j denote its processing time, w_j denote its weight and d_j denote its due date. Pre-emption is not allowed. The actual processing time of job j in a schedule is given by $p_j = b_j t$, where t represents its starting time. Jobs form a batch if all of these jobs are dispatched to a customer together in a single delivery. The batch delivery date is equal to the completion time of the last job in the batch. The nonnegative delivery cost $C(y)$ is assumed to be a non-decreasing function of the number of batches y . For any schedule σ , we define:

- $C_j(\sigma)$ is the time at which job j is delivered to its customer,
- $L_j(\sigma) = C_j(\sigma) - d_j$ is the lateness of job j ,
- $U_j(\sigma) = 1$ if job j is late, while $U_j(\sigma) = 0$, if job j is delivered to its customer by its due date,
- $y(\sigma)$ is the number of batch deliveries and
- $C(y)$ is the delivery cost function, which is a non-decreasing function of y .

The objective functions that we consider works with the delivery cost $C(y)$ and a scheduling cost. First we denote

- $\sum C_j$ is the total completion time of the jobs,
- $\sum w_j C_j$ is the total weighted completion time of the jobs,
- $L_{\max} = \max_{j \in J} \{L_j\}$ is the maximum lateness of the jobs and
- $\sum U_j$ is the total number of late jobs.

An example of the classification scheme is problem 1 $|P_j = b_j t, r_j = t_0| \sum C_i + C(y)$, which denotes the minimization of the total delivery cost and job completion times on a single machine under simple linear deterioration.

We make use of the following results which are given without proof.

Lemma 1: In any of the scheduling problems that we consider, there is no idle time between the jobs on the machine.

Lemma 2: For any optimal schedule, the sequence of jobs within each batch is immaterial.

3. Main results

3.1. Sum of completion times

Lemma 3: For problem 1 $|P_j = b_j t, r_j = t_0| \sum C_i + C(y)$, the cost is minimized by sequencing the jobs according to non-decreasing order of deterioration rate b_j (SDR).

Proof: Consider an optimal schedule σ^* . Since all jobs within a delivery batch can be sequenced in non-decreasing order of deterioration rate b_j without affecting the cost, we assume that non-decreasing order of b_j for jobs within a batch holds for σ^* . If σ^* contains jobs that are not sequenced in non-decreasing order of b_j , then we must have a job j that is the last job to be processed in some batch B , and another job i that is the first job to be processed in the next batch B' , where $b_j > b_i$.

Consider another schedule σ that is created by interchanging jobs j and i , and forming delivery batches containing jobs $B \cup \{i\} \setminus \{j\}$ and $B' \cup \{j\} \setminus \{i\}$ in σ , where the first of these batches is delivered at the earlier time than batch B in σ^* and the second of these batches is delivered at the same time as batch B' in σ^* . All the other delivery batches are identical and delivered at the same time in σ as in σ^* . A finite number of repetitions of this argument establishes that there exists an optimal schedule in which the jobs are sequenced in SDR order.

As a result of Lemma 3, we assume that the jobs are indexed in SDR order, so that $b_1 \leq b_2 \leq \dots \leq b_n$. In the following, we design the dynamic programming algorithm for problem 1 $|P_j = b_j t, r_j = t_0| \sum C_i + C(y)$. Then the total cost of the partial schedule is a function value, while the number of deliveries and the index of the current last job which is processed and delivered are state variables. More

precisely, $f(k, y)$ denotes the minimum total cost for processing and delivering jobs $1, 2, \dots, k$ using y deliveries, with the last delivery at time $t_0(1 + b_1) \dots (1 + b_k)$, where $0 \leq y \leq k \leq n$. We propose the following dynamic programming algorithm to solve the problem $1 | P_j = b_j t, r_j = t_0 | \sum C_i + C(y)$.

Algorithm DP1

- **Step 1: (Initialization)** Number jobs in SDR order. Set $f(0, 0) = 0$.
- **Step 2: (Recursion relation)**

$$f(k, y) = \min_{0 \leq j < k} \{f(j, y - 1) + (k - j)t_0(1 + b_1) \dots (1 + b_k) + C(y) - C(y - 1)\} .$$

If $k = n$, go to Step 3; otherwise set $k = k + 1$ and repeat Step 2.

- **Step 3: (Optimal solution)**

$$\min_{1 \leq y \leq n} \{f(n, y)\}$$

and use backtracking to find the corresponding optimal schedule.

Theorem 1: Algorithm DP1 gives an optimal schedule for

$$1 | P_j = b_j t, r_j = t_0 | \sum C_i + C(y)$$

in $O(n^3)$ time.

Proof: There are $O(n^2)$ states (k, y) , and for each state the recurrence relation requires $O(n)$ time. Therefore, the overall time complexity of Algorithm DP1 is $O(n^3)$.

3.2. Sum of weighted completion times

The NP-hardness of the problem $1 | P_j = b_j t, r_j = t_0 | \sum w_i C_i + C(y)$ remains open. In the following, we present several properties of the optimal schedule.

Property 1: There exists an optimal sequence for $1 | P_j = b_j t, r_j = t_0 | \sum w_i C_i + C(y)$ such that the delivery batch is sequenced in non-decreasing order of $(F_B - 1)/(w_B F_B)$, where $w_B = \sum_{j \in B} w_j$ denotes the total weights of jobs in batch B , $F_B = \prod_{j \in B} (1 + b_j)$.

Proof: Consider an optimal schedule σ^* . If σ^* contains batches that are not sequenced in non-increasing order of $\frac{F_B - 1}{w_B F_B}$, then we must have a pair of batches B_i, B_j such that batch B_i starting at time S is followed by batch B_j , and $\frac{F_{B_i} - 1}{w_{B_i} F_{B_i}} > \frac{F_{B_j} - 1}{w_{B_j} F_{B_j}}$. So we have the objective value of batch B_i and B_j in σ^* , $w_{B_i} S \cdot F_{B_i} + w_{B_j} S \cdot F_{B_i} F_{B_j}$.

Consider a new schedule σ which is obtained from σ^* by interchanging batches B_i and B_j . Under σ , we have $w_{B_j}S \cdot F_{B_j} + w_{B_i}S \cdot F_{B_i}F_{B_j}$. Then we obtain that

$$\begin{aligned} &w_{B_i}S \cdot F_{B_i} + w_{B_j}S \cdot F_{B_i}F_{B_j} - (w_{B_j}S \cdot F_{B_j} + w_{B_i}S \cdot F_{B_i}F_{B_j}) = \\ &= S(w_{B_i}F_{B_i}(1 - F_{B_j}) - w_{B_j}F_{B_j}(1 - F_{B_i})) \geq 0. \end{aligned}$$

Since all other completion times are unchanged, this contradicts the optimality of σ^* . We conclude that the non-decreasing order of $F_B - 1/(w_B F_B)$ is the optimal schedule.

Property 2: For any two jobs $i, j \in J$ to be scheduled consecutively, if $b_i > b_j, w_j > w_i$ and $w_i b_i > w_j b_j$, there is an optimal schedule in which job j immediately precedes job i .

Proof: Consider an optimal schedule σ^* . Obviously, all jobs within a delivery batch can be sequenced in order from Property 2. Then there exists a pair of (i, j) in σ^* such that job i is followed by j . A job i that is the last job to be processed in some batch B_k , and another job j that is the first job to be processed in the next batch B_{k+1} . Let S denotes the starting time of job i , \bar{W} denotes the total weight in B_k except job i , D_{k+1} denotes the delivery time of B_{k+1} . Then

$$\begin{aligned} \sum_{l \in B_k} w_l C_l &= (w_i + \bar{W})C_{B_k}(\sigma^*) = (w_i + \bar{W})S \cdot (1 + b_i), \\ w_j C_j(\sigma^*) &= w_j D_{k+1}. \end{aligned}$$

Consider a new schedule σ that is created by interchanging jobs i and j , and form delivery batches containing jobs $B'_k = B_k \cup \{j\} \setminus \{i\}$ and $B'_{k+1} = B_{k+1} \cup \{i\} \setminus \{j\}$. Thus,

$$\begin{aligned} \sum_{l \in B'_k} w_l C_l &= (w_j + \bar{W})C_{B'_k}(\sigma) = (w_j + \bar{W})S \cdot (1 + b_j), \\ w_i C_i(\sigma) &= w_i D_{k+1}. \end{aligned}$$

It follows that

$$\begin{aligned} &\sum_{l \in B_k} w_l C_l + w_j C_j(\sigma^*) - \sum_{l \in B'_k} w_l C_l - w_i C_i(\sigma) = \\ &= (w_i + \bar{W})S \cdot (1 + b_i) + w_j D_{k+1} - (w_j + \bar{W})S \cdot (1 + b_j) - w_i D_{k+1} = \\ &= \bar{W}S(b_i - b_j) + (D_{k+1} - S)(w_j - w_i) + S(w_i b_i - w_j b_j) \geq 0. \end{aligned}$$

A finite number of repetitions of this argument establishes that there exists an optimal schedule in which the jobs are sequenced by Property 2.

3.3. Maximum lateness

Lemma 4: For problem $1 | P_j = b_j t, r_j = t_0 | L_{\max} + C(y)$, there exists an optimal schedule in which the jobs are sequenced according to an earliest due date (EDD) rule.

As a result of Lemma 4, we assume that the jobs are indexed in EDD order, so that $d_1 \leq d_2 \leq \dots \leq d_n$. In the following, we design the dynamic programming algorithm for problem $1 | P_j = b_j t, r_j = t_0 | L_{\max} + C(y)$, the maximum lateness of the partial schedule is a function value, while the number of deliveries and the index of the current last job which is processed and delivered are state variables. More precisely, $f(k, y)$ denotes the minimum value of the maximum lateness for processing and delivering jobs $1, 2, \dots, k$, using y deliveries, with the last delivery at time $t_0(1 + b_1) \dots (1 + b_k)$, where $0 \leq y \leq k \leq n$. A formal statement of this dynamic programming algorithm is as follows.

Algorithm DP2

- **Step 1: (Initialization)** Number jobs in EDD order. Set $f(0, 0) = -\infty$.
- **Step 2: (Recursion relation)**

$$f(k, y) = \min_{0 \leq j < k} \{ \max \{ t_0(1 + b_1) \dots (1 + b_k) - d_{j+1}, f(j, y - 1) \} \} .$$

If $k = n$, go to Step 3; otherwise set $k = k + 1$ and repeat Step 2.

- **Step 3: (Optimal solution)**

$$\min_{1 \leq y \leq n} \{ f(n, y) + C(y) \}$$

and use backtracking to find the corresponding optimal schedule.

Some remarks should be made about algorithm DP2. In step 2, the recurrence relation selects a batch $\{j + 1, \dots, k\}$ of jobs to be delivered at time $t_0(1 + b_1) \dots (1 + b_k)$. From the EDD indexing of the jobs, job $j + 1$ has the smallest due date and hence also the maximum lateness in this batch, the lateness of job $j + 1$ is compared with the maximum lateness of the jobs that have been scheduled earlier.

Theorem 2: Algorithm DP2 gives an optimal schedule for

$$1 | P_j = b_j t, r_j = t_0 | L_{\max} + C(y)$$

in $O(n^3)$ time.

Proof: There are $O(n^2)$ states (k, y) , and for each state the recurrence relation requires $O(n)$ time. Therefore, the overall time complexity of Algorithm DP2 is $O(n^3)$.

3.4. Number of late jobs

Lemma 5: For problem $1|P_j = b_j t, r_j = t_0|\sum U_j + C(y)$, there exists an optimal schedule in which the on-time jobs are sequenced according to an earliest due date (EDD) rule.

We assume that a job which would be late is neither product nor delivered. As a result of Lemma 5, we assume that the on-time jobs are indexed in EDD order. For problem $1|P_j = b_j t, r_j = t_0|\sum U_j + C(y)$, we describe a dynamic programming algorithm that either appends a job to some previous schedule of on-time jobs, or specifies that this job is late. A subsequent decision is made about whether a batch delivery is scheduled on completion of an appended on-time job. The completion time of the current partial schedule is stored as the function value, more precisely, we recursively compute value function $f(k, y, u, j)$ which represents the minimum completion time for processing the on-time jobs $J_1, J_2, \dots, J_j, \dots, J_k$. All processed jobs J_1, J_2, \dots, J_{j-1} are delivered using y deliveries, J_j is the first job in the last batch of the current partial schedule that is not yet scheduled for delivery, and the total number of late jobs is u , where $0 \leq y \leq k \leq n, 0 \leq u \leq n$, and $0 \leq j \leq k$.

Algorithm DP3

- **Step 1: (Initialization)** Number jobs in EDD order. Set $f(k, y, u, j) = \infty$, if $j > 0, f(k, y, u, j) > d_j$. Set $f(0, 0, 0, 0) = 0$.

- **Step 2: (Recursion)**

$$f(k, y, u, j) = \min \begin{cases} f(k - 1, y, u - 1, j), \\ f(k - 1, y, u, j) + p_k \\ \quad \text{if } 0 < j < k \text{ and } f(k - 1, y, u, j) + p_k \leq d_j, \\ \min_{j' \in J} \{f(k - 1, y - 1, u, j') + p_k\} \quad \text{if } j = k, \end{cases}$$

where $J = \{j' | 1 \leq j' \leq k - 1, f(k - 1, y - 1, u, j') + p_k \leq d_k\}$.

If $k = n$, go to Step 3; otherwise set $k = k + 1$ and repeat Step 2.

- **Step 3: (Optimal solution)**

$$\min \left\{ u + C(y) \mid \min_{1 \leq j \leq n} \{f(n, y, u, j)\}, 0 \leq u \leq n, 0 \leq y \leq n \right\}$$

and use backtracking to find the corresponding optimal schedule.

Some remarks should be made about algorithm DP3. In step 2, the first term of the minimization in the recurrence relation schedules job k to be late; the second term schedules job k to be on time and belonging to the current batch of jobs, provided that job k can be completed no later than time d_j , job j can be dispatched by its due date, no decision has yet been made about when to delivery the batch

containing jobs j and k ; the third term schedules a delivery for a batch containing j' as its first job, if $j' > 0$, starts a new batch with job k which is scheduled to be on time.

Theorem 3: Algorithm DP3 gives an optimal schedule for

$$1 | P_j = b_j t, r_j = t_0 | \sum U_j + C(y)$$

in $O(n^4)$ time.

Proof: There are $O(n^4)$ states (k, y, u, j) . The first and second terms in the recurrence relation require constant time for each state, the third term requires $O(n)$ time for each of the $O(n^3)$ states for $j = k$. Therefore, the overall time complexity of Algorithm DP3 is $O(n^4)$.

4. Conclusion

We have studied a single machine batch delivery problem under simple linear deterioration, and presented several models for scheduling problems which include a delivery cost. The aim is to find simultaneously a number of batches, a partition of the jobs into batches and a job sequence so as to minimize the scheduling cost and the delivery cost. We provided several algorithms for scheduling jobs on machine and forming batches for delivery. Therefore, our work has practical implications for the way in which scheduling and delivery decisions are made. For future research, it would be interesting to focus on the scheduling problems with batch delivery costs on parallel machines.

References

- [1] T. C. E. CHENG, H. G. KAHLBACHER: *Scheduling with delivery and earliness penalties*. Asia Pacific Journal of Operational Research 10 (1993), No. 2, 145–152.
- [2] F. AHMADIZAR, S. FARHADI: *Single-machine batch delivery scheduling with job release dates, due windows and earliness, tardiness, holding and delivery costs*. Computers & Operations Research 53 (2015), 194–205.
- [3] N. G. HAL, C. N. POTTS: *Supply chain scheduling: Batching and delivery*. Operations Research 51 (2003), No. 4, 566–584.
- [4] Y. Q. YIN, D. S. YE, G. C. ZHANG: *Single machine batch scheduling to minimize the sum of total flow time and batch delivery cost with an unavailability interval*. Information Sciences 274 (2014), 310–322.
- [5] B. MOR, G. MOSHEIOV: *Batch scheduling with a rate-modifying maintenance activity to minimize total floutime*. IJ Production Economics 153 (2014), 238–242.
- [6] E. SELVARAJAH, R. ZHANG: *Supply chain scheduling at the manufacturer to minimize inventory holding and delivery costs*. IJ Production Economics 147 (2014) 117–124.
- [7] M. ROSTAMI, O. KHEIRANDISH, N. ANSARI: *Minimizing maximum tardiness and delivery costs with batch delivery and job release times*. Applied Mathematical Modelling 39 (2015), No. 16, 4909–4927.

- [8] S. BROWNE, U. YECHIALI: *Scheduling deteriorating jobs on a single processor*. Operations Research *38* (1990), No. 3, 495–498.
- [9] G. MOSHEIOV: *Scheduling jobs under simple linear deterioration*. Computers & Operations Research *21* (1994), No. 6, 653–659.
- [10] T. C. E. CHENG, Q. DING, B. M. T. LIN: *A concise survey of scheduling with time-dependent processing times*. European Journal of Operational Research *152*, (2004), No. 1, 1–13.
- [11] J. PEI, P. M. PARDALOS, X. B. LIU, W. J. FAN, S. L. YANG: *Serial batching scheduling of deteriorating jobs in a two-stage supply chain to minimize the makespan*. European Journal of Operational Research *244* (2015), No. 1, 13–25.
- [12] Y. Q. YIN, W. H. WU, T. C. E. CHENG, C. C. WU: *Single-machine scheduling with time-dependent and position-dependent deteriorating jobs*. IJ Computer Integrated Manufacturing *28* (2015), No. 7, 781–790.

Received December 6, 2016

Aim and Scope

Acta Technica (formerly Acta Technica CSAV) is a refereed international journal founded in 1956. It is devoted to presenting progress in electrical engineering, electronics, mechatronics, thermodynamics, hydromechanics, materials science and engineering, mechanics of solids and structures, plasma physics, and others, together with corresponding mathematical and computer tools. It also covers interdisciplinary, coupled and newly emerging problems (e.g. nanotechnology, bioelectromagnetics, etc.).

Frequency: Quarterly, four times a year.

Submission of Contributions

Only contributions satisfying the following requests can be accepted:

- original works not yet published and not being under consideration for publication elsewhere,
- relating the aim and scope of the journal,
- written in a sufficiently good English and sent electronically.

The reprint of the published paper together with the complete issue will be provided to each author in electronic form in PDF.

Form of manuscript. Any standard format of T_EX (preferable) or MS Word. Use double spacing, number the pages and indent paragraphs.

Structure, style and notation. Detailed instructions are presented at

http://journal.it.cas.cz/author_guide.pdf

Read them carefully before elaborating the manuscript.

Figures. Acceptable formats: PDF, PNG (recommended for line art) and JPEG (recommended for photographs). Use black-and-white or greyscale figures. Avoid using hair lines (problems with printing).

Delivering the manuscripts. Via e-mail to the editorial office (see the inside front cover). The Editor will confirm the acceptance to the corresponding author.

Review stage. Manuscripts are usually evaluated by two independent reviews. The referees' identities are not released.

Proof stage. Authors obtain proofs in PDF via e-mail to correct possible errors. Do not return a corrected manuscript but send a list of corrections by an e-mail message (e.g. as an attachment file).

Copyright. Before publishing the paper, the authors are asked by the Editor to sign transfer of the copyright to the Publisher.

ACTA TECHNICA

Volume 61 (2016), Number 4A